Ab Initio Exploration of Interface Structures and Their Properties

Submitted by Ned Thaddeus Taylor, to the University of Exeter as a thesis for the degree of Doctor of Philosophy in Physics, October 2020.

This thesis is available for Library use on the understanding that it is copyright material and that no quotation from the thesis may be published without proper acknowledgement.

I certify that all material in this thesis which is not my own work has been identified and that any material that has previously been submitted and approved for the award of a degree by this or any other University has been acknowledged.

(Signature) . . . . . .

Ned Thaddeus Taylor

Abstract

In this thesis, material interfaces, structures and properties are studied at the atomic scale, with an emphasis on their use in clean energy applications. Interfaces can exhibit intriguing and unique physical phenomena not seen in periodic crystals. Oxide interfaces are the main focus due to the wealth of phenomena they can exhibit, in addition to the composite materials' abundance, stability and relative ease of fabrication. $CaCu_3Ti_4O_{12}$ samples have previously been shown to exhibit colossal permittivity, which has been attributed to their grain boundaries. The high permittivity of the samples is attributed to the formation of a thin dilute metal at the interface between the grain and inter-grain materials. This understanding should allow for one to artificially engineer systems that exhibit colossal permittivity, which would have uses in areas such as gas sensing and electric capacitors. The need to properly characterise interfaces is then discussed. The $BaTiO_3/SiO_2$ system is used as an example to highlight the need to properly measure and characterise interface regions, as a new material, $Ba_2TiSi_2O_8$, can form across the junction. The work then shifts to the use of interfaces directly in device designs. All-oxide solar cells have great potential to be cheaper and easier to manufacture than current silicon-based solar cells. A set of materials are explored to identify a potential all-oxide solar cell design. The setup of $CaO/(Sn:Ca)_{7:1}O/TiO_2$ is put forward as a potentially viable design for a p–i–n solar cell device. Next, oxide perovskites are investigated to identify their capabilities as photocatalytic materials for the purposes of water-splitting. $SrSnO_3$ is identified as a potential candidate for water-splitting. By introducing a thin ZrO_2 overlayer to the surface of $SrSnO_3$, the photocatalytic properties of the slab can be improved. This allows allows for bifunctional water-splitting on the surface of the $SrSnO_3|ZrO_2$ overlay system. Finally, ARTEMIS, a tool to aid in interface studies is discussed. This tool is designed to generate potentially viable interfaces, with a rudimentary function for predicting interface separation through bonding analysis. The results presented here should be of great use to anyone exploring energy technologies, as well as those studying the fundamentals of interfaces.

Acknowledgements

This thesis and all the hard work behind it was possible due to the amazing support and help of friends, family and colleagues over the past few years. I would first like to thank those colleagues and friends who have helped with the development of this work; Edward Allery Baker, Edmund Chan, Shane Graham Davies, Joe Pitfield and Isiah Edward Mikel Rudkin. I would like to give particular thanks to Conor Jason Price and Francis Huw Davies. Conor has been especially helpful with much of the work and discussions of this thesis. Meanwhile, Frank has shared in this journey since the start, providing both help and friendship during these times.

Of course, I cannot forget to mention Dr Steven Paul Hepplestone, without whom this work would not exist. He has provided the project, support, inspiration and drive to help me through this all. I am also thankful of my second supervisor, Dr Eros Mariani, who has been instrumental in me starting and completing this work. Additionally, Dr Sharon Strawbridge and Prof. G. P. Srivastava have been involved in useful discussions, which aided my understanding of core concepts and analysis of this work.

Elizabeth Martin, Rosamund Herapath and Milo Baraclough, along with many of the above people, have been there for me, providing friendship and relaxation in the form of board games, pubs, films and more. They, along with Austin, have helped me get through this time. Thank you also to Joseph Martin Stell for being there as both a friend and a proofreader, giving vital feedback on this work.

I would like to give a particular thanks for Oliver Froom for fuelling and helping grow my interest in science and discovery. During my time at school, he showed me how both science and creativity can go hand in hand.

I also want to thank my assessors, Prof. Srivastava and Dr Matt Watkins, for the enjoyable viva, in addition to Prof. Saverio Russo for ensuring that the viva was conducted smoothly.

Finally, I would like to give a special thank you to my family (with special thanks to my Mum, my Dad, Noah and Brogan Mae) and Jessica Ann Bray who have put up with me and supported me during these times. They have helped me in any way they could.

Funding acknowledgements

I would like to thank the University of Exeter College of Engineering, Mathematics and Physical Sciences for providing funding, which allowed much of this research to be conducted. Many thanks to the XM^2 Exeter Centre for Doctoral Training in Metamaterials (Grant No. EP/L015331/1) for providing additional financial and training support, as well as for allowing me to be part of a collaborative and friendly community of PhD students; the skills that I have learnt through the courses they have offered have been invaluable. The work detailed in this thesis has been supported by the UK's HEC Materials Chemistry Consortium and their funding from the EPSRC (Grant Nos. EP/L000202, EP/R029431), which has enabled us to use the ARCHER UK National Supercomputing Service. Simulations have also been performed using both the GW4 Isambard and University of Exeter High-Performance Computing facilities. Finally, I would like to thank Solaris Photonics for funding me during a 4-month studentship during my PhD. I am very grateful for these organisations who, due to their large contributions, allowed me to conduct research in a range of varied fields.

Contents

List of Figures

List of Tables

List of Publications

Chapter 3

- Ned Thaddeus Taylor, Francis Huw Davies, Shane Graham Davies, Conor Jason Price, *The Fundamental Mechanism Behind Colossal Permittivity in Oxides*, Advanced Materials, **31**(51), (2019), p. 1904746.
  DOI: 10.1002/adma.201904746

Chapter 4

- Ned Thaddeus Taylor, Francis Huw Davies and Steven Paul Hepplestone, *First principles electronic and elastic properties of fresnoite* $Ba_2TiSi_2O_8$, Materials Research Express, **4**(12), (2017), p. 125904.
  DOI: 10.1088/2053-1591/aa99e8

Chapter 5

- Ned Thaddeus Taylor, Arnaldo Galbiati, Monica Saavedra and Steven Paul Hepplestone, *Calcium-Stannous Oxide Solid Solutions for Solar Devices*, Applied Physics Letters, **117**(15), (2020), p. 153901.
  DOI: 10.1063/5.0024947

Chapter 6

- Ned Thaddeus Taylor, Conor Jason Price, Alexander Petkov, Marcus Ian Romanis Carr, Jason Charles Hale and Steven Paul Hepplestone, *The Potential of Overlayers on Tin-Based Perovskites for Water-Splitting*, The Journal of Physical Chemistry Letters, **11**(10), (2020), pp. 4124–4130.
  DOI: 10.1021/acs.jpclett.0c00964

Chapter 7

- Ned Thaddeus Taylor, Francis Huw Davies, Isiah Edward Mikel Rudkin, Conor Jason Price, Tsz Hin Chan and Steven Paul Hepplestone, *ARTEMIS: Ab initio Restructuring Tool Enabling the Modelling of Interface Structures*, Computer Physics Communications, **257**, (2020), p. 107515.
  DOI: 10.1016/j.cpc.2020.107515

Author's declaration

Analysis of all of the work presented in this thesis was performed jointly by Mr Ned Thaddeus Taylor and Dr Steven Paul Hepplestone. Useful discussions were held with Dr Eros Mariani in analysing key results.

The work in Chapter 3 was motivated by discussions with a company, Deregallera, interested in exploring colossal permittivity materials for potential energy storage applications. Mr Francis Huw Davies, Mr Conor Jason Price and Mr Shane Graham Davies helped Mr Taylor and Dr Hepplestone in the analysis of the orbital-projected density of states, as well as the partial charge density results.

The work in Chapter 4 was motivated by discussions with a company, Deregallera, interested in exploring $BaTiO_3/SiO_2$ core-shells as potential high permittivity structures and its main focus is on the characterisation of an interface material. The majority of the work was performed by Mr Taylor. Mr F. Davies performed calculations of the Raman-active phonon frequencies and helped in analysing these results.

The study detailed in Chapter 5 was performed for a company, Solaris Photonics, to investigate the potential of particular materials for use in all-oxide solar cells. The company commissioned Mr Taylor and Dr Hepplestone for four months to explore the effects alloying on the photovoltaic properties of SnO, as well as to explore potential electron and hole transport layers in the hope of devising a functioning all-oxide photovoltaic cell.

The work presented in Chapter 6 was a collaborative effort between Mr Price and Mr Taylor. Initial studies of the bulk and clean-surface properties of the four oxide perovskites presented were performed by Mr Price, Mr Alexander Petkov, Mr

Marcus Ian Romanis Carr and Mr Jason Charles Hale for their Physics Masters projects. During this initial stage, Mr Taylor helped supervise the projects along with Dr Hepplestone. For further accuracy and consistency, Mr Taylor simulated the various bulk and clean-surface structures. Results for adsorptions and overlayers were jointly performed by Mr Price and Mr Taylor.

Chapter 7 details ARTEMIS, the software program developed by Mr Taylor, Dr Hepplestone, Mr Isiah Edward Mikel Rudkin and Mr F. Davies. ARTEMIS was written by these authors, whilst discussions relating to the methods used within the program also included Mr Price and Mr S. Davies. Testing of the program was performed by the aforementioned people, as well as Mr Edward Allery Baker, Mr Joe Pitfield and Mr Tsz Hin Chan.

List of Symbols

The following list describes several symbols that are commonly used within the body of this work.

h	Planck's constant	$6.62607004 \times 10^{-34}$ J s
$\hbar$	Reduced Planck's constant	$1.054571816 \times 10^{-34}$ J s
e	Elementary charge	$1.60217662 \times 10^{-19}$ C
m_e	Electron mass	$9.10938356 \times 10^{-31}$ kg
ε_0	Permittivity of free space	$8.85418782 \times 10^{-12}$ F m^{-1}
F	Faraday constant	9.64853321×10^{4} C mol^{-1}
R	Ideal gas constant	8.31446262×10^{4} J K^{-1} mol^{-1}
i	Imaginary unit	$\sqrt{-1}$
∇	Del operator	
∇^2	Laplace operator	
E_vacuum	Vacuum energy	eV
E_Fermi	Fermi energy	eV
E_g	Band gap energy	eV
E_VBM	Energy of the valence band maximum	eV
E_CBM	Energy of the conduction band minimum	eV
E_HOMO	Energy of the highest occupied molecular orbital	eV

E_{LUMO}	Energy of the lowest unoccupied molecular orbital	eV
χ_{h}	Hole affinity	eV
μ	Chemical potential	eV
μ^0	Chemical potential at standard conditions	eV
E_f	Formation energy	eV

List of Abbreviations

The following list describes several abbreviations that are commonly used within the body of this work.

ARTEMIS *Ab initio* Restructuring Tools Enabling the Modelling of Interface Structures

BTO $BaTiO_3$

BTSO $Ba_2TiSi_2O_8$

CBM Conduction Band Minimum

CCTO $CaCu_3Ti_4O_{12}$

CGA Conjugate Gradient Algorithm

DFT Density Functional Theory

DOS Density Of States

GGA Generalised Gradient Approximation

HOMO Highest Occupied Molecular Orbital

HSE Heyd–Scuseria–Ernzerhof

LLL Lenstra-Lenstra-Lovász

LUMO Lowest Unoccupied Molecular Orbital

PBE Perdew-Burke-Ernzerhof

PC	Photocatalysis
PEC	Photoelectrochemical Cell
PV	Photovoltaic
PV-E	Photovoltaic-Electrolysis
RC	Resistor-Capacitor
SCF	Self Consistent Field
VASP	Vienna *Ab initio* Simulation Package
VBM	Valence Band Maximum
VESTA	Visualization for Electronic and Structural Analysis

Chapter 1

Introduction

“Later there will be, I hope, some people who will find it to their advantage to decipher all this mess."

— Évariste Galois

1.1 A short story on interfaces in devices

Since the dawn of mankind, humans have had a fascination with materials. From understanding how the work to how they can be used, materials have been a prevalent part of human history. The focus of such interest is strongly tied to the properties they may exhibit; in tools, this has been their strength, sharpness, and durability, with clothing, the flexibility and thermal conductivity are of use, for jewellery, it tends to be their optical properties, and in devices, the main focus is on electronic properties.

The use of materials has allowed humans to overcome their natural limitations and provide themselves with characteristics displayed by the materials around them. In the Roman era, asbestos was often woven into cloth to prevent them from being flammable [1]. In the modern era, materials are being woven into clothes to harness energy from the sun [2]. The efficiency and capability of technology is often limited only by the properties of the materials used.

The study of fundamental material properties dates back thousands of years to

Democritus and Leucippus in the 5^{th} century BCE, who are recorded as first presenting the concept of *atomos* – the indivisible building-block of matter. This is even more prevalent in *Natural History*, the works by Pliny the Elder summarising the Roman empire at the time of the 1^{st} century CE [1]. Two of the 37 books that comprise this magnum opus are devoted solely to mineralogy (with a third on metallurgy). In the aforementioned work, the properties and understandings of various minerals, metals and crystals are detailed, including asbestos (book 19), diamond (book 20), haematite (book 36) and amber (book 37).

The study of material sciences was expanded upon in the 1600s by Galileo and Newton, who set out to investigate the interactions of matter. At this time, Boyle focused strongly on the composition of individual elements and made considerable progress in techniques to allow their detection and analysis. In the 1700s, Lavoisier recognised and predicted the existence of many elements, including hydrogen, oxygen, silicon and sulphur. In the 1800s and early 1900s, various theories were developed in an attempt to fully describe the compositional make-up of matter; these were called *atomic theories*.

Solid sphere model: John Dalton is credited with the first modern atomic theory based on experiments with atmospheric gases in 1803. He built an atomic theory to describe these particles called *atoms* (based on the aforementioned Greek concept of *atomos*). These were indivisible, with each atom being of a particular type or *element*. Atoms of the same element were identical, and compounds are combinations of different types of atoms.

The understanding was further refined in the 1900s when use of electron microscopes enabled scanning and visualisation of the atomic structure of materials by those such as J. J. Thomson, Ernest Rutherford, Niels Bohr and Erwin Schrödinger.

Plum pudding model: With his discovery of electrons – subatomic, negatively charged particles – in 1897, J. J. Thomson determined that atoms were, in fact, divisible, and he went on to describe atoms as electrons scattered throughout a spherical cloud of positive charge in 1904.

Nuclear model: The next major advancement came from Ernest Rutherford in 1911, who determined that atoms were, in fact, mostly empty space, with a small positive charge located at the centre of the atom – the nucleus. This was determined by firing positively-charged alpha-particles at a thin sheet of gold foil. Interestingly, most of the alpha particles passed through with little deflection (passing through the empty space of the atoms); however, some were deflected at large angles (associated with being incident on the nucleus). This model stated that the nucleus was composed of integer multiples of protons (positively charged subatomic particles). Whilst a better model, it did not describe how electrons remain in orbit around the nucleus.

Planetary model: In 1913, Niels Bohr put forward a theory as to how electrons remain in orbit around the nucleus. Electrons were said to orbit the nucleus at fixed distances and energies. This gave the idea of quantised energy levels of electrons in an atom, where electrons could not take energy levels outside of this set.

Quantum model: In 1926, Erwin Schrödinger expanded upon the description of electrons, stating that they do not, in fact, move around the nucleus in orbital paths. Instead, they have a wave-like property to them, resulting in them being more like *clouds* surrounding the nucleus. The density of the electron-cloud defines the probability of an electron existing there. The higher density regions of the electron cloud were defined as orbitals, which are associated with the aforementioned quantised electron energy levels.

Discovery of the neutron: Up until this point, the nucleus was simply considered as being composed of integer multiples of protons. However, in 1932, James Chadwick discovered that there exists a neutral-charge subatomic particle that can reside in the atomic nucleus – the neutron.

At this time, we now have a picture of the atom as follows. An atom, composed mostly of empty space. At the centre of this atom is the nucleus, a positively charged particle composed of integer multiples of protons and neutrons. Sur-

rounding this nucleus is a negatively-charged electron cloud, where regions of higher density are associated with orbitals exhibiting quantised energy levels.

Alongside the understanding of atomic structure, methods for measuring the crystal structure (the arrangement of the individual atoms), such as X-ray diffraction [3], were being developed. Both of these areas allowed for a much greater understanding of materials such as silicon, which paved the way for devices based on semiconducting materials; with these new devices came the challenge interfaces.

Interfaces

One of the key fascinations that humans have shown with materials is the concept of combining them (which, inevitably, results in *interfaces*). Few places is this interest more apparent/prevalent than with LEGO building bricks – this is a toy designed specifically around the concept of a system of interlocking blocks. The success of LEGO – and the general shortcomings of their competitors – is due to the company's strong focus on fine-tuning the frictional properties of each brick in order to achieve tight-fitting connections, whilst still maintaining a relative ease of separability. Whilst the appeal of the product to the user is to join blocks, it is clear that the crucial aspect for the company is in the connection itself. By connecting multiple items together, one can combine the properties of two objects to return one with both. In the case of LEGO, these properties are typically height, strength and function – whilst an individual piece is relatively weak, when put together, they can be used to support the weight of a human, break steel, or even work as a fully-functioning car. The worldwide phenomenon that is the LEGO company is essentially predicated on the interface between two plastic toy bricks. However, where the join between blocks of LEGO is smooth and clear-cut, the interface between materials is generally not so well-defined.

1.2 Outline

In this thesis, an in-depth study of interfaces and their potential for device applications is presented, with a focus on oxide interfaces. Particular emphasis is also placed on identifying the most energetically favourable interface to form between any two crystals. Interfaces are explored for their affect on the properties of a material (i.e. permittivity, phase and composition) and their affect on photovoltaic and photocatalyst capabilities. The remainder of this chapter will detail the uses and key features of interfaces presented in literature thus far.

The second chapter outlines the necessary background methods and theory upon which this work is built. It explores the precursor assumptions, as well as the derivation of the theories behind density functional theory, which is used to determine the electronic and structural properties of materials in this body of work. The third chapter details an investigation into a prevalent oxide interface in literature, namely $CaCu_3Ti_4O_{12}$ grain boundaries, to explore properties that can arise due to the presence of an interface – with this example being colossal permittivity. In the fourth chapter, a study focusing on the material fresnoite ($Ba_2TiSi_2O_8$) that can form at the interface between two other materials, $BaTiO_3$ and Si (or SiO_2), is presented. The chapter aims at characterising an interface material in order to highlight the structural changes that an interface can give rise to. In Chapter 5, the potential of an all-oxide solar cell is explored. The p–i–n interface architecture of solar cells is considered and, as such, the band alignment between the active layer and numerous candidate transport layer materials are investigated. A potential setup for an all-oxide photovoltaic cell is presented. In Chapter 6, a detailed study of the potential of oxide perovskite surfaces as photocatalysts is presented, with one candidate in particular exhibiting promising capabilities. The inclusion of a thin overlayer on this material is studied, showing how it can further enhance its photocatalytic properties. In Chapter 7, we discuss the fundamental theory underlying interfaces and how this can be used to determine and predict new interfaces between materials. In the final chapter, a summary of this work is presented along with aims of where this work can be taken next.

1.3 Interfaces

An interface is defined as a point/area where two materials make physical contact. Such contact can arise either through material growth (through natural or artificial processes) or by moving materials into contact (when multiple materials are grown or cleaved and then placed in contact with each other). The properties at this point of contact tend to differ from either of the two individual materials, with new properties emerging that are dependent on the interface instead. These properties are often novel and unique [4–6], which often arise due to the breaking of periodicity of the two parent materials

In this thesis, A|B will be used to refer to any interface between materials A and B; A(hkl)/B($h'k'l'$) will denote a specific interface between materials A and B, with their orientations (planes of termination) given by (hkl) and ($h'k'l'$), respectively.

1.3.1 Types of interfaces

There exist many types of interfaces, appearing both in natural structures and man-made devices. These can include (but are not limited to) those between two solids (either 2D|2D, 2D|3D or 3D|3D interfaces), between a solid and a liquid, and interfaces between a solid or liquid and vacuum or gas. Surfaces can be considered merely as the interface between a solid and a vacuum/gas – in this body of work, it is defined as the interface between a solid and vacuum.

During natural growth of crystals (along with lab growth of a crystal from constituent melts), multiple crystal grains tend to form, with their size depending on the duration and temperature of the growth process [7]. When these form, interfaces are present at the points of contact between multiple grains. Such interfaces are generally termed as grain boundaries; however, depending on the grain sizes and the growth conditions, new inter-grain materials can form in this region. Interfaces formed via these means tend to be rather rough, with it being difficult to define a clear location to define them; instead, they can often cover a larger region, with the parent grains diffusing through each other [8].

Interfaces will arise in a device during its construction, both those that are unavoidable and intended; these include component|substrate, component|contact and component|component interfaces. Such interfaces persist after manufacturing of the device and can strongly affect the component properties, leading to changes in the efficiency of the device. Consideration of these must be taken into account when designing a device as they can, sometimes, even prevent the functioning of a device, e.g. via formation of Schottky barriers [9, 10].

Finally, some interfaces are desired parts of devices, with their properties being those intended for use by the device. Such interfaces tend to be difficult and demanding to manufacture, as their properties are often present only when the interface is smooth. With recent advancements, atomically smooth interfaces can be constructed between oxides, even within nanometre-scale devices [11].

A common term used to define an interface between conductors (or semiconductors) is an *electrical junction*. Junctions exhibit two possible forms – rectifying and non-rectifying [3]. Non-rectifying junctions are often termed *ohmic contacts*. There are various types of rectifying junctions, including metal-semiconductor junctions and p–n junctions. Devices based around interfaces can take various forms: heterostructures, heterojunctions, p–n junctions, metal–semiconductor interfaces and metal–metal interfaces.

1.3.2 Band alignment

When two materials are in contact, a major contributor to the resulting electronic properties of the overall system is the relative alignment of the two materials' energy levels. Consider, first, the case of a surface. Here, the electronic energy levels of the material can be given with respect to the the electrostatic potential of the vacuum (i.e. the vacuum level/energy), which should be a global constant for any real system, allowing this to be used as a reference energy level for all systems. In such a system, the energy required to free an electron from the material (i.e. photoemission) is dependent on the difference in energy between the material's Fermi energy (chemical potential) and the vacuum energy (i.e. the work function/hole affinity of the material). If we now consider interfaces between two

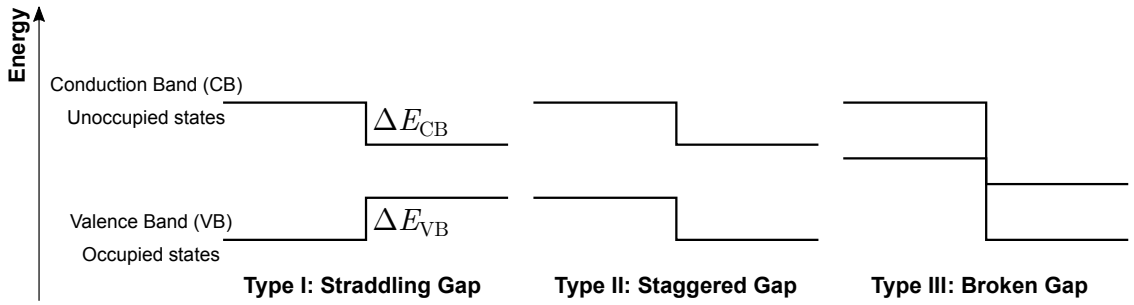

Figure 1.1: The three types of band alignment between two semiconducting/insulating materials.

materials, the difference between the two sets of energy levels can be determined by giving both sets with respect to the vacuum level. In this system, the natural direction of current flow across such an interface is dependent on this alignment.

Surface band alignment

The *work function* of a metal is defined as the difference in energy between the electrostatic potential of the vacuum E_{vacuum} and the Fermi energy E_{F} of the metal (i.e. the energy required to excite/liberate an electron from the metal to the vacuum) [3]. The work function W can be written as $W = E_{\mathrm{vacuum}} - E_{\mathrm{F}}$.

For semiconductors, there exist quantities similar to the work function: *hole* and *electron affinities* [12]. The hole affinity χ_{h} is the energy required to excite a valence electron from the valence band maximum (VBM) to the vacuum and can be written as $\chi_{\mathrm{h}} = E_{\mathrm{vacuum}} - E_{\mathrm{VBM}}$. This can also be seen as exciting a hole from the vacuum level into the valence band. The electron affinity χ_{e} is the energy required to excite an electron at the conduction band minimum (CBM) to the vacuum (i.e. liberate a conducting electron), $\chi_{\mathrm{e}} = E_{\mathrm{vacuum}} - E_{\mathrm{CBM}}$. The difference between these two affinities is the band gap E_g of the semiconductor, $E_g = \chi_{\mathrm{h}} - \chi_{\mathrm{e}}$.

Interface band alignment

We now consider an interface formed between two materials – Material 1 and Material 2. Depending on the relative energy of occupied and unoccupied states for these two materials, there are three main types of band alignment [3] (displayed

in Figure 1.1): 1) Type I band alignment – Straddling Gap – occurs when the highest occupied and lowest unoccupied states of Material 2 lie within the band gap of Material 1 (i.e. the band gap of Material 1 straddles that of Material 2). 2) Type II band alignment – Staggered Gap – forms when the highest occupied state of Material 1 lies within the band gap of Material 2 and the lowest unoccupied state of Material 1 lies above the lowest unoccupied state of Material 2. 3) Type III band alignment – Broken Gap – forms when both the highest occupied and lowest unoccupied states of Material 1 lie above the lowest unoccupied state of Material 2. Here, Materials 1 and 2 are simply placeholder names and, as such, can be swapped with each other and the definitions still hold.

At the interface between two materials, it is common for atomic reconstruction to occur in order to compensate for missing bonds of the surface atoms and to relieve strain built up by joining two materials. Sometimes, this reconstruction can be significant enough to form new phases and new materials from the constituent elements of the two individual materials [13]. Depending on the band alignment, as well as the interaction of the two materials, the specific alignment of bands can sometimes lead to the formation of barriers or wells that alter the electronic conduction characteristics across this region.

1.3.3 Non-rectifying junctions – Ohmic contacts

In a non-rectifying junction, a voltage applied across the interface causes current to flow in one direction; if the voltage direction is reversed, then so is the current flow, with the same magnitude. This occurs when forming an interface between two metals, or between a metal and a semiconductor, where the Fermi level of the metal lies outside of the band gap of the semiconductor. Such an interface is called an *ohmic contact*.

1.3.4 Rectifying junctions

Rectification is the process of producing a large current flow when a voltage is applied across a junction in one direction (forward bias), but producing only a small

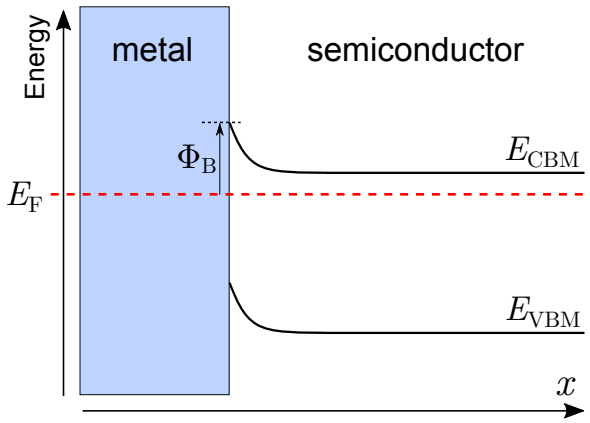

Figure 1.2: Band diagram depicting a Schottky barrier Φ_B at a metal-semiconductor junction.

current flow (or none at all) when applying a voltage in the opposite direction (reverse bias) [3]. If an alternating voltage is applied across the junction, then the current will flow mainly in one direction (i.e. the current has been rectified). When forward bias is applied, many electrons are thermally excited in the semiconductor, which allows them to pass over the barrier. Under a reverse bias, there is a much reduced current, which is due to a small leakage of thermally excited electrons in the metal being able to overcome the barrier. Rectifying junctions can form in metal-semiconductor and semiconductor-semiconductor junctions.

A charge depletion region forms within the semiconductor near the interface in which free charge combines with opposite charge from the other side of the interface. At high biases, the depletion layer will break down.

Schottky barriers

At a metal-semiconductor junction, a potential energy barrier tends to form – a *Schottky barrier* – affecting the electron band edges near the interface. In its vicinity, bending of the band edges are exhibited in the semiconductor, leading to the formation of a potential energy barrier at the interface, which is felt by the carriers. The presence of such barriers is predicted by the Schottky-Mott rule [9, 10, 14, 15].

A Schottky barrier arises due to charge depletion within the region of the semiconductor near the interface, which leads to bending of the band edges within

this semiconductor. The specific direction of the bending (i.e. towards or away from the vacuum level E_{vacuum}) is dependent on whether the semiconductor loses (towards E_{vacuum}) or gains (away from E_{vacuum}) electrons, and the size of the depletion region is dependent on the specific metal-semiconductor pair. The height of this Schottky barrier should be calculable from the work function of the metal and the electron and hole affinities of the semiconductor; however, this is rarely true due to the presence of interface defect states. A similar rule exists for semiconductor-semiconductor interfaces, called *Anderson's rule*; however, this has also been shown to rarely work for real systems [16–18].

The Schottky-Mott rule states that the height of the Schottky barrier in a metal-semiconductor junction is proportional to the work function of the metal and the electron/hole affinity of the semiconductor. However, this is rarely the case as defect states localised to the interface tend to form within the band gap of the semiconductor. The Fermi level of the metal tends to become pinned by the interface defect states to the centre of the semiconductor band gap (*Fermi level pinning*), thus, leading the Schottky barrier height to more often be dependent on the height of the semiconductor band gap.

In a rectifying Schottky barrier under a small applied voltage, there forms an associated high resistance. When a large voltage bias is applied, the current flow is governed by thermionic emission.

p–n junctions

Another form of rectifying junction is the *p-n junction* that forms between p-type and n-type doped semiconductors [3]. This is similar to the Schottky barrier in some senses. In the vicinity of the interface, the available charges in the p-type and n-type semiconductors combine and deplete the available charge. Far from the interface, the available carriers remain. In doing so, the Fermi level is pinned to the middle of the acceptor and donor levels of the two materials.

The following energy levels are given with respect to the vacuum energy and any movement of dopant levels are accompanied by an equivalent movement of the band gap in which it resides (see Figure 1.3 for a graphical depiction of the

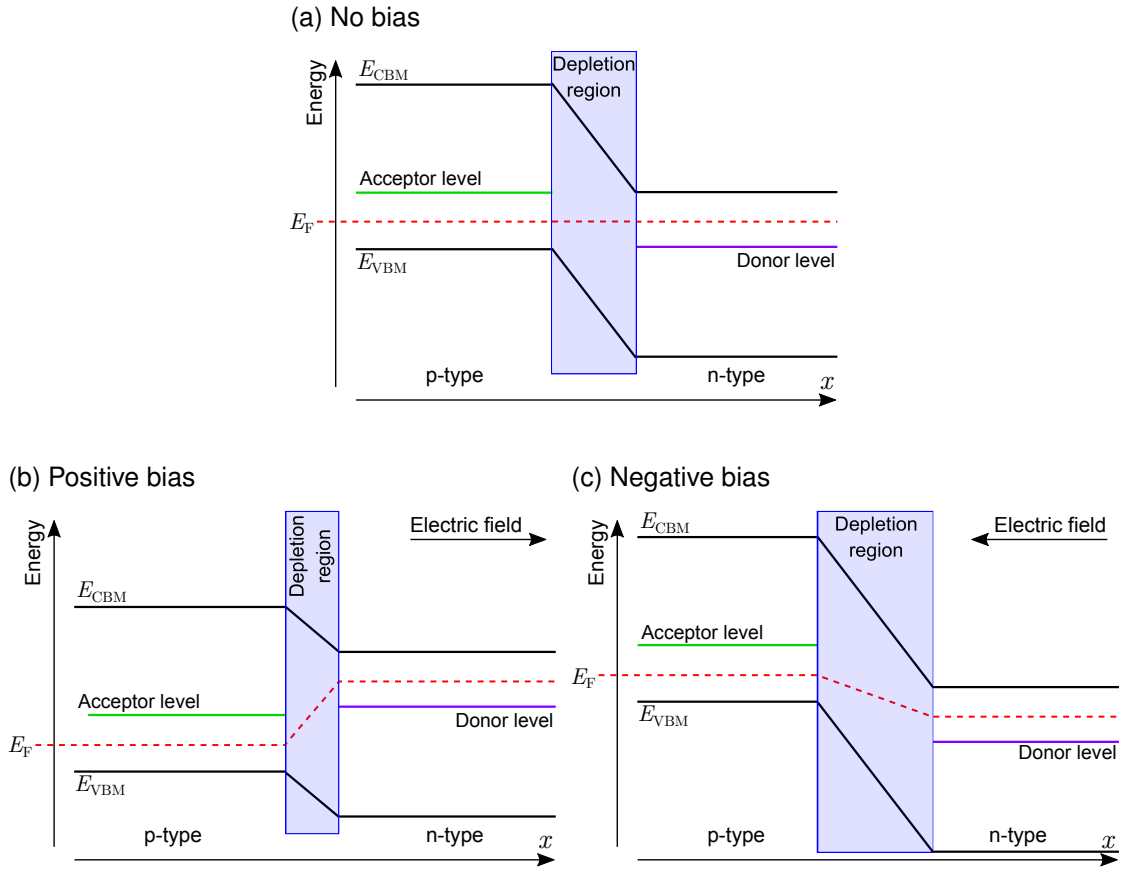

Figure 1.3: Diagram depicting a p–n junction between two semiconductors under (a) no bias, (b) a positive bias and (c) a negative bias . The semiconducting material on the left is p-type doped, whilst the semiconductor on the right is n-type doped. E_{F} denotes the Fermi energy. The shaded blue region denotes the depletion region.

effects of biases on a p–n junction). When a forward (positive) bias is applied across this junction, the acceptor level decreases in energy, whilst the donor level increases in energy. In doing so, current is allowed to flow as the donor level is raised above the acceptor level, meaning that the donor charges can freely fall into the acceptor level. This decreases the width of the depletion region. When a reverse (negative) bias is applied, the width of the depletion region increases, the acceptor level increases in energy and the donor level decreases in energy, thus increasing the barrier height of the junction. This further prevents current flow from being established across the junction.

1.3.5 The role of interfaces in devices

For many years, interfaces have shown great use in a range of devices, including resistive random-access memory (RRAM) [19], metal-oxide-semiconductor field-effect transistors (MOSFETs) [20] and p–n junctions [12]. Various reviews over the past decade have highlighted the new and fascinating properties that interfaces can exhibit [5, 6, 21], with there being a particular focus towards those formed from oxides in part due to their relative stability in air, and relative ease of growth and control.

In this work, we shall pay particular attention to the uses of oxide interfaces for energy-focused applications. Such interface structures have shown great potential in the areas of energy generation, storage and transport. Many studies have looked into their potential for use in photovoltaics [19], photocatalysis [22], electron transport [23] and short-term storage via capacitors [6].

Colossal permittivity

Over the past couple of decades, colossal permittivity (typically defined as a relative permittivity of $> 10^3$) has seen great attention due to its promise of improving the capabilities of capacitors [24–26]. This unusually high permittivity tends to link to grain boundaries that form within materials, a naturally occurring interface that forms during grain growth [27–29]. Other systems designed to exhibit colossal permittivity involve growing pure crystals [30] of a single or solid-solutions of multiple [31] ferroelectric materials on substrates. These artificial systems have shown vastly increased permittivity values and, in both cases, the question has been raised whether the interface between the material and its substrate aids in this [32–34].

Solar cells

In photovoltaics, sunlight is absorbed by a material (the *active layer*) and converted into an electron and a hole. This material is attached to a circuit with the

intent being to drive a current around the circuit by separating the electron–hole pair. Whilst this description does not highlight any important interfaces (as the absorption of light by the material can occur far from the surface), the need for interfaces arises when attempting to separate the electron–hole pair. In order to separate these pairs, an electric field needs to be applied across the active layer; a similar result can be achieved by placing a p- and n-type material either side of the active layer to form a p–i–n junction. Interfaces clearly exist between each of these components, which all affect the efficiency of the device. Finally, one method for improving the efficiency of a solar cell is to introduce multiple active layers within the device, a *multi-junction* solar cell. By specifically tailoring the interfaces present in solar cells, one can drastically improve the efficiency of the device [35, 36].

Water-splitting

The process of splitting water into hydrogen and oxygen gas through use of sunlight it called *photocatalysis*. In this process, all chemical reactions occur at the interface between the catalyst and the water. Many of the properties that define whether a material is a good photocatalyst are linked to its surface [37]: the binding energy of the individual reactants to the surface, the surface band gap, and the hole and electron affinities of the material. In order to improve the capabilities of a photocatalyst, particular interest is paid to modifying its surface properties [38–40].

1.4 Summary

In this chapter, an introduction to the properties of interfaces has been presented. The various types of interfaces, along with their presence in both naturally grown and artificially constructed systems, have been discussed, with the main types being surfaces, metal-semiconductor interfaces and semiconductor-semiconductor interfaces. It has been shown how interfaces can both plague the efficiency of a device, as well as be the central desired property of a device. Interfaces are com-

posed of two parent materials, but tend to display properties unique to the point of contact of the two materials. The presence of interfaces in devices intended for capacitor, photovoltaic and photocatalytic use has been outlined. In the following chapter, the theoretical methods and general solid-state background physics used throughout this body of work are detailed.

Chapter 2

Crystals and *ab initio* methods

"It's very hard to talk quantum using a language originally designed to tell other monkeys where the ripe fruit is"

— Terry Pratchett

2.1 Introduction

The previous chapter introduced interfaces, along with properties unique to them. In order to study an interface, one must first understand the underlying crystals and the consequences of forming an interface. After understanding the crystal form, focus shifts to the structural form of the interface; where this requires investigation of a multitude of structures in order to determine the true interface formed during experiment. After defining the structural form of the interface, an exploration of the properties, namely electronic, associated with the parent crystals and their mutual interface must be undertaken. To do so, a theory to tackle the many-body interacting system of electrons is preferred.

In this chapter, an outline the background concepts and theory behind condensed matter physics and structural prediction is given. The fundamentals of this field, from crystal structure to *ab initio* methods for calculating electronic properties are detailed and discussed. Information with regards to structural prediction, with a focus on those methods pertaining to interface structural prediction, is also discussed.

2.2 Crystal structure

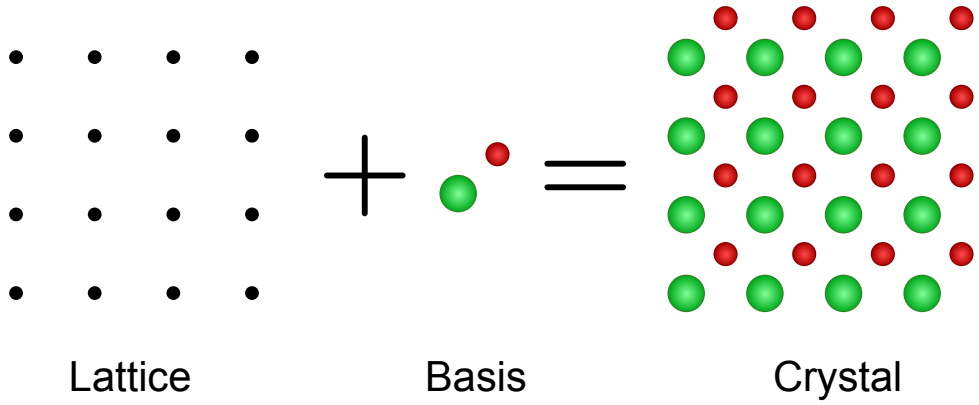

Figure 2.1: Image depicting a basis mapping onto a set of lattice points to form a crystal structure.

The crystal form is a state of matter that displays an ordered periodic structure. Here, the structure of the material is described solely by the type and location of the nuclei within a single repeat unit – the primitive cell – and the symmetries that define the repetition – the translations. The properties of a crystal are also defined uniquely within the primitive cell, with properties outside of this cell being symmetrically equivalent.

The type and position of the atoms within the primitive cell is defined as the basis. The set of translation vectors that move the primitive cell to all other cells in the crystal is called the lattice. The combination of the basis with each individual translation vector within the set generates the crystal structure, and, as such, the crystal is defined as

$$\text{crystal} = \text{lattice} + \text{basis}.$$

2.2.1 Lattice and crystal symmetries

The infinite set of translation vectors that move one unit cell to all others forms a lattice of points in real space, which is often termed as the *Bravais lattice*. The translation vectors plus the addition operators form a group, as the sum of any

two translations returns a third that is already within the set. This group is called the *translation group*, which is a purely crystalline property. For d-dimensions, the entire translation group can be reduced down to just d primitive translation vectors – the lattice vectors $\mathbf{a}_i$, where $i = 1, d$ – that, through linear combinations of integer multiples of each, can reproduce the entire translation group. Together, these lattice vectors define a parallelepiped with volume Ω_{cell} – the primitive cell.

A general translation vector for a d-dimensional lattice can be written as

$$\mathbf{T}(\mathbf{n}) \equiv \mathbf{T}(n_1, n_2, \cdots, n_d) = \sum_{i=1}^{d} n_i \mathbf{a}_i, \tag{2.1}$$

where $\mathbf{a}_i$ is the i^{th} lattice vector and n_i is any integer value. For the case of three dimensions, the form of a translation vector would be

$$\mathbf{T}(\mathbf{n}) \equiv \mathbf{T}(n_1, n_2, n_3) = n_1 \mathbf{a}_1 + n_2 \mathbf{a}_2 + n_3 \mathbf{a}_3. \tag{2.2}$$

It is quite often useful to redefine the lattice as a matrix, the *lattice matrix*,

$$\mathbf{A} = \begin{pmatrix} a_{11} & a_{12} & a_{13} \\ a_{21} & a_{22} & a_{23} \\ a_{31} & a_{32} & a_{33} \end{pmatrix} \tag{2.3}$$

where the the rows of the matrix are the individual lattice vectors $\mathbf{a}_1$, $\mathbf{a}_2$ and $\mathbf{a}_3$ (the first index of the elements defines the associative lattice vector and the second index defines the dimension of the element). The lattice matrix offers more simple methods for determining the lattice features over that of the lattice vectors, whilst also being general for any d-dimensional lattice. For example, the volume Ω_{cell} of the primitive cell is simply the determinant of the lattice matrix.

The lattice can be separated further into its geometry and symmetry. The lattice geometry describes the repetition of a unit cell according to axial lengths, often termed *lattice constants*, and the interaxial angles. In three dimensions, these lengths and angles can have the form of 1 of 7 *lattice systems* – triclinic, monoclinic, orthorhombic, tetragonal, cubic, hexagonal and trigonal. Within these

systems, there also exist *lattice types* – primitive, body centred, face centred and base centred. Combining these results in 14 unique detailed descriptors for general lattices; the 14 Bravais lattices. Each of these Bravais lattices has a different relation between the three lattice lengths and angles that are general descriptors of the periodicity of the lattice.

The symmetry of a lattice can be described by considering symmetry operations that, when applied to the crystal, leave a particular point in space fixed, (i.e. rotations). The group formed of these symmetry operations is called the *point group*. By considering both the point group and the 7 lattice systems, 32 unique *crystallographic point groups* are identified, which are independent of the lattice type. It should be noted that these point groups are apart from the translation group of the lattice and can be used to describe the symmetries of a non-periodic structure, such as a molecule.

The combination of the lattice types and the point groups leads to the full 230 unique *space groups*, with each being a full descriptor of the symmetries of the lattice and, when combined with the lattice lengths and angles can fully recreate the lattice structure.

2.2.2 Reciprocal lattice and Brillouin zone

As seen in the previous section, the lattice in real (direct) space is very useful for describing and understanding the crystal structure. However, in order to study the properties of a crystal, such as their diffraction properties, it is extremely helpful to define the reciprocal lattice. The space generated by the reciprocal lattice points is called the *reciprocal space* (also termed as inverse space, momentum space, Fourier space, and $\mathbf{k}$-space). Just as real space has translation vectors $\mathbf{T}(\mathbf{n})$, there are equivalent translation vectors $\mathbf{G}(\mathbf{m})$ between any two reciprocal lattice points

$$\mathbf{G}(\mathbf{m}) \equiv \mathbf{G}(m_1, m_2, \cdots, m_d) = \sum_{i=1}^{d} m_i \mathbf{b}_i, \tag{2.4}$$

where, again, d defines the number of dimensions. In three dimensions, the form is

$$\mathbf{G}(\mathbf{m}) \equiv \mathbf{G}(m_1, m_2, m_3) = m_1\mathbf{b}_1 + m_2\mathbf{b}_2 + m_3\mathbf{b}_3. \tag{2.5}$$

$\mathbf{b}_i$ are primitive translation vectors of the reciprocal space, the *reciprocal lattice vectors*, with the general definition

$$\mathbf{B} = 2\pi(\mathbf{A}^{\mathrm{T}})^{-1}. \tag{2.6}$$

From this, it can be shown that $\mathbf{G} \cdot \mathbf{T} = 2\pi N$, where N is an integer. Hence, the following mapping exists between direct lattice and reciprocal lattice:

$$\exp(\mathrm{i}\mathbf{G} \cdot \mathbf{T}) = 1. \tag{2.7}$$

The Wigner-Seitz cell, the primitive cell of the reciprocal lattice, can be constructed by using the vectors $\mathbf{b}_1$, $\mathbf{b}_2$ and $\mathbf{b}_3$. This cell is also called the central *Brillouin zone*, with volume Ω_{BZ} equal to

$$\Omega_{\mathrm{BZ}} = \det|\mathbf{B}| = \frac{\Omega_{\mathrm{cell}}}{(2\pi)^3}. \tag{2.8}$$

As the Brillouin zone is constrained by the point group symmetry of the reciprocal lattice and, hence of the corresponding direct lattice, there exists a reduced Brillouin zone that uniquely describes the full central Brillouin zone (which itself describes the entire reciprocal space). Take, for example, a crystal with M point operations: for any function $f(\mathbf{k})$ of a vector $\mathbf{k}$ inside the Brillouin zone, there exists unique values only for $\mathbf{k}$-vectors lying in the $(1/M)^{th}$ part of the Brillouin zone. This reduced segment is called the *irreducible Brillouin zone*.

2.2.3 Basis

As mentioned previously, the basis is a descriptor of the type and position of atoms in the primitive cell, relative to a chosen origin; as such, the basis can be defined as a set of position vectors for each atomic species present in the crystal. Whilst the basis vectors $\boldsymbol{\tau}$ can be represented in either Cartesian or lattice (direct) coordinates, we will mainly use three-dimensional direct coordinates throughout the body of this work:

$$\boldsymbol{\tau}_{sj}(\mathbf{u}_{sj}) = u_{1,sj}\mathbf{a}_1 + u_{2,sj}\mathbf{a}_2 + u_{3,sj}\mathbf{a}_3 \equiv \{u_{1,sj}, u_{2,sj}, u_{3,sj}\}, \tag{2.9}$$

where s is the species index, j is the atomic index unique for each species, and $0 \leq u_i < 1$. Here, $u_{i,sj}$ denotes the distance along the i^{th} lattice vector that the j^{th} atom of the s^{th} species is located (i.e. direct coordinates).

The full position vector $\mathbf{R}$ of any atom within the crystal is given by the linear combination of a lattice translation vector and the basis vector,

$$\mathbf{R} = \mathbf{T} + \boldsymbol{\tau}. \tag{2.10}$$

It is worth noting that the set of basis atoms, too, can be reduced using the point group. As the point group defines unique points within the primitive cell, the primitive cell can be reduced down to just these points – where the entire cell can be reconstructed by applying the point group operations to the reduced cell. If we reduce the basis in the same manner, we find an irreducible subbasis, where atoms within this set are unique. The positions of this reduced set of atoms can now be defined using Wyckoff positions, which are the particular points that are left invariant after applying the point group operations. The full crystal can be reconstructed by applying all possible permutations of the space group symmetry operators to the irreducible atomic basis.

2.2.4 Miller planes

An interface between two parent crystals is the contact of the surfaces of each crystal; to form an interface one must first form surfaces for the two parent crystals. When cleaving a crystal, it tends to split along definite crystallographic planes with high concentrations of lattice points [41, 42]; other methods of forming crystal surfaces, such as growth, also tend towards these planes. As such, it is important for surface and interface physics to understand the crystallographic planes of a material. Such crystallographic planes are termed the *Miller planes*, which correspond to planes of atoms present within the crystal [43].

The orientation of a crystal plane can either be described by non-collinear three points in the plane, or by the vector normal to this plane. Both methods are valid ways of defining Miller planes. Here, we outline the latter method.

We first define a reciprocal vector $\mathbf{g}$, described by three integer values, h, k and l, the *Miller indices*;

$$\mathbf{g}_{hkl} = h\mathbf{b}_1 + k\mathbf{b}_2 + l\mathbf{b}_3. \tag{2.11}$$

We then define the real-space planes perpendicular to this reciprocal vector as being the Miller planes, denoted as (hkl). It is clear that this vector is, itself, one of the reciprocal lattice vectors, as h, k and l are always integers.

(hkl) is commonly written with integers that have the smallest possible greatest common divisor, as their ratios are the defining feature of the plane. As mentioned previously, materials tend to cleave along planes with high concentrations of lattice points; such planes tend to be related to sets of small Miller indices [41].

Miller indices can also be used to denote the *Miller direction* $[hkl]$ that define a direction in the direct lattice – this vector is not generally normal to the Miller plane.

See Appendix A for an alternative description of Miller planes.

2.3 Periodic boundary conditions

For any function defined within a d-dimensional crystal with translation vectors $\mathbf{T}$ (2.1), the function must satisfy the condition

$$f(\mathbf{r} + \mathbf{T}(n_1, n_2, \cdots)) = f(\mathbf{r}), \tag{2.12}$$

where $\mathbf{r}$ is the variable position vector for the function. This condition is the *Born-von Karman boundary condition*, which states that any function that describes a crystal is also subject to the same periodicity of the crystal (i.e. the function and the crystal both have the same boundary conditions) [3]. This can, instead, be represented in Fourier space by Fourier transforming the function at wave vector $\mathbf{q}$. When considering a a large volume of crystal Ω_{crystal} composed of $N_{\text{cell}} = N_1 \times N_2 \times \cdots$, we can restrict the Fourier components simply to those that are periodic within this crystal. Each of these Fourier components must, then, satisfy the Born-von Karman periodic boundary condition in each dimension,

$$\exp(\mathrm{i}\mathbf{q} \cdot N_1\mathbf{a}_1) = \exp(\mathrm{i}\mathbf{q} \cdot N_2\mathbf{a}_2) = \cdots = 1. \tag{2.13}$$

In doing so, wave vector $\mathbf{q}$ is restricted to the discrete values that satisfy $\mathbf{q} \cdot N_i\mathbf{a}_i = 2\pi \times \text{integer}$ for each dimension i. Hence, the Fourier transform is

$$f(\mathbf{q}) = \frac{1}{\Omega_{\text{crystal}}} \int_{\Omega_{\text{crystal}}} f(\mathbf{r}) \exp(\mathrm{i}\mathbf{q} \cdot \mathbf{r}) d\mathbf{r}. \tag{2.14}$$

For a periodic function, we can expand the Fourier transform as follows:

$$\begin{aligned} f(\mathbf{q}) &= \frac{1}{\Omega_{\text{crystal}}} \sum_{n_1, n_2, \cdots} \int_{\Omega_{\text{cell}}} f(\mathbf{r}) \exp\left(\mathrm{i}\mathbf{q} \cdot (\mathbf{r} + \mathbf{T}(n_1, n_2, \cdots))\right) d\mathbf{r} \\ &= \frac{1}{N_{\text{cell}}\Omega_{\text{cell}}} \sum_{n_1, n_2, \cdots} \exp(\mathrm{i}\mathbf{q} \cdot \mathbf{T}(n_1, n_2, \cdots)) \times \int_{\Omega_{\text{cell}}} f(\mathbf{r}) \exp(\mathrm{i}\mathbf{q} \cdot \mathbf{r}) d\mathbf{r}, \end{aligned} \tag{2.15}$$

where $\Omega_{\text{crystal}} = N_{\text{cell}}\Omega_{\text{cell}}$. In order for Equation (2.14) and Equation (2.15) to be the same, the exponent containing the translation vector must be unity; this

occurs when $\mathbf{q} \cdot \mathbf{T}(n_1, n_2, \cdots) = 2\pi \times \text{integer}$, with all other values of $\mathbf{q}$ leading to the Fourier transform equalling zero. One can extend this further to show that, as $\mathbf{T}(n_1, n_2, \cdots)$ is a sum over integer multiples of the primitive lattice vectors $\mathbf{a}_j$, then $\mathbf{q} \cdot \mathbf{a} = 2\pi \times \text{integer}$.

The restriction of the Fourier components $\mathbf{q}$ leaves us with the reciprocal lattice. By defining the reciprocal lattice vectors $\mathbf{b}_j$, where $j = 1, d$, as

$$\mathbf{b}_j \cdot \mathbf{a}_i = 2\pi\delta_{ij} \quad \text{for} \quad j = 1, \cdots, d, \tag{2.16}$$

the only non-zero Fourier components are found to be $\mathbf{q} = \mathbf{G}$, where the $\mathbf{G}$ vectors are a sum of integer multiples of the reciprocal lattice vectors (2.4) (i.e. the reciprocal lattice). We can now define the Fourier transform of our function as

$$f(\mathbf{G}) = \frac{1}{\Omega_{\text{cell}}} \int_{\Omega_{\text{cell}}} f(\mathbf{r}) \exp(\mathrm{i}\mathbf{G} \cdot \mathbf{r}) d\mathbf{r}. \tag{2.17}$$

Here, we have seen that a function $f(\mathbf{r})$ defined within a crystal can be transformed into reciprocal space, where the Fourier components $\mathbf{G}$ of this reciprocal form $f(\mathbf{G})$ are restricted to a set of values that are defined by the periodicity of the cell.

Bloch's theorem

Previously, we mentioned that any function of a crystal must be constrained to the same periodicity as the crystal. This can be re-postulated in terms of operators: for a periodic crystal, any operator must be invariant to any lattice translation $\mathbf{T}(\mathbf{n})$. Let us consider the Hamiltonian operator $\hat{H}$ for the Schrödinger equation for independent particles

$$\hat{H}\psi_i(\mathbf{r}) = \left[-\frac{\hbar^2}{2m_{\mathrm{e}}} \nabla^2 + V(\mathbf{r}) \right] \psi_i(\mathbf{r}) = \epsilon_i \psi_i(\mathbf{r}), \tag{2.18}$$

where $\mathbf{r}$ is a position vector, ∇ is the derivative operator, $V(\mathbf{r})$ is an external potential, and ϵ_i and ψ_i are eigenvalues and eigenfunctions of the system, respectively.

The operator $\hat{H}$ is invariant to all lattice translations since $V(\mathbf{r})$ has periodicity of the crystal and the derivative operator is invariant to any translation. As such, we can define a translation operator, $\hat{\mathcal{T}}_{\mathbf{n}}$, that, when acting on the wave function, displaces the arguments of said wave function by vector $\mathbf{n}$,

$$\hat{\mathcal{T}}_{\mathbf{n}}\psi(\mathbf{r}) = \psi\left[\mathbf{r} + \mathbf{T}(\mathbf{n})\right] = \psi(\mathbf{r} + n_1\mathbf{a}_1 + n_2\mathbf{a}_2 + \cdots). \tag{2.19}$$

Here, $\mathbf{n} = (n_1, n_2, \cdots)$ is the argument of the lattice translation vector $\mathbf{T}$ (Equation (2.1)). As the Hamiltonian operator is invariant to any lattice translations $\mathbf{T}(\mathbf{n})$, then it must be commutative with the translation operator,

$$\hat{H}\hat{\mathcal{T}}_{\mathbf{n}} = \hat{\mathcal{T}}_{\mathbf{n}}\hat{H}. \tag{2.20}$$

A key feature of the translation operator is that the product of any two translation operators (which each represents a translation vector) results in a third translation operator; the translation vector represented by this resultant operator is merely the summation of the two initial translation vectors. This can be written as the relation

$$\hat{\mathcal{T}}_{\mathbf{n}_1}\hat{\mathcal{T}}_{\mathbf{n}_2} = \hat{\mathcal{T}}_{\mathbf{n}_1+\mathbf{n}_2}. \tag{2.21}$$

The eigenvalues $t_{\mathbf{n}}$ associated with the translation operator $\hat{\mathcal{T}}_{\mathbf{n}}$ when acting on the wave function $\psi(\mathbf{r})$,

$$\hat{\mathcal{T}}_{\mathbf{n}}\psi(\mathbf{r}) = t_{\mathbf{n}}\psi(\mathbf{r}), \tag{2.22}$$

must obey the relations

$$\hat{\mathcal{T}}_{\mathbf{n}_1}\hat{\mathcal{T}}_{\mathbf{n}_2}\psi(\mathbf{r}) = t_{(\mathbf{n}_1+\mathbf{n}_2)}\psi(\mathbf{r}) = t_{\mathbf{n}_1}t_{\mathbf{n}_2}\psi(\mathbf{r}). \tag{2.23}$$

Using the relations between translation eigenvalues (2.23), we rewrite the general translation eigenvalue $t_{\mathbf{n}}$ as a product of a primitive set $t(\mathbf{a}_i)$

$$t_{\mathbf{n}} = \prod_{i=1}^{d} [t(\mathbf{a}_i)]^{n_i}. \tag{2.24}$$

It is clear that the modulus of each $t(\mathbf{a}_j)$ must be unity, otherwise, any function that obeys Equation (2.24) would not be bounded and, hence, be either zero or infinite. From this, along with the requirement that the eigenfunctions satisfy the periodic boundary conditions of Equation (2.13), we can deduce the form of each $t(\mathbf{a}_i)$ to be

$$t(\mathbf{a}_i) = \exp(\mathrm{i}2\pi/N_i). \tag{2.25}$$

where N_i is the number of cells along the i^{th} dimension. This normalisation arises as the product of all possible translations along the i^{th} dimension must be unity, $(t(\mathbf{a}_i))^{N_i} = 1$. Using the definition of primitive reciprocal lattice vectors from Equation (2.16), we can define $t_{\mathbf{n}}$ as

$$t_{\mathbf{n}} = \exp(\mathrm{i}\mathbf{k} \cdot \mathbf{T}_{\mathbf{n}}), \tag{2.26}$$

where

$$\mathbf{k} = \sum_{i=1}^{d} \frac{n_i}{N_i} \mathbf{b}_i \tag{2.27}$$

is a reciprocal space vector. Here, $\mathbf{k}$ has been restricted to values within one primitive cell of the reciprocal lattice, with $\mathbf{k}$ having the same number of values as the number of cells, N_{cell}.

By substituting Equation (2.26) into Equation (2.22), we get the desired result of

$$\hat{\mathcal{T}}_{\mathbf{n}} \psi(\mathbf{r}) = \psi(\mathbf{r} + \mathbf{T}_{\mathbf{n}}) = \exp(\mathrm{i}\mathbf{k} \cdot \mathbf{T}_{\mathbf{n}}) \psi(\mathbf{r}) \tag{2.28}$$

which is the *Bloch theorem*. This theorem states that eigenstates of the translation operators vary from one cell to another with a phase factor of $\exp(\mathrm{i}\mathbf{k} \cdot \mathbf{T}_{\mathbf{n}})$. It follows on that we can rewrite the wave function in the form

$$\psi_{\mathbf{k}}(\mathbf{r}) = \exp(\mathrm{i}\mathbf{k}\cdot\mathbf{r})u_{\mathbf{k}}(\mathbf{r}) \tag{2.29}$$

where $u_{\mathbf{k}}(\mathbf{r})$ is called the *cell-periodic part* and has the periodicity of the underlying crystal ($u_{\mathbf{k}}(\mathbf{r}+\mathbf{T_n}) = u_{\mathbf{k}}(\mathbf{r})$).

Here, it has been shown that, whilst eigenstates of the independent-particle Hamiltonian do not generally have the periodicity of the corresponding crystal, these eigenstates can still be represented as a plane-wave times by a function with the periodicity of said crystal. This plane-wave has only $\mathbf{k}$-vectors within the primitive cell, with its number of possible values equal to the number of cells within the crystal. This theorem is very general as this derivation has made no assumption as to the particle being considered nor the strength of the potential. As such, the Bloch theorem is a widely applicable theory throughout condensed matter physics.

2.4 Mathematics of *ab initio* electronic structure calculations

In the previous section, we have introduced the concept of the Schrödinger equation for a system of independent particles. Whilst this case has its uses, most properties of a crystal are related to more complex systems, namely those involving interacting particles. Through analytical means, the full Schrödinger equation can be solved exactly only for a few cases (such as the system of independent particle), even using numerical solution by integration is not feasible for most other cases. To circumvent this, approximations are introduced and used in order to reduce the problem to a much simpler one. In this section, we shall outline various methods employed in condensed matter physics to simplify the problem. For simplicity and brevity of equations, Hartree atomic units ($\hbar = m_{\mathrm{e}} = e^2 = 1$) will be

used throughout the remainder of this chapter, unless specified otherwise.

2.4.1 Variational principle

Here, we outline the variational method, which is the most commonly used approach to solve the Schrödinger equation in condensed matter physics [44]. We start with a Hamiltonian H and a function ψ – where ψ can be varied as long as it remains normalised. Whilst ψ is not, in general, an eigenfunction of $\hat{H}$, the expectation value of the Hamiltonian for such a function can still be defined as

$$\left\langle \hat{H} \right\rangle = \int \psi^* \hat{H} \psi dv, \tag{2.30}$$

where v represents all integration coordinates.

Functions ψ that result in $\left\langle \hat{H} \right\rangle$ being stationary are eigenfunctions of the energy (i.e. the Schrödinger equation is equivalent to a stationary condition) – this is the variational principle. Here, stationary refers to expectation values that do not vary to the first order under small variations of function. To prove this, we will introduce a small variation $\delta\psi$ into the wave function. As, in general, such a variation removes normalisation, we shall use the general form of the expectation value valid also for non-normalised functions:

$$\left\langle \hat{H} \right\rangle = \frac{\int \psi^* \hat{H} \psi dv}{\int \psi^* \psi dv}. \tag{2.31}$$

By considering a small modification of the wave function, $\psi \to \psi + \delta\psi$, the expectation value becomes

$$\begin{aligned} \left\langle \hat{H} \right\rangle + \delta \left\langle \hat{H} \right\rangle =& \frac{\int \left(\psi^* + \delta\psi^*\right) \hat{H} \left(\psi + \delta\psi\right) dv}{\int \left(\psi^* + \delta\psi^*\right) \left(\psi + \delta\psi\right) dv} \\ =& \frac{\int \psi^* \hat{H} \psi dv + \int \delta\psi^* \hat{H} \psi dv + \int \psi^* \hat{H} \delta\psi dv}{\int \psi^* \psi dv + \int \delta\psi^* \psi dv + \int \psi^* \delta\psi dv}. \end{aligned}$$

We now employ the following approximations, which are valid here as the considered perturbation $\delta\psi$ of the wave function is defined as being small. We first omit

second-order terms in $\delta\psi$, then use the approximation $1/(1+x) \simeq 1-x$ (where $x << 1$). In doing so, we get

$$\left\langle \hat{H} \right\rangle + \delta \left\langle \hat{H} \right\rangle \approx \left(\int \psi^* \hat{H} \psi dv + \int \delta\psi^* \hat{H} \psi dv + \int \psi^* \hat{H} \delta\psi dv \right) \times \frac{1}{\int \psi^* \psi dv} \left(1 - \frac{\int \delta\psi^* \psi dv}{\int \psi^* \psi dv} \frac{\int \psi^* \delta\psi dv}{\int \psi^* \psi dv} \right). \tag{2.32}$$

By applying the multiplication, we define the change in the expectation value due to the perturbation as

$$\delta \left\langle \hat{H} \right\rangle = \frac{\int \delta\psi^* \hat{H} \psi dv}{\int \psi^* \psi dv} + \frac{\int \psi^* \hat{H} \delta\psi dv}{\int \psi^* \psi dv} - \left\langle \hat{H} \right\rangle \left(\frac{\int \delta\psi^* \psi dv}{\int \psi^* \psi dv} + \frac{\int \psi^* \delta\psi dv}{\int \psi^* \psi dv} \right). \tag{2.33}$$

As one of the terms in the parentheses is the complex conjugate of the other, and the remaining terms outside are also complex conjugates of each other – which can be shown by noting that $\hat{H}$ is a Hermitian operator – we can simplify Equation (2.33) to

$$\delta \left\langle \hat{H} \right\rangle = \left(\frac{\int \delta\psi^* \hat{H} \psi dv}{\int \psi^* \psi dv} + \text{c.c.} \right) - \left\langle \hat{H} \right\rangle \left(\frac{\int \delta\psi^* \psi dv}{\int \psi^* \psi dv} + \text{c.c..} \right). \tag{2.34}$$

If we assume that ψ is chosen such that $\left\langle \hat{H} \right\rangle$ is stationary with respect to any variation (i.e. it is at a minima), then $\delta \left\langle \hat{H} \right\rangle = 0$, which leads to

$$\int \delta\psi^* \left[\hat{H} - \left\langle \hat{H} \right\rangle \right] \psi dv + \text{c.c.} = 0, \tag{2.35}$$

with $\delta\psi$ being an arbitrary variation. Hence

$$\left[\hat{H} - \left\langle \hat{H} \right\rangle \right] \psi = 0, \tag{2.36}$$

which shows that ψ is a solution of the Schrödinger equation:

$$\hat{H}\psi = E\psi. \tag{2.37}$$

Here, we see that, within a small perturbation from the minima, the wave function ψ is an eigenfunction of the energy, which relates to the Schödinger equation being equivalent to the stationary condition. This is the variational principle.

Ground state energy

Let us now investigate how the variational principle allows us to determine the ground state energy. We start by considering the eigenfunctions ψ_n of the Hamiltonian H which has associated eigenvalues E_n;

$$\hat{H}\psi_n = E_n\psi_n. \tag{2.38}$$

The ground state is labelled as $n = 0$, so the ground state energy is E_0. We can expand the complete wave function ψ into a summation of the the energy eigenfunctions ψ_n, as the energy eigenfunctions are a complete orthonormal set. Using the form

$$\psi = \sum_n c_n\psi_n, \tag{2.39}$$

we get

$$\begin{aligned}\left\langle \hat{H} \right\rangle &= \frac{\int \psi^* \hat{H} \psi dv}{\int \psi^* \psi dv} \\ &= \frac{\sum_n |c_n|^2 E_n}{\sum_n |c_n|^2} \\ &= E_0 + \frac{\sum_n |c_n|^2 (E_n - E_0)}{\sum_n |c_n|^2}.\end{aligned} \tag{2.40}$$

All energy eigenvalues E_n must have greater than or equal energy to the ground state energy; $E_n \geq E_0$, as is the definition of the ground state energy. Hence, the second term in Equation (2.40) must be positive or zero. This tells us that any function ψ results in an expectation energy that is an upper limit for the energy

of the ground state. By varying ψ over a set of functions, one can identify the function that minimises $\langle H \rangle$. This is the *variational method*:

$$\left\langle \hat{H} \right\rangle \geq E_0. \tag{2.41}$$

The variational method can be reapplied for the first, and higher-order, excited states, in order to approximate all of the stationary eigenstates; e.g.

$$\left\langle \hat{H} \right\rangle \geq E_1. \tag{2.42}$$

It should be noted, however, that the errors are cumulative in this method. Therefore, any approximations of highly excited states are unlikely to be very accurate. As such, only the ground state and first few excited states of a complicated quantum system should be truly meaningful.

2.4.2 Orthonormal basis sets

Here, we reduce the variational method down to an algebraic problem. In order to do so, we expand the total wave function ψ into a finite set of basis functions and apply the variational method to this new basis set in order to determine the optimal coefficients of expansion. From Equation (2.37), we define a functional, $G[\psi]$,

$$G[\psi] = \langle \psi | \hat{H} | \psi \rangle - E \langle \psi | \psi \rangle \tag{2.43}$$

and impose the stationary condition on it.

It should be noted that, in general, it is not possible to write the function ψ as a linear combination of a finite number of basis functions. However, as it is impractical to work with an infinite basis set, we limit ψ to being a linear combination of N functions and find the ψ function fitting this form that best approximates the true ground state. This expansion of the total wave function, ψ, is written as

$$\psi = \sum_{i=1}^{N} c_i b_i, \tag{2.44}$$

where b_i are an orthnormal basis set. Due to the definition of the basis set, the following orthonormality relations hold:

$$\langle b_i | b_j \rangle \equiv \int b_i^* b_j dv \equiv \delta_{ij}. \tag{2.45}$$

By substituting Equation (2.44) into Equation (2.43), we obtain

$$\begin{aligned} G(c_1, \cdots, c_N) &= \sum_{i,j} c_i^* c_j H_{ij} - E \sum_{i,j} c_i^* c_j \delta_{ij} \\ &= \sum_{i,j} c_i^* c_j \left(H_{ij} - E\delta_{ij} \right), \end{aligned} \tag{2.46}$$

where H_{ij} are the matrix elements of the square matrix Hamiltonian:

$$H_{ij} = \langle b_i | \hat{H} | b_j \rangle . \tag{2.47}$$

By means of the variational method, we can minimise Equation (2.46) with respect to its coefficients, $\frac{\partial G}{\partial c_i} = 0$, which gives us

$$\sum_{i,j} (H_{ij} - E\delta_{ij}) c_j = 0. \tag{2.48}$$

In general, this system has only the trivial solution of $c_j = 0$. For systems where non-trivial solutions exist, the following condition must be met:

$$\det |H_{ij} - E\delta_{ij}| = 0 \tag{2.49}$$

This is known as the secular equation and can be written in matrix form as

$$\mathbf{Hc} = E\mathbf{c}. \tag{2.50}$$

$\mathbf{H}$ is the $N \times N$ Hamiltonian square matrix, whose elements are H_{ij}. The solution, $\mathbf{c}$, is the vector composed of coefficients c_i and is also defined as the eigenvectors. From Equation (2.50), we get N eigenvector solutions, one for each row in the matrix $\mathbf{H}$:

$$\psi_k = \sum_i C_{ik} b_i, \qquad k = 1, \cdots, N, \tag{2.51}$$

where C_{ik} is a fundamental matrix composed of c_j (as c_j can be described as linearly independent solutions of the system). As such, each independent eigenvector can must satisfy $\hat{H}\psi_k = E_k\psi_k$ and, taking the i^{th} element, can be written as

$$(\hat{H}\psi_k)_i = \sum_j H_{ij} C_{jk} = E_k C_{ik}. \tag{2.52}$$

Equation (2.52) can be solved using the process of diagonalisation. This can be performed due to the form of C, in which it can be viewed as a transformation matrix between the starting set of N basis functions b_i to the final N set ψ_k. Because of this property, one can show that, if the basis set b_i are orthonormal, then the ψ_k functions are orthonormal as well

$$\begin{aligned}
\int \psi_j^* \psi_k d\mathbf{r} &= \int \sum_{i,l} C_{lj}^* b_l^* C_{ik} b_i d\mathbf{r} \\
\int \delta_{jk} d\mathbf{r} &= \int \sum_{i,l} C_{lj}^* C_{ik} \delta_{lj} d\mathbf{r} \\
\int \delta_{jk} d\mathbf{r} &= \int \sum_{i} C_{ij}^* C_{ik} d\mathbf{r} \\
\delta_{jk} &= \sum_i C_{ij}^* C_{ik}.
\end{aligned} \tag{2.53}$$

In matrix notation, this can be expressed as

$$(C^{-1})_{ij} = C_{ji}^* \equiv C_{ij}^\dagger, \tag{2.54}$$

where it is clear that C is a unitary matrix. We shall now consider the effect of the transformation matrix C on the Hamiltonian:

$$\begin{aligned}\left(C^{-1}\hat{H}C\right)_{kn} &= \sum_{i,j}\left(C^{-1}\right)_{ki} H_{ij}C_{in} \\ &= \sum_{i} C^{*}_{ik}\sum_{j} H_{ij}C_{jn} \\ &= \sum_{i} C^{*}_{ik}E_{n}C_{in} \\ &= E_{n}\sum_{i} C^{*}_{ik}C_{in} \\ &= E_{n}\delta_{kn}.\end{aligned} \tag{2.55}$$

Here, we find that the transformation matrix, C, reduces H to a diagonal matrix, with the non-zero N diagonal elements are the eigenvalues. We can now reconsider the eigenvalue problem as a search for a transformation matrix that moves us from the original basis to a new basis set in which H has the form of a diagonal matrix.

Plane-wave basis sets

Previously, we have shown that a finite orthogonal basis set can be used to approximate the total wave function of a system; we shall now consider the form of the individual basis functions. Plane-waves are particularly useful in describing a set of individual basis functions that represent electronic states due to the following features they exhibit: 1) their non-localised form makes them good descriptors for the states of loosely-bound (valence) electrons, 2) their form allows a set of them to easily represent an orthogonal basis, and 3) their amplitude is periodic, allowing them to work well within periodic boundary conditions.

We start by defining the independent particle Schrödinger-like equation for a set of non-interacting electrons within an effective potential $V_{\text{eff}}(\mathbf{r})$ as

$$\hat{H}_{\text{eff}}(\mathbf{r})\psi_{j}(\mathbf{r}) = \left[-\frac{1}{2}\nabla^{2} + V_{\text{eff}}(\mathbf{r})\right]\psi_{j}(\mathbf{r}) = \epsilon_{j}\psi_{j}(\mathbf{r}). \tag{2.56}$$

We then define our total wave-function as a linear combination of the set of plane-wave basis functions,

$$\psi_i(\mathbf{r}) = \sum_{\mathbf{q}} c_{i,\mathbf{q}} \times \frac{1}{\sqrt{\Omega}} \exp(\mathrm{i}\mathbf{q}\cdot\mathbf{r}) = \sum_{\mathbf{q}} c_{i,\mathbf{q}} \left|\mathbf{q}\right\rangle, \tag{2.57}$$

where Ω is the periodic volume over which the plane-waves are being considered, $c_{i,\mathbf{q}}$ are the expansion coefficients of the wave function and i denotes the band index. Each of these plane-waves satisfy orthogonality,

$$\langle \mathbf{q}'|\mathbf{q}\rangle \equiv \frac{1}{\Omega}\int_{\Omega} \exp(-\mathrm{i}\mathbf{q}'\cdot\mathbf{r}) \exp(\mathrm{i}\mathbf{q}\cdot\mathbf{r}) d\mathbf{r} = \delta_{\mathbf{q}\mathbf{q}'}. \tag{2.58}$$

By inserting Equation (2.57) into Equation (2.56) and solve for the expectation value of the effective Hamiltonian, we return the Schrödinger equation in Fourier space:

$$\sum_{\mathbf{q}} \langle \mathbf{q}'|\hat{H}_{\mathrm{eff}}|\mathbf{q}\rangle \, c_{i,\mathbf{q}} = \epsilon_i c_{i,\mathbf{q}}. \tag{2.59}$$

When expanding out the left-hand side, we must handle both the kinetic energy operator and the effective potential. The matrix elements of the kinetic energy operator simply acts as

$$\langle \mathbf{q}'|-\frac{1}{2}\nabla^2|\mathbf{q}\rangle = \frac{1}{2}\left|q\right|^2 \delta_{\mathbf{q}\mathbf{q}'}. \tag{2.60}$$

The effective non-local potential term is more demanding and, first, requires us to define the potential in Fourier space:

$$\begin{aligned} V_{\mathrm{eff}}(\mathbf{r},\mathbf{r}') &= \sum_{m,m'} \exp(-\mathrm{i}\mathbf{G}_m\cdot\mathbf{r}) V_{\mathrm{eff}}(\mathbf{G}_m,\mathbf{G}_{m'}) \exp(\mathrm{i}\mathbf{G}_{m'}\cdot\mathbf{r}') \\ V_{\mathrm{eff}}(\mathbf{G},\mathbf{G}') &= \frac{1}{\Omega_{\mathrm{cell}}}\int_{\Omega_{\mathrm{cell}}}\int_{\Omega_{\mathrm{cell}}} \exp(-\mathrm{i}\mathbf{G}'\cdot\mathbf{r}') V_{\mathrm{eff}}(\mathbf{r},\mathbf{r}') \exp(\mathrm{i}\mathbf{G}\cdot\mathbf{r}) d\mathbf{r} d\mathbf{r}', \end{aligned} \tag{2.61}$$

where $\mathbf{G}_m$ are the reciprocal lattice vectors and Ω_{cell} is the volume of the primitive cell. This leads to the matrix elements of the potential:

$$\langle \mathbf{q}'|V_{\mathrm{eff}}|\mathbf{q}\rangle = \sum_{m} V_{\mathrm{eff}}(\mathbf{G}_m,\mathbf{G}_{m'}) \delta_{\mathbf{q}'-\mathbf{q},\mathbf{G}_{m'}-\mathbf{G}_m} \tag{2.62}$$

Here, the components due to the effective potential are only non-zero when $\mathbf{q}'$ and $\mathbf{q}$ differ by some reciprocal lattice vector $\mathbf{G}_m$. As such, we define $\mathbf{q} = \mathbf{k} + \mathbf{G}_m$ and $\mathbf{q}' = \mathbf{k} + \mathbf{G}_{m'}$, which allows us to redefine the Schrödinger equation for any given k:

$$\sum_{m'} H_{mm'}(\mathbf{k}) c_{i,m'}(\mathbf{k}) = \epsilon_i(\mathbf{k}) c_{i,m}(\mathbf{k}), \tag{2.63}$$

where the Hamiltonian matrix elements are defined as

$$\begin{aligned} H_{mm'}(\mathbf{k}) &= \langle \mathbf{k} + \mathbf{G}_m | \hat{H}_{\text{eff}} | \mathbf{k} + \mathbf{G}_{m'} \rangle \\ &= \langle \mathbf{k} + \mathbf{G}_m | -\frac{1}{2}\nabla^2 + V_{\text{eff}} | \mathbf{k} + \mathbf{G}_{m'} \rangle \\ &= \frac{1}{2} |\mathbf{k} + \mathbf{G}_m|^2 \delta_{mm'} + V_{\text{eff}}(\mathbf{k} + \mathbf{G}_m, \mathbf{k} + \mathbf{G}_{m'}). \end{aligned} \tag{2.64}$$

The individual eigenvalues and eigenfunctions for this problem are labelled using the index i. Equation (2.63) presents the basic Schrödinger equation in a periodic crystal, which can be used to derive the electronic properties of said crystal.

Bloch theorem revisited: electron bands

Whilst a method for deriving the Bloch theorem using translation symmetry has been provided in Section 2.3, we shall present a simpler derivation by applying Fourier analysis.

Each eigenfunction of the Schrödinger equation (2.63) for a given $\mathbf{k}$ is given by Equation (2.57), with the sum over $\mathbf{q}$ being restricted to $\mathbf{q} = \mathbf{k} + \mathbf{G}_m$, which can be written as

$$\psi_{i,\mathbf{k}}(\mathbf{r}) = \sum_m c_{i,m}(\mathbf{k}) \times \frac{1}{\sqrt{\Omega}} \exp(\mathrm{i}(\mathbf{k} + \mathbf{G}_m) \cdot \mathbf{r}) = \exp(\mathrm{i}\mathbf{k} \cdot \mathbf{r}) \frac{1}{\sqrt{N_{\text{cell}}}} u_{i,\mathbf{k}}(\mathbf{r}), \tag{2.65}$$

where $\Omega = N_{\text{cell}} \Omega_{\text{cell}}$ and

$$u_{i,\mathbf{k}}(\mathbf{r}) = \frac{1}{\sqrt{\Omega_{\text{cell}}}} \sum_m c_{i,m}(\mathbf{k}) \exp(\mathrm{i}\mathbf{G}_m \cdot \mathbf{r}), \tag{2.66}$$

which has the periodicity of the crystal. This, again, is the Bloch theorem, but with a form now given for the cell-periodic part.

As each possible wave vector $\mathbf{k}$ defines a unique Schrödinger equation (2.63), $\mathbf{k}$ can be used as the state index, with the associated eigenvalues and eigenvectors for $\mathbf{k}$ being independent – except when values of $\mathbf{k}$ differ by integer multiples of the primitive reciprocal lattice vectors. In the limit of large volume Ω, we retrieve continuous 'bands' of eigenvalues $\epsilon_i(\mathbf{k})$ as the associated $\mathbf{k}$ points form a dense continuum – this limit corresponds to an infinitely periodic crystal. For each wave vector $\mathbf{k}$, there exists a discrete set of eigenstates (with index i) that can be found by diagonalising the Hamiltonian (2.64) using the basis set of discrete Fourier components $\mathbf{k} + \mathbf{G}_m$, where $m = 1, 2, \cdots$.

2.4.3 Born-Oppenheimer approximation

In this section, we shall derive the adiabatic approximation for electrons and ions, and then reduce this down to the 0^{th}-order Born-Oppenheimer correction (often termed the Born-Oppenheimer correction) [44, 45].

Until now, we have considered only independent electrons within an effective external potential. We now describe the many-body system of interacting electrons within a periodic crystal of nuclei (ions). Here, the kinetic energy operator is split into the electronic, $\hat{T}_{\text{el}}$, and ionic, $\hat{T}_{\text{ion}}$, kinetic energy operators. The effective potential now becomes a linear combination of the electron–electron, $V_{\text{el–el}}$, electron–ion, $V_{\text{el–ion}}$, and ion–ion, $V_{\text{ion–ion}}$, interaction potentials. For such a system, the Hamiltonian operator is

$$\hat{H} = \hat{T}_{\text{el}} + \hat{T}_{\text{ion}} + \hat{V}_{\text{el–el}} + \hat{V}_{\text{el–ion}} + \hat{V}_{\text{ion–ion}}. \tag{2.67}$$

Due to the electron–ion term, it appears that the electrons and ions are coupled and depend on one another. However, we want to determine whether the two

particle types (electrons and ions) can be decoupled and solved for separately. We shall now investigate what happens when this is considered the case.

In the first step of the Born-Oppenheimer approximation, the ionic kinetic energy operator $\hat{T}_{\mathrm{ion}}$ and the ion–ion interaction potential operator $\hat{V}_{\mathrm{ion–ion}}$ are ignored. As the nuclei are much more massive than the electrons, the nuclei can be approximated as being fixed at some equilibrium position due to their almost static response to fields on the electronic timescale – the *clamped-nuclei approximation*. In this regime, we can consider the ions as classical objects that have a fixed coordinate system.

The second step of the Born-Oppenheimer approximation involves reintroducing the ionic kinetic energy operator back into the Schrödinger equation and solving for the nuclear motion. Note that the ion–ion interaction potential is reintroduced as a constant classical potential $V_{\mathrm{ion–ion}}$ that merely applies a static shift to the eigenvalues. The reason for the different approaches towards these two operators is as follows: The ionic kinetic energy operator acts on both the electronic and ionic wave functions by performing a derivative, which will affect the states. The ion–ion interaction potential merely looks at the overlap between the electronic and ionic states, which offers little or no additional information. Here, we provide a proof for how the ionic and electronic parts can be separated and solved for separately.

We first separate the Hamiltonian into the electron Hamiltonian $\hat{H}_{\mathrm{el}}$ and the ion kinetic energy $\hat{T}_{\mathrm{ion}}$ operators (with the classical ion–ion interaction energy $V_{\mathrm{ion–ion}}$ being included in the electron Hamiltonian):

$$\hat{H}\Psi_s = \hat{H}_{\mathrm{el}}\Psi_s + \hat{T}_{\mathrm{ion}}\Psi_s = E_s\Psi_s \tag{2.68}$$

where s is the state index of the coupled system and Ψ_s is the wave function relating to that state. We shall let the wave functions have separable coupled, $\chi_{si}(\mathbf{R})$, and electronic, $\phi_i(\mathbf{r};\mathbf{R})$, contributions:

$$\Psi_s = \sum_i \phi_i(\mathbf{r};\mathbf{R})\chi_{si}(\mathbf{R}),$$
$$|\Psi_s\rangle = \sum_i |\phi_i\rangle\,|\chi_{si}\rangle\,. \tag{2.69}$$

Here, the wave function has been presented in both traditional function and bra-ket notation. If the states are always coupled, then ϕ_i will be unity. The electron wave function is determined by $\mathbf{r}$, which is itself has a parametric dependence on $\mathbf{R}$. Hence, ϕ_i has a functional dependence on $\mathbf{R}$. Substituting Equation (2.69) into Equation (2.68) results in

$$\left(\hat{H}_{\rm el} + \hat{T}_{\rm ion}\right)\sum_i \phi_i(\mathbf{r};\mathbf{R})\chi_{si}(\mathbf{R}) = E_s \sum_i \phi_i(\mathbf{r};\mathbf{R})\chi_{si}(\mathbf{R}). \tag{2.70}$$

We shall now derive the ionic Schrödinger equation to prove that it has no contributions due to electrons, which will prove that they can be decoupled. First we evaluate the following integral

$$\begin{aligned}\int \phi_j^*(\mathbf{r};\mathbf{R})\left(\hat{H}_{\rm el} + \hat{T}_{\rm ion}\right)\sum_i \phi_i(\mathbf{r};\mathbf{R})\chi_{si}(\mathbf{R})d\mathbf{r} \\ = E_s \int \phi_j^*(\mathbf{r};\mathbf{R})\sum_{i'}\phi_{i'}(\mathbf{r};\mathbf{R})\chi_{si'}(\mathbf{R})d\mathbf{r},\end{aligned} \tag{2.71}$$

We re-postulate this in bra-ket notation, where the electronic wave functions are represented only by their index in the angle brackets:

$$\sum_i \langle j|\left(\hat{H}_{\rm el} + \hat{T}_{\rm ion}\right)|i\rangle\,|\chi_{si}\rangle = E_s \sum_{i'}\langle j|i'\rangle\,|\chi_{si'}\rangle\,. \tag{2.72}$$

Evaluation of this expression follows:

$$\begin{aligned}
\sum_i \langle j|\Big(\hat{H}_{\rm el}+\hat{T}_{\rm ion}\Big)|i\rangle\,|\chi_{si}\rangle &= E_s\,|\chi_{sj}\rangle \\
\sum_i \Big(\,\langle j|\hat{H}_{\rm el}|i\rangle+\,\langle j|\hat{T}_{\rm ion}|i\rangle\Big)\,|\chi_{si}\rangle &= E_s\,|\chi_{sj}\rangle \\
\sum_i \Big(E_i\,\langle j|i\rangle+\,\langle j|\hat{T}_{\rm ion}|i\rangle\Big)\,|\chi_{si}\rangle &= E_s\,|\chi_{sj}\rangle \\
E_j\,|\chi_{sj}\rangle+\sum_i \langle j|\hat{T}_{\rm ion}|i\rangle\,|\chi_{si}\rangle &= E_s\,|\chi_{sj}\rangle \\
E_j\,|\chi_{sj}\rangle-E_s\,|\chi_{sj}\rangle &= -\sum_i \langle j|\hat{T}_{\rm ion}|i\rangle\,|\chi_{si}\rangle\,.
\end{aligned}$$

Using the definition of the ionic kinetic energy operator, $\hat{T}_{\rm ion}=\sum_\alpha \frac{-1}{2M_\alpha}\nabla^2_\alpha$ (where α is the ionic index), we expand out the right-hand side term:

$$\begin{aligned}
\sum_i \langle j|\hat{T}_{\rm ion}|i\rangle\,|\chi_{si}\rangle = & \\
&= \sum_\alpha \frac{-1}{2M_\alpha}\left[\sum_i \langle j|\nabla_\alpha\cdot\nabla_\alpha|i\rangle\,|\chi_{si}\rangle\right] \\
&= \sum_\alpha \frac{-1}{2M_\alpha}\left[\sum_i \big(\,\langle j|\nabla^2_\alpha|i\rangle+2\,\langle j|\nabla_\alpha|i\rangle\,\nabla_\alpha+\langle j|i\rangle\,\nabla^2_\alpha\big)\,|\chi_{si}\rangle\right] \\
&= \sum_\alpha \frac{-1}{2M_\alpha}\left[\sum_i \big(\,\langle j|\nabla^2_\alpha|i\rangle+2\,\langle j|\nabla_\alpha|i\rangle\,\nabla_\alpha\big)\,|\chi_{si}\rangle\right]+\sum_\alpha \frac{-1}{2M_\alpha}\nabla^2_\alpha\,|\chi_{sj}\rangle \\
&= \sum_\alpha \frac{-1}{2M_\alpha}\left[\sum_i \big(\,\langle j|\nabla^2_\alpha|i\rangle+2\,\langle j|\nabla_\alpha|i\rangle\,\nabla_\alpha\big)\,|\chi_{si}\rangle\right]+\hat{T}_{\rm ion}\,|\chi_{sj}\rangle\,.
\end{aligned} \tag{2.73}$$

We introduce two additional terms, A and B, to account for the ij-matrix elements (the terms contained within the brackets on the right-hand side) and define them as

$$A_{ji}=-\sum_\alpha \frac{1}{M_\alpha}\,\langle j|\nabla_\alpha|i\rangle\,\nabla_\alpha, \tag{2.74}$$

$$B_{ji}=-\sum_\alpha \frac{1}{2M_\alpha}\,\langle j|\nabla^2_\alpha|i\rangle\,. \tag{2.75}$$

Substituting Equations (2.74) and (2.75) into Equation (2.73) results in

$$E_j \left|\chi_{sj}\right\rangle - E_s \left|\chi_{sj}\right\rangle = -\hat{T}_{\text{ion}} \left|\chi_{sj}\right\rangle - \sum_i \left(B_{ji} + A_{ji}\right) \left|\chi_{si}\right\rangle , \tag{2.76}$$

which is referred to as the *diagonal Born-Oppenheimer correction*, or the *adiabatic correction*. This correction accounts for the interaction between phonons and electrons. If we now separate the terms where $i = j$ and $i \neq j$, we get the following equation

$$E_j \left|\chi_{sj}\right\rangle + \hat{T}_{\text{ion}} \left|\chi_{sj}\right\rangle - E_s \left|\chi_{sj}\right\rangle + \left(B_{jj} + A_{jj}\right) \left|\chi_{si}\right\rangle = -\sum_{i \neq j} \left(B_{ji} + A_{ji}\right) \left|\chi_{sj}\right\rangle . \tag{2.77}$$

In the adiabatic approximation, we can neglect all terms where electrons are excited by the ionic kinetic energy (meaning that we can ignore all terms where $i \neq j$, off-diagonal terms in A and B). The justification for this follows: whilst electronic eigenvalues and eigenfunctions might change due to ionic motion, the electrons remain in their same state. We now have

$$\left(\hat{T}_{\text{ion}} + E_j + B_{jj} + A_{jj}\right) \left|\chi_{sj}\right\rangle = E_s \left|\chi_{sj}\right\rangle . \tag{2.78}$$

which is an ionic Schrödinger equation that is determined only by the coupled electronic–ionic wave functions. As the state $|j\rangle$ is normalised ($\nabla \langle j|j\rangle = \nabla [1] = 0$), $\langle j|\nabla|j\rangle$ and A_{jj} both equal zero, which reduces the previous equation down to

$$\left(\hat{T}_{\text{ion}} + E_j + B_{jj}\right) \left|\chi_{sj}\right\rangle = E_s \left|\chi_{sj}\right\rangle . \tag{2.79}$$

We can then group the eigenvalues of the electrons, E_j, with the B_{jj} term together as a modified potential for the nuclei $U_j(\mathbf{R}) = E_j(\mathbf{R}) + B_{jj}(\mathbf{R})$. This allows us to, for the adiabatic approximation, describe the ionic motion purely in terms of the energy of the each electronic state j,

$$\left[\sum_\alpha \frac{-1}{2M_\alpha} \nabla_\alpha^2 + U_j(\mathbf{R}) - E_{nj}\right] \left|\chi_{nj}\right\rangle = 0, \tag{2.80}$$

where n labels the ionic states. The full set of states s is described, in the adiabatic approximation, as the product of the ionic and electronic states. As the coupled wave function is determined only by the electronic wave functions, it is valid – or, at least, consistent with what has been done up until this point – to neglect the coupling. In doing so, we interpret the coupled wave functions, $\chi_{si}(\mathbf{R})$ as the ionic wave functions, $\chi_{ni}(\mathbf{R})$;

$$\begin{aligned} \Psi_s(\mathbf{r}, \mathbf{R}) &= \sum_i \phi_i(\mathbf{r}; \mathbf{R}) \chi_{ni}(\mathbf{R}), \\ |\Psi_s\rangle &= \sum_i |\phi_i\rangle \, |\chi_{ni}\rangle \, . \end{aligned} \tag{2.81}$$

In the Born-Oppenheimer approximation, we take one further step by ignoring the B_{jj} terms. This can often be done as the term is typically very small due to the large masses of the ions causing them to respond much more slowly than the electrons, such that they appear to the electrons as a static background potential. The neglecting of the B_{jj} term is also the basis of the *frozen phonon* method. This leaves us with

$$\left(\hat{T}_{\text{ion}} + E_j\right) |\chi_{nj}\rangle = E_s \, |\chi_{nj}\rangle \, . \tag{2.82}$$

All of this allows us to separate the electronic Schrödinger equation

$$\hat{H}_{\text{el}} \, |\phi_i\rangle = \left(\hat{T}_{\text{el}}(\mathbf{r}) + \hat{V}_{\text{el–el}}(\mathbf{r}) + \hat{V}_{\text{el–ion}}(\mathbf{r}, \mathbf{R})\right) |\phi_i\rangle \, , \tag{2.83}$$

which is an eigenvalue equation that describes the electrons only.

2.5 The many-body problem

Here, we consider a many-body system of interacting particles, with the particles being electrons and atomic nuclei (ions). If we take this system in the time-independent, non-relativistic regime, then the energy and dynamics of the system are described by the Schrödinger equation

$$\hat{H}\Psi_i = E_i\Psi_i, \tag{2.84}$$

where i is the index denoting the state of the system, E_i is the energy eigenvalue of the i^{th} state, Ψ_i is the coupled electron–ion wave function describing the i^{th} state, and $\hat{H}$ is the Hamiltonian operator. We can define $\hat{H}$ in terms of the kinetic energy $\hat{T}$ and Coulomb interaction (potential) operators $\hat{V}$ as

$$\hat{H} = \hat{T}_{\mathrm{ion}} + \hat{T}_{\mathrm{el}} + \hat{V}_{\mathrm{el\text{–}el}} + \hat{V}_{\mathrm{el\text{–}ion}} + \hat{V}_{\mathrm{ion\text{–}ion}}. \tag{2.85}$$

Here, subscripts ion and el label the ionic and electronic terms, respectively, with $\mathrm{el\text{–}el}$, $\mathrm{el\text{–}ion}$, and $\mathrm{ion\text{–}ion}$ being the electron–electron, electron–ion and ion–ion interaction terms, respectively. We can expand each of these terms as follows (with the order of the terms being maintained):

$$\begin{aligned}\hat{H} = &-\sum_{\alpha}^{N_{\mathrm{ion}}} \frac{1}{2M_\alpha}\nabla_\alpha^2 - \frac{1}{2}\sum_{\mu}^{N_e}\nabla_\mu^2 \\ &+ \frac{1}{2}\sum_{\alpha\neq\beta}^{N_{\mathrm{ion}}} \frac{Z_\alpha Z_\beta}{|\mathbf{R}_\alpha - \mathbf{R}_\beta|} - \sum_{\mu,\alpha}^{N_e,N_{\mathrm{ion}}} \frac{Z_\alpha}{|\mathbf{r}_\mu - \mathbf{R}_\alpha|} + \frac{1}{2}\sum_{\mu\neq\nu}^{N_e} \frac{1}{|\mathbf{r}_\mu - \mathbf{r}_\nu|},\end{aligned} \tag{2.86}$$

where M_α, Z_α and $\mathbf{R}_\alpha$ are the mass, atomic number and position vector of the α^{th} ion, and $\mathbf{r}_\mu$ is the position vector of the μ^{th} electron.

The wave function describing the i^{th} state is a function of the electronic and ionic positions, as well as the electron spin σ – where the electronic arguments are functionally dependent on the ionic positions. This can be written as

$$\Psi_i \equiv \Psi_i(\mathbf{r}_1, \sigma_1, \ldots, \mathbf{r}_{N_e}, \sigma_{N_e}; \mathbf{R}_1, \ldots, \mathbf{R}_{N_{\mathrm{ion}}}). \tag{2.87}$$

Whilst this Schrödinger equation is exact for the non-relativistic region, there is no analytical solution for it, except for trivially simple problems. By applying the Born-Oppenheimer approximation outlined in Section 2.4.3, we are able to reduce the wave function in Equation (2.87) to the decoupled electronic and ionic wave

functions. In doing so, the kinetic energy of the ions can be considered separately and, as their masses are more than 10^3 times greater than that of an electron, they can be taken as being stationary on the electronic timescale.

2.5.1 Solving the many-body Schrödinger equation

For a system of N particles, the density $n(\mathbf{r})$ is given by the expectation value of the density operator $\hat{n}(\mathbf{r}) = \sum_{i=1,N_e} \delta(\mathbf{r} - \mathbf{r}_i)$,

$$n(\mathbf{r}) = \frac{\langle\Psi|\hat{n}(\mathbf{r})|\Psi\rangle}{\langle\Psi|\Psi\rangle} = N\frac{\int |\Psi(\mathbf{r}, \mathbf{r}_2, \cdots, \mathbf{r}_N)|^2 \, d\mathbf{r}_2 \cdots d\mathbf{r}_N}{\int |\Psi(\mathbf{r}_1, \mathbf{r}_2, \cdots, \mathbf{r}_N)|^2 \, d\mathbf{r}_1 d\mathbf{r}_2 \cdots d\mathbf{r}_N}. \tag{2.88}$$

The total energy E for a system is given by the expectation value of the Hamiltonian operator $\hat{H}$,

$$E = \frac{\langle\Psi|\hat{H}|\Psi\rangle}{\langle\Psi|\Psi\rangle} \equiv \left\langle\hat{H}\right\rangle = \left\langle\hat{T}\right\rangle + \left\langle\hat{V}_{\text{el–el}}\right\rangle + \int V_{\text{ext}}(\mathbf{r})n(\mathbf{r}) + E_+, \tag{2.89}$$

where $\hat{T}$ is the kinetic energy operator of each particle, $\hat{V}_{\text{int}}$ is the potential operator relating to the particles interacting with each other, V_{ext} defines external potentials exerted on the particles and E_+ are any extra classical energies that raise the energy of the ground state (ion–ion interaction in the case of electrons).

The eigenstates of the many-body Hamiltonian are stationary points of Equation (2.89), which may be found by varying the numerator whilst maintaining the constraint of orthonormality ($\langle\Psi|\Psi\rangle = 1$). To do this, one can use the method of Lagrange multipliers,

$$\delta\left[\langle\Psi|\hat{H}|\Psi\rangle - E\langle\Psi|\Psi\rangle\right] = 0. \tag{2.90}$$

This is equivalent to the Rayleigh-Ritz principle [46], which states that the functional

$$\Omega_{\text{RR}} = \langle\Psi|\hat{H} - E|\Psi\rangle \tag{2.91}$$

is stationary at any eigensolution $|\Psi_m\rangle$. By varying the state $\langle\Psi|$, one gets

$$\langle\delta\Psi|\hat{H} - E|\Psi\rangle = 0. \tag{2.92}$$

Due to the requirement that this must hold for all possible $|\delta\Psi\rangle$, the only ket $|\Psi\rangle$ that can satisfy this is one that satisfies the time-independent Schrödinger equation

$$\hat{H}\,|\Psi\rangle = E\,|\Psi\rangle\,. \tag{2.93}$$

2.6 Hartree-Fock method

Here, we outline the Hartree and Fock approximations introduced to reduce the complexity of the many-body problem. The first approximation of these was developed by Hartree in 1928 [47], which considers the many-body interacting electron system as, instead, a system of N_e non-interacting electrons. In doing so, the electronic wave function can be rewritten as the product of N_e single-electron wave functions ψ_i (i.e. N_e decoupled wave functions). In doing so, the wave function can be written as

$$\Phi_{\mathrm{HP}}(\mathbf{x}_1, \cdots \mathbf{x}_{N_e}) = \psi_1(\mathbf{x}_1) \cdots \psi_{N_e}(\mathbf{x}_{N_e}) = \prod_{i=1}^{N_e} \psi_i(\mathbf{x}_i), \tag{2.94}$$

where $\mathbf{x}_i$ includes both the spatial ($\mathbf{r}_i$) and spin (σ_i) coordinates of the i^{th} electron; this wave function Φ_{HP} is called the Hartree Product. Due to the decoupling of these single-electron wave functions, it should be noted that they are, hence, orthogonal.

If we exchange the coordinates of any two fermions within a system, then the resulting wave function should result in a sign change to that of the original, due to the antisymmetric property of fermions. If we perform this action with electrons within the Hartree Product, we do not see this behaviour. This is a strong flaw in the Hartree method that was resolved in 1930 independently by both Slater [48]

and Fock [49,50], with Slater representing the form of this improved wave function using single determinant function [51]:

$$\Phi(\mathbf{x}_1, \cdots, \mathbf{x}_{N_e}) = \frac{1}{\sqrt{N!}} \begin{vmatrix} \psi_1(\mathbf{x}_1) & \cdots & \psi_1(\mathbf{x}_{N_e}) \\ \vdots & \ddots & \vdots \\ \psi_{N_e}(\mathbf{x}_1) & \cdots & \psi_{N_e}(\mathbf{x}_{N_e}) \end{vmatrix}. \tag{2.95}$$

Not only does this Slater determinant satisfy the antisymmetric nature of electrons, it also satisfies the Pauli exclusion principle as, if we set $\psi_1 = \psi_2$, then the determinant will be zero. This would represent the chance of finding two electrons in the same state, which is forbidden. Another interesting property of the Slater determinant is that all electrons are found to be indistinguishable, with each electron being associated with every orbital.

By using the Slater determinant for the form of the many-body electron wave function, we can employ variational method, outlined in Section 2.4.1, to obtain an upper bound to the true energy of the system. This approximation of the energy can be written as

$$E_{\mathrm{HF}} = \langle \Phi | \hat{H}_{\mathrm{HF}} | \Phi \rangle = \sum_{i=1}^{N_e} \langle i | \, \hat{h} \, | i \rangle + \frac{1}{2} \sum_{i,j=1}^{N_e} \left(\langle i | \, \hat{\mathcal{V}}_{ij} \, | j \rangle - \langle i | \, \hat{\mathcal{V}}_{jj} \, | i \rangle \right), \tag{2.96}$$

where the the first term on the right-hand side contains the single-electron kinetic energy and electron–ion attraction:

$$\langle i | \hat{h} | j \rangle = \int \psi_i^*(\mathbf{x}_i) \left[-\frac{1}{2} \nabla_i^2 - \sum_{\alpha=1}^{N_{\mathrm{ion}}} \frac{Z_\alpha}{|\mathbf{r}_i - \mathbf{R}_\alpha|} \right] \psi_j(\mathbf{x}_i) d\mathbf{x}_i. \tag{2.97}$$

The remaining terms on the right-hand side relate to electron exchange term (accounts for spin-correlation effects) and the electron–electron repulsion (Coulomb term):

$$\langle i | \, \hat{\mathcal{V}}_{jk} \, | l \rangle = \int \psi_i^*(\mathbf{x}_i) \psi_j(\mathbf{x}_i) \frac{1}{|\mathbf{r}_i - \mathbf{r}_j|} \psi_k^*(\mathbf{x}_j) \psi_l(\mathbf{x}_j) d\mathbf{x}_i d\mathbf{x}_j. \tag{2.98}$$

Here, $\mathbf{r}$ denotes the spatial coordinate associated with the combined spatial-spin

coordinate $\mathbf{x}$.

In Equation (2.96), we have included the fictitious $i = j$ *self-interaction* term. However, as the Coulomb and exchange terms are equal for $i = j$, the two terms in the summation cancel, causing this self-interaction to be omitted. Hence, a minimisation of the total energy can be performed to give the Hartree-Fock equations

$$\hat{F}\psi_i(\mathbf{x}_i) = \sum_{j=1}^{N_e} \epsilon_{ij}\psi_j(\mathbf{x}_i) \tag{2.99}$$

where $\hat{F}$ is the Fock operator, defined as

$$\hat{F} = \hat{h} + V_{\mathrm{H}} + \hat{V}_{\mathrm{ex}}. \tag{2.100}$$

with the Coulomb (Hartree) term being

$$V_{\mathrm{H}}(\mathbf{x}_i) = \sum_{j=1}^{N_e} \int \frac{|\psi_j(\mathbf{x}_j)|^2}{|\mathbf{r}_i - \mathbf{r}_j|} d\mathbf{x}_j \tag{2.101}$$

and the exchange operator is

$$\hat{V}_{\mathrm{ex}} = -\sum_{j=1}^{N_e} \frac{\psi_j(\mathbf{x}_i)}{\psi_i(\mathbf{x}_i)} \int \frac{\psi_j^*(\mathbf{x}_j)\psi_i(\mathbf{x}_j)}{|\mathbf{r}_i - \mathbf{r}_j|} d\mathbf{x}_j. \tag{2.102}$$

As with Equation (2.96), the energy associated with the Hartree-Fock approximation can be written as follows:

$$\hat{F}\psi_i(\mathbf{x}) = \epsilon_i\psi_i(\mathbf{x}). \tag{2.103}$$

where only the diagonal terms remain due to the orthogonality condition displayed by the single-electron wave functions.

One of the major limitations of using the Hartree-Fock approximation for describing systems of electrons is its only partial description of the electron correlation; it only accounts for the electron exchange part, often termed Fermi correlation.

Whilst the Hartree-Fock method perfectly captures the electron exchange interaction – *Fermi correlation* – the method's major limitation lies in its inability to account for the rest of electron correlation – *Coulomb correlation* – which severely limits its ability to correctly describe electronic properties of materials. Electron exchange is defined as the correlation effect of exchanging the positions of two parallel-spin electrons. Coulomb correlation captures the effects of interactions between electrons of different spins. Electron exchange is often simply called as *exchange* and Coulomb correlation is generally abbreviated to *correlation*.

The following section (2.7) outlines the density functional theory method that, whilst accounting for the electron correlation term (which it tends to overestimate), also underestimates the exchange term. It should be clear now that the balance of describing both exchange and correlation is one of the main issues and difficulties between (and within) the various *ab initio* methods available for describing the electronic structure of a material.

2.7 Density Functional Theory

In 1964, Hohenberg and Kohn published an article that defines the energy of a system of interacting particles as a functional of the density of those particles, and that the charge density is described uniquely by external potentials present in the system [52]. These theorems presented density as a fundamental descriptor for many of the properties of a system, which paved the way for a new *ab initio* tool for solving the many-body problem, density functional theory. Whilst these theorems are extremely interesting, they alone cannot be used to make the many-body problem numerically solvable.

A year later, this was expanded upon by Kohn and Sham, who repostulated the many-body system of interacting particles, instead, as a system of non-interacting Kohn-Sham particles that has the same ground state as the interacting system [53]. This allowed for the many-body problem to be reduced drastically down solving for a self-interacting density, which can be solved for numerically.

Together, these three theorems allowed for the difficulty of the many-body prob-

lem to be drastically reduced down to solving for an auxiliary system with a single particle interacting with the background charge (mean-field), which can be solved for numerically. The validity and limitations of these three theorems are discussed in the following sections.

2.7.1 Hohenberg-Kohn theorem

Theorem I:

For any system of interacting particles, in an external potential $V_{ext}(\mathbf{r})$, the potential $V_{ext}(\mathbf{r})$ is determined uniquely, except for a constant, by the ground state particle density, $n_0(\mathbf{r})$.

The first theorem of Hohenberg-Kohn states that the external potential in which interacting particles reside can be perfectly described by the ground state density of those interacting particles. Hence, the ground state particle density can also be derived from the external potential.

In order to prove this, one can use proof by contradiction. First, let us consider two external potentials $V_{\text{ext}}^{(1)}(\mathbf{r})$ and $V_{\text{ext}}^{(2)}(\mathbf{r})$ that lead to the same ground state particle density $n_0(\mathbf{r})$. These two external potentials will lead to two different Hamiltonians, $\hat{H}^{(1)}$ and $\hat{H}^{(2)}$, that each have their own unique ground state wave functions, $\Psi^{(1)}$ and $\Psi^{(2)}$, which both have the same ground state density $n_0(\mathbf{r})$. As $\Psi^{(2)}$ is not the ground state wave function of $\hat{H}^{(1)}$, one can say

$$E^{(1)} = \left\langle \Psi^{(1)} \middle| \hat{H}^{(1)} \middle| \Psi^{(1)} \right\rangle \leq \left\langle \Psi^{(2)} \middle| \hat{H}^{(1)} \middle| \Psi^{(2)} \right\rangle . \tag{2.104}$$

By assuming that the ground state is non-degenerate, we can now rewrite the last part of the equation as

$$\begin{aligned} \left\langle \Psi^{(2)} \middle| \hat{H}^{(1)} \middle| \Psi^{(2)} \right\rangle &= \left\langle \Psi^{(2)} \middle| \hat{H}^{(2)} \middle| \Psi^{(2)} \right\rangle + \left\langle \Psi^{(2)} \middle| \hat{H}^{(1)} - \hat{H}^{(2)} \middle| \Psi^{(2)} \right\rangle \\ &= E^{(2)} + \int d^3r [V_{\text{ext}}^{(1)}(\mathbf{r}) - V_{\text{ext}}^{(2)}(\mathbf{r})] n_0(\mathbf{r}), \end{aligned} \tag{2.105}$$

which leads to

$$E^{(1)} < E^{(2)} + \int d^3r[V_{\text{ext}}^{(1)}(\mathbf{r}) - V_{\text{ext}}^{(2)}(\mathbf{r})]n_0(\mathbf{r}). \tag{2.106}$$

The same hypothesis can be posed for $E^{(2)}$ in order to get

$$E^{(2)} < E^{(1)} + \int d^3r[V_{\text{ext}}^{(2)}(\mathbf{r}) - V_{\text{ext}}^{(1)}(\mathbf{r})]n_0(\mathbf{r}). \tag{2.107}$$

The two equations Equation (2.106) and Equation (2.107) can be summed together to get the contradictory inequality of $E^{(1)} + E^{(2)} < E^{(2)} + E^{(1)}$. This gives us the desired result that no two different external potentials (different by something other than just a constant shift) can give rise to the same ground state charge density.

Theorem II:

A universal function for the energy $E[n]$ in terms of the density $n(\mathbf{r})$ can be defined, valid for any external potential $V_{ext}(\mathbf{r})$. For any particular $V_{ext}(\mathbf{r})$, the exact ground state energy of the system is the global minimum value of this functional, and the density $n(\mathbf{r})$ that minimises the functional is the exact ground state density $n_0(\mathbf{r})$.

For the second theorem, Hohenberg and Kohn state that the energy relating to the kinetic T and interaction $E_{\text{el–el}}$ energies of a system of interacting particles can be expressed simply as a functional of the density n. This is expressed as

$$\begin{aligned} E[n]_{\text{HK}} &= T[n] + E_{\text{el–el}}[n] + \int d^3r V_{\text{ext}}(\mathbf{r})n(\mathbf{r}) + E_{\text{ion–ion}} \\ &\equiv F_{\text{HK}} + \int d^3r V_{\text{ext}}(\mathbf{r})n(\mathbf{r}) + E_{\text{ion–ion}}, \end{aligned} \tag{2.108}$$

where $E_{\text{ion–ion}}$ is the interaction energy of the nuclei. F_{HK} is the internal energies relating to the interacting electron system (kinetic and interaction energies),

$$F_{\text{HK}} = T[n] + E_{\text{el–el}}[n]. \tag{2.109}$$

As such, even the total energy of the system is a functional of just the density; which must be the case for all electron systems as the two energy terms in Equation (2.109) are functionals of only the density.

If we now use both theorems together, we can show how the Hohenberg-Kohn functional is equal to the expectation value of the Hamiltonian in the unique ground state. We first consider a system that experiences an external potential $V_{\text{ext}}^{(1)}(\mathbf{r})$ with a corresponding ground state density $n^{(1)}(\mathbf{r})$. The ground state wave function for this system is $\Psi^{(1)}$

$$E^{(1)} = E_{\text{HK}}[n^{(1)}] = \left\langle \Psi^{(1)} \middle| \hat{H}^{(1)} \middle| \Psi^{(1)} \right\rangle . \tag{2.110}$$

If we now try to describe this system using a different density, $n^{(2)}(\mathbf{r})$, which, as we now know, must corresponds to a different wave function $\Psi^{(2)}$. It follows that the energy $E^{(2)}$ of this state must be greater than the energy $E^{(1)}$ relating to the ground state density as

$$E^{(1)} = \exp\left\{ \hat{H}^{(1)} \right\} \Psi^{(1)} \leq \left\langle \Psi^{(2)} \middle| \hat{H}^{(1)} \middle| \Psi^{(2)} \right\rangle . \tag{2.111}$$

From this, we have shown that the energy in terms of the Hohenberg-Kohn functional evaluated at the ground state density $n_0(\mathbf{r})$ is indeed lower than the energies obtained by evaluating this at any other density $n(\mathbf{r})$.

These theorems were extended further by Levy [54, 55] and Lieb [56] to be valid for degenerate ground states, as well as offering a method for determining the form of the energy functional.

2.7.2 Kohn-Sham theorem

The Kohn-Sham theorem analogises the system of interacting electrons to that of a set of independent, non-interacting electron-like particles; these two systems are then said to have the same energy. This is done using two assumptions:

1. The exact ground state density can be represented by the ground state

density of an auxiliary system of non-interacting particles. This is called the "*non-interacting-V representability*" although there are no rigorous proofs for real systems of interest, we assume its validity.

2. The auxiliary Hamiltonian is chosen to have the usual kinetic operator and an effective local potential $V_{\text{eff}}(\mathbf{r})$ acting on an electron at point $\mathbf{r}$.

Here, we intend to perform calculations on the auxiliary system of independent-particles, with the Hamiltonian of the system (using Hartree atomic units) being

$$\hat{H}^{\sigma}_{\text{aux}} = -\frac{1}{2}\nabla^2 + V^{\sigma}_{\text{eff}}(\mathbf{r}), \tag{2.112}$$

with a spin of σ. As we do not currently define the form of the potential $V^{\sigma}(\mathbf{r})$ acting on the system, this method can apply for all $V^{\sigma}(\mathbf{r})$. By applying this method for a range of $V^{\sigma}(\mathbf{r})$, we are able to define functionals for a range of densities. We start by stating that this auxiliary system of non-interacting Kohn-Sham particles has the same charge density $n(\mathbf{r})$ as the true system:

$$n(\mathbf{r}) = \sum_{\sigma} n^{\sigma}(\mathbf{r}) = \sum_{\sigma}\sum_{i=1}^{N^{\sigma}} \left|\psi^{\sigma}_{i}(\mathbf{r})\right|^2, \tag{2.113}$$

where i is the orbital index, N^{σ} is the total number of orbitals for spin σ, and ψ^{σ}_{i} are single-electron wave functions, termed as Kohn-Sham orbitals. This density has been given as the sum of squares of the orbitals for each spin.

The independent-particle kinetic energy T_s is given by

$$T_s = -\frac{1}{2}\sum_{\sigma}\sum_{i=1}^{N^{\sigma}} \langle\psi^{\sigma}_{i}|\nabla^2|\psi^{\sigma}_{i}\rangle = -\frac{1}{2}\sum_{\sigma}\sum_{i=1}^{N^{\sigma}} \int \left|\nabla\psi^{\sigma}_{i}(\mathbf{r})\right|^2 d\mathbf{r}. \tag{2.114}$$

The Hartree term for the energy relating to Coulomb interaction, E_{H}, is introduced to account for the electron density, $n(\mathbf{r})$, interacting with itself:

$$E_{\text{H}}[n] = \frac{1}{2}\int \frac{n(\mathbf{r})n(\mathbf{r}')}{|\mathbf{r}-\mathbf{r}'|} d\mathbf{r}d\mathbf{r}'. \tag{2.115}$$

We now rewrite the Hohenberg-Kohn energy from Equation (2.108) with the form

$$E_{\mathrm{KS}} = T_s[n] + \int V_{\mathrm{ext}}(\mathbf{r}) n(\mathbf{r}) d\mathbf{r} + E_{\mathrm{H}}[n] + E_{\mathrm{ion\text{–}ion}} + E_{\mathrm{xc}}[n]. \tag{2.116}$$

with $V_{\mathrm{ext}}(\mathbf{r})$ being the external potential due to the ions (in addition to any other external fields, assumed to be independent of spin), $E_{\mathrm{ion\text{–}ion}}$ is the energy due to ion–ion interaction, and E_{xc} is the energy due to exchange-correlation effects.

In Equation (2.116), we have grouped all of the many-body effects into the $E_{\mathrm{xc}}[n]$; these being exchange and correlation. If we compare the form of the Kohn-Sham energy functional to that of the Hohenberg-Kohn energy functional in Equation (2.108), we find that we can write this exchange-correlation term as

$$E_{\mathrm{xc}}[n] = F_{\mathrm{HK}}[n] - (T_s[n] + E_{\mathrm{H}}[n]), \tag{2.117}$$

or, also as

$$E_{\mathrm{xc}}[n] = \left\langle \hat{T} \right\rangle - T_s[n] + \left\langle \hat{V}_{\mathrm{el\text{–}el}} \right\rangle - E_{\mathrm{H}}[n], \tag{2.118}$$

where $\hat{V}_{\mathrm{el\text{–}el}}$ is the electron–electron interaction term. From this form, we see that the exchange-correlation energy is the difference between the kinetic and internal interaction energies of the true system to that of the fictitious independent-particle system (where the electron–electron interaction has been replaced with the Hartree energy).

Here, to solve for the ground state of the Kohn-Sham auxiliary system, we need to minimise with respect to the density. Whilst the kinetic energy of the auxiliary system T_s is a functional of the orbitals ψ_i^σ, all other terms in Equation (2.116) are functionals of the density. With this being the case, one can vary the wave function and use the chain rule in order to derive the variational equation

$$\frac{\delta E_{\mathrm{KS}}}{\delta \psi_i^{\sigma *}(\mathbf{r})} = \frac{\delta T_s}{\delta n^\sigma(\mathbf{r})} + \left[\frac{\delta E_{\mathrm{ext}}}{\delta n^\sigma(\mathbf{r})} + \frac{\delta E_{\mathrm{H}}}{\delta n^\sigma(\mathbf{r})} + \frac{\delta E_{\mathrm{xc}}}{\delta n^\sigma(\mathbf{r})} \right] \frac{\delta n^\sigma(\mathbf{r})}{\delta \psi_i^{\sigma *}(\mathbf{r})} = 0, \tag{2.119}$$

where the wave functions are orthonormalised ($\langle \psi_i^\sigma | \psi_j^{\sigma'} \rangle = \delta_{i,j}\delta_{\sigma,\sigma'}$). By using the definitions of T_s and $n^\sigma(\mathbf{r})$ from Equations (2.113) and (2.113), we can write the following terms:

$$\frac{\delta T_s}{\delta n^\sigma(\mathbf{r})} = -\frac{1}{2}\nabla^2\psi_i^\sigma(\mathbf{r}); \quad \frac{\delta n^\sigma(\mathbf{r})}{\delta \psi_i^{\sigma *}(\mathbf{r})} = \psi_i^\sigma(\mathbf{r}). \tag{2.120}$$

We now use these equations with the the Lagrange multiplier method to obtain the Kohn-Sham Schrödinger-like equations

$$\left(H_{\mathrm{KS}}^\sigma - \varepsilon_i^\sigma\right)\psi_i^\sigma(\mathbf{r}) = 0, \tag{2.121}$$

where ε_i^σ are the eigenvalues and H_{KS}^σ is the effective Hamiltonian for Kohn-Sham particles with spin σ,

$$H_{\mathrm{KS}}^\sigma(\mathbf{r}) = -\frac{1}{2}\nabla^2 + V_{\mathrm{KS}}^\sigma(\mathbf{r}), \tag{2.122}$$

and the effective Kohn-Sham potential V_{KS}^σ is

$$\begin{aligned} V_{\mathrm{KS}}^\sigma(\mathbf{r}) &= V_{\mathrm{ext}}(\mathbf{r}) + \frac{\delta E_{\mathrm{H}}}{\delta n^\sigma(\mathbf{r})} + \frac{\delta E_{\mathrm{xc}}}{\delta n^\sigma(\mathbf{r})} \\ &= V_{\mathrm{ext}}(\mathbf{r}) + V_{\mathrm{H}}(\mathbf{r}) + V_{\mathrm{xc}}^\sigma(\mathbf{r}). \end{aligned} \tag{2.123}$$

Here, the system of interacting electrons has been replaced with an auxiliary system of Kohn-Sham particles that has the same ground state density. In doing so, the problem has simplified drastically down to solving Equation (2.121), where all the complicated terms have been collected into the V_{xc}^σ term in the potential.

Exchange-correlation hole

We have seen that the Kohn-sham approach explicitly separates out the independent particle kinetic energy and long-range Hartree terms, leaving the exchange-correlation functional $E_{\mathrm{xc}}[n]$. This functional can be approximated as semi-local functional of the density, allowing it to be expressed in the form

$$E_{\mathrm{xc}}[n] = \int n(\mathbf{r})\epsilon_{\mathrm{xc}}([n], \mathbf{r})d\mathbf{r}, \tag{2.124}$$

with $\epsilon_{\mathrm{xc}}([n], \mathbf{r})$ being an energy per electron at point $\mathbf{r}$ that depends only on the density $n^{\sigma}(\mathbf{r})$ within a neighbourhood of point $\mathbf{r}$. As the Coulomb interaction is independent of spin, only the total density $n(\mathbf{r})$ is present in Equation (2.124), with the spin information being contained into $\epsilon_{\mathrm{xc}}([n], \mathbf{r})$. It must be noted that this energy density is not uniquely defined by the integral in Equation (2.124).

Even though we have not uniquely defined the energy density $\epsilon_{\mathrm{xc}}([n], \mathbf{r})$, a relation between it and the exchange-correlation hole defined in Appendix B can be found by varying the electronic charge from zero to its actual value e – these two cases represent the non-interacting case and the actual case, respectively. To do this, the density must be kept constant during the variation. With these constraints, the only terms that will be affected are the Hartree and exchange-correlation terms, as these are the only terms defining the internal interactions of the system. The change in energy due to this variation is given by

$$E_{\mathrm{xc}}[n] = \int_0^{e^2} \langle \Psi_\lambda | \frac{dV_{\mathrm{int}}}{d\lambda} | \Psi_\lambda \rangle \, d\lambda - E_{\mathrm{H}}[n] = \frac{1}{2} \int n(\mathbf{r}) \frac{\bar{n}_{\mathrm{xc}}(\mathbf{r}, \mathbf{r}')}{|\mathbf{r} - \mathbf{r}'|} d\mathbf{r} d\mathbf{r}', \tag{2.125}$$

where $\bar{n}_{\mathrm{xc}}(\mathbf{r}, \mathbf{r}')$ is the coupling-constant-averaged hole

$$\bar{n}_{\mathrm{xc}}(\mathbf{r}, \mathbf{r}') = \int_0^1 n_{\mathrm{xc}}^{\lambda}(\mathbf{r}, \mathbf{r}') d\lambda. \tag{2.126}$$

Here, we have obtained $n_{\mathrm{xc}}(\mathbf{r}, \mathbf{r}')$ by taking the hole described in Appendix B and summing over parallel and anti-parallel spins.

Using Equations (2.125) and (2.126), we can show that the exchange-correlation energy density can be written as

$$\epsilon_{\mathrm{xc}}([n], \mathbf{r}) = \frac{1}{2} \int \frac{\bar{n}_{\mathrm{xc}}(\mathbf{r}, \mathbf{r}')}{|\mathbf{r} - \mathbf{r}'|} d\mathbf{r}. \tag{2.127}$$

Hence, we have shown that the exact exchange-correlation energy can be understood in terms of the potential energy due to the exchange-correlation hole aver-

aged over the interaction from $e^2 = 0$ to $e^2 = 1$. For the case of $e^2 = 0$, the wave function is simply the independent-particle Kohn-Sham wave function, meaning that correlation is fully suppressed, $n_{\mathrm{xc}}^{\sigma,\sigma'}(\mathbf{r}, \mathbf{r}') = n_{\mathrm{x}}^{\sigma,\sigma'}(\mathbf{r}, \mathbf{r}')$ (where the exchange hole is given in Appendix B). As the density is kept constant whilst varying the electronic charge, the exchange-correlation density is implicitly a functional of the density. Finally, the exchange-correlation energy $E_{\mathrm{xc}}[n]$ can be considered as an interpolation between the exchange-only and full correlated energies for a given density $n^{\sigma}(\mathbf{r})$.

It should be noted that the Kohn-Sham method was initially shown to work for the homogeneous electron gas. Solving an auxiliary system of non-interacting Kohn-sham particles in place of the real many-body electron system in order to determine the ground state density of the true system has not yet been proven for the general case. The theory of Kohn-Sham is used on the basis of proof by exhaustion.

2.7.3 Exchange-correlation functionals

We have now shown three of the major methods that density functional theory is built upon, making it an applicable theory. Firstly, the potential in which a set of interacting particles sit can be determined uniquely by the ground state particle density. Second, there exists a universal function for the energy of a system – given in terms of the particle density – that depends on the external potential, with the global minimum of this functional defining the ground state of the system. Third, the exact system of interacting particles can be represented by an auxiliary system of non-interacting particles that exhibits the same ground state density. These three founding principles of density functional theory allow us to postulate solving for the ground state charge density for electrons in a crystal. However, there is still one major difficulty in applying density functional theory, with this being that the functional $E_{\mathrm{xc}}[n]$ is generally unknown. There do, however, exist many attempts to provide a form for the exchange-correlation energy functional that work to varying degrees of success for different sets of molecules and crystals. This is where the term 'functional soup' arises; defining the multi-

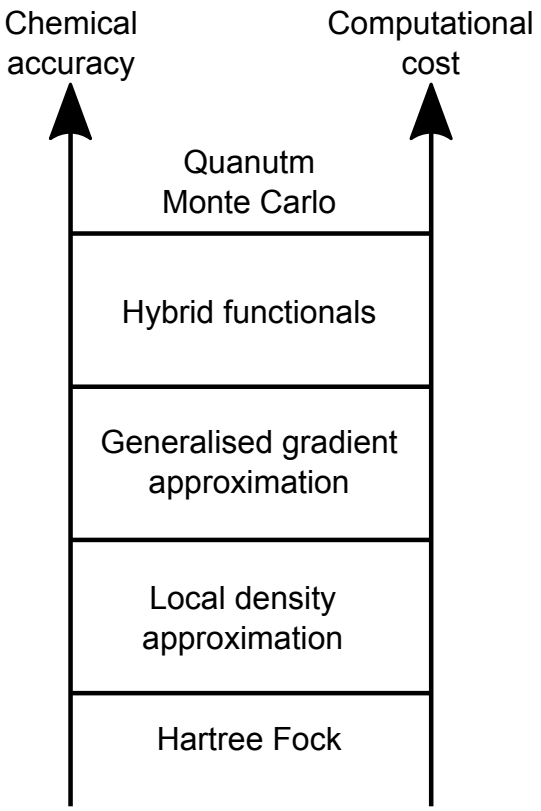

Figure 2.2: Jacob's ladder used to represent the relative cost and accuracy of various forms of *ab initio* theory available for solving the many-body problem.

tude of functionals available to density functional theory that attempt to perform best for different situations.

As no general form is yet known for the exchange-correlation density, there exist many attempts to provide it with a form; these different attempts are defined as approximations to density functional theory. Here, we outline the basic form of three approximations: 1) local density approximation, 2) generalised gradient approximation, and 3) hybrid functionals. Within certain approximations of density functional theory, there exists further differences through the exact choice of functional used to represent the exchange-correlation functional. All of these different approximations and functionals attempt to balance computational cost with chemical accuracy. As such, we tend to see trade-offs when choosing between different functional forms.

Local Density Approximation (LDA)

The first form we shall discuss is the local density approximation (LDA), which assumes that the electronic charge density in the system under consideration corresponds to that of a homogeneous electron gas, where the charge density $n(\mathbf{r})$ is a slowly varying quantity in space. Using this assumption, we can express the functional as

$$E_{\mathrm{xc}}^{\mathrm{LDA}}[n(\mathbf{r})] = \int \epsilon_{\mathrm{xc}}^{\mathrm{LDA}}[n(\mathbf{r})]n(\mathbf{r})d\mathbf{r}, \tag{2.128}$$

where $\epsilon_{\mathrm{xc}}^{\mathrm{X}}[n(\mathbf{r})]$ is the X-calculated exchange-correlation energy per electron of a uniform electron gas of density $n(\mathbf{r})$ (X defines the functional form, which is LDA in Equation (2.128)). The corresponding potential is given by

$$V_{\mathrm{xc}}^{\mathrm{LDA}}(\mathbf{r}) = \frac{d}{dn}\left\{\epsilon_{\mathrm{xc}}^{\mathrm{LDA}}[n(\mathbf{r})]n(\mathbf{r})\right\} \tag{2.129}$$

It is common to redefine the mean electron density n in terms of the interelectronic spacing r_s as

$$n^{-1} = \frac{4\pi}{3}r_s^3, \tag{2.130}$$

which allows us to redefine the exchange-correlation potential as

$$V_{\mathrm{xc}}^{\mathrm{LDA}}(\mathbf{r}) = \epsilon_{\mathrm{xc}}^{\mathrm{LDA}} - \frac{r_s}{3}\frac{d\epsilon_{\mathrm{xc}}^{\mathrm{LDA}}}{dr_s}. \tag{2.131}$$

It is valid to use the mean electron density here as we are in the slowly varying approximation. Due to the use of only the charge density at the point being considered, LDA typically encounters errors of over-binding of compounds, which leads to higher binding energies and a general underestimation of lattice parameters. Some of the most notable functionals available for LDA include Hedin-Lundqvist (HL) [57], Perdew-Zunger (PZ) [58], and Vosko-Wilk-Nusiar (VWN) [59].

Generalised Gradient Approximation (GGA)

The generalised gradient approximation (GGA) extends LDA further by considering the exchange-correlation energy density as, not only a functional of the charge density, but also the first-order derivative of the charge density [60–62]. This semi-local correction to LDA allows for GGA to outperform its predecessor in multiple areas including band gap values and lattice constants.

The GGA exchange-correlation energy can be written as

$$E_{\mathrm{xc}}^{\mathrm{GGA}}[n(\mathbf{r})] = \int \epsilon_{\mathrm{xc}}^{\mathrm{GGA}}[n(\mathbf{r}), \nabla n(\mathbf{r})] n(\mathbf{r}) d\mathbf{r} \tag{2.132}$$

with the potential being

$$V_{\mathrm{xc}}^{\mathrm{GGA}}(\mathbf{r}) = \left[\epsilon_{\mathrm{xc}}^{\mathrm{GGA}} + n \frac{\partial \epsilon_{\mathrm{xc}}^{\mathrm{GGA}}}{\partial n} + \nabla \left(n \frac{\partial \epsilon_{\mathrm{xc}}^{\mathrm{GGA}}}{\partial \nabla n} \right) \right] \tag{2.133}$$

Unlike with LDA, there is no universal form for GGA functionals. As such, there are multiple functionals that each attempt to implement the form best for certain uses; however, the form proposed by Perdew, Burke and Ernzerhof (PBE) [63] is one of the most common GGA functionals and the one that we use for this set of works (with the original paper having well over 35,000 citations at the time of writing this thesis [64]). GGA is typically more accurate than LDA, but comes with increased computational cost. For this extra cost, there is a return of a greatly reduced error in the bond dissociation energy, an improved transition-state barriers and an improvement in the band gap values. In contrast to LDA, GGA is known to typically overestimate the lattice parameters by about $5\ \%$ [65, 66].

Hybrids

As mentioned previously, the Hartree-Fock approximation perfectly estimates the exchange energy; whereas DFT tends to lead to an underestimation of the exchange and an overestimation of the Coulomb correlation. To combat this, the Hybrid functionals mix part of the Hartree-Fock complete exchange with that of

exchange calculated from DFT (most commonly using GGA) [67],

$$E_{\mathrm{xc}}^{\mathrm{hybrid}} = \alpha E_{\mathrm{x}}^{\mathrm{HF}} + (1-\alpha) E_{\mathrm{x}}^{\mathrm{DFT}} + E_{\mathrm{c}}^{\mathrm{DFT}}, \tag{2.134}$$

where E_x and E_c relate to exchange and correlation energy functionals, respectively. The mixing parameter α is either variable or fixed, depending on the choice of hybrid functional (but typically around $20\ \%$). The partial use of the Hartree-Fock exchange, along with introducing correlation calculated via GGA allows for a much more accurate picture. However, this improvement comes with a much higher computational cost, as exact exchange must also be determined (which can be extremely expensive for implementations of density functional theory using plane-wave basis sets). The gain associated with this computational cost increase includes vastly improved lattice parameters, vibrational frequencies and band gap values [68]. For the most commonly used hybrid functionals – PBE0 [69], and B3LYP [70, 71] – GGA is the choice of density functional approximation used in the mixing. HSE06 [72, 73] is also based on the GGA method and is a screened hybrid functional, where a screening is applied to the long-range part of the Hartree-Fock exchange in order to reduce computational cost.

We presented here different levels of computational accuracy available when using density functional theory. A pictorial representation of the relative accuracy versus computational cost of different *ab initio* computational methods for solving many-body problems is given in the form of Jacob's ladder, seen in Figure 2.2.

2.7.4 Pseudopotentials

Whilst Bloch's theorem allows us to expand our electronic wave function as a set of discrete plane waves, there is great difficulty in describing tightly bound, strongly localised electrons with plane waves, requiring a linear combination of a large number to be sufficient. To combat this, we employ the *pseudopotential* (frozen-core) method, in which we instead describe the tightly bound, core electrons as a background potential that screens out the ionic cores around which they reside; here, the potential due to each individual ionic nuclei is replaced with

a weaker potential that has been screened out by the core electrons, effectively combining the two. This assumption is possible as the core electrons have little importance in many of the physical properties of a material, such as chemical bonding and shallow occupied states.

We start by assuming that the lowest N_{core} energy eigenvalues E_c and eigenfunctions ψ_c of the Hamiltonian corresponding to the electronic states are already known:

$$\hat{H}\psi_c = E_c\psi_c, \quad c = 1, \cdots, N_{\text{core}}. \tag{2.135}$$

Consider the transformation of the single-particle wave function ψ_v to one that is orthogonal to the core electron wave functions ψ_c,

$$|\phi_v\rangle = |\psi_v\rangle - \sum_{c=1}^{N+\text{core}} \alpha_{cv} |\psi_c\rangle . \tag{2.136}$$

By performing the transformation, we construct a smooth valence function ϕ_v corresponding to a valence state v that is orthogonal to the core states ψ_c. Through use of the orthogonality constraint of $\langle\psi_c|\phi_v\rangle = 0$, the coefficients α_{cv} are defined as

$$\alpha_{cv} = \langle\psi_c|\psi_v\rangle . \tag{2.137}$$

The expectation value of this Hamiltonian and energy can be written as (see Appendix C for derivation)

$$\langle\phi_{v'}|\hat{H} - E|\phi_v\rangle = \langle\psi_{v'}| \left[\hat{H}^{\text{eff}} - E\right] |\psi_v\rangle . \tag{2.138}$$

To solve this, we need to use the secular equation,

$$\det \left| \langle\psi_{v'}|\hat{H}^{\text{eff}}|\psi_v\rangle - E\delta_{i,j} \right| = 0, \tag{2.139}$$

where the effective (single-particle) Hamiltonian is

$$\begin{aligned}\hat{H}^{\text{eff}} &= \hat{H} + \sum_c (E - E_c) \left|\psi_c\right\rangle \left\langle\psi_c\right| \\ &= -\frac{1}{2}\nabla^2 + V(\mathbf{r}, \mathbf{r}') + \sum_c (E - E_c) \left|\psi_c\right\rangle \left\langle\psi_c\right| \end{aligned} \tag{2.140}$$

Here, $\hat{H} = -\frac{1}{2}\nabla^2 + V(\mathbf{r}, \mathbf{r}')$ is the ordinary crystal Hamiltonian and $V(\mathbf{r}, \mathbf{r}')$ is the unscreened non-local nuclear potential. We have now constructed a pseudo-Hamiltonian with the same eigenvalues as the original, but with smoother wave functions. The new, smoother potential can be written as

$$V^{\text{eff}}(\mathbf{r}, \mathbf{r}') = V(\mathbf{r}, \mathbf{r}') + \sum_c (E - E_c) \left|\psi_c\right\rangle \left\langle\psi_c\right| . \tag{2.141}$$

Note that the energy eigenvalues of the valence electrons are always greater than those of the core electrons, thus, the term is always positive. This positive term represents a repulsion that reduces the strong attractive potential of the ionic nuclei, effectively screening them out to leave a new *pseudopotential*.

Here, we have presented an expansion of the orthogonal plane-wave method [74] to obtain the pseudopotentials [75, 76]. Whilst there are many forms that more accurately match the results of all-electron calculations (i.e. ultrasoft, norm-conserving, projector augmented wave), the basic principle is the same.

A simple local pseudopotential is generally insufficient to accurately describe most elements. The inclusion of angular (semi-local) and radial (fully non-local) dependence on the potential allows for more accurate description of the ionic potential to be felt for different quantum number electrons valence electrons.

The projector augmented wave (PAW) method [77] is a descendent of the orthogonal plane-wave method detailed above. The method differs in that it introduces projectors (a smooth, non norm-conserving function) and auxiliary localised functions that represents the rapidly varying part of the density (the augmentation function). Whilst this method is similar to that of ultrasoft, and has even been shown that ultrasoft can be derived from the PAW method [78], they have key differences that make the PAW method more transferable. Two of these are: 1) The PAW method is often considered an all-electron method, retaining a form similar to

the orthogonal plane-wave method (Equation (2.136)) for the full all-electron wave function. 2) The PAW method can be used as a pseudopotential form and then used to reconstruct an approximate full wave function from the pseudopotential calculation. This method should also be superior to norm-conserving methods in that it can more accurately describe valence states at the beginning of an atomic shell (i.e. $1s$, $2p$, $3d$, etc.).

The main advantage of the PAW method over other pseudopotential methods is that it is formally exactly equivalent to all-electron methods with a frozen core, but computationally comparable to more typical pseudopotential calculations. The PAW method dynamically updates the projection of the core region during the self consistent cycle, which is done through expansion of the core region in a local atomic basis set. Whilst this often increases the cost of each iteration, it typically reduces the total number of iterations required to achieve consistency.

The density functional theory results presented in this work are calculated using non-local, projector augmented wave pseudopotentials [78].

2.8 Calculation of atomic geometries

By using the methods outlined in the previous sections, the total energy for a many-body system can be obtained. With this information, it is next important to determine the correct geometric structure of a crystal. For a fixed stoichiometry, the most energetically favourable structure will be the ground state configuration of those atoms. As such, by modelling a large set of potential atomic arrangements using the same stoichiometry, one can determine the most stable phase.

Modelling a large sets of atomic arrangements for a set stoichiometry to determine its ground state structure encounters many issues relating to number of structures within the set, time of calculations and similarity of structures within the set. As such, another methods for determining the ground state arrangement of a crystal is detailed below.

2.8.1 Atomic geometry relaxation

In 1983, Bendt and Zunger presented the concept of relaxation of both the electronic and ionic degrees of freedom. In this method, relaxation of the atomic geometry and self-consistency in the electronic charge density can be attempted sequentially. For a chosen atomic geometry, the electronic charge density is solved for to within a reasonable degree of self-consistency in order to obtain the resulting forces and relax the atomic positions accordingly.

First, the forces must be determined for a given geometry. To do so, one must first achieve self-consistency for the electronic charge density. Using the charge density, one can take the first-order derivative of the energy of the system with respect to position. It has been shown by Hellmann and Feynman that these quantum mechanical forces are equivalent to the classical definition of a force and, as such, can be used to find the forces on the ions [79, 80].

Here, the conjugate gradient method is applied (as detailed in Appendix D. For N atoms in the unit cell, we need to solve the $3M$-dimensional non-linear equation for the force $F[n, \{\tau\}]$,

$$\mathbf{F}[n, \{\tau\}] = 0, \tag{2.142}$$

for the equilibrium geometry $\{\tau_0\}$. Here, we shall assume that the electronic charge density remains fixed, corresponding to the previously considered geometry.

In the n^{th} iteration of atomic relaxation, we have an atomic configuration $\{\tau^{(n)}\}$ as our best approximation to the equilibrium geometry. To proceed to the $(n+1)^{st}$ iteration, we must 1) choose a direction $\mathbf{d}^{(n)}$, 2) find the solution $\alpha^{(n+1)}$ that minimises $E[n, \{\tau^{(n)} + \alpha^{(n+1)}\mathbf{d}^{(n)}\}]$ and set $\{\tau^{(n+1)}\} = \{\tau^{(n)} + \alpha^{(n+1)}\mathbf{d}^{m}\}$ and 3) calculate the total energy $E[n, \{\tau^{(n+1)}\}]$ and force $F[n, \{\tau^{(n+1)}\}]$. After having updated the geometry, we then relax the electronic degrees of freedom. This process is iterated until either the total energy or forces are converged to within a decided tolerance.

As outlined in Appendix D, the conjugate gradient method relies on a unique conjugate direction $\mathbf{d}^{(n)}$ for each step n in order to maintain the minimisation performed in the previous steps. For the first step, this is defined as $\mathbf{d} = F[n, \tau]$ (note, if this choice was maintained for all steps, then the method would be equal to steepest descent). The form of the conjugate directions for each step can be rewritten in the form

$$\mathbf{d}^{(n)} = F(\tau^{(m)}) + \sum_{i=1}^{n-1} \gamma^{(i)} \mathbf{d}^{(i)}. \tag{2.143}$$

Note that, whilst the energy functional $E[n, \{\tau\}]$ from density functional theory is not generally quadratic in $\{\tau\}$, the use of the conjugate gradient algorithm for in simultaneous electronic and atomic relaxation is found to be robust [81].

2.8.2 Structural prediction

Structural prediction has been of great interest to the field of condensed matter for some time [81–83]. The main focus of structural prediction for this work is on the matching of lattice descriptors for two materials in order to determine the most energetically favourable interface to form between cleaved surfaces of the parent crystals, or from growth of one crystal on top of another.

Lattice matching

Lattice matching is the method of identifying whether the face of a chosen cell of one crystal matches the face of a cell relating to another crystal (this could be the same crystal if considering dislocations or grain boundaries between different Miller planes of the same material) [84].

The method of lattice matching involves searching over sets of lattice vectors of either crystal to determine vectors of comparable lengths within the two crystals, and then identifying which sets of vectors have the same angle. This is all performed to within predefined tolerances, as it is unlikely to find identical matches

between different crystals. The search can either be limited to specific Miller planes, or performed over the entire lattice.

In order to identify potential lattice matches between two parent crystals, a set of lattice translation vectors $\mathbf{U} \equiv \{\mathbf{u}_i\}$ (where $\mathbf{u}_i$ is an individual translation vector of the basis set) must be generated for each lattice,

$$\mathbf{u} = \mathbf{a}_1\hat{\boldsymbol{\imath}} + \mathbf{a}_2\hat{\boldsymbol{\jmath}} + \mathbf{a}_3\hat{k}, \quad |\mathbf{u}| \leq l_{\max}. \tag{2.144}$$

Quantities relating to one of the two parent crystals are distinguished with use of a prime ($'$). The two basis sets of translation vectors are then compared in order to identify pairs of vectors $\mathbf{u}_1, \mathbf{u}_1'$ that match in magnitude. Once all potential pairs have been identified, the pairs are cycled through in both sets, with their combined angles, $\hat{\mathbf{u}}_1 \cdot \hat{\mathbf{u}}_2$ and $\hat{\mathbf{u}}_1' \cdot \hat{\mathbf{u}}_2'$, being compared in order to identify successful lattice matches.

The two main conditions required in order to find a successful lattice match can be written as follows:

1) $|\mathbf{u}_1| \simeq |\mathbf{u}_1'|, \quad |\mathbf{u}_2| \simeq |\mathbf{u}_2'|$ (length match).

2) $\frac{\mathbf{u}_1 \cdot \mathbf{u}_2}{|\mathbf{u}_1||\mathbf{u}_2|} \simeq \frac{\mathbf{u}_1' \cdot \mathbf{u}_2'}{|\mathbf{u}_1'||\mathbf{u}_2'|}$ (angle match).

For sets where these conditions are met, interfaces can be generated. With these interfaces, *ab initio* methods can be used to identify the energy and forces associated with cleaving the crystals and forming the interface; this allows for one to perform geometric relaxation of the generated interfaces and, then, identify the most energetically favourable interface between two crystals (commonly identified by comparing the different values of energy cost per unit area of the interface).

2.9 *Ab initio* simulation details

In this thesis, first principles calculations, within the framework of density functional theory, were performed using the Vienna *Ab initio* Simulation Package

(VASP) [85–87]. The generalised gradient approximation Perdew-Burke-Ernzerhof (PBE) [63] functional was used to perform structural and electronic relaxations of systems presented in this thesis, unless specified otherwise. The projector augmented wave method [78] was used to describe the interaction between core and valence electrons, and a plane-wave basis set was chosen to model the electronic wave functions.

Whilst testing was performed using a plane-wave basis set energy cut-off between 500–1000 eV, it was found that 700 eV obtained all features identified by higher energy cut-offs whilst offering reduced computational cost (see Appendix F for more details). As such, all results presented in this work were obtained using an energy cut-off of 700 eV for the plane-wave basis set.

Table 2.1: The pseudopotential valency for each atomic species used in this thesis.

Species	valency
H	$1s^1$
Li	$1s^2 2s^1$
O	$2s^2 2p^4$
F	$2s^2 2p^5$
Al	$3s^2 3p^1$
Si	$3s^2 3p^2$
Ca	$3s^2 3p^6 4s^2$
Ti	$3p^6 3d^4 4s^2$
Ni	$3d^8 4s^2$
Cu	$3d^{10} 4s^1$
Sr	$4s^2 4p^6 5s^2$
Mo	$5s^1 4d^5$
Sn	$5s^2 5p^2$
Ba	$5s^2 5p^6 6s^2$
W	$6s^1 5d^5$

All *k*-point grids used for calculations presented in this thesis were Γ-centred and generated using the Monkhorst-Pack scheme [88], except for band structure calculations, where precise *k*-point paths along the high-symmetry lines were

taken (see Appendix E for further details on *k*-point sampling). All systems were geometrically relaxed, using the conjugate gradient algorithm, to within 0.01 eV/Å and electronic self-consistency was accurate to within 10^{-7} eV. Surface structures were formed using symmetrically equivalent terminations on either side of the slab. A 14 Å vacuum gap was introduced to separate the two surfaces in order to remove interaction of the two across the vacuum gap. The valence electrons that each pseudopotential considered for its respective atomic species used in this thesis are presented in Table 2.1.

Density Functional Perturbation Theory (DFPT) [89, 90] is used in this work to calculate both the dielectric tensor and the phonon frequencies (here, we only consider the Raman frequencies) of a material. As implemented in VASP, the Hessian matrix is constructed by introducing symmetrically unique displacements to the system and obtaining the second order derivatives. For elastic and phonon results, the Hessian can be used directly to determine these values. The polarisations caused by these ionic displacements can also be calculated to determine the dielectric tensor. For the low frequency response (static regime), both the electronic and ionic contributions to the dielectric tensor are calculated; whereas, for the high frequency response (infinite regime), only the electronic contributions are considered. For DFPT calculations, a higher simulation accuracy is required to properly determine the Hessian matrix. In VASP, the ionic contributions to the elastic tensor are not determined using DFPT. In this work, these are, instead, determined using the finite difference method [91].

Further details regarding *k*-point grid sizes, functional choices and other differences can be found in each work's respective chapter. All figures in this thesis that depict ball and stick models of atomic structures were generated using the VESTA atomic structure visualisation package (VESTA 3) [92]. All figures and tables in this thesis that refer to being "obtained from first principles calculations" are obtained using DFT-PBE calculations, unless otherwise specified.

The scheme employed by VASP for achieving self-consistency in solving the Kohn-Sham equations can be selected using the `IMIX` tag in the `INCAR` file. The default for this tag (which is used for this work) employs a combination of the Broyden [93] and Pulay [94] mixing schemes. The Broyden method iteratively

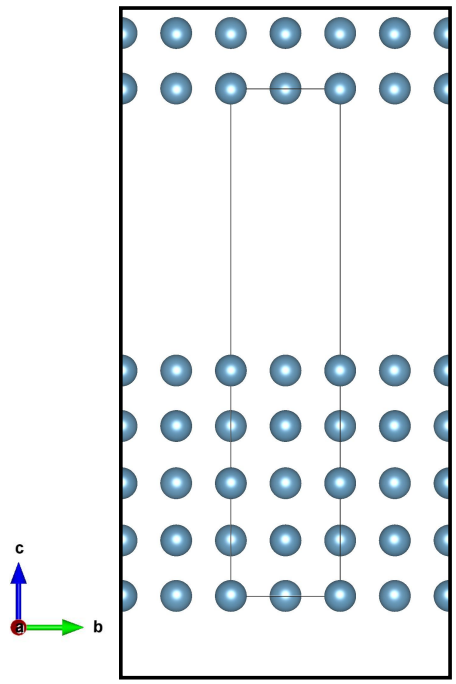

Figure 2.3: An example artificial periodic structure. An infinitely repeating structure along the c-axis of calcium (001) slabs separated by a 14 Å vacuum region. The small black box denotes the unit cell of this periodic structure.

improves an approximate of the Jacobian matrix to find the optimal solution, whereas the Pulay method combines the input vectors assuming linearity to minimise the residuals. The implementation in VASP transforms the Broyden and Pulay into each other for certain choices of weights of the previous iterations [87,95].

2.9.1 Artificial periodic systems

Due to the use of periodic cells for simulations, the concept of *artificial periodic systems* arises. This term defines a system where periodicity is not desired, but is, instead, an effect of working in a periodic space. In Figure 2.3, we present an example system of an atomic slab with a vacuum region; due to the periodicity, this slab appears either side of the vacuum gap, with this pattern repeating infinitely. To compensate for this unwanted periodicity in perpendicular to the surface plane, a sufficiently large vacuum gap (14 Å wide) is introduced between the periodic slabs to try and reduce (and, if possible, eliminate) interaction between the neighbouring surfaces either side of the vacuum region.

Chapter 3

Colossal permittivity in $CaCu_3Ti_4O_{12}$

"There are three stages in scientific discovery. First, people deny that it is true, then they deny that it is important; finally they credit the wrong person."

— Bill Bryson

3.1 Introduction

The work in this chapter is motivated by the interest in studying systems in which the interface affects the apparent properties of the overall macroscopic system. The phenomenon of colossal permittivity is introduced in this section, with a focus on this unusual property in the material $CaCu_3Ti_4O_{12}$. The chapter starts with descriptions of the dielectric properties, effects and phenomena currently known. A study of the previous background literature is then presented in an attempt to ascertain trends and commonalities between experimental results over the past 20 years. Then follows a detailed discussion of the results. The bulk and surface properties of $CaCu_3Ti_4O_{12}$ are presented and used to help characterise the interfaces studied later. Next, the investigation of the *grain|grain boundary* interface for $CaCu_3Ti_4O_{12}$ at the atomic scale is outlined, with the focus placed on how this work can describe all previously observed features associated with colossal permittivity. A mechanism is put forward as the atomic-scale origin of colossal permittivity in $CaCu_3Ti_4O_{12}$ and is explored further by using circuit-models to determine how the system geometry affects its dielectric properties. Finally, a summary of

the work is presented.

3.2 Colossal permittivity

Colossal permittivity materials display values of relative permittivity ε_r typically greater than 10^3 and exhibit extreme polarisation in an applied electric field. Given such high values for the permittivity, such materials offer new possibilities in gas sensing, electronic capacitors and high power density energy storage [96–98]. The latter pair can be of vital importance throughout the world in electricity transmission across power grids. For the purposes of energy storage devices, permittivity in the static ($\omega = 0$) regime is of interest. Colossal permittivity was first observed in the year 2000 in the material known as calcium copper titanate, $CaCu_3Ti_4O_{12}$ (CCTO) [99].

3.2.1 Dielectric response of homogeneous materials

Dielectric materials are insulating materials that do not conduct electricity when under an external applied electric field. They, instead, become polarised, forming an electric field opposing that of the one applied. However, this induced field exhibits a smaller magnitude than the applied one, which is dependent on the permittivity of the material. This induced field can be used to store electrical energy, where the storage time after the external field is removed also relates to the permittivity of the dielectric medium. Permittivity is a complex value, containing both a real and imaginary component, defined as

$$\varepsilon_r = \varepsilon_r' - \mathrm{i}\varepsilon_r'' = \varepsilon_r' - \mathrm{i}\frac{\sigma}{\omega}. \tag{3.1}$$

Here σ is the conductivity of the medium, ω is the frequency of the external field and ε_r' and ε_r'' are both non-negative, real values [1]. The real term (ε_r') describes

[1] The negative sign convention is used to make the imaginary permittivity term non-negative for dissipative materials, using the time dependence $\exp(\mathrm{i}\omega t)$.

the capacity of the material where, for a dielectric medium between two metal plates, the capacity (C) is defined as

$$C = \frac{\varepsilon_r' \varepsilon_0 A}{d}, \tag{3.2}$$

where A is the area of one of plate and d is the distance between the two plates. The imaginary component to permittivity (ε_r'') is related to the conductivity σ – and, hence, the resistivity ρ – of the material via the equation

$$\sigma = \frac{1}{\rho} = \varepsilon_0 \varepsilon_r'' \omega. \tag{3.3}$$

In order to describe the quality of a dielectric medium, a comparison is made between the real and imaginary parts of permittivity;

$$\tan\delta = \frac{\varepsilon_r''}{\varepsilon_r'}. \tag{3.4}$$

This fraction is a descriptor of the conductivity and loss of the material and is, hence, termed the *dielectric loss*. When $\tan\delta = 0$, the medium is termed as a perfect dielectric – this means that it is lossless. When $\tan\delta << 1$, then the material is a poorly conducting low-loss medium, whereas when $\tan\delta \approx 1$, it becomes a lossy medium that cannot maintain an induced field for long after the applied field has been removed. As $\tan\delta$ tends towards infinity, the dielectric tends towards a perfect conductor.

An example for the dielectric response of a material is shown in Figure 3.1. Here, we see five specific regions relating to different frequency regimes. At high frequencies, atomic and electronic resonances are the main contributors – due to their fast response time. These high frequency responses can be seen as the polarisation or oscillation of the electrons and ions. At lower frequencies, we encounter atomic and dipolar relaxation of the material in response to the field. The microwave range covers the dipolar response, which involves relaxation of the orientation of dipoles within the material. The ionic response in the short radio wave range is due to geometric relaxation of the ions. The final regime on the

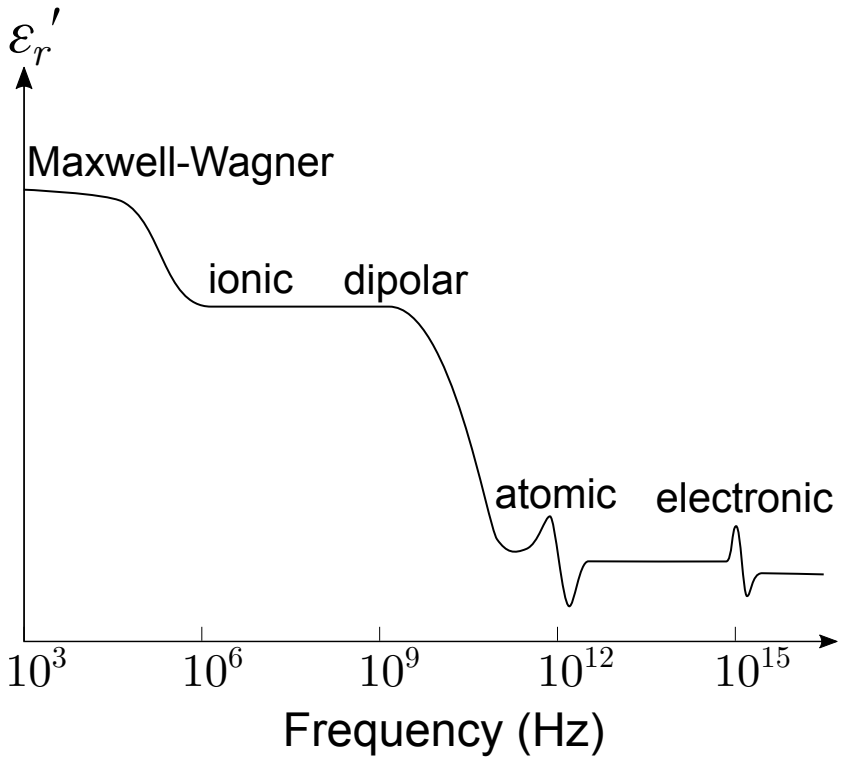

Figure 3.1: An example dielectric response for the real part of permittivity (ε_r') of a complex medium. The higher frequencies are dominated by atomic and electronic resonances, whereas the lower frequencies are related to ionic and dipolar relaxations. The low frequency range is then attributed to a Maxwell-Wagner effect, which arises due to space charge polarisation.

graph, relating to long radio waves, is due to large-scale space charge separation (termed the *Maxwell-Wagner effect*), which can be caused by partially conducting regions within the medium. Both the presence and strength of these various features of the dielectric response are strongly material dependent; for example, the Maxwell-Wagner effect is mainly associated with inhomogeneous materials and, as such, is unlikely to be present in homogeneous materials.

For the remainder of this chapter, real permittivity will be referred to as permittivity. The contributions relating to the imaginary component of permittivity will instead be accounted for using dielectric loss.

3.2.2 Dielectric response of inhomogeneous materials: The Maxwell-Wagner effect

Whilst the dielectric behaviour of homogeneous materials is well understood, that of inhomogeneous materials is much more complicated. The permittivity and dielectric loss of a more complicated material can be strongly affected by particles of conducting impurities dispersed within it. Though an exact description of the losses produced by these defects can be very difficult to obtain, the Maxwell-Wagner effect offers a useful analytical model for the dielectric behaviour of inhomogeneous materials containing spheroidal particles. This phenomenon was first tackled by Maxwell, who modelled planar sheets of materials, each with differing ratios of conductivity versus dielectric constant [100]. The phenomenon was later generalised by Wagner [101] and Sillars [102].

Irregularities in the dielectric behaviour of solids can, in many cases, be attributed to the presence of higher conductivity regions within them. For example, insulators can display a higher apparent conductivity due to embedded semiconducting or metallic particles. The exact effect of these inclusions depends on many of their properties (i.e. particle sizes, shapes, orientations and conductivity). In order to take into account the potential variation of some of these parameters, Maxwell-Wagner assumes a Gaussian spread of sizes, orientations and ellipsoidalities.

The dielectric response of an inhomogeneous dielectric material can be largely frequency dependent due to the build-up of charge at points of dielectric non-linearity (at interfaces between different dielectric media). When regions of higher conductivity are embedded within an insulating region, the apparent conductivity of the overall system appears higher in alternating fields than steady ones.

When an electric field $\mathbf{E} = \sum_i^3 E_i \mathbf{a}_i$ is incident on such a system, the conducting particles become polarised. Charge accumulates at the interface between these conducting regions and the large non-conducting region, forming macroscopic polarisation $\mathbf{P} = \sum_i^3 P_i \mathbf{a}_i$; this causes a large increase in polarisability at low frequencies. Through choice of the shape of the conducting regions, one can tune the effective permittivity of the system due to the relation

$$\varepsilon_{r,ij} = 1 + \frac{1}{\varepsilon_0}\frac{dP_i}{dE_j}, \tag{3.5}$$

where the subscripts i and j represent the lattice vectors and, as such, the permittivity is seen to be axially dependent. Such an inhomogeneous system can be interpreted as a single material with a single permittivity tensor and conductivity tensor. Hence, by changing the geometry of the system, a wide range of dielectric responses can be displayed.

Systems with various effective dielectric responses can be created by dispersing conducting particles inside a dielectric material, due to the mismatch of the dielectric response of the two materials [102]. In order to engineer high permittivity materials, one can disperse conducting particles inside a large dielectric material. When applying an external electric field, electrons within the conducting particles respond quickly to the field, gathering at the interface between the particle and the insulating bulk. Therefore, a large polarisation is formed between these conducting electrons and the ions in the conducting particles, even under small external fields. Such a system can be shown to have an effective permittivity much higher than that of the individual components, due to the overall dielectric response of the system as a whole [103].

The Maxwell-Wagner model allows for a system containing insulating and conducting regions to be compared to an LCR circuit, simplifying the calculation and allowing for a more analytical approach to an otherwise complicated system.

3.2.3 Impedance spectroscopy

A common technique for measuring the dielectric response of a material is to perform impedance spectroscopy on it, which returns the real (Z') and imaginary (Z'') impedance responses of the material for a range of frequencies. Figure 3.2 depicts an example impedance spectroscopy measurement. Each semicircle is attributed to a different component of the system (i.e. electrode, grain, grain boundary). From these, the dielectric response of each individual component can be determined. The apparent offset of the first semicircle from zero along Z' in

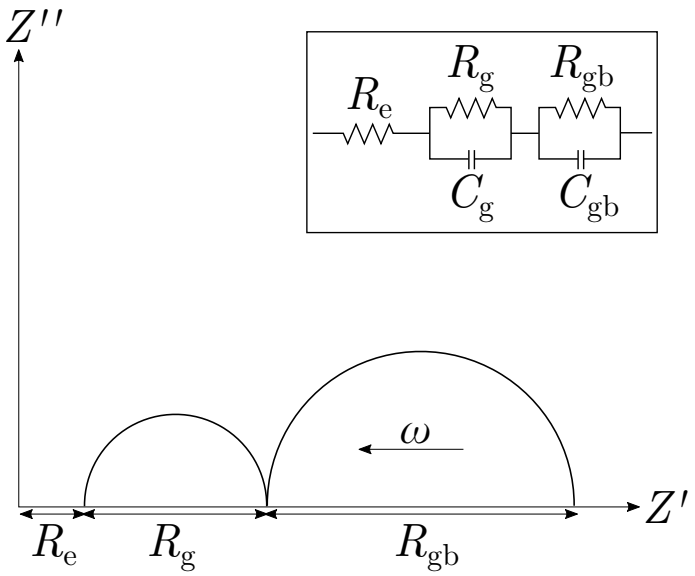

Figure 3.2: An example impedance spectroscopy graph of a multi-component circuit. The figure inset depicts how the component arrangement that would result in such an impedance response. The subscript e relates to electrode terms, g to grain terms and gb to grain boundary terms. Decreasing Z' values relate to larger frequencies.

the impedance spectroscopy is typically linked to the resistance of the electrode. The electrical impedance Z of a component is

$$Z = Z' - \mathrm{i}Z'' = R - \mathrm{i}\frac{1}{\omega C}, \tag{3.6}$$

where R is the resistance of the component. By using the relation between resistance and resistivity,

$$R = \frac{\rho L}{A}, \tag{3.7}$$

along with Equation (3.3), one can determine the imaginary part of relative permittivity:

$$Z' = \frac{L}{\varepsilon_0 \varepsilon_r'' \omega A}. \tag{3.8}$$

Here, A is the cross sectional area of the component normal to the flow of current and L is the length of the component parallel to the flow of current. By using Equations (3.2) and (3.6), the imaginary impedance term can be related to the real part of permittivity,

$$Z'' = \frac{\varepsilon_r' \varepsilon_0 A}{\omega d}. \tag{3.9}$$

For a component that has both resistive and capacitive terms, the areas from Equations (3.8) and (3.9) can be considered as equivalent, as can the lengths. We now have a means of giving an effective permittivity, or dielectric response, of a multi-component system by analogising it to a single-component system.

3.2.4 Proposed applications

High permittivity materials have been considered for improving microelectronics through improving random access memory devices [104–106]. As the capacitance is proportional to the permittivity, a higher permittivity material can be used to make a smaller capacitor. Therefore, such materials are believed to be very important for scaling down electronics. This increase in capacitance can also be seen as an increase in energy density. As such, such capacitors could be used to bridge the gap in energy density between capacitors and batteries, leading to the possibility of a new form of energy storage [96–98, 107, 108].

Colossal permittivity materials have also been considered for gas sensing technologies. Materials with large permittivity values tend to exhibit strong sensitivity of their dielectric properties to their local environment. This high degree of dielectric sensitivity can be used to probe the concentration of various gases within the atmosphere [109, 110].

It must be noted that, whilst the real and imaginary parts of the dielectric response are dependent on each other, as seen via the Kramers-Kronig relation [111] (which holds for both homogeneous and inhomogeneous materials), the values for each component at a specific frequency are strongly independent of each other. This is due to the relation uses the response of the real part across the entire frequency range to determine the response of the imaginary part across the entire frequency range, and vice versa. As such, these two values can be treated as uncoupled for a system with many different responses, in particular for this work as we are only interested in a small frequency window of 0–1 MHz.

3.3 Background

The perovskite-related structure of $CaCu_3Ti_4O_{12}$ (CCTO) was first documented with its discovery in 1967 [112], yet no notable characterisation of its properties was performed until 2000, when Subramanian *et al.* [99] measured its dielectric properties. At this time, its permittivity was observed to be over 10^4 at room temperature. This value was greater than not only materials with the $AA'_3B_4O_{12}$ chemical composition, but also most other materials known at the time, which typically display permittivity values of ~1–10 (with even materials described as high dielectrics only reaching around 100 [20, 113–115]). Since then, permittivities greater than ~10^3 have gained the term *colossal permittivities*. It soon became an attractive alternative to other high permittivity materials, such as $BaTiO_3$, due to its high dielectric constant reported over a wide range of temperatures (100–600 K) [99, 116, 117] and frequencies (10^2–10^6 Hz) [99, 117–119]. CCTO has also been shown to be relatively straightforward to manufacture, only requiring single-step synthesis methods heating precursor oxides to temperatures between $1,000$ and $1,200$ °C (such as solid-state reaction, wet-chemistry or sol-gel) [110]. With these features, along with its ability to maintain its structural phase across a temperature range of 35–1273 K, CCTO has seen a lot of research in device applications in areas such as gas sensing, electronic capacitors and high power density energy storage [96–98, 120, 121].

Even though it has been two decades since the colossal permittivity of CCTO was measured, there is still uncertainty in the field surrounding the origin of these high values. The irregularly high permittivities of other materials, such as $BaTiO_3$, tend to be related to their intrinsic properties, such as polarisation [122, 123]. It has been shown, however, that the high permittivity exhibited by CCTO is not an intrinsic property of the material and, instead, is an extrinsic phenomenon that arises at the boundary between the individual grains that naturally form during crystal growth (the *grain boundary*) [124–126]. Many qualitative arguments have been put forward for the origin of this unusual property, but the fundamental mechanism behind this is still unknown.

CCTO has a 20-atom rhombohedral primitive cell with the perovskite-like chemi-

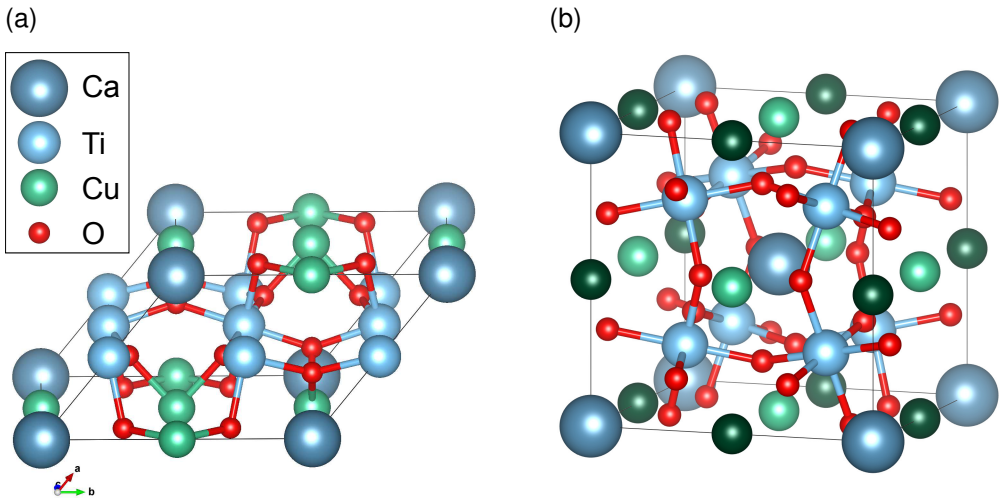

Figure 3.3: Ball and stick model of $CaCu_3Ti_4O_{12}$ unit cells. (a) The 20-atom rhombohedral primitive cell of $CaCu_3Ti_4O_{12}$. (b) The 40-atom anti-ferromagnetic cubic unit cell of $CaCu_3Ti_4O_{12}$. Different colours of the Cu atoms denote opposing spins.

cal formula of (A:A')BO_3, known as a double perovskite (see Figure 3.3a). However, to properly capture its magnetic ordering, a 40-atom cubic cell is required (see Figure 3.3b) [127, 128]. In this extended cell, the two primitive cells have opposite spins, properly describing the anti-ferromagnetic ground state. The 40-atom cell has a lattice constant of 7.391 Å and a space group of Im^3, with the crystal structure being shown in Figure 3.3b. Both theoretical and experimental studies have extensively explored the permittivity of bulk CCTO and have shown that the dielectric constant of the bulk is much lower than that of the overall sample, with the static and infinite responses being 40–150 and 6, respectively [116, 129–134]. It should be noted that this is still a rather large dielectric response for a bulk material, and this is associated with its large bulk polarisability.

3.3.1 Crystal growth techniques

When samples of CCTO are grown, a natural structure of grains separated by grain boundary regions forms. These grains are formed of crystalline CCTO – which is often identified as semiconducting [125, 128] – whilst the material that grows between the crystalline grains, the *inter-grain material*, is formed of non-

stoichiometric quantities of the composite elements of CCTO. This inter-grain material is shown to be insulating [123, 125, 135]. The geometry and electrical properties of this structure are strongly dependent on the growth conditions and techniques employed. As such, these samples can display largely different grain shapes, grain sizes, grain boundary region widths and stoichiometries. As the formation of this grain|grain boundary structure is unavoidable with many of the growth techniques used – and the properties relating to this structure strongly affect the dielectric response [124, 136–141] – they must be carefully considered when determining the mechanism responsible for colossal permittivity in these samples.

3.3.2 Proposed mechanisms behind colossal permittivity

In the first paper studying the dielectric properties of CCTO, Subramanian *et al.* [99] noted the unusually high permittivity exhibited by the material. At the time, they compared it to CuO-covered-(Ba,Sr)TiO_3 systems and suggested that a similar mechanism was occurring in CCTO. In the 1990s, Yang *et al.* described a system of semiconducting grains consisting of (Ba,Sr)TiO_3 and $BaZrO_3$ covered by an insulating region of CuO [142, 143] and showed it to exhibit large permittivities of the order of 10^4. In these systems, the abnormal dielectric properties were attributed to the semiconductor and surrounding insulating material acting as capacitors in series – this was termed as the *barrier layer mechanism*. To explore this in CCTO, Subramanian *et al.* measured samples with different levels of copper deficiency and showed that lower concentrations of copper coincided with a decrease in permittivity. From this, they concluded that the reduced copper precluded the formation of a copper-rich region at the grain boundary, which resulted in a weaker barrier layer effect.

In 2002, Sinclair *et al.* [125] put forward the idea of internal barrier layer capacitance (IBLC) being the cause of colossal permittivity within CCTO. Through the use of impedance spectroscopy, they showed that the material consisted of semiconducting grains and insulating grain boundaries. Sinclair *et al.* built upon the theory of barrier layer mechanism put forward by Subramanian *et al.* by attributing

the barrier layer to an insulating copper-rich material forming at the boundaries between the semiconducting grains. IBLC has often been characterised experimentally by the Maxwell-Wagner effect [134, 144, 145], yet the microscopic origin behind this has not yet been determined.

Early on, electrode effects on CCTO samples were also suggested as a cause for the high permittivity values [116, 146, 147]. However, through impedance spectroscopy, it has since been shown that, whilst having an effect on the permittivity, it was not the main contributor to this phenomenon [135, 148, 149]. As the impedance plots were dominated by arcs attributed to the grain boundary resistances, it was concluded that the electrode resistance and any subsequent effects were minor in comparison those of the grain boundary. Furthermore, studies involving multiple electrode materials found that there was little change in the electrical properties based on material choice [135, 148, 150].

Another theory of the mechanism causing colossal permittivity was put forward by Adams and Sinclair *et al.* [124], where they describe Schottky-type barriers forming at the grain boundary region. This was further examined by both Adams *et al.* [150] and Kim *et al.* [151] in 2006 (as well as Felix *et al.* in 2011 [152]), who both employed impedance spectroscopy in order to analyse the system under electric fields. They found that the grain boundary resistance decreases with increasing DC bias, which confirms that the grain boundary resistance is nonlinear. In their analysis, they outline the nonlinearity as a key descriptor of diode-like back-to-back Schottky barriers [153], which would, hence, be present at the grain boundaries.

In an attempt to identify the internal morphology of CCTO samples, Cohen *et al.* outlined various potential models that could give rise to colossal permittivities at low frequencies ($< 10^6$ Hz) from a system of grains and grain boundaries [154]. From their investigation, it was concluded that the most plausible model incorporated conducting grains surrounded by insulating grain boundaries. This model should agree with the generally accepted view of semiconducting grains and insulating grain boundaries, as long as the grains are sufficiently doped.

With the literature being in general agreement that the colossal permittivity arises

from an IBLC mechanism between the semiconducting grains and insulating grain boundaries, focus turned to analysing these boundary regions in order to characterise its composition [108, 136, 155–158]. Impedance spectroscopy and energy dispersive X-ray (EDX) methods were employed to characterise the dielectric properties and the interface region elemental composition of various samples, respectively. In doing so, it could be determined how different inter-grain material compositions affect the dielectric properties. Whilst there is general agreement that there is little calcium content within this region [159], some show higher titanium concentration [27, 156, 160, 161], whereas others show higher copper concentration [108, 159, 160, 162–166].

Increasing the concentration of titanium in the precursor compounds has been shown to help control the phase of materials. Excess titanium promotes the formation of anatase TiO_2 and stabilises the CCTO formation and grain growth [162, 167] (resulting in a decrease in the grain boundary resistivity), whereas a deficiency introduces copper oxide phases, Cu_xO, where $x = 1, 2$ [162, 168, 169] (resulting in an increase in grain boundary resistivity). Moreover, this copper oxide tends to localise at the grain boundary region [98, 155, 158, 163, 170–172] and is associated with an increase in the permittivity of the overall sample [24, 155, 158, 163]. Whilst small increases of TiO_2 can lead to larger permittivities [167], it is generally found that increasing the concentration above $0.01\ \%$ results in lower permittivity values [161, 167, 173]. By understanding these, initial chemical concentrations in the growth process could be tuned to better promote the desired properties of the grain boundary region.

Whilst there exist many mechanisms proposed for the origin of colossal permittivity in CCTO, most have a common thread of a new material forming between the grains, in the grain boundary region. However, none of these can simultaneously account for high loss factors, low breakdown voltages [174], occasional low resistance over grain boundaries [175], or how colossal permittivity scales with system size [160]. Colossal permittivity ranges by orders of magnitude in different materials [27, 176], but also in samples of the same stoichiometry [155]. This means there is an intrinsic effect in these materials responsible for IBLC.

Since 2010, most work with $CaCu_3Ti_4O_{12}$ has focused on doping the system in or-

der to improve its dielectric properties further [109,177–181]. Yet, without a quantitative explanation of the cause of this colossal permittivity, choice of dopants and growth techniques cannot be made to best enhance the features that cause this phenomenon. Without an understanding of the grain boundaries at the atomic level, the system's theoretical maximum cannot be realised.

3.3.3 Internal Barrier Layer Capacitance

The internal barrier layer capacitance is often described using the Maxwell-Wagner effect. The insulating inter-grain material is analogised to the large dielectric medium, with the grains (which are often identified as semiconducting) considered as the embedded conducting particles. In this picture, the charge carriers within the grains are able to respond relatively quickly to an applied electric field, but get pinned at the interface between the conducting grains and insulating inter-grain material, preventing the overall flow of current through this structure. Due to this, a large build-up of carriers forms at one grain edge, with the opposite one being depleted of charge, which appears as a large polarisation over each grain. This presents itself as a large dielectric response, with large separation of charges possible in the individual grains, but also a relatively high loss due to the ease of carrier movement in the semiconducting grain.

3.4 *Ab intitio* simulation details

Our calculations were performed using *k*-point grids with *k*-point densities equivalent to those used for analysing the $CaCu_3Ti_4O_{12}$ (CCTO) 40-atom unit cell, with geometric relaxations and electronic calculations using $4\times4\times4$ and $7\times7\times7$ grids, respectively. All *k*-point grids were Γ-centred and generated using the Monkhorst-Pack scheme [88]. For a detailed description of the process used to determine the necessary *k*-point grid size and energy cutoff, see Appendix F.

To accurately describe the insulating properties of CCTO and Cu_xO, the Hubbard GGA+U model was used [182, 183]. This approach was required for this chap-

ter as the d-orbital electrons of $CaCu_3Ti_4O_{12}$ and CuO are over-correlated by the GGA-PBE functional, resulting in them being more loosely bound to (mainly) the copper atoms of the materials. To compensate for this, the Hubbard +U model adds an attractive potential into the electron–electron interaction terms (affecting only the d-orbital densities), effectively reducing this overly strong repulsion predicted by the correlation term of GGA-PBE. As implemented in VASP, this potential can be applied to specific orbitals of specific species. This issue of over-correlation typically occurs for d-elements where the valence band maximum (VBM) and conduction band minimum (CBM) of a crystal are composed of the same localised orbitals (i.e. Mott insulators). Here, we used the reduced $U-J$ Hubbard method, which replaces the parameter U with the parameter $U-J$, as it has been shown that this scheme is sufficient for most systems requiring a Hubbard correction [183]. We fully explored the range $U = 0$ to 10 eV to confirm our results held for all values. For the results presented, a +U correction of $U = +4$ eV was used for the Cu and Ti in $CaCu_3Ti_4O_{12}$, and $U = +7$ eV for the Cu in CuO. No Hubbard correction was applied to bulk Cu_2O. For interface systems, the same Hubbard correction was applied to all atoms of the same species throughout the system (with the largest +U taking precedence). Using these values of +U, the experimental bulk band gaps of both CCTO and CuO were reproduced, with those being 1.5 eV [184] and 1.2 eV [185], respectively, Meanwhile, Cu_2O did not have a +U correction applied as it has been found to not be necessary to reproduce the insulating property of the material [186, 187]. The charge analyses of these systems were performed using the Bader technique [188].

To generate the interfaces, we used our in-house code ARTEMIS (discussed in Chapter 7), which generates interface structures and the corresponding slabs of material for atomic scale analysis. Our CCTO and CuO slab thicknesses were increased in thickness until convergence of various electronic properties was reached. As such, we used CCTO regions of 2.5 unit cell thickness in our grain boundary systems. The same analysis was performed for CuO and Cu_2O, with the optimum thickness being 3 unit cells for each. This comparison allowed us to consider CCTO|Cu_xO interfaces in general. We modelled the CCTO (001) surface at the interface as other planes brought further complications as they are generally found to be polar, with dangling bonds or non-stoichiometric surfaces,

which can lead to instability of the surface. We also considered various Cu_xO phases and cleavage planes, looking for surfaces and phases which matched to the (001) surface of CCTO within a $6\ \%$ strain tolerance. The Cu_xO strain tolerance for the $x = 1$ (terminated on (100)) and $x = 2$ (terminated on (001)) were $5.06\ \%$ and $1.31\ \%$ respectively.

For the remained for this chapter, we consider the CCTO(001)/CuO(100) structure as the archetype interface and will refer to it as CCTO/CuO. The interface system consists of 2.5 CCTO unit cells, terminated on TiO_2 planes, next to a 3 unit cell slab of monoclinic CuO (100) that has been orthorhombically-strained. The other interface structure presented in this chapter is that of CCTO(001)/Cu_2O(001), consisting of 2.5 CCTO unit cells, terminated on the TiO_2 plane, next to a Cu_2O (001) slab composed of 3 bulk unit cells. In total, 10 unique interface structures composed of CCTO and Cu_xO have been considered for this study. These unique interfaces consist of a set of different orientations and terminations, with all displaying qualitatively similar results to those presented in this chapter. Due to others either being less energetically favourable, or involving substantial reconstruction of the Cu_xO region (leading to amorphous Cu_xO), we have focused on the two interfaces discussed in this thesis.

3.5 Bulk properties

3.5.1 Calcium copper titanate

Since being identified as a colossal permittivity material, the bulk properties of CCTO have been extensively explored both experimentally and theoretically. Provided in this section are the bulk properties of CCTO calculated for this worked.

The structure of CCTO is known to be dynamically stable [131, 189–191]. By comparing the total energy of CCTO bulk with that of its constituent oxides – CaO, CuO (monoclinic) and TiO_2 (anatase) – the formation energy of this compound can be determined. The equation for formation energy E_f is

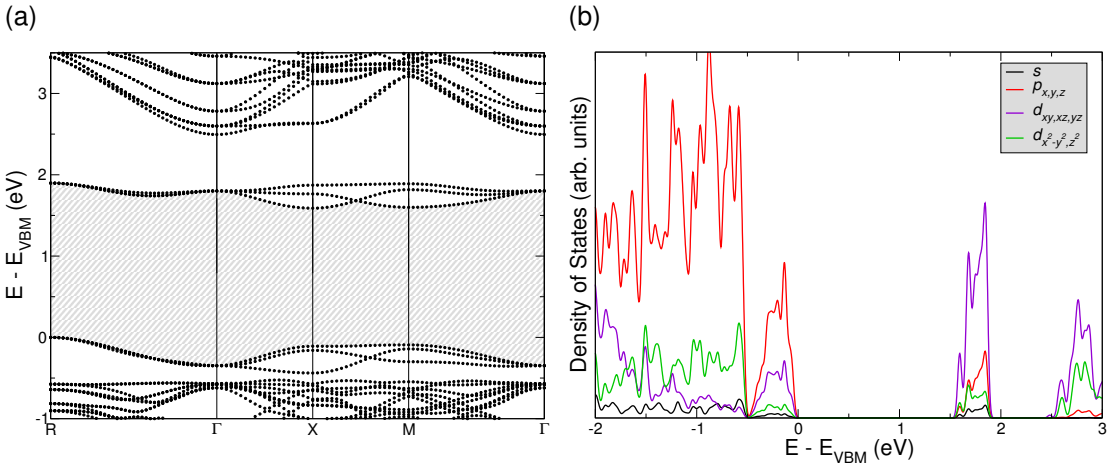

Figure 3.4: (a) The band structure and (b) orbital-projected density of states of bulk $CaCu_3Ti_4O_{12}$, obtained from first principles calculations. Energies are given relative to the valence band maximum (VBM).

$$E_{f,\mathrm{CCTO}} = E_{\mathrm{CCTO}} - E_{\mathrm{CaO}} - 3E_{\mathrm{CuO}} - 4E_{\mathrm{TiO_2}}, \tag{3.10}$$

where E_{x} is the total energy of compound x. CCTO exhibits a formation energy of -4.1 ± 1 meV/atom, where the negative energy specifies that the elements are more stable in the CCTO compound than in the constituent oxides (see Appendices F and G.1 for more information on determining formation energy). The error associated with the formation energy derives from the change in constituent material total energies when calculated using different energy cutoff values.

Whilst the literature offers two potential values for the band gap of this semiconductor – 1.5 eV [184] or 3.2 eV [96] – Ricci *et al.*, [192] have explained these discrepancies as a direct result of the multiple potential transitions in the CCTO band structure. In agreement with this, our electronic band structure (Figure 3.4a) shows two distinct electronic regions in the unoccupied states. The first region occurs at 1.5 eV above the valence band maxima (VBM); this region is expected to exhibit a rather low conductivity associated with the bands due to their relatively flat dispersions and, as such, their exciton binding energy is very localised (much higher effective mass in this band. In addition, the fewer bands in this region will cause it to be far less prominent in absorption and emission spectra. At higher energies, the second conduction band region appears at 2.5 eV (which

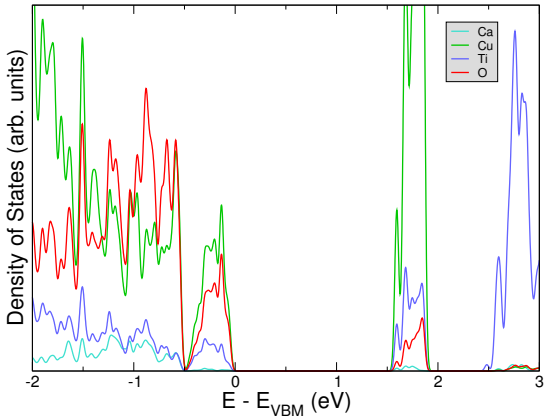

Figure 3.5: Species-projected density of states of bulk $CaCu_3Ti_4O_{12}$, obtained from first principles calculations. Each species has been normalised to the number of atoms of that species in the unit cell. As such, each line represents the average contribution from one atom of that species to the total density of states. Energies are given relative to the valence band maximum (VBM).

likely corresponds to 3.2 eV experimentally). This region shows much more dispersive bands and a greater band density, which would result in a much higher conductivity and stronger absorption. Hence, in experimental setups, the second conduction band region will likely be much easier to excite and easier to observe. This is likely the cause of the discrepancy in literature over the band gap size. As such, we attribute the value of 1.5 eV to the band gap of CCTO and the 3.2 eV gap to the difference between the valence band maxima and the minima of the second conduction region.

Here we discuss the bulk orbital-projected density of states (PDOS) of CCTO (Figure 3.4b) for later ease of comparison with the interface structures containing this material (see Appendix H for a description of projected density of states). In CCTO, the p orbitals are degenerate and are the dominant contributors to the valence band region, supplying minor contributions to the first conduction band region. The d_{xy}, d_{xz} and d_{yz} ($\mathrm{t_{2g}}$) orbitals are also degenerate, contributing mainly to the conduction bands, with a minor contribution to the valence band region. The $d_{x^2-y^2}$ and d_{z^2} orbitals (the $\mathrm{e_g}$ states) are degenerate and show significantly less contribution to the bands than those previously mentioned, with only showing slight contribution to the conduction bands and showing some contribution to the lower valence band region.

Figure 3.5 displays the species-projected density of states for bulk CCTO. We find that copper and oxygen are the main contributors to the valence band regions, with small contributions from titanium. Whilst the lower valence region (below 0.5 eV) sees similar contribution from calcium than it does from titanium, the upper valence region (above 0.5 eV) sees almost no contributions from calcium. Note that, as there are four times as many oxygen atoms as there are copper within the material, the oxygen atoms are dominant over the entire valence band. In the first conduction region, we find that copper is the dominant species, with significantly less contribution from the other species. However, in the second conduction band region, we find that titanium is the dominant contributor, with almost no contributions from other species.

3.5.2 Copper oxide

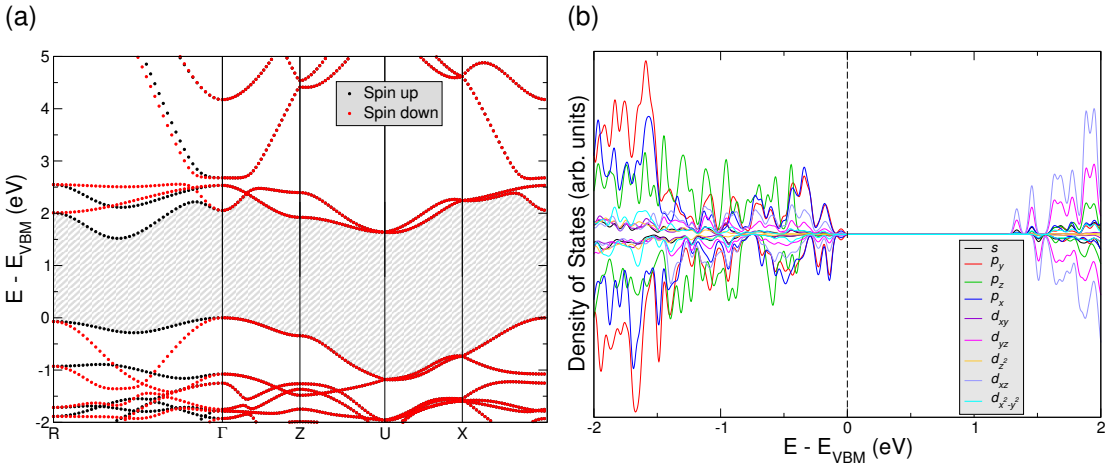

Figure 3.6: (a) The band structure and (b) orbital-projected density of states of bulk CuO, obtained from first principles calculations. Energies are given relative to the valence band maximum (VBM).

As both CuO and Cu_2O are known to form at the grain boundaries in CCTO samples [158], we now in investigate the properties of these two potential phases of the inter-grain material. As discussed in the previous section, it is apparent that phases of copper oxide form at the interface, leading to larger values of permittivity. Therefore, it is important to understand the properties of this inter-grain material.

We first discuss the CuO phase. To correctly model the magnetic and electronic properties of this material, a Hubbard +U correction of 7 is required on the d orbitals of the copper atoms [193, 194] (with no +U added to the oxygen atoms). Without the inclusion of a +U potential, CuO is incorrectly predicted as being metallic, which is also seen in literature [186]. We find the material to be antiferromagnetic and insulating, with a band gap of 1.2 eV, which agrees well with experimental results [185]. Figure 3.6 shows the band structure and density of states of CuO. We find that the t_{2g} states are non-degenerate, with d_{xz} and d_{yz} being the dominant orbitals in the conduction band. The d_{xy} orbital shows little contribution to the density of states over the range of 2 eV below and above the Fermi-level. The results also show a split in the p orbitals, with p_y and p_x being the main contributors to states near the valence band maxima and p_z shows no contribution to the valence band between the Fermi-level and 0.5 eV below.

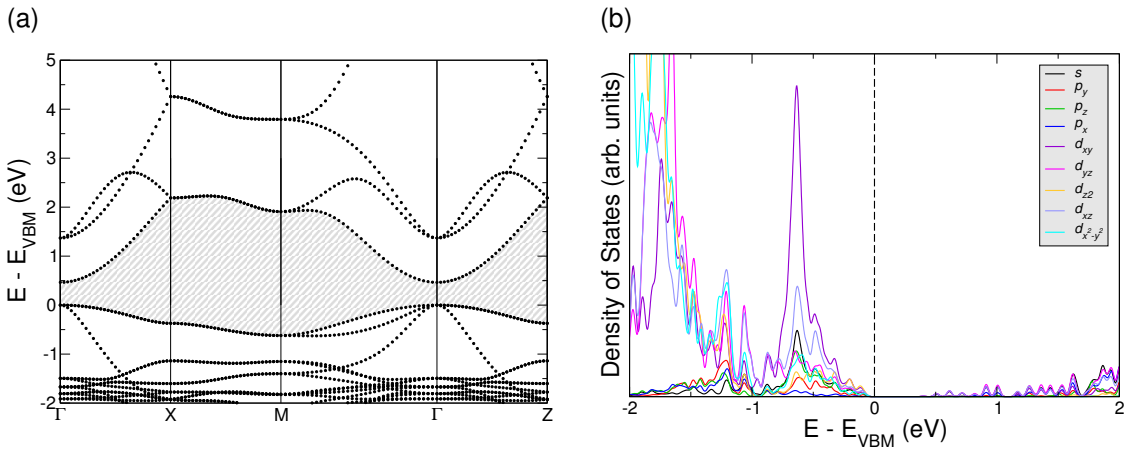

Figure 3.7: (a) The band structure and (b) orbital-projected density of states of bulk Cu_2O, obtained from first principles calculations. Energies are given relative to the valence band maximum (VBM).

The electronic band structure and density of states for Cu_2O are presented in Figure 3.7. As described in the literature, a Hubbard +U potential is not necessary to obtain the correct magnetic ordering for this material. It is also worth noting that using a +U correction on this system only allows for an increase in the band gap by a few meV, in agreement with the literature [186, 187] (this is because GGA+U should only be used to resolve issues relating to the VBM and CBM being formed of the same localised orbitals, such as in Mott insulators). We find the antiferromagnetic, insulating ground state of Cu_2O, with a band gap of 0.47 eV,

which an underestimation of the experimental value of 2.17 eV [186]. We find that the density of states are spin-independent and, as such, only present one of them. For this crystal, we see far less order in the orbitals than in CuO, with none of the orbitals being degenerate. The d_{xy} orbitals are the main contributor to the states near the valence band maximum, whereas the s d_{yz} and d_{xz} orbitals are the main contributors to the conduction band states, with p_x exhibiting greater contributions above 0.75 eV. In the band structure, we see a significant disparity between the dispersion of the valence and conduction band regions. The conduction bands are far more dispersive than most of the valence bands near the valence band maximum, which presents itself a lower density of states in that region.

3.6 Surface terminations & stabilities

In order to understand the interface region, we must first understand the surfaces involved. As such, we first model the potential surfaces of CCTO in order to determine the most favourable one to form at these interfaces.

Having explored the inter-grain material, we now look to the potential surface terminations of CCTO. To investigate the effect of different terminations on properties of CCTO grains, we consider two possible terminations normal to the [001] direction - the $CaCu_3O_4$- and the TiO_2-surface terminations. In chapter, we focus on surfaces formed by cleaving through the (001) Miller plane as other planes bring further complications such as dangling bonds, non-stoichiometric surfaces and creating a net electric field due to the system becoming polar which leads to instability [195]. The (001) plane is a commonly considered termination for perovskites due to being non-polar [196], as well as being the most energetically favourable Miller plane for perovskites to cleave through [197–199]. The $CaCu_3O_4$- and the TiO_2-terminated surfaces have formation energies of 0.138 eV/Å^2 and 0.136 eV/Å^2, respectively (see Appendix G.2 for details on surface formation energy). With such similar formation energies, both surface terminations must be considered as any real sample is likely to contain a mixture of both, dependent on the local chemical potential. The two terminations exhibit slight reconstruction of the electronic states near the surface (Figures 3.8a and 3.8c), showing reduction in the

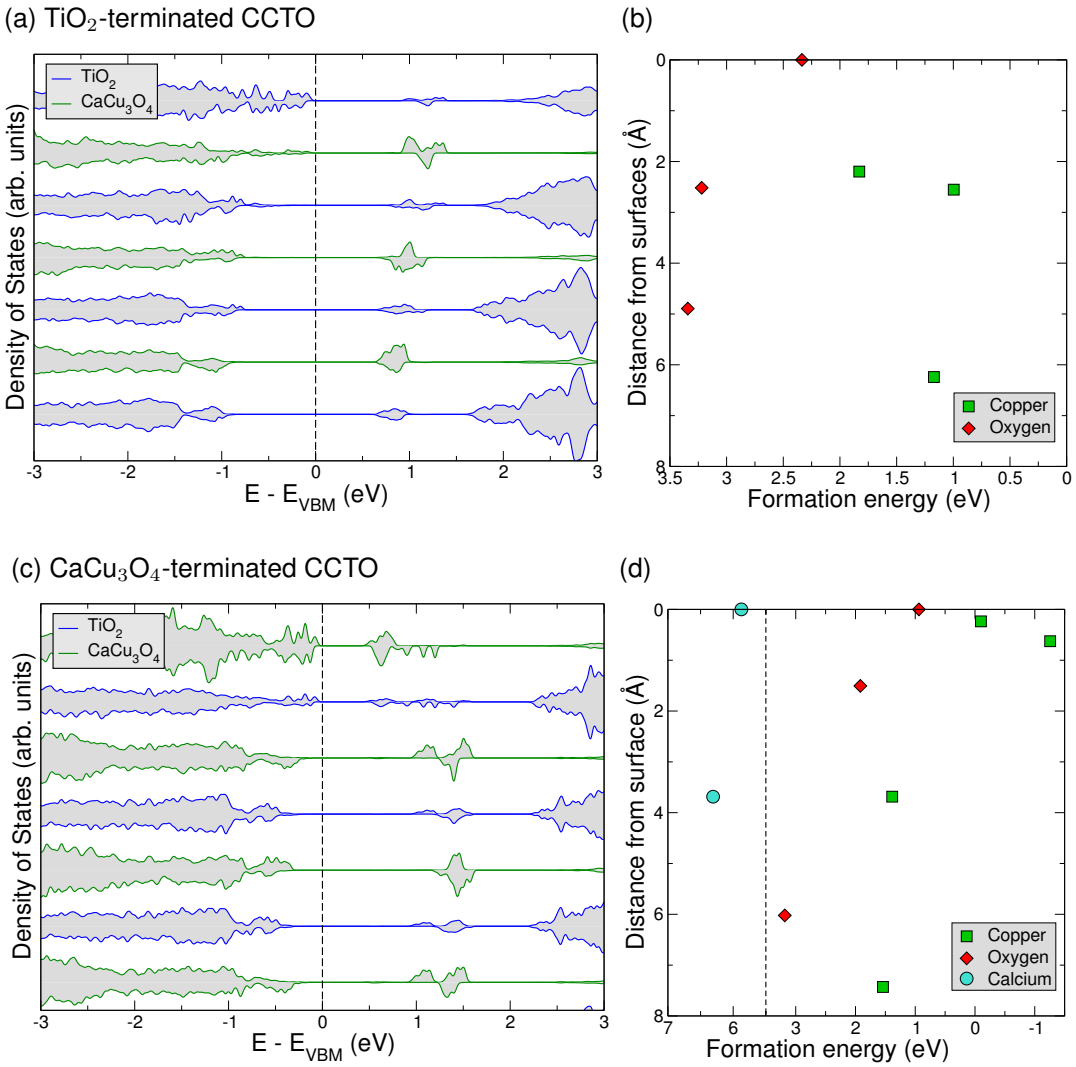

Figure 3.8: Electronic and energetic properties of CCTO slabs terminated on TiO_2 and $CaCu_3O_4$ surfaces, obtained from first principles calculations. Layer-projected density of states of (a) TiO_2 and (c) $CaCu_3O_4$ terminated surfaces, where the colour legend denotes the atomic stoichiometry associated with each layer. Formation energy of vacancies as a function of distance from the surface for the (b) TiO_2 and (d) $CaCu_3O_4$ terminations. Energies in the densities of states are given relative to the valence band maximum (VBM).

overall band gap down to 0.47 eV for the $CaCu_3O_4$-termination and 0.66 eV for the TiO_2-termination. For both surfaces, it is seen that the centres of each slab exhibit density of states similar to that of the bulk, retaining the bulk band gap. The $CaCu_3O_4$ surface sees a narrowing of the gap at the surface due to a curvature of the band edge of the first conduction region towards the surface. Whereas the TiO_2 surface exhibits a curvature of the valence band edge towards the sur-

face. Both of these curvatures are caused by pooling of charge at the surfaces, which forms an effective electric field over the slab, drawing charge carriers to the surface; this charge pooling also causes slight reconstruction of the surface states.

3.6.1 Defect migration

With copper-rich phases being common in the grain boundary region [163, 168, 169], it is important to study the stability of copper and oxygen in CCTO as a function of depth from the surface. As such, we consider how vacancy formation energies vary as a function of their distance from the surface by calculating whether these vacant atoms are more stable in the CCTO slab or in their respective bulk material (see Appendix G.4 for details on vacancy formation energy calculations). For the $CaCu_3O_4$-terminated slab (Figure 3.8d), we find that the formation energies of the copper and oxygen vacancies are increasingly favourable the closer to the surface they are. Copper vacancies at the surface show negative formation energies, meaning that they would rather be situated in bulk Cu than form the $CaCu_3O_4$ termination. Vacancies in TiO_2 terminated slabs are higher in energy than their comparative cases in the $CaCu_3O_4$ surfaces as shown in Figure 3.8b, though still lower than in bulk CCTO. The most favourable copper and oxygen vacant sites have also then been modelled on the same $CaCu_3O_4$ surface, which have been found to exhibit even greater negative formation energies; the vacancy has a formation energy of -1.23 eV when compared to the vacant atoms in CuO bulk. As can be seen, the formation of copper and oxygen vacancies in the $CaCu_3O_4$-terminated surface is highly favourable, in agreement with the previously discussed copper migration. The creation of these vacancies depletes the top layer of copper and oxygen, which results in the TiO_2 layer below being exposed (and, thus, becoming the surface layer). This means that the only stable surface for the (001) plane of CCTO is the TiO_2-terminated surface. We are, therefore, left with an interface between TiO_2-terminated CCTO grains and the inter-grain Cu_xO material.

For both surfaces, it is also worth noting that the formation energy of vacancies

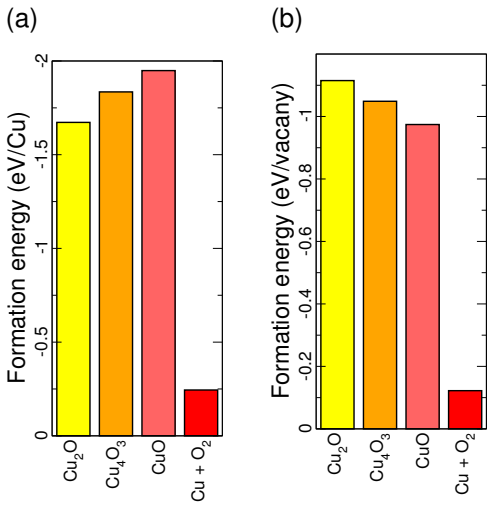

Figure 3.9: The formation energy of various copper oxide phases from the most energetically favourable Cu and O vacancies from the $CaCu_3O_4$ terminated CCTO slab, obtained from first principles calculations. The energy cost of forming various Cu_xO_y phases in oxygen-rich (a) and oxygen-poor (b) environments from the two aforementioned vacancies.

as a function of distance from the surface become more energetically favourable the closer to the surface (except for the sub-surface Cu vacancy in the TiO_2-terminated slab). This can be seen as a form migration of vacancies. If a vacancy forms in the centre of the slab, then an atom of that vacant site closer to the surface would likely move to occupy the empty site, thus forming a vacancy closer to the surface (depending on the energetic barriers and temperature of the system). This process could keep happening until the vacant site has, effectively, migrated to the surface. Near the surface, this mechanism would have to compete with the energetic favourability the atom residing in the inter-grain material instead. For copper and oxygen atoms, then, this would be the various copper oxide phases forming in this region.

3.6.2 Formation energy of various Cu_xO phases

In the previous section, we discussed the potential for copper and oxygen to migrate from the CCTO grains. We now consider the energetic feasibility these vacant atoms forming a inter-grain material and what compounds these could form.

When in the presence of oxygen, copper is known to form copper oxide, either CuO or Cu_2O, depending on the availability of oxygen [200]. To determine the formation energy E_f of these various compounds from CCTO surface vacancies, we use

$$E_f = xE_{\text{Cu-vac}} + yE_{\text{O-vac}} - (x+y)E_{\text{slab}} - E_{\text{Cu}_x\text{O}_y}, \tag{3.11}$$

where $E_{\text{X-vac}}$ is the most energetically favourable X-site vacancy in the CCTO $CaCu_3O_4$-terminated slab ($E_{\text{Cu}_x\text{O}_y}$ can also be substituted for $E_{\text{Cu+O}_2}$). For Figure 3.9a, the formation energy is divided by the number of copper-site vacancies x, whereas for Figure 3.9b, the formation energy is divided by the total number of vacancies $x+y$. By considering the energetics of forming the different oxides from these vacancies, we find that forming Cu_xO_y is much more favourable than forming oxygen gas and bulk copper (Figure 3.9). The values of x and y are dependent on the conditions in which the CCTO sample is grown. Our results show that in a copper-rich environment (oxygen deficient), Cu_2O will be the most favourable phase (Figure 3.9b). Conversely, in a copper deficient environment (oxygen-rich), CuO is found to be the most favourable phase (Figure 3.9a). This discussion provides further justification for considering the interfaces between CCTO and either CuO or Cu_2O.

Note that the poor estimation of binding energy obtained by PBE has not been corrected for here. However, the correction would only introduce an additional 0.7 eV/O, which would not be sufficient to make it comparable to the formation energies of any of the copper oxide phases. This correction has been obtained by comparing the PBE O_2 binding energy to the experimental energy required to split H_2O into H_2 and O_2 gas (for further detail, see Equation (6.16).)

3.7 Copper oxide grain boundaries

Creating interfaces theoretically between CCTO and Cu_xO can prove challenging as, in general, there is a poor lattice matching between CCTO and either form of Cu_xO. Despite this, we observe for the CCTO/CuO interface a low formation

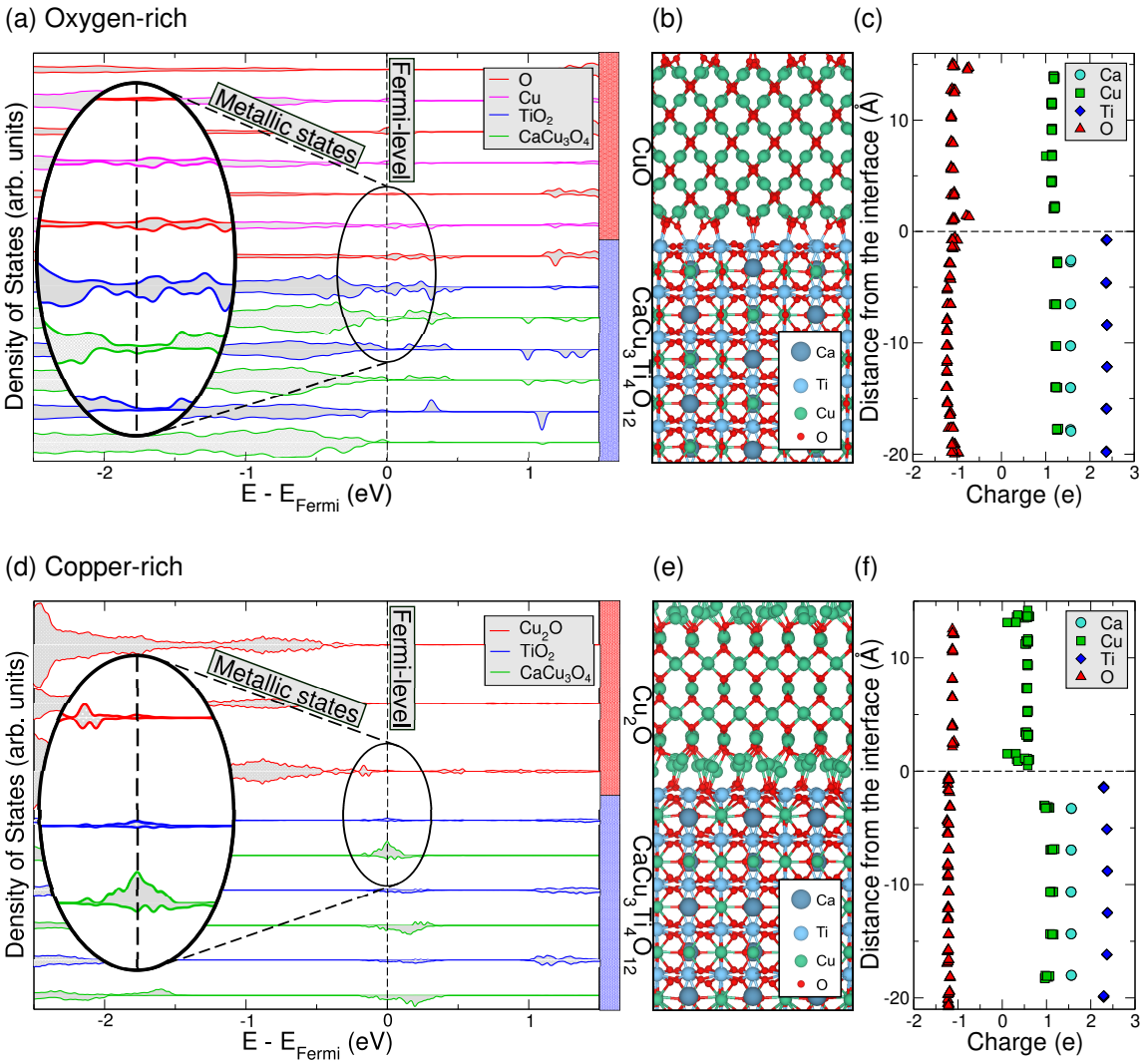

Figure 3.10: Electronic and geometric properties of the (a-c) CCTO/CuO and (d-f) CCTO/Cu_2O interfaces, obtained from first principles calculations. The layer-projected density of states of the (a) CCTO/CuO and (d) CCTO/Cu_2O systems. The colour legend denotes the atomic stoichiometry associated with each layer. The red/blue colour bars denote the Cu_xO/CCTO regions. Ball and stick models depicting the (b) CCTO/CuO and (e) CCTO/Cu_2O interfaces, both viewed along the CCTO [110] direction. The CuO region is terminated on an oxygen layer (oxygen-rich), and the Cu_2O region is terminated on a copper layer (copper-rich). Charge distribution analysis of the (c) CCTO/CuO and (f) CCTO/Cu_2O interfaces. Energies are given relative to the Fermi energy.

energy of 0.036 eV/Å^2 and for the CCTO/Cu_2O a formation energy of 0.228 eV/Å^2 (see Appendix G.3 for details outlining interface formation energy). In the Cu_2O case, strain is a significant contributor, with the formation energy of the interface

reducing to 0.158 eV/Å^2 when strain effects are accounted for. Whilst both systems exhibit low formation energies, the results show a greater preference for forming the CCTO/CuO interface over that of the CCTO/Cu_2O and thus making this system significantly more likely. However, as grain boundaries regions consist of multiple phases of Cu_xO [158, 201], we present both to emphasise the broadness of the results.

Figure 3.10 shows the relaxed atomic geometry and electronic configurations of the two boundaries, CCTO/CuO and CCTO/Cu_2O. Figures 3.10a and 3.10d, show that the density of states associated with the interface layers are metallic. These states spread up to 3 Å from the interface and do not appear in the centre of material, showing they are localised to the interface. Furthermore, far from the interface, the two bulk materials are insulating as their theoretical band gaps are recovered. If the copper oxide layer is less than 1 nm in thickness, then these metallic interface states merge, resulting in a continuous metallic region across the thin Cu_xO layer. Furthermore, regardless of whether the interface is oxygen-rich (Figure 3.10e) or copper-rich (Figure 3.10e) we find that both boundaries show this metallic behaviour.

Having considered various thicknesses of the CuO region between 0.5 and 1.5 nm, we find that the metallic nature of the interface is present regardless of the thickness of the CuO region. The CuO region becomes insulating above 1 nm. Below this thickness, the charge density associated with the two interfaces interact across the thin Cu_xO layer, effectively preventing each interface from being treated in isolation (i.e. the two interfaces directly interact with each other), which leads to a collapse of the internal barrier layer capacitance.

In order to analyse the charge distribution, we perform Bader charge analysis, which identifies local minima in the charge densities and associates the charge within a volume around each atom up to a turning point to that atom [188]. This charge value is then compared to the charge of the atom species' pseudopotential to determine the amount of charge gained or lost with respect to the natural electron number of that atom. Using this method, we are able to plot the amount of charge relating to each atom as a function of distance from the interface for the two interface systems (Figures 3.10c and 3.10f). Here, we see that charges are

only distorted within 3 Å from the interface into the copper oxide, with only slight distortion of the charge in the CCTO region of the CCTO/CuO interface. As an isolated oxygen atom typically has 8 electrons, it requires 2 more to fill its outer p orbital. To fulfil this, it bonds with atoms that prefer to lose electrons (i.e. copper, calcium, titanium) in order fill its outer p orbital. As such, the preferred state of an oxygen is a negative charge state, where it has gained two electrons; for the other atoms in this system, bonding results in a more positive charge state. In the oxygen-rich interface system (CCTO/CuO), we see that the oxygen atoms in both the CCTO and CuO regions increase in charge the closer to the interface they are; this relates to a reduction in bonding. For the copper-rich interface system (CCTO/Cu_2O), the copper atoms around the interface exhibit a less positive charge state, relating to a reduced bonding environment. It is clear that for either case, there are insufficient bonds available to form across the interface to compensate for the bonds cleaved through when forming either surface. This highlights the main issue that occurs at this grain boundary (both experimentally and theoretically); due to the large differences in geometries and bonding environments of the CCTO and Cu_xO materials, it is highly unlikely that a suitable phase of Cu_xO will form as the inter-grain material that will not result in a bonding imbalance and, hence, a metal layer at the interface. Even if such an inter-grain material is possible, it is even more unlikely to form throughout all of the grain boundary regions of a single sample. Thus, this metal layer should be present in almost any sample of CCTO, resulting in the sample exhibiting colossal permittivity.

The metal layer has significant consequences for the system's dielectric characteristics. The shell of charge is localised around the grain, embedded in a Cu_xO shell (Figure 3.11), which prevents conduction. However, when an electric field is applied, this charge is drawn to one side of the grain. This effect creates a massive effective response in the polarisation when an electric field is applied, akin to the Maxwell-Wagner effect commonly noted in the IBLC model. Thus, this is presented as the fundamental mechanism, at the atomic scale, responsible for colossal permittivity. This metallic interface detailed here leads to charge build-up at the interface in the grain boundary region, as shown in Figure 3.12a. This figure supports recent measurements for the current den-

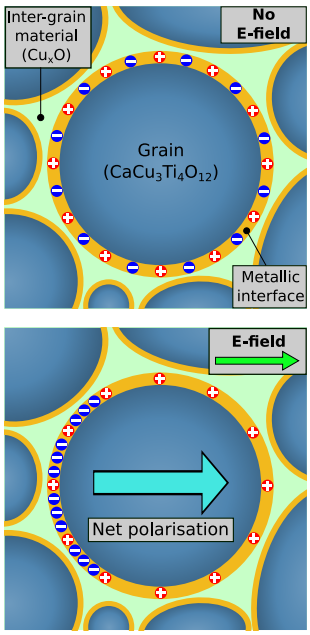

Figure 3.11: Schematic of the microscopic dielectric response of a colossal permittivity material. Diagram displaying charge confinement to the metallic interface between the non-metallic regions of Cu_xO and $CaCu_3Ti_4O_{12}$ (the red and blue circles denote positive fixed ions and free-flowing electrons, respectively). In response to an electric field ($\mathbf{E}$-field), these charges are seen to flow past the $CaCu_3Ti_4O_{12}$ but are still confined to this interface region due to the surrounding insulating Cu_xO inter-grain material.

sity [175] as higher charge density equates to higher current density. This argument also explains the Scanning Electron Microscopy measurements [202] that show a higher charge density in the grain boundary region and how the permittivity of samples typically increases when the grain boundary resistance decreases [27, 117, 139, 147, 160, 164, 173, 175, 203, 204]. Works highlighting increased current [202, 205] and the presence of negatively charged states [206] at the grain boundary region can also be exampled by this metallic interface.

It is important to understand that, unlike most oxide interfaces, this metallic behaviour is not created by oxygen vacancies, which is the normal mechanism for metallic interfaces in oxides [207] but actually due to the unusual structure of the interface. Here, we determine that the metallic region is caused by states unique to the interface created by the disorder in stoichiometry of the two materials at the interface, which results in one or more species being in excess. These interface states explain that the freeze out in colossal permittivity, observed at very

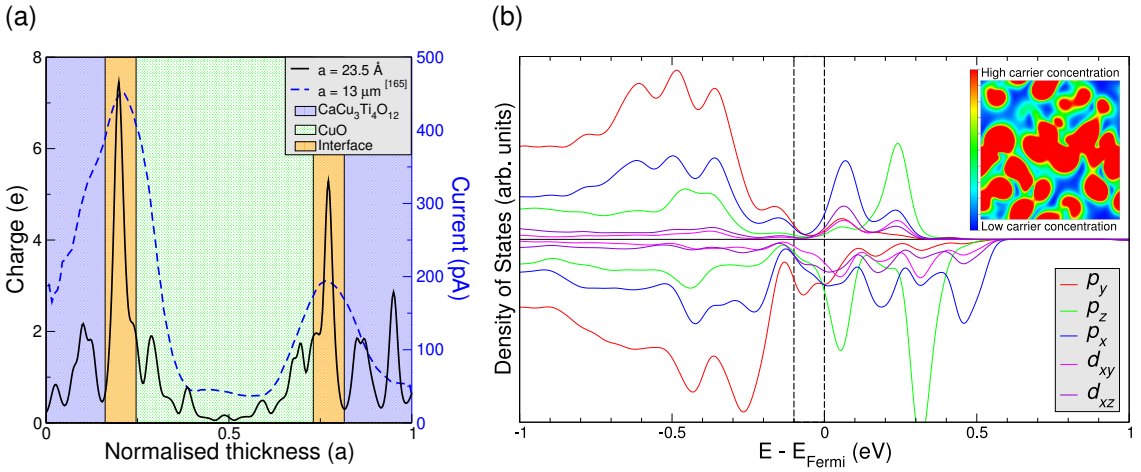

Figure 3.12: Electronic properties of the metallic interface in the CCTO/CuO system, obtained from first principles calculations. (a) Dependence of the free charge (current) on location within the CCTO/CuO system, denoted by the black (blue) line. The black line denotes a 1D plot of the partial charge density ranging from -0.1 eV to the Fermi energy along the [001] direction. The blue line displays experimental measurements of current at different points through a CCTO sample (data adapted from Reference 175). The different regions of the sample are labelled. (b) The Orbital density of states associated with the interface states of the CCTO/CuO system shown in Figure 3.10b, with energies relative to the Fermi energy. The inset depicts a colour map representing a 2D cut of the partial charge for the structure taken in the (001) plane at the interface between the CCTO and CuO regions, with an energy range of -0.1 eV to the Fermi energy (energy range between the two dashed lines in the main figure). Red and blue denote greater and lesser charge, respectively.

low temperatures [118] is clearly attributed to the narrowing of these states in the metallic interface.

3.7.1 Orbital analysis

To understand the nature of the metallic layer, we explore the nature of the states at the interface in the CCTO/CuO system. From analysis of projected orbitals at the interface, as demonstrated by Figure 3.12b, we can attribute the states near the Fermi-level to a combination of oxygen-p orbitals and copper-d orbitals.

These interface states have three characteristics that differentiate them from the bulk: 1) the interface p orbitals are split, whereas they are degenerate in bulk CCTO; 2) the interface shows no significant d_{yz} contribution (< 0.4 %), contrary to bulk CCTO; 3) at the interface, the p_z and p_x orbitals contribute more than the p_y ($p_z = 31.5\%$, $p_x = 30.1$ %, and $p_y = 10.1$ % contributions), whereas, in bulk CuO, the p_y is dominant. This is different from oxygen vacancies, where the missing atoms lead to a redistribution of charge on the nearby metal atoms. In addition, this characterisation of the interface reveals that the metallic interface cannot be ascribed to a charge build up due to the band alignment, creating neither a Schottky barrier, nor a two-dimensional electron gas. Both cases are characterised by a continuous distortion of the valence bands (or conduction bands), which result in a charge build-up at the interface between the two regions due to a potential well forming. Such a potential well would be demonstrated by the valence band maxima or conduction band minima showing high correspondence to their bulk counterparts, which is not the case here. Similarly, the conductive layers are not a result of conduction via π-bonds [208], as such bonding would show a regular, ordered pattern in the charge density across the interface. The topological plot, Figure 3.12b inset, demonstrates no features that can be attributed to such bond order and, thus, cannot be the cause of the metallic interfacial properties.

Hence, the previous discussion allows us to rule out the four most common mechanisms for a metallic interface, i.e. 1) oxygen vacancies, 2) charge build up due to band alignment, 3) conductive chains of π-bonds forming along the interface plane, and 4) by the energetic arguments discussed earlier, the formation of a Cu metal resulting in conduction. Thus, the metallic interface is caused by dopant or defect states localised to the interface formed by mismatched bonding between the two regions.

3.7.2 Oxygen vacancies

Thus far, we have shown that the oxygen vacancies are not responsible for the metallic interface, but it is important to understand how such vacancies would impact on the above discussion. In the literature, there have been numerous ex-

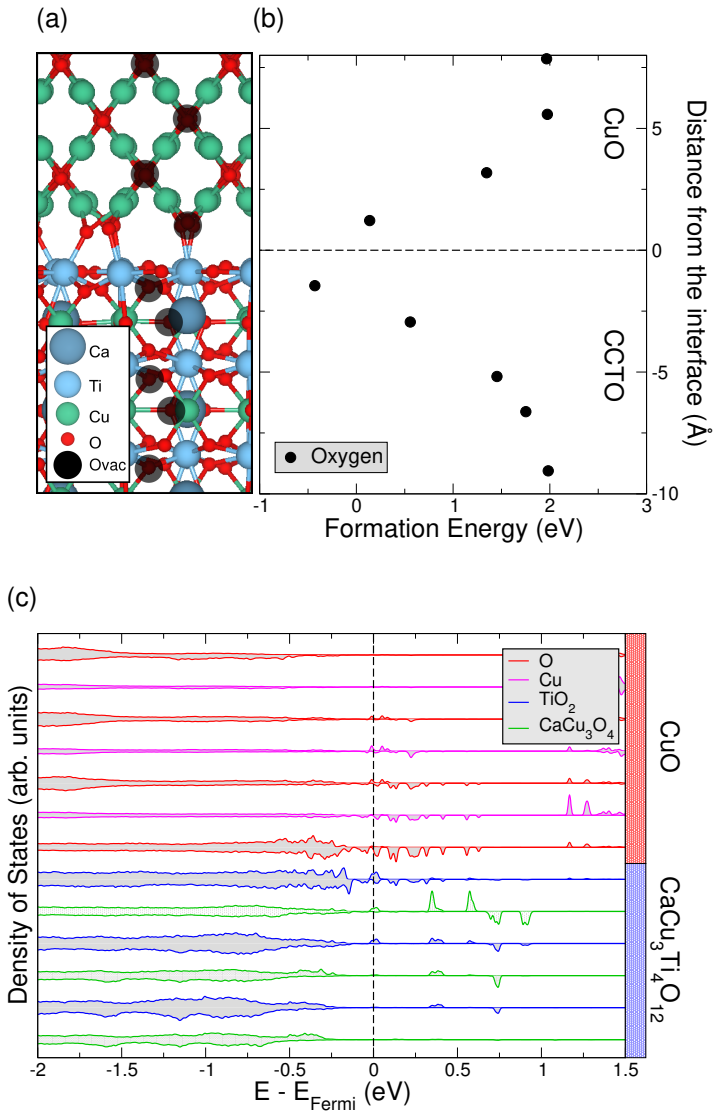

Figure 3.13: Energetic and electronic properties of oxygen vacancies near the CCTO/CuO interface, obtained from first principles calculations. (a) Ball and stick model depicting the simulated locations of individual oxygen vacancies in the CCTO/CuO interface system. (b) The formation energy of the vacancies as a function of distance from the interface with individual locations depicted in (a). (c) Layer-projected density of states of the CCTO/CuO interface with an oxygen vacancy located at the interface. The colour legend denotes the stoichiometry associated with each layer. The blue/red colour bars denote the CCTO/CuO regions. Energies in the density of states are given relative to the Fermi energy.

perimental studies of the affects of oxygen vacancies on the dielectric properties of CCTO samples [209–211]. Notably, in 2004, Fang *et al.* [209] annealed CCTO samples in oxygen atmospheres, which resulted in a reduction in the permittiv-

ity. Later, in 2013, Masingboon *et al.* [210] explored the capacitance of CCTO samples and found that an increase in capacitance was linked to an increase in oxygen vacancies forming in the grain boundary region.

To explore oxygen vacancies in the CCTO/CuO interface, we first model ones at various distances from the interface to determine the most favourable location for them to form. The formation energy of individual oxygen vacancies is energetically more favourable near the interface, rather than in either the bulk CCTO or CuO regions, with a difference of 2.4 eV when compared to bulk CCTO (Figure 3.13). The introduction of these vacancies increases the number of states near the Fermi-level (Figure 3.13c), increasing the carrier concentration of the dilute metal, which, in turn, increases its conductivity. This increased conductivity means that the system has a greater amount of charge to polarise, thus resulting in a higher colossal permittivity. This helps to explain how the variation in growth conditions can have a strong affect on the permittivity [212]. Critically, this result also explains the positive correlation between oxygen vacancy concentration and colossal permittivity [209–211].

3.8 Impedance model

Whilst the initial intention of this project was to calculate the dielectric response of a CCTO/CuO grain boundary structure using ab initio methods, this is no longer possible due to the metallic nature of the interface. As the interface is metallic, the introduction of an electric field across this system would result in an infinite response from the electrons near the Fermi-level (a polarisation cannot be calculated for a metal). In the grain structure, the metallic regions are pinned between the non-metallic grain and inter-grain materials, allowing charge to flow around the grains, but not between them. However, in our modelled structure discussed above, the metallic interface is infinitely periodic in the interface plane, allowing charge to flow freely. As such, to explore the dielectric properties of the grain system, we draw an analogy between it and a circuit model.

To illustrate how the atomic scale picture affects the macroscale, we have mod-

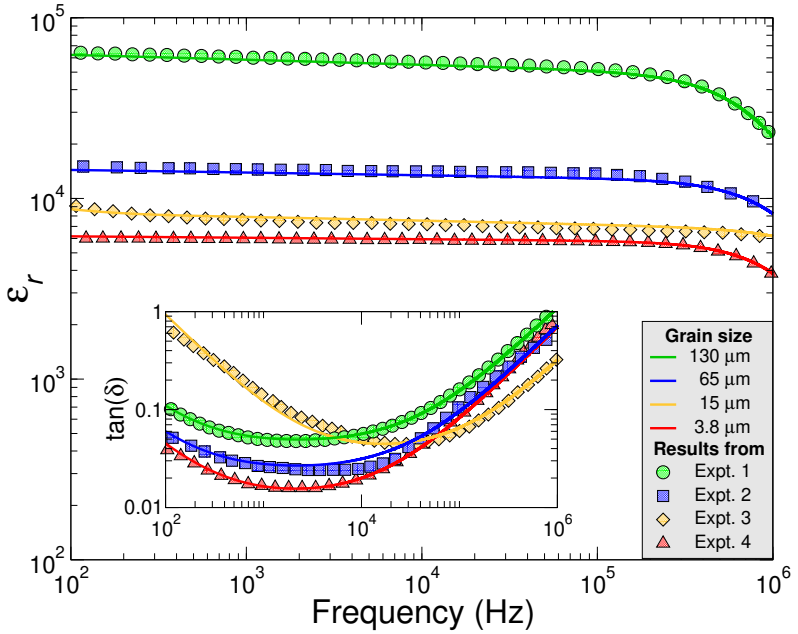

Figure 3.14: Dielectric response in colossal permittivity materials, obtained from circuit model calculations. Permittivity (ε_r) and dielectric loss ($\tan(\delta)$) plots of a resistor-capacitor circuit model and experimental data (experimental data 1, 2, 3 and 4 adapted from References 136, 137, 124 and 138, respectively).

elled the the dielectric characteristics of the colossal permittivity material shown in Figure 3.11 as a series of resistor-capacitor (RC) elements (see schematic in Figure 3.15). The electrodes (electrode), grains (CCTO), inter-grain materials (CuO) and metallic interface (metal) are each taken as individual RC elements. This is analogous to applying impedance spectroscopy to such a system, [124, 213, 214] allowing for the measurement of permittivity (ε_r) and loss ($\tan(\delta)$), where loss is a description of the lifetime of the polarisation of the material in the absence of an external field. In Table 3.1, we present how each component of the circuit, and their respective contributions to the dielectric response of the entire system, change the impedance spectra.

Impedance calculations [215–217] are performed using a constant phase element approach [218]. This involves describing each component in the system as RC parallel elements. CCTO grains and Cu_xO inter-grain materials are described as RC elements, whilst the metallic interface and electrodes are described as purely resistor elements. From this, we gain a large network of grains, interfaces and grain boundaries connected between two electrodes. We are able to assign an effective impedance to this overall system by appropriately summing impedance

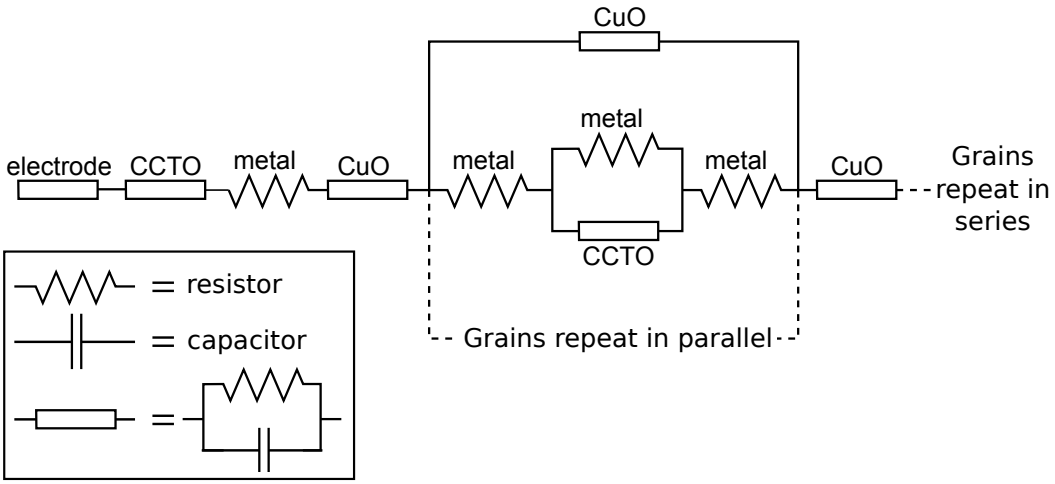

Figure 3.15: The proposed circuit model used as an analogue to the grain-grain boundary structure present in $CaCu_3Ti_4O_{12}$ samples.

values of the series and parallel components. This effective impedance can be written as

$$\begin{aligned} Z =& 2Z_{\text{electrode}} \\ &+ (n+1)Z'_{\text{CuO}} \\ &+ 2\left(\frac{1}{Z_{\text{CuO}}} + m\left(R'_{\text{metal}} + \frac{Z_{\text{CCTO}}R_{\text{metal}}}{Z_{\text{CCTO}} + R_{\text{metal}}}\right)^{-1}\right)^{-1} \\ &+ n\left(\frac{1}{Z_{\text{CuO}}} + m\left(2R'_{\text{metal}} + \frac{Z_{\text{CCTO}}R_{\text{metal}}}{Z_{\text{CCTO}} + R_{\text{metal}}}\right)^{-1}\right)^{-1}, \end{aligned} \tag{3.12}$$

where, n and m define the number of grains parallel and perpendicular to the current, respectively. Primed ($'$) elements denote those whose elements are in series with the CCTO grain element (i.e. perpendicular to the flow of current). The inter-grain material of CuO is taken as one large lattice in which the CCTO grains and metal layers are embedded.

Using our RC model, we show that an increase in grain size results in a larger permittivity (Figure 3.14), supporting existing experimental observations [124, 136–138]. As a consequence of larger grain size, the volume of the surrounding dilute metal shell increases; as such, there is a greater amount of trapped charge that is able to be polarised under an applied electric field (Figure 3.11). Other adjustments to the system cannot account to for the large changes in the dielectric

Table 3.1: Contributions of the RC circuit model components and their geometries to the dielectric properties.

Increasing variable	ε_r 1st plateau		$\tan\delta$ peak	
	magnitude	**frequency regime**	**magnitude**	**frequency occurs at**
In-field grain length	Increase	Smaller	Increase	Lower
Out-of-field grain length	Decrease	No change	No change	Lower
In-field inter-grain length	Decrease	Larger	Decrease	Higher
Out-of-field inter-grain length†	No change	Smaller	Decrease	Lower
In-field interface length†	Increase	No change	No change	No change
Out-of-field interface length	No change	Larger	No change	Higher
In-field contact length†	No change	Smaller	Increase	No change
Out-of-field contact area	No change	No change	No change	No change
ρ_{grain}	No change	Smaller	No change	Lower
$\rho_{\text{interface}}$	No change	Smaller	No change	Lower
ρ_{contact}	No change	No change	No change	No change
ρ_{circuit}	Increase	Smaller	Increase	Lower
$\rho_{\text{inter-grain}}$	No change		Reduces loss at low frequencies	

† Significantly smaller contributions compared to the other components.

response (Table 3.1).

The results of the circuit model can also be used to describe the effect that grain size has on breakdown. Shown by Chung *et al.* [219], the breakdown of CCTO appears to be inversely related to the grain size. As the grain size increases, the breakdown decreases. As the increase in grain size is caused by an increase in sintering time, one can also consider this as a decrease in grain boundary size (the longer a sample is sintered for, the more material moves from the disordered grain boundary material and into the ordered grain. Hence, a larger grain here is linked to a thinner Cu_xO region, and, thus, a smaller separation between the metallic interfaces, which requires a smaller electric field to overcome the now thinner insulating Cu_xO.

A colossal permittivity metamaterial could be engineered by embedding metal shells inside of an insulating solid, mimicking the structure shown in Figure 3.11. This provides a route to producing artificial colossal permittivity materials. This mechanism offers new insight into the metallic behaviour seen in a range of oxide

interfaces, due to the origin being different from the majority. To investigate this phenomenon further, we propose applying a large magnetic field perpendicular to the a.c. electric field. This will result in a polarisation component perpendicular to both fields.

3.9 Summary

In this chapter, we have employed first principles density functional theory methods to investigate colossal permittivity in $CaCu_3Ti_4O_{12}$. In doing so, we attribute the fundamental phenomenon behind this to an unusual metal interface forming in the grain boundary region. This metallic interface is unusual in that it is not created by oxygen vacancies, but due to the breakdown in stoichiometry at the interface. Due to the confined shells of charge created, an applied field moves the charge to one side of the grain, resulting in a massive polarisation and thus colossal permittivity.

The formation of the metallic interface has then been compared with the extensive background literature of experimental data available for the system and have shown how this mechanism describes all common and irregular results seen. This effect can be enhanced by either adding (or in reality increasing) the concentration of oxygen vacancies or by increasing the grain sizes. The results presented here provide a new understanding of oxide interfaces and colossal permittivity and provide a future for how both could be manipulated and characterised.

In the following chapter, we shall consider a system that depicts a similar architecture of grains (cores) embedded in a surrounding grain boundary material (shells). We shall focus on the interfaces formed in such a system and explore new materials that can form at the interface between two different materials.

Chapter 4

Fresnoite

“Nature isn’t classical, dammit, and if you want to make a simulation of nature, you’d better make it quantum mechanical, and by golly it’s a wonderful problem, because it doesn’t look so easy."

— Richard Feynman

4.1 Introduction

The previous chapter involved the investigation of naturally-forming interfaces – grain boundaries – and how these can change the properties of the macroscale system. We mentioned how materials can form at these grain boundary regions with their forms being dependent on the growth conditions. Here, we shall analyse a material that can form at a interface between $BaTiO_3$ and SiO_2.

This chapter starts with a detailed discussion of $BaTiO_3$@SiO_2 core-shell structures and the interest that surrounds them. It is discussed how fresnoite, $Ba_2TiSi_2O_8$, is present at the interface between $BaTiO_3$ and SiO_2 for a wide range of growth conditions. As such, it is decided that, to fully understand the interface between $BaTiO_3$ and SiO_2, a full characterisation of $Ba_2TiSi_2O_8$ is first needed. The results are then presented, discussed and a comparison between characterisation using a GGA and a screened-hybrid functional is made. First, the crystal properties of fresnoite are presented. The screened-hybrid functional is shown to much more closely resemble experimental data. Next, the mechanical properties

are calculated, namely the elastic tensor and Raman frequencies. The dielectric and electronic properties are then presented and analysed. Lastly, a summary is presented.

In order to fully understand the electronic and elastic characteristics of materials, such as fresnoite, first principles methods such as density functional theory are necessary [220]. Very little literature is currently available on first principles calculations for $Ba_2TiSi_2O_8$, with only one paper partially exploring its electronic properties via the generalised gradient approximation (GGA) of DFT [221]. It is, therefore, unclear whether such results can be fully reliable as it is well known that GGA significantly underestimates the band gap of semiconductors, as well as electron localisation [222]. Our choice of the Heyd-Scuseria-Ernzerhof (HSE06) hybrid functional [72, 73] is due to its improved accuracy for electron localisation and band gap values [222]. An alternate approach would be to consider GW calculations [223]; the GW method is fundamentally different from that of DFT, it can more accurately calculate realistic band gaps in non-metallic systems at greater computational cost. However, it has been recently shown [224–226] that for systems without a defect, HSE06 calculations accurately capture the bulk properties as well as GW calculations, for a lower computational cost. Hence, our approach here is focused on the application of HSE06.

4.2 Background

Due to the high permittivity exhibited by $BaTiO_3$ (BTO) (ε_r' greater than 5000 at 1 kHz) [227, 228], it is seen as a material with great potential for device applications, such as capacitors [229], energy storage devices [107], phased array radar [230] and random access memory [231]. However, as with most materials that exhibit large relative permittivities, it is accompanied by a high dielectric loss [31, 107], reducing its effectiveness for energy storage applications. There has been a recent focus on overcoming this issue by forming composites that can exhibit both the high permittivity found in BTO and the low dielectric loss of materials such as silica, SiO_2 [232–234]. To this end, BTO@SiO_2 core-shell composites have been made that exhibit the high breakdown voltage of SiO_2 whilst maintain-

ing the high permittivity of the BTO [30, 235, 236], giving them greater promise for use in high energy density capacitors. However, it has been shown that, during growth, a layer of $Ba_2TiSi_2O_8$ (BTSO), forms across a diffusion length into both materials originating from the interface [237, 238]. Whilst these core-shell structures have been shown to exhibit both desired properties experimentally, theoretical studies of BTO|SiO_2 interfaces do not mirror these results [239, 240]. It should also be noted that experimental studies of BTSO have not shown it to exhibit unusually high permittivity values [241–244]. As such, it is likely that the interfaces of either BTO|BTSO or BTSO|SiO_2 are likely responsible for the properties seen in experiment.

It should also be noted that, as many manufacturing processes for BTO involve growth on silica wafers, intermediate fresnoite layers can form during the process [237]. Therefore, regardless of whether the interest is in core-shells of BTO@SiO_2 or merely growing samples of BTO on SiO_2 wafers, BTSO will likely be present in the system, an additional practical motivation for understanding the its properties. As such, a clear understanding of the properties of BTSO is desirable.

Fresnoite was first reported in 1965 after naturally occurring deposits of the crystal were found in eastern Fresno County [245]. Since then, crystals of the material have been grown successfully with relative ease [246–248], allowing for detailed experimental characterisation of its piezoelectric and dielectric properties [246]. BTSO has the space group $P4bm$, experimental lattice parameters of $a = 8.529$ Å and $c = 5.211$ Å, and displays a melting temperature of 1445 °C [247], with no known phase transition below this temperature [246, 247]. The tetrahedral TiO_5 structure present in fresnoite makes it highly polar [249], causing it to exhibit piezoelectricity [250, 251], nonlinear optical properties [246, 248] and ferroelectricity [252]. Due to this highly polar structure, modelling surfaces of fresnoite becomes rather challenging as most potential cleavage planes form non-stoichiometric and charged surfaces.

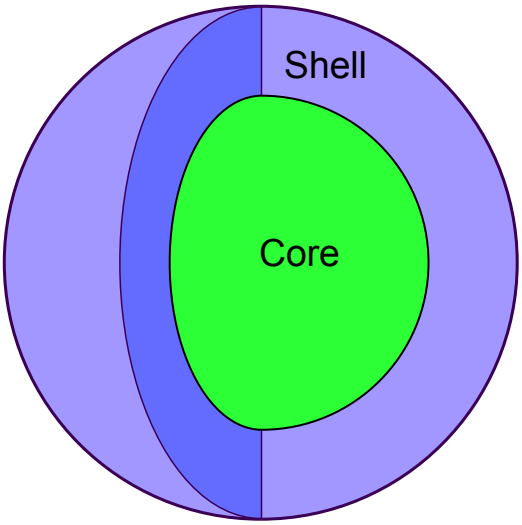

Figure 4.1: Diagram of a core-shell structure.

4.2.1 Core-Shells

Whilst the growth and study of colloidal solutions of metal nanoparticles has been prevalent in the literature for nearly two centuries [253, 254], the study of semiconductors began in the 1980s [255–258]. These colloidal semiconductors have seen much focus due to their ability to show improved, and sometimes new, semiconducting properties over that of their bulk materials [259, 260]. In the 1990s, this process was then furthered by coating the nanoparticles in other compounds in order to form layered structures, synthesising core-shells [261] (see Figure 4.1 for an example structure). These composites offer highly functional materials with sometimes novel properties. Due to their structure, the resulting properties can be modified by changing not only the composite materials, but also their shape, the number of layers and the core to shell ratio [262]. This high level of tunability allows for a large range of potential systems, with many possible properties.

4.2.2 Interface between $BaTiO_3$ and SiO_2

Interfaces between BTO and SiO_2 (or Si) can form fresnoite. Whilst there are growth conditions in which fresnoite does not form at the interface between these two materials, it is more common that it does. Typically, BTO@SiO_2 systems without the fresnoite phase tend to show lower permittivity values [236, 263], whilst small proportions of it can result in higher permittivity values [30,32,235,237,264–

267]. However, too much fresnoite will reduce the desired effect [243]. There is, hence, the need for a fine balance between the high permittivity of BTO and low loss of SiO_2, which is mediated by the fresnoite interfacial layer.

4.3 *Ab initio* simulation details

In this chapter, results are presented using the GGA-PBE functional and the screened hybrid HSE06 functional [268]. In order to optimise the structure of BTSO, the internal atomic coordinates were fully relaxed using PBE until the residual Hellmann-Feynman forces acting on every atom became smaller than 0.01 $\mathrm{eV/Å}$. The theoretical lattice constants were then found for both PBE and HSE06 whilst maintaining the experimental ratio of a/c, which was done to better compare with experimental data. The structural optimisation was carried out using an energy cutoff of 600 eV and a $4 \times 4 \times 6$ Monkhorst-Pack *k*-point mesh [88]. To better understand the localisation of electrons within fresnoite, Bader charge analysis [188] was performed on BTSO and BTO using both functionals. For dielectric tensor, elastic tensor and Raman calculations, a higher energy cutoff of 650 eV was used along with a $6 \times 6 \times 8$ Γ-centred Monkhorst-Pack *k*-point mesh to sample the Brillouin zone using the PBE functional.

4.4 Characterisation of an interface material

To fully understand the properties that can arise from this material in an interface system, one must first have a comprehensive understanding of its properties as a bulk material. Here, we present a first principles exploration of the electronic, dielectric and mechanical properties of fresnoite $Ba_2TiSi_2O_8$ using the GGA-PBE and hybrid-HSE06 functionals. The reason for this comparative study between the two choices of functionals stems from the points put forward in Section 2.7.3, namely the improvement to the structural and electronic properties (charge transfer and band structure). In doing so, a more accurate characterisation of the electronic and optical response of this material can be obtained, which can help

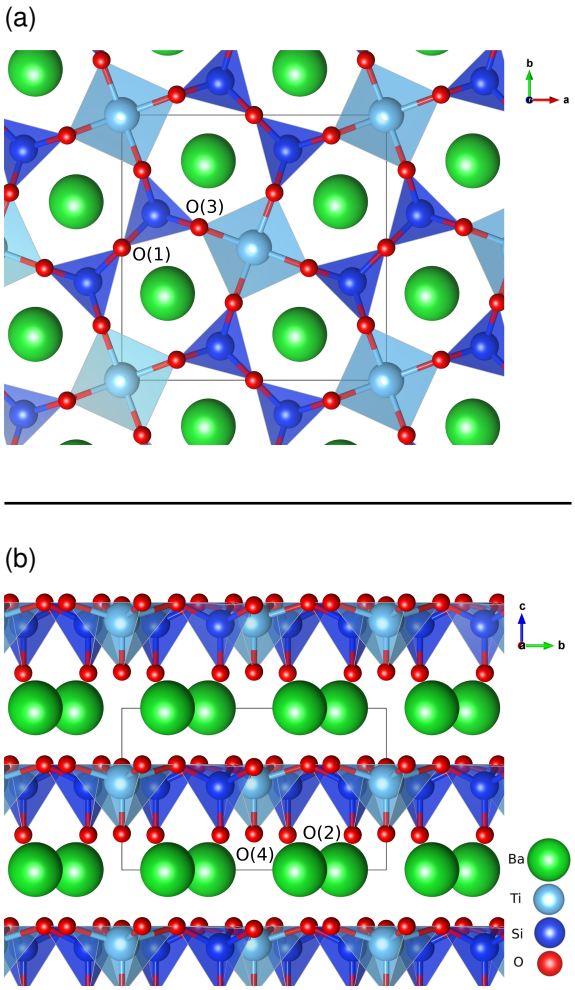

Figure 4.2: Ball and stick models depicting the crystal structure of $Ba_2TiSi_2O_8$ seen in the (a) (001) and (b) (100) planes, with the unit cell being outlined in both. The TiO_5 pentahedrons and SiO_4 tetrahedrons are highlighted, where O(4) and O(2) are located at the bottom of them, respectively.

drastically when comparing to experimental studies.

4.4.1 Crystal properties

Figure 4.2 displays the crystal structure of BTSO. Ba and Si are in Wyckoff position $4(c)$, whereas Ti is in $2(a)$. Whilst the other atomic species each display only one type, oxygen displays four distinct types, with O(1) in Wyckoff position $2(b)$, O(2) in $4(c)$, O(3) in the general $8(d)$ potion and O(4) in $2(a)$. Fresnoite has a tetragonal unit cell, displaying a space group of $P4bm$, with experimental lattice parameters of $a = 8.529$ Å and $c = 5.211$ Å [247]. Presented in Table 4.1 are

Table 4.1: Theoretical and experimental lattice parameters, cohesive energy and band gap of $Ba_2TiSi_2O_8$ and tetragonal $BaTiO_3$ unit cells.

	Method	Lattice parameter (Å)		Cohesive energy (eV/atom)	E_g (eV)
		a	c		
$Ba_2TiSi_2O_8$	PBE[a]	8.6500	5.2918	-6.297	3.793
	HSE06[a]	8.56500	5.2398	-6.989	5.717
	Expt.[b]	8.529	5.211	–	–
$BaTiO_3$	PBE[a]	4.03	4.048	-6.331	1.788
	HSE06[a]	3.98	3.998	-5.978	3.114
	Expt.	3.998[c]	4.018[c]	6.314[d]	3.2[c]

[a] This work

[b] Reference [247]

[c] Reference [269]

[d] Reference [270]

the theoretical lattice constants obtained using PBE and HSE06. From the PBE functional, these parameters are found to be $a = 8.650$ Å and $c = 5.292$ Å. With the HSE06 functional, these parameters become $a = 8.565$ Å and $c = 5.240$ Å. We can see that the HSE06 functional allows for a much improved estimation of the lattice constants, which is to be expected, with an error of less than 0.6 % with respect to the experimental values.

$Ba_2TiSi_2O_8$ is known, both experimentally and theoretically, to be favoured over that of separate $BaTiO_3$ and SiO_2 [271]. Due to this, at the right temperature of growth, fresnoite forms at the interface between $BaTiO_3$ and SiO_2 up to a diffusion thickness from the interface. On its own, BTSO shows no interesting dielectric properties, with a permittivity of around 12 across a range of 1–100 kHz [242, 244, 250]. To determine the chemical stability of BTSO theoretically, we calculate the formation energy of the crystal. To obtain the formation energy of fresnoite, we must compare its total energy to that of the composite oxides (see Appendix G). Due to its complex stoichiometry, multiple configurations of stable oxides can be compared as composites. Here, we compare the formation of $Ba_2TiSi_2O_8$ to that of $BaTiO_3$, SiO_2, BaO and TiO_2. The first comparison is made by considering

BaO, $BaTiO_3$ and SiO_2 as the compounds used to grow BTSO:

$$E_{f_1,\mathrm{BTSO}} = E_{\mathrm{BTSO}} - E_{\mathrm{BaO}} - E_{\mathrm{BTO}} - 2E_{\mathrm{SiO_2}}. \tag{4.1}$$

Here, E_{A} denotes the total energy of one chemical unit of the material A. Using this definition, the formation energy per unit of BTSO is -2.928 eV. The negative value defines BTSO to be more favourable than these composite oxides.

Another comparison can instead be made against just BTO and SiO_2 as the growth compounds. Here, however, stoichiometry with BTSO cannot be achieved. To resolve this, a second material must be formed from the reaction. Here, 2 units of BTO and 2 units of SiO_2 are combined, resulting in 1 unit of BTSO and 1 unit of TiO_2, with the formation energy being defined as:

$$E_{f_2,\mathrm{BTSO}} = E_{\mathrm{BTSO}} + E_{\mathrm{TiO_2}} - 2E_{\mathrm{BTO}} - 2E_{\mathrm{SiO_2}}. \tag{4.2}$$

Using this formula, we obtain a formation energy of -1.667 eV. This reaction process is seen to be less stable than the previous, which is likely due to the stronger chemical stability of BTO when compared to BaO and TiO_2 (BTO has a formation energy of -1.261 eV from the compounds of BaO and TiO_2). Regardless, both chemical processes exhibit negative formation energies, which clearly shows that BTSO is more chemically stable than its growth compounds.

4.4.2 Mechanical properties

The elastic properties of fresnoite are presented in Table 4.2. The tetragonal structure of BTSO breaks symmetry between the C_{11} and C_{33} elastic constants. We find that our results agree well with the experimental values for direct deformation. From Figure 4.2, one can extract the bulk modulus, B, through use of the equation

$$B = V_0 \frac{\partial^2 E}{\partial V^2}, \tag{4.3}$$

Table 4.2: Theoretical and experimental elastic moduli, C_{ij} (in units of GPa), of $Ba_2TiSi_2O_8$, $BaTiO_3$ and quartz SiO_2. The elastic constants are defined in their usual notations.

Material	C_{11}	C_{12}	C_{13}	C_{33}	C_{44}	C_{66}
$Ba_2TiSi_2O_8$[a]	180.57	84.06	45.25	102.56	23.47	66.74
$Ba_2TiSi_2O_8$[b]	165.5	57.7	43.6	99.9	31.7	69.4
$BaTiO_3$[a]	280.52	102.65	101.34	271.62	120.23	120.76
SiO_2[c]	81.1	8.3	7.5	104.8	49.7	36.4

[a] This work, calculated using PBE

[b] Expt. [248]

[c] Local density approximation. [278]

where V is volume, E is the total energy of the material and V_0 is the volume at zero pressure. In this case, the value of 131.73 GPa is obtained for the single crystal. This value lies between that of BTO (175 GPa) [272] and quartz silica (37.2 GPa) [273, 274]. Values for polycrystalline elastic moduli can also be obtained from the elastic tensor via the Voigt-Reuß-Hill approach [275] . For BTSO, we find the values of the bulk, shear and Young's moduli to be 85.06 GPa, 35.57 GPa and 94.60 GPa, respectively. For single-phase BTO, we show a Young's modulus of 247 GPa, in good agreement with literature [276]. From these results, we see find that polycrystalline BTSO is more flexible than that of BTO. The difference between the two values of bulk modulus for BTSO are due to the difference between single crystal and polycrystalline structures. The bulk modulus shows that the system becomes more susceptible to deformation when under pressure with increasing SiO_2 content. The mechanical stability of a system is defined using the Born stability criteria [277]. The elastic constants, presented in Table 4.2, show the system is stable, according to these criteria.

By comparing the value of C_{11} for BTSO to that of BTO and SiO_2, the elasticity along the [100] direction is found to be the average of the two. Whereas, for the elasticity along the [001] direction, we find fresnoite to be lower than that of both BTO and SiO_2; through the inclusion of Si and O in BTSO, the direct deformation in c becomes close to the value found in pure SiO_2.

Table 4.3: Raman-activate phonon frequencies of $Ba_2TiSi_2O_8$, calculated using PBE.

Mode number	A_1	B_1	B_2	E
	Frequency (cm^{-1})			
1	108.567599	38.214216	86.308234	49.934423
2	125.590279	159.280804	136.882766	75.346482
3	211.314167	324.568544	139.348692	107.981567
4	246.963528	346.949356	254.622529	114.743744
5	268.205099	448.681377	388.125932	152.840538
6	446.527377	854.019813	423.117658	176.465284
7	555.008999		544.006739	188.182915
8	628.996167		638.728551	206.664157
9	853.603009		889.963443	255.529978
10	915.104215		961.793413	298.740370
11	994.884744			322.380920
12				351.945957
13				364.979379
14				451.223322
15				514.336224
16				545.658933
17				824.997166
18				864.366343
19				932.125583
20				975.193524

The O(4)–Ti–O(3) bond angles are found to be $106.4°$, whereas the O(2)–Si–O(3) and O(2)–Si–O(1) bond angles are $115.4°$ and $110.7°$, respectively. In comparison, the bond angle for O–Ti–O in BTO is $90°$, and the angle for O–Si–O is $109.5°$ in quartz silica. The larger Ti–O bonding angle found in fresnoite suggests that the Si–O bonding is dominant; whilst the larger Si–O bonding angle than in SiO_2 is likely caused by the large ionic Ba–O bonds in fresnoite.

Raman frequencies are obtained for BTSO, which show that the system is dy-

Table 4.4: Theoretical and experimental values for the relative permittivity of $Ba_2TiSi_2O_8$ in the static and high-frequency regimes, ε^0_{ii} and ε^∞_{ii}, respectively. Theoretical values are calculated using PBE.

	ε^∞_{xx}	ε^∞_{zz}	ε^0_{xx}	ε^0_{zz}
$Ba_2TiSi_2O_8$ [a]	3.365	3.200	14.548	11.774
$Ba_2TiSi_2O_8$ [b]	–	–	15	11

[a] This work, calculated using PBE

[b] Experimental result from Reference [251]

namically stable as it exhibits no modes below 0 cm^{-1}. Through factor group analysis, BTSO is shown to have 47 Raman-active modes, split into 11 A_1, six B_1, 10 B_2 and 20 E modes, where the E modes are doubly degenerate. The strongest peak exhibited in Raman spectra, at around 876 cm^{-1} [279, 280], is found in our analysis. We see good agreement in the vibrations that give rise to these modes. For example, the bands between 600–700 cm^{-1} are due to Si–O(1)–Si stretching; whereas the bands between 800-925 cm^{-1} are due to SiO_3 stretching. We find that two bands around 854 cm^{-1} are due to symmetric and antisymmetric stretching of the Ti–O(4) bonds. Bands are found at 864 cm^{-1} and 890 cm^{-1} that correspond to symmetric and antisymmetric stretching modes of the SiO_3 groups.

4.4.3 Dielectric properties

We perform linear response calculations using DFPT to obtain the dielectric tensor for BTSO using the PBE functional. In doing so, we find the dielectric constants along the a and c axes (ε_{xx} and ε_{zz}, respectively) (Table 4.4), which compare well with those found in experiment – 15 and 11 for ε^0_{xx} and ε^0_{zz}, respectively [244, 250, 251]. Due to the isotropy of the [100] and [010] directions, ε_{xx} and ε_{yy} are equal. In comparison to the relative static permittivity of SiO_2 (3.9), fresnoite displays values roughly three times larger. Yet it is much lower than the exceptionally high values of dielectric constant of BTO (over 10^3). This is to be expected though, as the large dielectric constant exhibited by BTO is caused by a pressure-induced phase change [281]. As fresnoite is not known to display any

other phases up to its melting point [221], this effect is not present.

Refractive indices can be obtained by using the approximation of $n = \sqrt{\varepsilon^{\infty}}$. Due to the uniaxial nature of BTSO, it displays two refractive indices, n_o and n_e, relating to the a and c axes, respectively. It, therefore, also displays a birefringence, Δn. From our theoretical values of the high frequency responses, we find refractive indices of $n_o = 1.8344$ and $n_e = 1.7889$, with $\Delta n = 0.0455$. Reference [282] shows experimental refractive indices of $n_o = 1.86109$ and $n_e = 1.84596$ in response to a wavelength of 0.31256 µm, with a birefringence of $\Delta n = 0.01513$. Oxygen defects strongly affect optical responses of the system, and are likely the cause of the discrepancy between our theoretical results and those found in experiment. Our results show a much higher birefringence than those found in the experimental values, showing a larger anisotropy. This suggests that the purer (less defective) the crystal is, the greater the anisotropy will be.

4.4.4 Electronic properties

Charge distribution

To better understand the electronic and polar properties, we first examine the charge distribution. By performing Bader charge analysis, we are able to obtain a more accurate picture of the localisation of electrons across the unit cell. In Figure 4.3, we present the charge distribution across the fresnoite unit cell for both the PBE and HSE06 functionals. In the system, strong oxidation occurs to the barium atoms, causing them to display strong ionic bonding with nearby oxygen atoms. This is typical of barium in oxides and is very similar in its behaviour to BTO (Table 4.5). Bader analysis shows very little charge on the silicon atoms and further analysis of the charge density suggests this is due to covalent bonding between them and their neighbouring oxygen. Although titanium shows partial ionic bonding between neighbouring oxygen atoms, it exhibits more covalent-like bonding than the barium, with the charge being shared between both the Ti and O atoms.

Comparison of the HSE06 and PBE functionals shows that the charge localisation

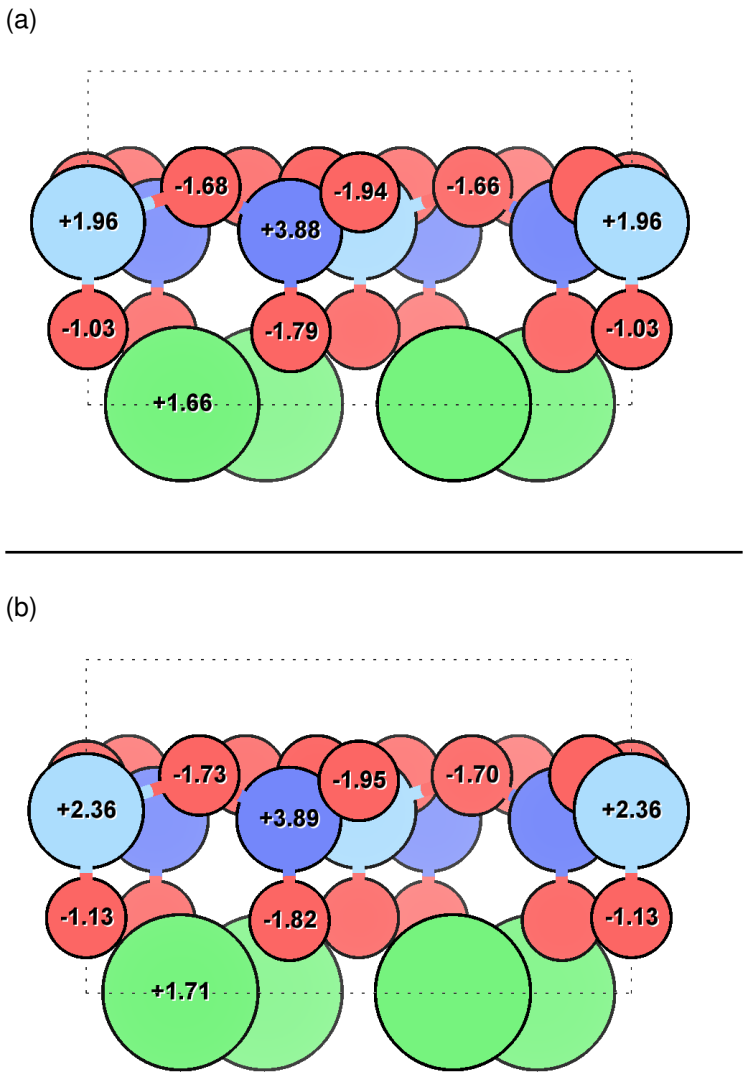

Figure 4.3: Ball and stick model depicting the Bader charge analysis of $Ba_2TiSi_2O_8$, performed using the (a) PBE and (b) HSE06 functionals. The numbers depict the amount of charge gained by each atom when compared to the isotropic charge of the respective atomic species.

broadly remains the same. Small charge redistribution is seen on the barium, and no charge redistribution occurs on the silicon. Significant charge redistribution is instead seen on the titanium and oxygen atoms. Overall, these results are expected as charge is generally found to be more delocalised with GGA functionals than the HSE06 functional.

The HSE06 functional calculations show slightly stronger oxidation occurring to the Ba atoms than the PBE functional. In general, Bader charge analysis reveals the Ba has a positive charge. In PBE calculations, this value is $+1.66$, whereas in HSE06, the value is $+1.71$, indicating the ionic bonding is stronger in the real sys-

Table 4.5: Bader charge analysis of the tetragonal unit cell of $BaTiO_3$ using the PBE and HSE06 functionals. Here, O(1) are the two O that lie in the Ti plane and O(2) the O atom that lies in the Ba plane.

Functional	Electrons gained			
	Ba	Ti	O(1)	O(2)
PBE	-1.640	-2.085	+1.235	+1.256
HSE06	-1.696	-2.307	+1.322	+1.360

tem than a PBE calculation would suggest. Although no change of charge is found on the silicon atoms, their neighbouring oxygen atoms see slight charge redistribution. O(2), O(1) and O(3) all exhibit an increase in charge comparing HSE06 with PBE. Similarly, silicon atoms show slightly increased ionicity and decreased covalency. In comparison, O(4) and Ti atoms all show significant differences in charges between the two functionals. Overall, an increased localisation of charge doesn't change covalent bonds much; whereas ionic bonding is shown to depend quite heavily on the choice of functional. This stronger ionisation is also visible in the band structures seen in Figure 4.4; the increased ionisation results in a larger band gap.

When comparing BTSO and BTO, we find that barium and titanium show similar charge characteristics, regardless of choice of functional. Through the introduction of silica to form BTSO, electron distribution across the oxygens is radically changed. Oxygens neighbouring silicon atoms gain roughly 1.8 electrons each - whereas O(4) gains only 1.13 electron. In both systems, Ti atoms ionise roughly 2.3 electrons each. Due to the polar nature of BTSO, Ti atoms undergo ionic bonding with oxygen in the Si-Ti plane, and more covalent-like bonding to oxygens near the Ba plane. This polar structure is also present with the Si atoms, but to a much smaller extent.

For HSE06, the in-plane bond lengths of Ti–O(4) are found to be 1.68 Å, which is shorter than the in-plane bonds in BTO (1.99 Å in-plane and 2.01 Å in-tetragonal-plane). Along with the average loss of 0.3 electrons for O(4) compared to BTO, this indicates the TiO bonds in fresnoite are more covalent-like. Because SiO_2 is dominant in this region, the TiO bonds orientated in the [001] direction are

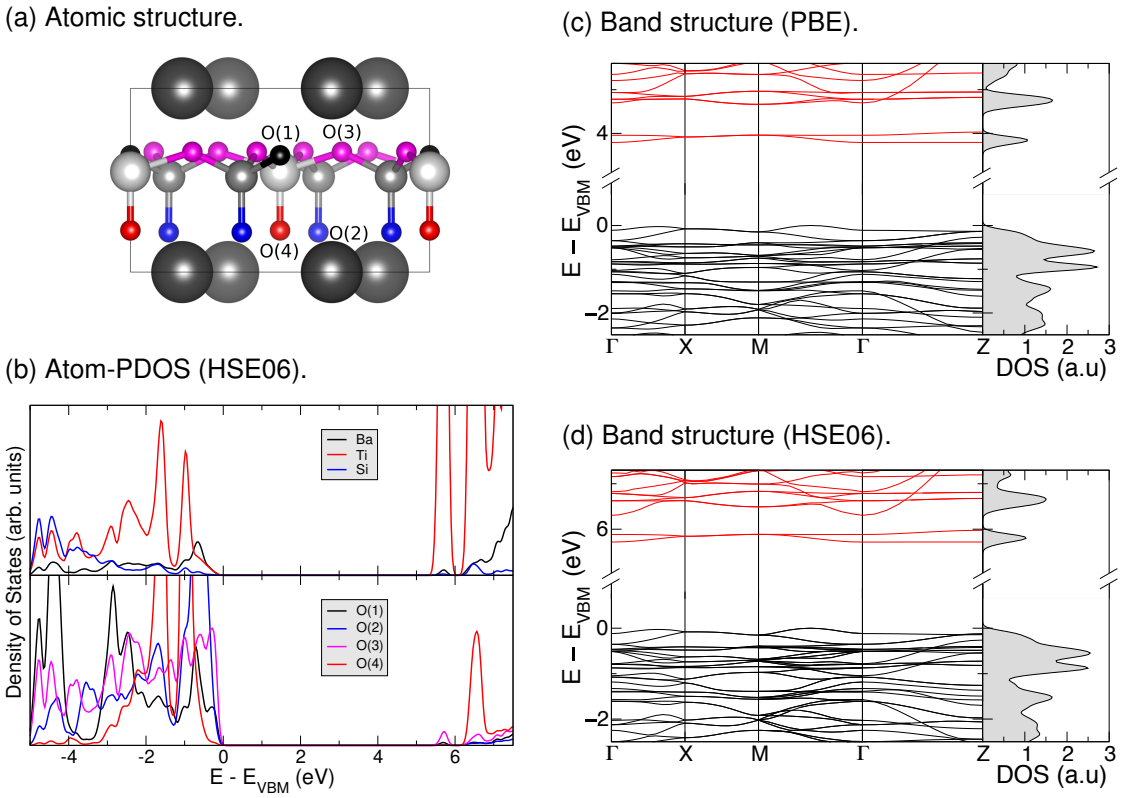

Figure 4.4: Electronic properties of $Ba_2TiSi_2O_8$, obtained from first principles calculations. (a) Ball and stick model of $Ba_2TiSi_2O_8$ used to distinguish between the four oxygen atoms. (b) Atom-projected density of states (atom-PDOS) for $Ba_2TiSi_2O_8$ calculated using the HSE06 functional. The colours of the oxygen atoms in (a) match their respective density of states in (b). The band structure and total density of states (in arbitrary units) for $Ba_2TiSi_2O_8$ using the (c) PBE and (d) HSE06 functionals. Energies are given relative to the valence band maximum (VBM).

decreased, preventing O(4) from extending further.

4.4.5 Band structure and density of states

Figure 4.4, displays the band structures and density of states of BTSO as calculated using PBE and HSE06. The band gap of fresnoite calculated using PBE is 3.79 eV, whereas the hybrid functional method of HSE06 gives the band gap as 5.72 eV (Table 4.1). By comparison, the experimental band gaps of $BaTiO_3$ and SiO_2 are 3.2 eV [269] and 8.9 eV [283], respectively, showing that inclusion of SiO_2 in BTSO significantly increases the band gap.

BTSO is shown to have an indirect band gap of 5.72 eV along the Γ–M direction, with a second indirect gap of 0.33 eV appearing above the first two conduction bands. This suggests that BTSO can display, not only a broadband response between the conduction band and valence band, but also a small optical response within the conduction band. This optical transition in the conduction band will look similar to that of defect transitions. Figure 4.4 shows that the electronic contributions due to the oxygen atoms create the valence band edge of BTSO, whilst the titanium orbitals are dominant in the conduction band. Strong hybridisation of the O(4) orbitals with the Ti orbitals can be seen in Figure 4.4b, in which both atoms display very similar features near to the band edges. Fresnoite exhibits an electronic structure in which the titanium orbitals are dominant in the conduction band, oxygen orbitals are the main contributor to the valence band edge and barium orbitals filling the lower valence band. This set of orbital contributions is similarly present in BTO [272, 284, 285].

By comparing Figure 4.3b and Figure 4.4b, the weaker localisation of charge on the O(4) atoms (when compared to the other O atoms in the system) is, again, attributed to a stronger covalent-like bonding between the Ti atoms above, as evidenced by the hybridisation of the O(4)–$2p$ and Ti–$3d$ orbitals. One of the largest differences between the two band structures in Figure 4.4 is the downward shift of a band near the conduction band edge. This band splitting and increased dispersion of the O(4)–$2p$ and Ti–$3d$ orbitals is a result of the charge redistribution in this bond between the two functionals. Due to this splitting, the anti-crossings present in these bands also increase with use of HSE06. As expected, there is no significant change of the bands within the valence region between functionals.

The band structure of BTSO calculated using HSE06 displays a strong difference between the band edges and the bands far from the band gap (sub-bands). Whilst the valence band maximum (VBM) and conduction band minimum (CBM) states are relatively dispersionless, the sub-bands show significant dispersion. Large anisotropy in the system is also present in the bands; we find both the band edges along Γ–Z display almost entirely flat bands, whereas the other directions display more dispersion - with a maximum band variation of 0.17 eV. Across the entire Brillouin zone, we find that two Ti electronic bands at the CBM are separated

from the rest of the conduction band and act like a defect in the band structure, with very little dispersion. We describe this state as defect-like as the difference in the energies of minima-maxima of the band is under 0.001 eV, which means the electron mobilities are expected to be very low along Γ–Z unless excited to the second set of conduction bands. This is due to the low percentage of Ti in the structure, constituting approximately 20 % of the potential Si/Ti sites. The conduction band is, therefore, highly sensitive to the titanium and its surrounding environment.

Finally, we present the effective masses of the electrons (m_{e}^{*}) and holes (m_{h}^{*}) at the CBM and VBM, respectively, obtained using the HSE06 functional. Due to the curvature, the values for $m_{\mathrm{e,h}}^{*}$ depend on the total range of the Brillouin zone considered. The value ranges represent us approximating the band edge within 15 % or 25 % of the Brillouin zone near to the band edge in the quadratic regime. It is found that holes travelling along the Γ–M direction display an m_{h}^{*} of 2.1–2.3 m_{e}. Whereas electrons at the conduction band edge exhibit an effective mass, m_{e}^{*}, of 4.7–5.7 m_{e} along Γ–M. By comparison, we notice the conduction band edge along Γ–Z displays an almost completely flat band. This suggests very little conduction along this direction with an effective mass of approximately 300 m_{e}. However, this value is difficult to quantify in a meaningful manner as we attempt to fit a nearly flat band to a quadratic. But we can confidently state a minimum value of at least 147 m_{e}. The non-dispersive nature of the band edge in this direction is due to the more layered-like structure along the c-axis, which has led to reduced bonding along that axis.

4.5 Summary

Electronic and mechanical properties of $Ba_2TiSi_2O_8$ have been obtained and compared using the generalised gradient approximation and hybrid functional methods. The Ti–$3d$ state is found to dominate the conduction band edge, whilst the O–$2p$ is the main contributor to the valence band edge. With the use of a hybrid functional, the band gap is corrected from 3.79 eV to 5.72 eV. The hybrid functional shows overall stronger ionic bonding and weaker covalent bonding within

the structure; both the barium and titanium atoms are found to show stronger ionic bonding than with the GGA functional. The calculated value of 131.73 GPa for the bulk modulus lies between the values for $BaTiO_3$ and SiO_2. Theoretical values for Raman frequencies of the system allow us to show it to be mechanically stable, as well as the origin of the vibrational modes. The elastic tensor values we obtain agree strongly with those found experimentally, showing the system to be highly anisotropic, as expected. Both the electronic and elastic properties of fresnoite show it to be a highly anisotropic system, with little dispersion visible in its band edges along Γ–Z and significant differences between the elastic moduli along the [100] and [001] directions. We believe that the more accurate HSE06 electronic structure of BTSO will give a better understanding of the optical and electron transport properties, as well as providing better understanding of its chemical structure, which will be helpful for further work on systems involving fresnoite.

This chapter acts as an aid in analysing $BaTiO_3$@SiO_2 core-shell structures, which show unusual dielectric properties. The study of the mechanical properties of $Ba_2TiSi_2O_8$ should aid in identifying when it appears at the interface between $BaTiO_3$ and SiO_2. The detailed discussion of the dielectric and electronic properties can help to determine where the unusual dielectric properties of $BaTiO_3$@SiO_2 core-shells originate from.

In the next chapter, we will explore photovoltaic devices in which interfaces and junctions are an integral part of the device itself. We shall investigate the band alignment between various layers within a heterostructure in order to form effective electric fields across the system that can drive charge carriers away from the centre layer.

Chapter 5

Solar cells

“We are star stuff harvesting sunlight."

— Carl Sagan

5.1 Introduction

We were commissioned by a company to study (Sn:Ca)$_x$O solid solutions for their potential as active layers within photovoltaic cells. During the study, we were asked to investigate the interfaces and potential transport layers that would be present within a solar cell using this material as the active layer.

In this study, we investigate Ca-dopants in SnO and how they affect the optical properties. We identify the dopant concentration relating to the most desirable optical properties for photovoltaics to be (Sn:Ca)$_{7:1}$O. With this solid solution being considered as the active layer of a photovoltaic cell, a set of oxides are studied to identify potential electron and hole transport layers for the p–i–n architecture. Finally, a device setup is presented as a possible all-oxide solar cell.

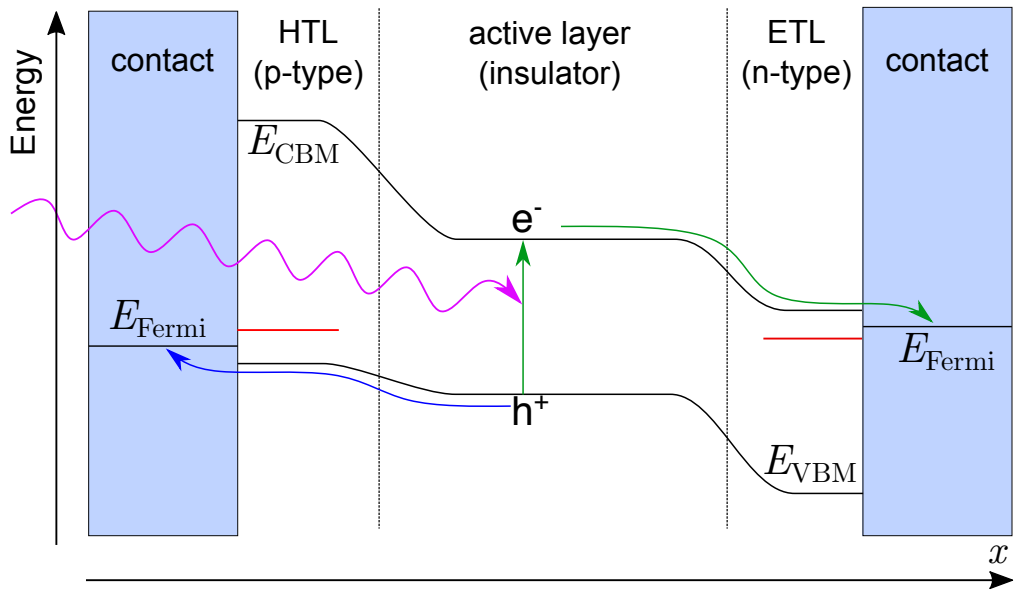

Figure 5.1: Diagram of the p–i–n solar cell architecture. The hole (electron) transport layer is abbreviated as HTL (ETL) in the graph.

5.2 Background

5.2.1 Photovoltaics

The purpose of photovoltaics is to convert solar energy into electrical energy. For such a device to work, a material is needed to absorb the incident light from the Sun, which can drive a current around a circuit. The size of the band gap of the material – the *active layer* – determines the amount of solar radiation the device can convert into electricity.

Due to the gaseous compounds in the Earth's atmosphere, the concentrations of different wavelengths within the solar spectrum at the Earth's surface vary drastically. This needs to be taken into account when designing a solar cell to harness the wavelength with the most energy; whilst shorter wavelengths exhibit higher energies, they typically exhibit a lower concentration at the surface of the Earth. When designing solar cells, using different materials, each with a unique band gap, as the active layer will allow each devices to take advantage of different parts of the solar spectrum.

Other factors that needs to be considered when determining the optimum band gap of a material for photovoltaics are the various loss processes. Through

these processes, absorbed energy will be lost to the system, unable to be converted into electrical energy. The main types of loss involve recombination of electron-hole pairs (i.e. radiative recombination, Shockley-Read-Hall recombination, Auger recombination), hot-phonon emission and deep trap states within the band gap [286, 287]. Many of these lead to faster decay routes for the electron-hole pair to take, reducing their lifetime and preventing them from being separated into the circuit.

By identifying the band gap that can best take advantage of the energy available from the solar spectrum, whilst also trying to mitigate the effects of losses, one can determine that the most efficient band gap for the light-absorbing layer of a single-junction solar cell to be 1.34 eV, which equates to the Shockley-Queisser maximum efficiency of 33.7 % [288, 289]. Whilst there are methods for overcoming this, such as quantum down-shifters [290] and multi-junction solar cells (which can now reach 47 % efficiency [291], these often come with increased manufacturing costs and greater potential for problems to arise within the device (due to the greater number of components).

There are two main types of photovoltaic cells, p–n junctions and p–i–n. Traditional silicon solar cells take advantage of the p–n junction design by being p-type doped on one side, and n-type doped on the other side. Oxide solar cells and perovskite solar cells take on the p–i–n design. Here, we will outline the setup of a p–i–n junction.

Figure 5.1 displays the band diagram of a p–i–n photovoltaic cell. In this setup, the majority of the device is the light-absorbing active layer; this layer is an insulator or semiconductor with a band gap as close to the 1.34 eV set out by the Shockley-Queisser limit. On one side of this layer is a p-type semiconductor that acts as the hole transport layer (HTL), with a metal contact attached to the HTL. On the other side is an n-type semiconductor, used as the electron transport layer (ETL), with a metal contact attached to this layer also. Whilst it is preferable for the HTL and ETL to have band gaps greater than that of the active layer, it is not vital. In such a setup, the light is typically incident on one of the two sides of the device.

In the p–i–n setup, incident light will be absorbed by the active layer, exciting an

electron-hole pair. Through careful choice of the HTL and ETL materials (depending on the choice of active layer material), an effective electric field will form over this device, causing the excited electrons to move through the ETL to the contact and the holes to be driven through the HTL to the contact on that side. This setup allows for the separation of charge carriers, which can then be connected to either a battery for charge storage or a circuit for immediate use. The architecture of p–i–n photovoltaic cells uses the interfaces between the various insulators to separate the charge carriers, reducing the chance of recombination.

For the p–i–n junction, the band alignment between the various layers is of vital importance. Typically, the transport layers need to be semiconducting/insulating materials, with band alignments to the active layer exhibiting Type II (staggered) structure. This allows for the electrons and holes to be driven in opposite directions, aiding in the separation of the charge carriers. The Fermi level of the contacts should then lie within the band gap of the neighbouring transport layer.

5.2.2 Modern solar cells – silicon

Currently, the material used most for light absorption in photovoltaic devices is silicon. The present maximum power conversion efficiency for a single-crystalline silicon solar cell is $26.7\ \%$ [292]. With a maximum possible efficiency of $29.4\ \%$ [293], there is still room for improvement. However, due to the band gap of crystalline silicon being smaller than $1.34\ \mathrm{eV}$, as well as strongly indirect, the efficiency cannot reach the Shockley-Queisser limit of $33.7\ \%$.

Whilst silicon solar cells themselves are not environmentally toxic, the processes involved in their manufacturing are often dangerous [292]. The methods of building silicon solar cells are usually energy-intensive and require the use of highly poisonous and environmentally toxic chemicals [294, 295]; these are typically used when mining and purifying the silicon, as well as when fabricating other cell components. Due to the handling of these dangerous chemicals, the manufacturing process can be very costly, which can detract from the positive attributes

of silicon solar cells.

5.2.3 Oxides in solar cells

Oxides take on a large set of roles in solar cells. From transparent contacts [296] to anodes/cathodes [297, 298] and active solar absorbers [299], oxides have potential in all components of photovoltaic devices. The versatility of these materials stems from the rich array of electronic properties they can display, along with their ease of fabrication [19]. They also have great promise in terms of sustainability, as many of them are formed of abundant, nontoxic elements. Developing a solar cell in which all components are made of oxides should also aid in the chemical stability of the device interfaces due to the materials all having similar chemical compositions.

Already, transparent conducting oxides such as ITO (Sn-doped In_2O_3) are used across light-absorbing and light-emitting technologies. Many properties of oxides can be taken advantage of to allow them to have strong conduction properties whilst still being transparent to visible light. These include their ease of being doped, their large band gaps, and their carrier transport properties (such as high mobilities) [300, 301].

Oxide solar cells have the potential to offer cheaper manufacturing costs than silicon solar cells. This is due to their relative stability and ease of production. As such, they typically do not use the hazardous chemicals that are required in crystalline silicon solar cell production. Furthermore, due to the wide range of oxides, there is a potential to improve the theoretical maximum efficiency by identifying one with a band gap closer to 1.34 eV than that of silicon. However, there exist numerous issues with oxides, hindering their uses. These issues include their short lifetime of photo-excited carriers and limited mobility of minority carriers [302]. Another issue arises due to them typically displaying band gaps above 2 eV, which is far above the aforementioned optimum value of 1.34 eV.

Identifying a material as a potential active layer of a solar cell is just the first step. The second component that one needs is contacts and, as discussed earlier, contacts are dependent on the transport layers. Oxides offer a wide range of

work functions (3.5–7.0 eV) [303]. Ones with low work functions, such as ZnO and TiO_2 are chemically stable and inert, unlike low work function metals (i.e. Ca and Mg). Oxides with high work functions have the advantage of being low-cost materials compared to high work function metals (i.e. Pt, Au) [301] and some can even exhibit work functions that exceed that of their metal counterparts.

Currently, the leading oxide for photovoltaics is Cu_2O [301]; however, for a single junction device, its efficiency is limited to 20 %. Here, we present a study on SnO and the potential efficiency gains that can be achieved through alloying/solid-state solutions. By effectively introducing a high concentration of dopants into a material, one can bring about significant changes in the electronic properties, potentially reducing the band gap.

5.2.4 Stannous oxide

Stannous oxide, SnO, has been explored recently as a candidate for the active layer of oxide solar cells [304]. The interest surrounding this material has mainly come from the s–p bonding it exhibits, which results in a delocalised character of the valence band states. Due to these delocalised valence bands, the holes in the crystal exhibit a low effective mass. The highly anisotropic structure of this material causes it to exhibit vastly different hole effective masses along [001] and [100] – 0.6 m_e along [001] compared to 5.6 m_e along [100]. This characteristic is similar to that observed in hybrid perovskites, which have seen significant efficiency advancements in a relatively short development timescale. Another interesting character of this material is its highly dispersive conduction bands, which are thought to allow long minority lifetimes. Whilst hybrid perovskites have seen strong interest in the field of photovoltaics, they are still held back by low chemical stability [305, 306], resulting in very short functional lifetimes as devices. This is a problem not exhibited by SnO, which is stable up to 400 °C [307], making it an effective alternative.

However, whilst there are intriguing characteristics of SnO for photovoltaics, it has a set of problems that currently prevent it from being considered as a material for photovoltaics. These problems stem from its small and strongly indirect funda-

mental band gap. The fundamental gap is 0.7 eV along Γ–M, whilst its optical gap is 2.1 eV at Γ. SnO shares this problem with silicon, which has a fundamental gap and an optical gap of 1.1 eV and 3.4 eV, respectively. Due to this strongly indirect characteristic, solar cells made of silicon need to be made fairly thick to improve absorption rates at the fundamental gap.

One potential method for improving the optical properties of a material is through solid solution. By mixing two materials with different properties, one can hope to form a new material that exhibits some of the characteristics of each. In the case of SnO, we need to introduce a material that exhibits a larger fundamental gap that is direct. Recent works in literature have investigated the effects of various dopants on the optical properties of SnO [304] and have shown that calcium oxide, CaO, can be used to increase its band gap. When forming a solid solution, one of the main questions, after determining the materials to mix, is the proportion of each material to use.

5.3 Methods

5.3.1 Schottky barrier height and band alignment

To determine Schottky barrier heights between a metal and a semiconductor, the highest occupied state for each region within the heterostructure needs to be identified. To do so, we first need to redefine the Fermi energy E_{Fermi} with respect to a constant of the material, regardless of the surrounding environment. A constant of a material is its average electrostatic potential. By taking the average of the local potential within a material P_{avg}, it can be used as a reference point for the highest occupied state of that material (see Appendix H for a description of the local potential). This new definition of the Fermi energy can be written as

$$\Delta = W - P_{\mathrm{avg}}. \tag{5.1}$$

Here, W is the work function of the metal, $W = E_{\mathrm{Fermi}} - E_{\mathrm{vacuum}}$. For a semicon-

ductor or insulator, a similar approach can be taken for the hole affinity χ_{h}:

$$\Delta = \chi_{\mathrm{h}} - P_{\mathrm{avg}}. \tag{5.2}$$

The value of Δ for each constituent can be used to identify the height of the Fermi energy (or hole affinity) for each material in a heterostructure. By taking the macroscopic average [308–310] of the electrostatic potential of a heterostructure, the aforementioned reference P_{avg} can be found within each region (material). With the average for each region located, the difference between the energies of the highest occupied states within each region can be defined as follows:

$$\Phi = (P_{\mathrm{avg},1} + \Delta_1) - (P_{\mathrm{avg},2} + \Delta_2). \tag{5.3}$$

For a metal–semiconductor junction, Φ is the Schottky barrier height. Whereas, for a semiconductor–semiconductor interface, the value of Φ would, instead, be the band alignment.

5.3.2 Hole affinities

To obtain a set value for the local potential of a material, the method of macroscopic averaging is employed to average the potential across the material slab using the periodicity of the atomic structure. By comparing the hole affinities (work functions) to the averaged local potential, the values of Δ can be obtained for each material.

Extreme care must be taken when comparing the theoretical hole affinity presented here to any experimental ionisation potential. The hole affinity can be strongly dependent on the surface of a material. The choice of surface termination (atomic species terminated on) and termination plane (Miller plane) can strongly affect the hole affinity (ionisation potential) of a material. As such, only direct comparisons between equivalent terminations should be made. The Miller planes used are discussed in Section 5.4. For MoO_3 slabs, the surface terminates on oxygen atoms. For all other materials, the Miller planes used here result

in only a single potential surface termination (i.e. a single stoichiometric surface for each material).

5.4 *Ab initio* simulation details

Our calculations were performed using *k*-point grids with *k*-point densities equivalent to those used for analysing the SnO bulk unit cell, with geometric relaxations and electronic calculations using $6 \times 6 \times 9$ and $12 \times 12 \times 18$ grids, respectively. All *k*-point grids were Γ-centred and generated using the Monkhorst-Pack scheme [88]. For slab (and interface) structures, the vacuum gap (and interface axis) were aligned along $\mathbf{c}$. The *k*-point grids for these systems were taken as $k_1/m \times k_2/n \times 1$, where k_1 (k_2) is the number of points used along $\mathbf{a}$ ($\mathbf{b}$) for the equivalent SnO bulk calculation and m (n) is the supercell expansion from that original SnO bulk unit cell. The value of 1 along $\mathbf{c}$ was chosen due to both the vacuum gap and layered-structure of SnO.

Electrostatic, or local potential plots were obtained by performing local potential calculations using the ionic and Hartree components of the potential. This is done as it much more rapidly converges to the vacuum energy than the exchange-correlation term of the functional, allowing for a more accurate calculation of the work functions and hole affinities.

Various phases and termination planes have been explored for materials in this chapter. Here, we present the studies of only the phases that resulted in the most energetically favourable interfaces with the active layer. For interface and slab structures, the following terminations and phases are presented: SnO (001), Ca (001), Ni (110), monoclinic γ-WO_3 (110), CaO (101), anatase TiO_2 (001), NiO ($54\bar{1}$), CaF_2 (101), LiF (001), α-MoO_3 (001).

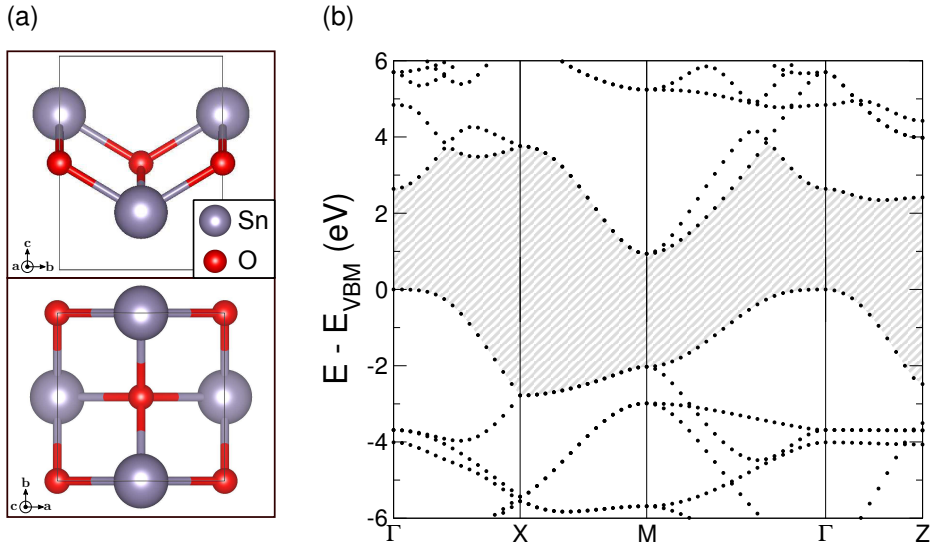

Figure 5.2: (a) Ball and stick model of the atomic structure of SnO. (b) The electronic band structure of SnO, obtained from first principles HSE06 calculations. The shaded region highlights the band gap of the system. Energies are given relative to the valence band maximum (VBM).

5.5 Effects of alloying on stannous oxide

Whilst SnO exhibits some properties that would allow it to be an efficient photovoltaic material, it still has many shortcomings. As mentioned previously, alloying SnO and CaO could allow us to overcome many of these limitations by forming a solid solution of the two that, hopefully, exhibits the desirable optical properties of each. This solid solution could reduce the effects of many forms of losses by allowing us to precisely tune its optical properties, leading the way to a very efficient solar light absorber. To understand more about how this alloying would affect the properties, we first explore the bulk properties of SnO and CaO, using HSE06.

5.5.1 Bulk properties

Experimentally, stannous oxide is known to have an indirect fundamental band gap of 0.7 eV [311]. Whilst low enough to allow for absorption of much of the solar spectrum, most of this energy will be lost through the processes outlined in Section 5.2.1 (relaxation to band edge and lower absorption rate for an indirect

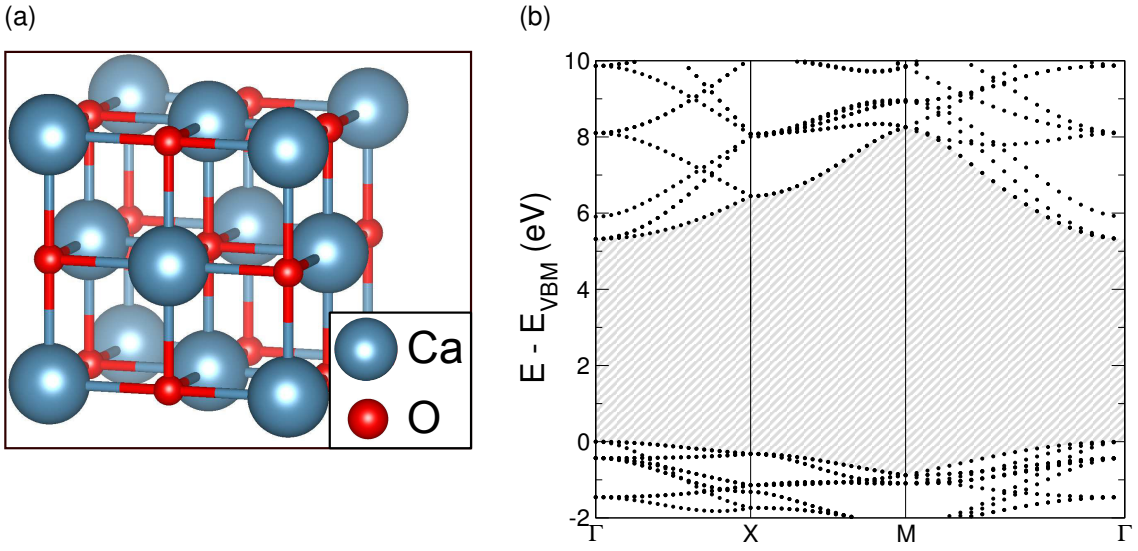

Figure 5.3: (a) Ball and stick model of the atomic structure of CaO. (b) The electronic band structure of CaO, obtained from first principles HSE06 calculations. The shaded region highlights the band gap of the system. Energies are given relative to the valence band maximum (VBM).

gap). Calcium oxide instead has a fundamental direct band gap of 7.1 eV [312], which is far too large for an effective photovoltaic material.

Stannous oxide, in the α-SnO phase, exhibits a tetragonal layered structure (see Figure 5.2a) with a theoretical layer separation of 5.039 Å. It has an indirect fundamental band gap between Γ and M (see Figure 5.2b), with a theoretical value of 0.88 eV; its optical gap is 2.64 eV. The valence and conduction bands near the band gap both display strongly dispersive characteristics, covering a range of over 2 eV across the Brillouin zone. This dispersive nature allows for charge carriers excited within the system to be highly delocalised.

Calcium oxide exhibits a rock-salt structure with a theoretical Ca–O bond length of 2.435 Å. It has a fundamental direct band gap of 5.32 eV at Γ (see Figure 5.3). Whilst the conduction band exhibits a strongly dispersive nature, the valence bands near the band gap are relatively flat, covering a range of less than 1 eV.

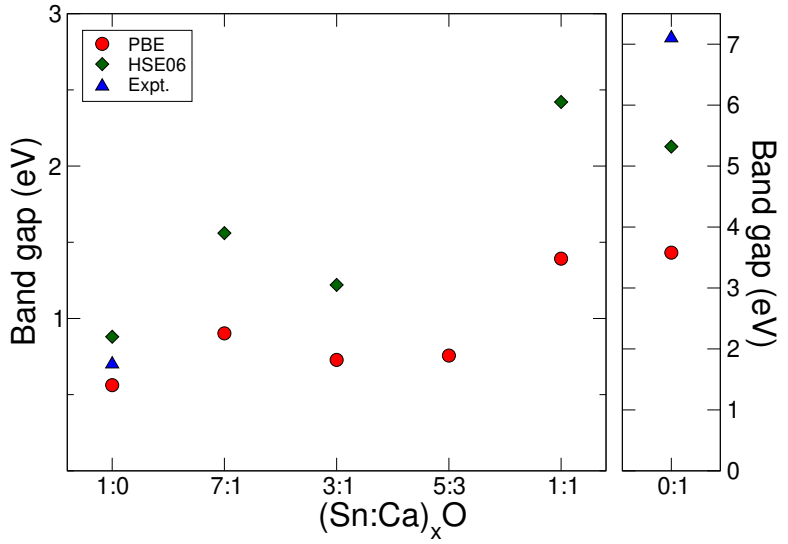

Figure 5.4: The dependence of dopant concentration on the fundamental electronic band gap size for $(Sn:Ca)_xO$. Where possible, the values obtained using PBE and HSE06 and experimental results have been compared. Experimental band gaps of SnO and CaO were obtained from References [311] and [312], respectively.

5.5.2 Tuning the optical gap through solid solution

Forming a solid solution of the two oxides, SnO and CaO, results in a compound with the chemical formula $(Sn:Ca)_xO$. By doing so, the aim is to increase the band gap of SnO by introducing small concentrations of Ca substitutions in Sn sites that should result in stronger ionic bonding. The goal is to also change the band gap from indirect to direct, as SnO has a much larger optical gap than its fundamental gap, which reduces its efficiency as a light-absorbing layer.

In Figure 5.4, the relation between the band gap and the solid solution ratio (x) is presented. Solid solution ratios lower than $1{:}1$ exhibit similar band gaps, within a range of 1.2–1.6 eV (HSE06 values), which would all be viable for photovoltaic applications. We determine that a solid solution with $x = 7{:}1$ will achieve a fundamental direct band gap of 1.56 eV at Γ, which is much closer to the optimum band gap of a single-junction solar cell – 1.34 eV – than pure SnO. It is possible that a composition closer to $x = 3{:}1$ could result in a more efficient solar cell as it exhibits a band gap of 1.22 eV; however, the gap is strongly indirect, so we focus instead on the $x = 7{:}1$ substitution level. It is also worth noting that, in these

Table 5.1: Formation energy of the four (Sn:Ca)$_x$O solid solutions studied in this work, obtained from first principles PBE calculations. The formation energy is defined as the energy difference between the solid solution and the constituent oxides, normalised by the number of oxygen.

x	E_{f} (eV/O)
7:1	0.0543
3:1	0.123
5:3	0.236
1:1	0.303

solid solutions, whilst the band structure exhibits clear changes from that of the unalloyed band structure, these alterations are not present in the form of defect states within the band gap. Instead, they present themselves as alterations to the dispersive bands in both the valence and conduction band regions.

In Table 5.1, we present the energetic cost of forming a solid solution in the α-SnO phase from the constituent oxides SnO and CaO, normalised to the number of oxygen:

$$E_{\mathrm{f},n:m} = \left(E_{n:m} - nE_{\mathrm{SnO}} - mE_{\mathrm{CaO}}\right)/(n+m), \tag{5.4}$$

where n (m) represents the number of SnO (CaO) units in the solid solution. E_{SnO} (E_{CaO}) is total energies of a single SnO (CaO) unit and $E_{\mathrm{n:m}}$ is the total energy of the (Sn:Ca)$_{\mathrm{n:m}}$O solid solution. It is apparent that, as the solid solution approaches equal parts of each oxide, the formation energy increases. Hence, for the concentrations studied, the most stable solid solution in the α-SnO phase is the $7{:}1$ ratio, with a formation energy of 0.0543 eV per oxygen atom. However, as smaller concentrations have not been explored, the trend suggests that no solid solution between these two oxides is more favourable than them remaining as individual oxides. Also note that, at higher ratios, amorphous structures may start to form.

To thoroughly explore the potential *dopant* arrangement within the structure, each dopant concentration was allowed to fully relax from the SnO and the CaO atomic

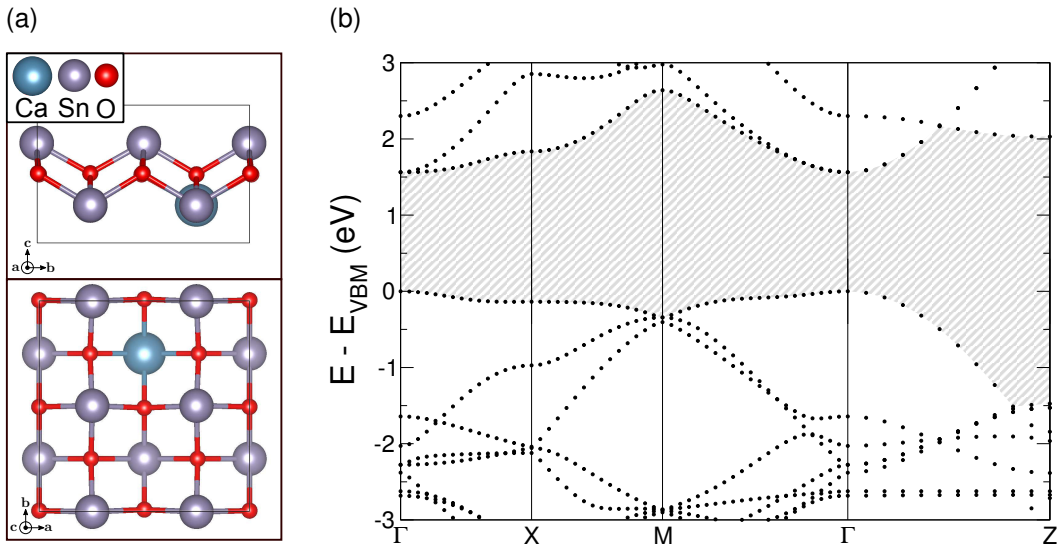

Figure 5.5: (a) Ball and stick model of the atomic structure and (b) electronic band structure of $(Sn:Ca)_{7:1}O$, obtained from first principles HSE06 calculations. The shaded region highlights the band gap of the system. Energies are given relative to the valence band maximum (VBM).

geometries. It was found that the SnO geometry was favourable for all concentrations other than $0{:}1$ (CaO). However, whilst the α-SnO phase is found to be more favourable for the solid solutions explored than the rock-salt phase (calcium oxide-like phase), we have not exhaustively searched through the phase space to determine if this is the most stable phase.

As with all alloying concentrations studied here, the $(Sn:Ca)_{7:1}O$ solid solution sees only slight atomic reconstruction. Whilst the α-SnO phase is maintained, the layer separation decreases from 5.039 Å to 5.022 Å. This decrease is also seen in the in-layer Sn–O bond lengths, which reduce from 2.251 Å in bulk SnO to 2.240 Å in the aforementioned solid solution. The reduction in Sn–O bond lengths is attributed to the larger Ca–O bond lengths of 2.294 Å (likely caused by the more ionic-like bonding exhibited by Ca atoms). Overall, by adopting a Ca atom in the SnO structure, the SnO substructure reduces in size.

Table 5.2: Formation energy and band gap of $(Sn:Ca)_{7:1}O$ in the three regimes of Ca atom arrangements, obtained from first principles PBE calculations. The optical gap of the *clustered* arrangement is 1.0791 eV.

Arrangement	E_f (eV/Ca)	E_g (eV)
clustered	0.0570	1.0573 (indirect Σ–Γ)
intermediate	0.0543	0.9943 (direct Γ–Γ)
even	0.0516	0.9141 (direct Γ–Γ)

5.5.3 Effects of solid solution arrangement

Having chosen the $7{:}1$ ratio for the SnO:CaO solid solution due to the improved band gap and low formation energy, we now explore further permutations of the $(Sn:Ca)_{7:1}O$ atomic structure by considering supercells with different arrangements of the Ca atoms (using the PBE functional). We have considered 3 regimes for the Ca atoms: *clustered*, *intermediate* and *even*. The three regimes represent the Ca *dopant* atoms being either clustered on neighbouring cation sites (*clustered*), arranged identically in each stacked layer (*intermediate* or vertically aligned), or evenly distributed throughout the supercell (*even*). These represent the 3 extrema arrangements and, as such, should be descriptive of the solid solution. In Table 5.2, we present the formation energy and band gap of these regimes. Firstly, we note the formation energies for all of these arrangements are very similar ($\Delta E_f = 0.0054$ eV). As such, any $(Sn:Ca)_{7:1}O$ solid solution grown would likely exhibit all of these regimes at different points within the sample. Secondly, the *even* distribution is the most energetically favourable form; this indicates that the Ca atoms have a tendency to be evenly distributed in a sample over that of a *clustered* distribution. Thirdly, the band gap shows a small dependence on the Ca arrangement, with a variation of $\Delta E_g = 0.0716$ eV. By considering the close formation energies, it is likely that any physical sample of this solid solution would likely have a variation in the bulk band gap.

A comparison of all the arrangements shows an increase in the band gap when compared to SnO, as well as a move to a direct band gap. The exception is the *clustered* form, where there is no significant difference between the direct and indirect gap sizes (0.0218 eV). The improvements to the optical properties are

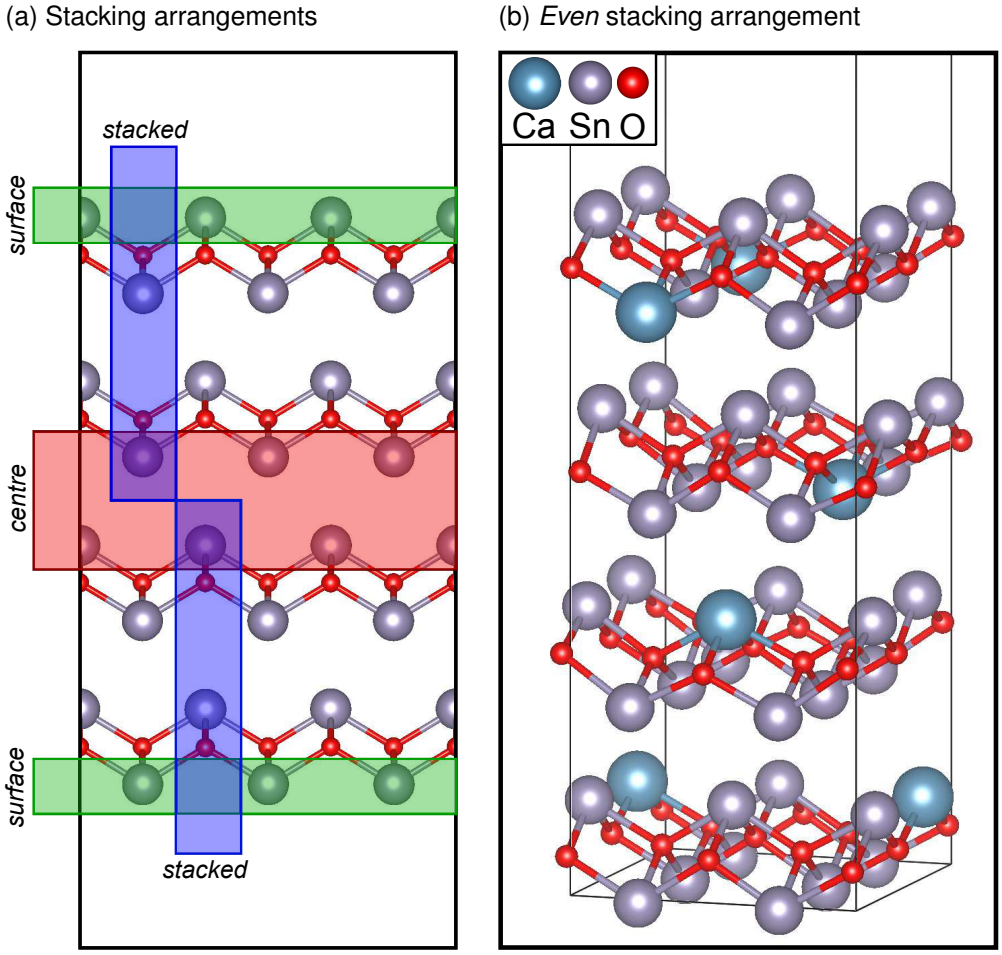

Figure 5.6: Diagram of the four stacking arrangements explored for the $(Sn:Ca)_{7:1}O$ solid solution. (a) The three less favourable stacking arrangements: *centre*, *surface* and *stacked*. (b) The atomic structure of the *even* stacking arrangement.

the main focus of this work. Finally, for future sections, the *even* arrangement discussed in this subsection is qualitatively equivalent to the *even* stacking order discussed in the following sections (both show a Ca arrangement where the Ca atoms are evenly distributed throughout the solid solution).

5.5.4 Effects of surfaces

For slab simulations, various stacking arrangements of the alloyed-SnO layers were explored to determine the most energetically favourable stacking (see Figure 5.6). The four arrangements considered were: 1) clustered dopants in the centre of the slab (*centre*), 2) clustered dopants at the slab surface (*surface*), 3)

Table 5.3: Formation energy of (Sn:Ca)$_{7:1}$O slab formation with particular stacking arrangements, obtained from first principles PBE calculations. The formation energy has been determined by comparing the energy of the slab with that of the bulk intermixed structure. All are normalised to a single Ca atom. Layer separation is measured as the distance between the midpoint of two layers. Centre layer separation defines the separation between the two layers in the centre of the slab, whilst surface separation defines the separation between the surface and subsurface layer.

Stacking	E_{f} (eV/Ca)	Layer separation (nm)	
		Centre	Surface
centre	0.412	4.921	5.083
surface	0.554	5.031	5.012
stacked	0.207	4.938	5.084
even	0.175	4.701	5.191

equally distributed across each layer with the dopants stacked directly above each other (*stacked*), and 4) equally distributed across each layer with the dopants being spatially separated along each axis (*even*). The formation energy of the four stacking arrangements as compared to the bulk solid solution are presented in Table 5.3; the most energetically favourable configuration is found to be the *even* form. The two distributed forms – *stacked* and *even* – are found to be significantly more energetically favourable (>0.2 eV/Ca) than the clustered forms – *centre* and *surface*. In Figure 5.5a, it can be seen that each layer of SnO has a zig-zag structure, with Sn atoms occupying the peaks and troughs of this design. As the Ca atoms occupy the Sn-sites, the slab structure allows these dopants to either face towards the surface or towards the centre of the slab. It was found that the Ca-dopants prefer to reside in the sites farthest away from the surface in each layer. Thus, for considering the properties of (Sn:Ca)$_{7:1}$O layers, we will now, given this result and that of the bulk, consider the *even* stacking.

To form slabs for each stacking arrangement discussed above, four fully stoichiometric layers of SnO were used as the template. Due to the short length of bonds along $\mathbf{c}$, layers were kept intact and, instead, cleaving was performed between layers. Next, Sn-sites were replaced with Ca atoms until the Sn:Ca ratio of $7{:}1$ was

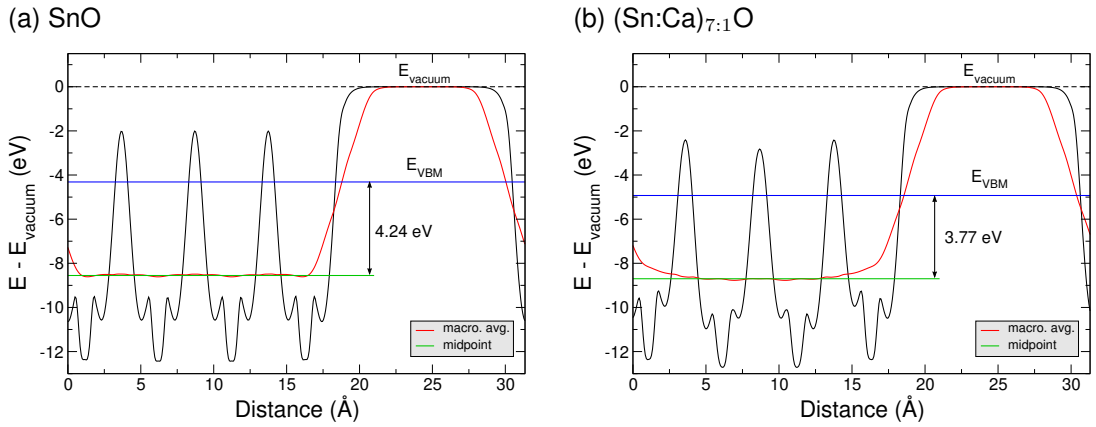

Figure 5.7: Electrostatic potential of (a) SnO and (b) $(Sn:Ca)_{7:1}O$, obtained from first principles PBE calculations. The green lines denote the midpoint of the macroscopic average of the electrostatic potential near the centre of the slab of the material. Energies are given relative to the vacuum energy.

achieved. As such, each stacking arrangement was stoichiometrically equivalent to each other and the bulk solid solution presented in Figure 5.5. The structure of the $(Sn:Ca)_{7:1}O$ solid solution is presented in Figure 5.6b. Whilst substantial reconstruction does not occur in any of the arrangements, slight changes are seen in the layer separation. In pure SnO slabs, the slab centre and surface layer separations are 5.036 Å and 5.035 Å, respectively. For the *even* stacking arrangement, we see a strong disparity between the centre and surface layer separations, with the former being compressed by 0.335 Å and the surface separation having expanded by 0.156 Å.

The electrostatic potential for SnO and the solid solution $(Sn:Ca)_{7:1}O$ are presented in Figure 5.7. When comparing the local potentials of the two materials, it can be seen that this high dopant concentration causes an increase in the hole affinity χ_{h}, which, in turn, reduces Δ. The hole affinity of SnO is 4.31 eV and Δ is 4.24 eV, whilst the hole affinity of $(Sn:Ca)_{7:1}O$ is 4.93 eV and Δ is 3.77 eV.

By increasing the hole affinity of the material, $(Sn:Ca)_{7:1}O$ allows for more oxides to work as hole transport layers. This is due to the preference for oxides to exhibit hole affinities typically greater than 5 eV [313–315].

5.6 Development of transport layers

Having established a potential photovoltaic active layer, we now need to consider transport layers to aid in the separation of charge carriers. We explore a set of candidate transport layers for the $(Sn:Ca)_{7:1}O$ solid solution. A detailed study of contact layers has not been performed here due to the Fermi-pinning that often occurs between metals and oxides [316].

5.6.1 Work functions and hole affinities of potential transport layers

Here, we explore a set of undoped candidate materials as potential electron and hole transport layers for $(Sn:Ca)_{7:1}O$. The properties that determine whether a material can act as an efficient electron/hole transport layer originate from its electronic structure. The electron and hole affinities and the conductivity of the charge carriers (i.e. the dispersion of the valence and conduction bands) define a material's capabilities as a transport layer. To be an effective transport layer, a material must either show a Type II (staggered) or Type III (broken) band alignment with the active layer, or exhibit a strongly bipolar conductivity for the holes and electrons (strongly different hole and electron effective masses). In this study, we focus on the former. Candidate materials with hole and electron affinities below (above) the hole and electron affinities of the active layer can act as an electron (hole) transport layer. If a Type I (straddled) band alignment is present instead, then the effective electric field experienced by both carriers will point in the same direction, driving both the electrons and holes to the same layer and likely increasing charge recombination rates.

In Table 5.4, we present the hole affinities of potential transport layers (work functions for metal contacts) and compare them to the hole affinity of the active layer. In doing so, one can identify whether a material is more suitable for hole or electron transport. Using the table alongside the previous criteria for identifying electron and hole transport layers, we can determine that WO_3 and CaO should behave as hole transport layers, whilst MoO_3 should be the only viable electron

Table 5.4: Hole affinities and work functions of various potential contact, transport and active layers for a photovoltaic cell. TiO_2 is presented in the anatase phase. Unless otherwise specified, hole affinities, work functions and theoretical band gap values are obtained from first principles PBE calculations.

Layer	Material	χ_{h} (eV)	$E_{g,\mathrm{theory}}$ (eV)	$E_{g,\mathrm{expt}}$ (eV)
Active layers	SnO	4.31	0.56	0.7 [311]
	$(Sn:Ca)_{7:1}O$	4.93	0.90	1.56[a]
Transport layers	WO_3	3.74	0.75	3.4 [317]
	CaO	4.09	3.58	7.1 [312]
	TiO_2	6.20	2.04	3.4 [318]
	NiO	6.7±0.1[b]	–	4.3 [319]
	CaF_2	6.69	7.38	11.2 [320]
	LiF	7.68	9.39	13.6 [321]
	MoO_3	8.50	1.73	3.1 [317]

Layer	Material	W (eV)
Metal contacts	Ca	2.76
	Al	4.54 [322]
	Au	6.16 [322]
	Ag	5.02 [322]
	Ni	5.77 [322]
	Cu	5.30 [322]

[a] HSE06 result

[b] Experimental result from Reference [303]

transport layer from the list. The other potential transport layers straddle the band gap of the active layer, which would force both charge carrier types to flow away from the transport layer. Note, due to the intrinsic n-type dopant state of TiO_2 (caused by inherent oxygen vacancies [323]), it is possible that this layer could act as a hole transport layer.

In Figure 5.8, the local potentials for Ca, CaO, TiO_2 and MoO_3 are presented (the work functions/hole affinities are detailed in Table 5.4). Comparing the hole affinities of two materials allows for an initial estimation of their relative band alignment,

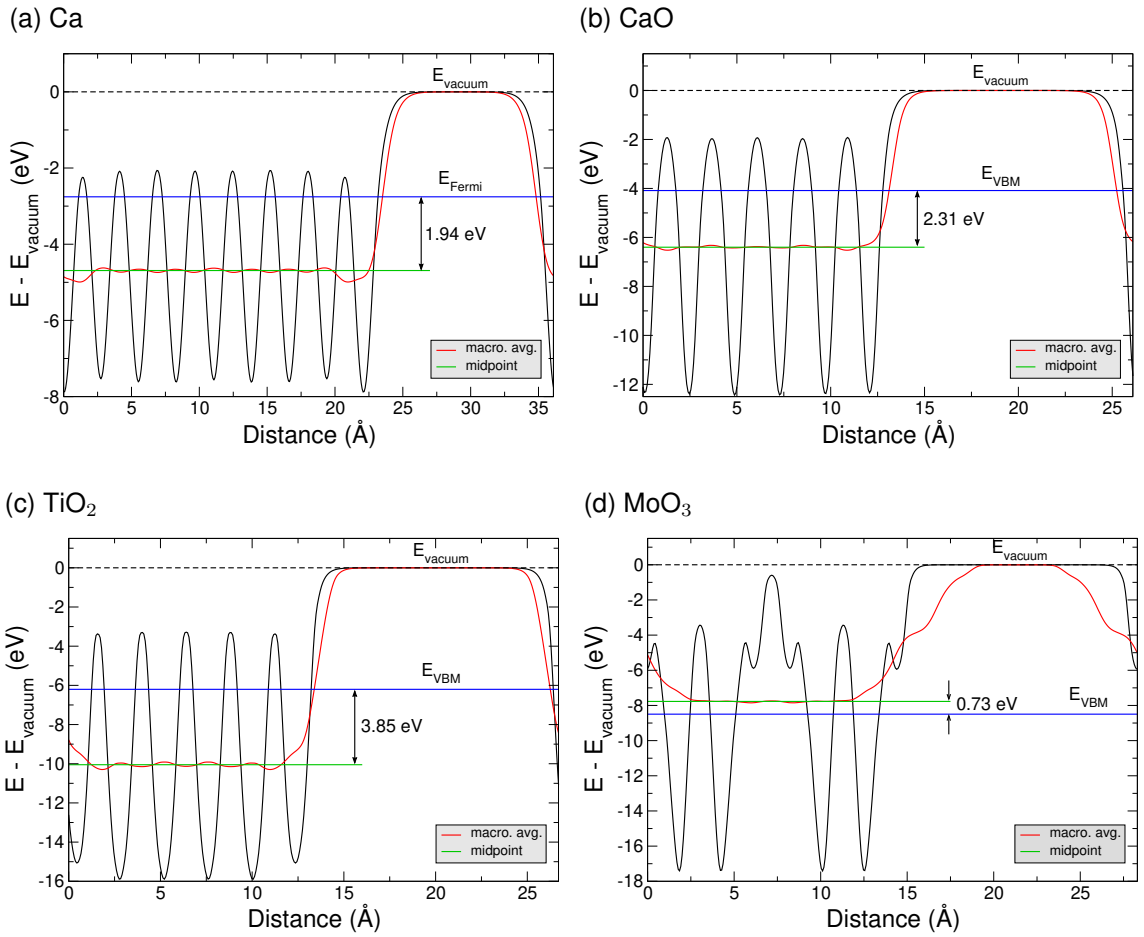

Figure 5.8: Electrostatic potential of (a) Ca, (b) CaO, (c) TiO_2 and (d), obtained from first principles PBE calculations. Energies are given relative to the vacuum energy.

but does not account for potential interactions between the two materials. These interactions can often lead to changes in the band alignment, which must be considered when determining the capabilities of a photovoltaic cell. Hence, modelling an interface structure containing the two materials is necessary in order to fully capture their band alignment.

Whilst direct comparison with experiment is not recommended, we point out here that our theoretical value of the hole affinity of WO_3, 3.74 eV, does not compare well with that of experiment – with ionisation potential values typically being close to 9.66 eV [317]. This difference of almost 6 eV is rather peculiar as changes in surface terminations and Miller planes are unlikely to account for such a large disparity. Furthermore, due to the chemical similarity of WO_3 and MoO_3, one would expect them to have similar ionisation potentials (which they do in exper-

iment [317]). This disparity could be a result of the many stable phases of WO_3 (which has multiple stable monoclinic and triclinic phases near to room temperature) [324], but would then be present in the experimental data also.

Other metals and oxides from Table 5.4 show smaller disagreement with affinities and work functions presented in literature. The experimental work function of Ca is known to be 2.86 eV when terminated on the (111) Miller plane, which is in good agreement with our result of 2.76 eV for the (101) plane. The 8.50 eV hole affinity of MoO_3 shows a closer agreement with experiment – 9.68 eV. For TiO_2 anatase, the experimentally obtained hole affinities range from 6.73 eV to over 8 eV [303, 325, 326], whereas our theoretical value is 6.20 eV. These can be strongly dependent on whether the result is of anatase, rutile, or a mix of the two and can be strongly surface dependent (with experimental reporting on the (101) plane). No experimental values for affinities could be found for CaO. As mentioned previously, for all hole affinities presented in this work, care must be taken when comparing to experimental data as these values can be strongly dependent on the material phase and termination plane.

5.6.2 Band alignment of transport layers with $(Sn:Ca)_{7:1}O$

In order to fully understand a p–i–n junction, the junction must first be explored without dopants. In doing so, it can be determined how the materials will align without the effect of dopants and whether the alignment is desired. Intrinsic dopants, such as oxygen vacancies require extensive exploration to determine their stable concentration and localisation. By exploring first the undoped systems, we can identify how the bands align without the pinning caused by intrinsic defect levels.

By generating interface structures using a transport layer and the active layer, one can determine the band alignment between the two layers by using Equation (5.3). Interfaces between the active layer $(Sn:Ca)_{7:1}O$ and a set of candidate materials have been modelled – WO_3, Ca, Ni, CaO, TiO_2, NiO, CaF_2, LiF and MoO_3. During atomic relaxation, it was found that Ni and NiO regions became unstable as they relaxed to *amorphous* phases. The interface between $(Sn:Ca)_{7:1}O$

Table 5.5: Predicted and calculated band alignments of a set of materials against $(Sn:Ca)_{7:1}O$. Predicted values are obtained by comparing the hole affinities of the two materials. Calculated values are obtained from the electrostatic potential of the interface structure consisting of the two materials. Positive (negative) values represent materials having valence band maxima above (below) that of the active layer. Results are obtained from first principles PBE calculations.

Material	Band alignment (eV)	
	Predicted	Calculated
Ca	2.17	1.15
CaO	0.84	0.92
TiO_2	-1.27	-0.17
CaF_2	-1.76	-1.74
LiF	-2.75	-3.15
MoO_3	-3.75	-1.47

and WO_3 resulted in an electric field forming across the system; as such, comparisons with and analysis of the system became challenging as accurate band alignment values could no longer be given (further issues could have arisen here as the relaxation of the system has occurred in the presence of this electric field, which may have modelled an unphysical growth environment). The rest of the interface structures were fully relaxed and their results are presented below.

The band alignments between the active layer $(Sn:Ca)_{7:1}O$ and the candidate transport layers are presented in Table 5.5. Whilst it appears easier to find transport layers with VBMs below that of the active layer, the band gaps tend to be much larger than the active layer. This leads to Type I band alignment occurring in many of the potential electron transport layer candidates. From Tables 5.4 and 5.5, it is apparent that both hole and electron transport layers are challenging to find for $(Sn:Ca)_{7:1}O$. Hole transport layers are limited by the higher chance of oxides to exhibit hole affinities greater than 5 eV, whilst the problem in finding electron transport layers is linked to the large band gaps (> 2 eV) typical of oxides.

From Table 5.5, the differences in band alignment between prediction using hole

affinities and exact calculation of them is clear. Whilst some band alignments see little change – (Sn:Ca)$_{7:1}$O/CaO and (Sn:Ca)$_{7:1}$O/CaF_2 – some see drastic changes – (Sn:Ca)$_{7:1}$O/TiO_2 and (Sn:Ca)$_{7:1}$O/MoO_3. This highlights the importance of direct calculation of the band alignments over that of prediction using the hole affinities. However, it is still worth noting that the qualitative results relating to which VBM sits higher are consistent.

To allow for a detailed study of the properties of the most viable heterostructures, the density of states for both the heterostructure and its constituent materials have been calculated. As such, the bulk density of states for Ca, CaO, TiO_2, MoO_3 and (Sn:Ca)$_{7:1}$O are presented in Appendix Figure I.1.

Figure 5.9 depicts the band alignment between (Sn:Ca)$_{7:1}$O and a set of potential transport layers – CaO, Ca, MoO_3 and TiO_2. The bold (dashed) lines in the local potentials (density of states) separate the different heterostructures that have been modelled. From the density of states for each of the heterostructures, it becomes apparent that interface states arise at the (Sn:Ca)$_{7:1}$O slab surface, with similar effects occurring in the surface of the neighbouring transport layer. For some systems, these are less apparent – such as with the (Sn:Ca)$_{7:1}$O/Ca heterostructure – whereas others show rather pronounced changes – as is the case with the (Sn:Ca)$_{7:1}$O/TiO_2 heterostructure.

The band alignment between (Sn:Ca)$_{7:1}$O and Ca is found to be 1.15 eV. Whilst metals are not normally considered for transport layers, the disparity in the density of states and the lack of states available near the (Sn:Ca)$_{7:1}$O valence bands should allow for a biased transport of the carriers. Furthermore, this disparity in available electron and hole states could lead to a higher number of electron carriers compared to holes. However, without a detailed study of the conductivity of the interface structure, this cannot be confirmed.

TiO_2 and (Sn:Ca)$_{7:1}$O have a band alignment of 0.17 eV, where the valence states of TiO_2 lie below those of the active layer. Due to the larger band gap of TiO_2, the conduction states lie above those of the active layer. This band structure exhibits a Type I band alignment. Due to these characteristics, it is unlikely for undoped TiO_2 to be a viable candidate for an electron transport layer.

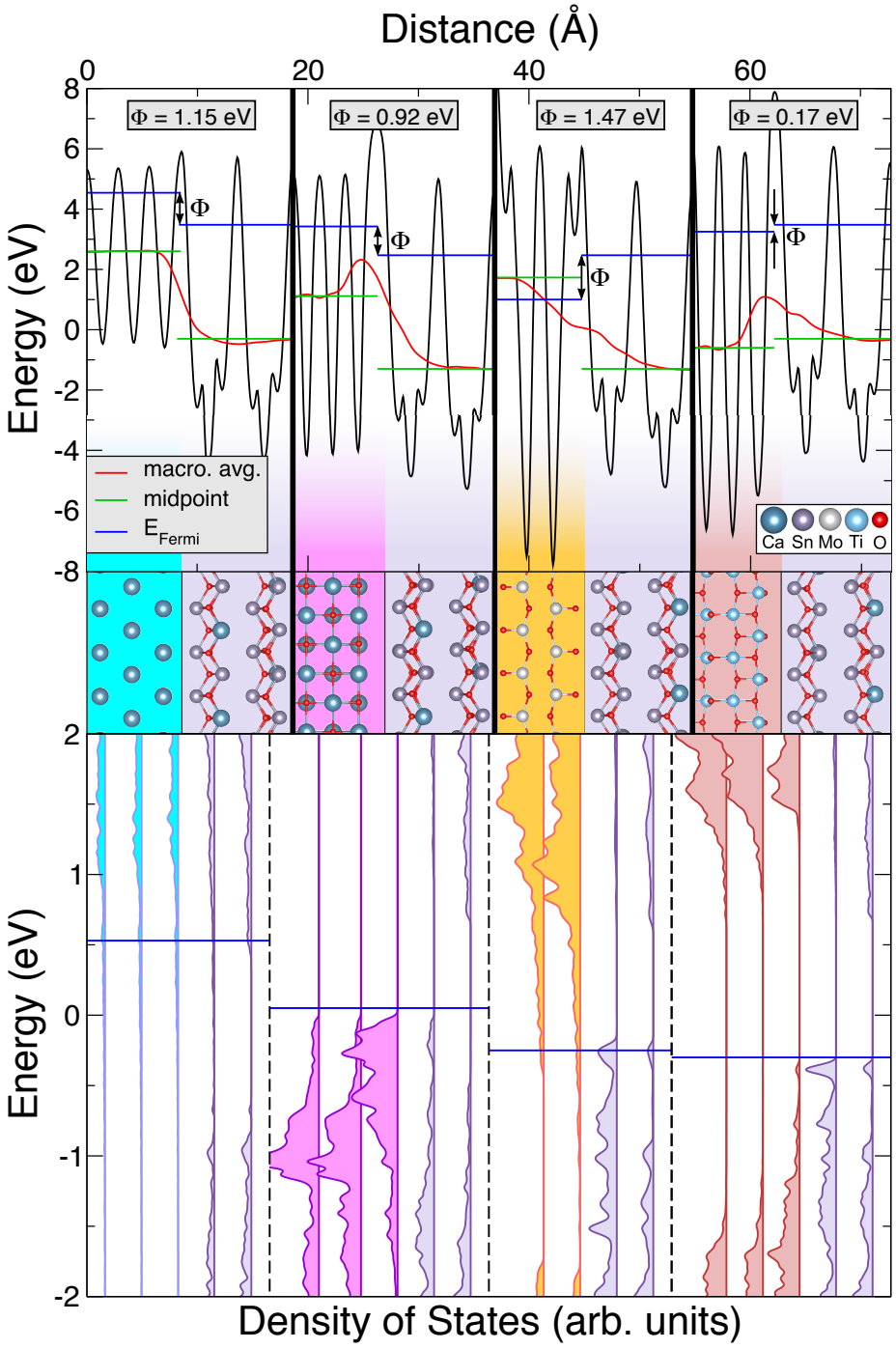

Figure 5.9: (top) Electrostatic potential, (middle) ball and stick model of the atomic structure and (bottom) layer-projected density of states of (left to right) $(Sn:Ca)_{7:1}O/Ca$, $(Sn:Ca)_{7:1}O/CaO$, $(Sn:Ca)_{7:1}O/MoO_3$ and $(Sn:Ca)_{7:1}O/TiO_2$ heterostructures, obtained from first principles PBE calculations. Φ denotes the band alignment of each heterostructure. The electronic states are aligned to the core states of the $(Sn:Ca)_{7:1}O$ slab-centre layers. The blue lines in both the top and bottom panels denote the Fermi energy in the respective region.

The band alignment between $(Sn:Ca)_{7:1}O$ and CaO is 0.92 eV. This results in the valence bands of CaO lying close to the conduction band of the active layer. The large band gap of CaO causes its conduction states to lie far above that of the active layer. This is a Type II band alignment. From the results presented here, CaO appears to be a suitable candidate for the hole transport layer.

When studying the interface between $(Sn:Ca)_{7:1}O$ and MoO_3, a similar situation arises as with TiO_2 and $(Sn:Ca)_{7:1}O$ – the MoO_3 band gap straddles that of $(Sn:Ca)_{7:1}O$. With the uncertainty of the band gap of MoO_3 (see Table 5.4), it is possible that it could work as an electron transport layer for $(Sn:Ca)_{7:1}O$. The large disparity between the barrier for the holes and the shallow step for the electrons could lead to a strong separation of the charge carriers.

Heterostructures composed of $CaO/(Sn:Ca)_{7:1}O/CaF_2$ (or $CaO/(Sn:Ca)_{7:1}O$/LiF) may be viable p–i–n junctions for solar cells. The holes would be driven through the CaO layer to the top contact, whilst the electrons would be stuck within the $(Sn:Ca)_{7:1}O$ active layer. However, this could cause issues with increased charging of the active layer without a method of discharging this layer.

From the heterostructures explored here, the most viable solar cell designs would be $CaO/(Sn:Ca)_{7:1}O/TiO_2$ and $Ca/(Sn:Ca)_{7:1}O/MoO_3$. However, the feasibility of these setups would depend strongly on the inherent oxygen vacancies that would likely form in the TiO_2, CaO and MoO_3 transport layers.

5.6.3 Discussion of the effects of doping

Until now, we have considered only materials without any form of doping. However, many oxides are known to be intrinsically doped, with most binary and ternary oxides being n-type doped through oxygen vacancies. On the other hand, monoxides are typically p-type doped. The doping can lead to radical changes in the band alignment and, thus, its effect should be considered.

Based on the previous section, we shall now look at two potential solar cell setups in more detail – $CaO/(Sn:Ca)_{7:1}O/TiO_2$ and $Ca/(Sn:Ca)_{7:1}O/MoO_3$. To consider the effects of oxygen vacancies in potential all-oxide solar cell setups, we model

a single oxygen vacancy per cell; this is equivalent to a concentration of 1 oxygen vacancy present per 24 TiO_2 unit for the $(Sn:Ca)_{7:1}O/TiO_2$ heterostructure (1.19×10^{21} cm^{-3}) and 1 in every 16 MoO_3 unit for the $(Sn:Ca)_{7:1}O/MoO_3$ heterostructure (1.07×10^{21} cm^{-3}). Whilst this concentration is much higher than would likely exist in a physical system, these represent the highest potential effect of oxygen vacancies on the band alignment (the extremum). Once the oxygen vacancies have been introduced into a system, all atoms within the system are atomically relaxed until the forces are converged to below 0.01 eV/Å.

For the $CaO/(Sn:Ca)_{7:1}O/TiO_2$ and $Ca/(Sn:Ca)_{7:1}O/MoO_3$ heterostructures, defects have not been considered in the Ca, CaO and $(Sn:Ca)_{7:1}O$ regions. As Ca is a single-species material, intrinsic defects have not been considered. Defects have not yet been explored in the CaO region as the oxide does not commonly form with n-type or p-type defects under normal conditions [327–329] (note, however, that these can be formed through heating). As SnO is known to be intrinsically p-type doped [311,330], oxygen vacancies should not occur in the structure; instead, tin vacancies are more likely to form. This presence of cation vacancies likely follows over into the $(Sn:Ca)_{7:1}O$ solid solution as both SnO and CaO show a preference towards intrinsic p-type doping. However, due to its unique chemistry, the $(Sn:Ca)_{7:1}O$ solid solution would likely lead to a more complicated defect chemistry and requires its own in-depth study.

Figure 5.10 depicts the effect of an oxygen vacancy in the $CaO/(Sn:Ca)_{7:1}O/TiO_2$ heterostructure, with the vacancy having been placed near the centre of the TiO_2 region. As can be seen, the introduction of an oxygen vacancy into the TiO_2 region results in n-type doping, in agreement with experiment [314, 331]. This doping results in two main changes to the density of states. Firstly, the TiO_2 material gains shallow n-type dopant states in the band gap. Secondly, the alignment of the density of states associated with the TiO_2 region is seen to be lower in energy by about 0.5 eV with respect to the defect-free TiO_2 region. With these changes to the band alignment, TiO_2 should be a more viable electron transport layer for the active layer of $(Sn:Ca)_{7:1}O$. Finally, the offset in the Fermi levels between the $(Sn:Ca)_{7:1}O/CaO$ and $(Sn:Ca)_{7:1}O/TiO_2$ regions is seen to be 0.525 eV, which means that a strong driving field would form across a device with this setup.

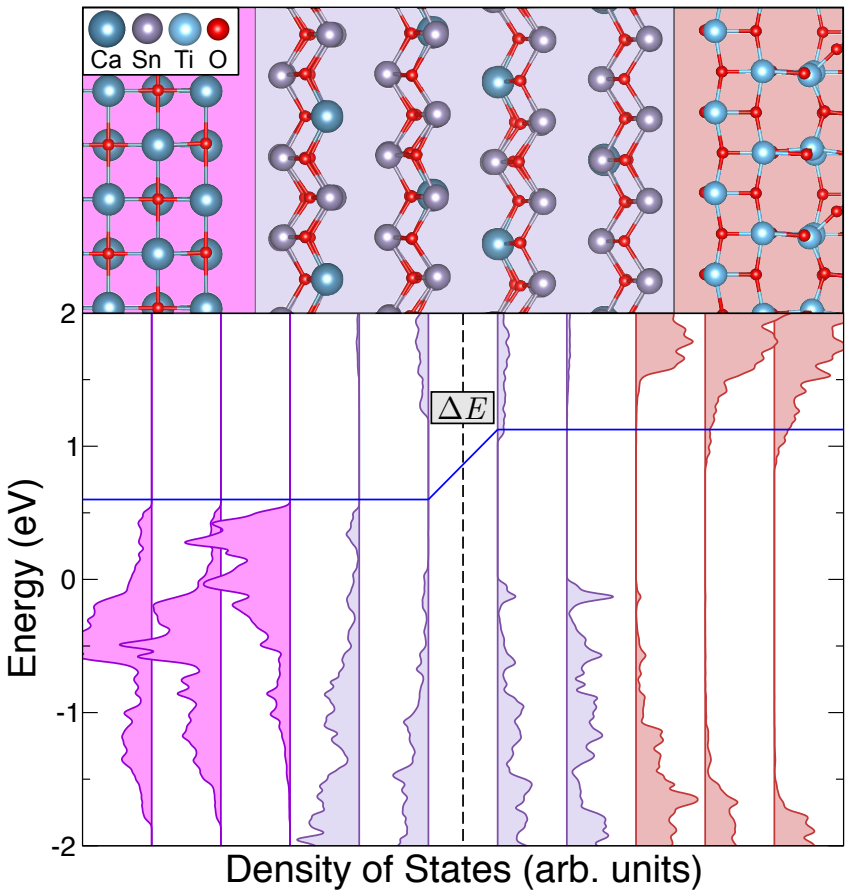

Figure 5.10: (top) Ball and stick model of the atomic structure and (bottom) layer-projected density of states of the CaO/(Sn:Ca)$_{7:1}$O and the (Sn:Ca)$_{7:1}$O/TiO$_2$, obtained from first principles PBE calculations. An oxygen vacancy is present in the centre of the TiO$_2$ region. The electronic states are aligned to the core states of the (Sn:Ca)$_{7:1}$O slab-centre layers. The blue lines denote the Fermi energy in each system. ΔE defines the difference between the Fermi energies (0.525 eV).

Figure 5.11 depicts the effect of oxygen vacancies in the Ca/(Sn:Ca)$_{7:1}$O/MoO$_3$ heterostructure. An oxygen vacancy has been introduced near the centre of the MoO$_3$ region. When comparing the atomic structure of the defected system with that of the defect-free system (Figure 5.9), we see substantial reconstruction of the MoO$_3$ region resulting in an anatase-like phase, which causes the layer separation to reduce by 0.08 Å. Similarly substantial reconstruction is observed in the density of states associated with the MoO$_3$ layers, with changes to both the valence and conduction bands. The most significant change, however, can be seen in the band gap region. Additional occupied states appear between -0.85 and -0.15 eV, extending well into the band gap (i.e. n-type doping, which is observed experimentally [314, 332]). Due to the substantial atomic rearrangement, it is dif-

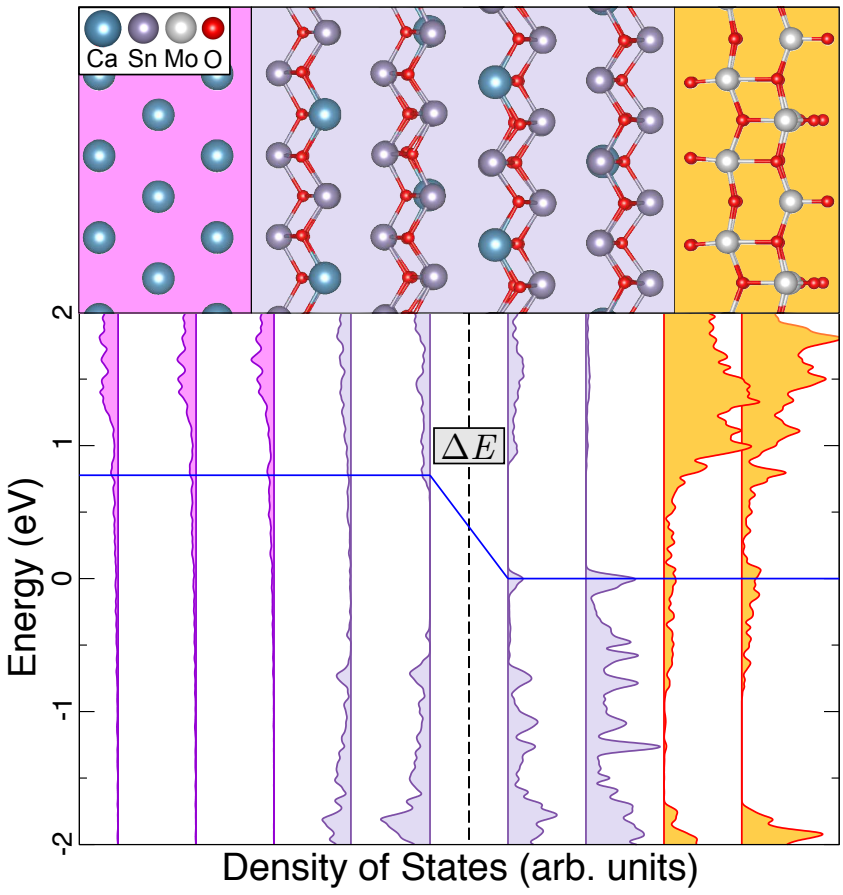

Figure 5.11: (top) Ball and stick model of the atomic structure and (bottom) layer-projected density of states of the Ca/(Sn:Ca)$_{7:1}$O and the (Sn:Ca)$_{7:1}$O/MoO$_3$, obtained from first principles PBE calculations. An oxygen vacancy is present in the centre of the MoO$_3$ region. The electronic states are aligned to the core states of the (Sn:Ca)$_{7:1}$O slab-centre layers. The blue lines denote the Fermi energy in each system. ΔE defines the difference between the Fermi energies (0.777 eV).

ficult to determine what changes are a result of the oxygen vacancy over those caused by the rearrangement of the MoO$_3$ layer. To more accurately capture this region, a larger system would be needed to model a lower oxygen vacancy concentration. However, the other layers of MoO$_3$ modelled in this interface system do not see a similar atomic reconstruction (as no oxygen vacancy is present in them) and, as such, display the same states as in the defect-free system, with no change to the band alignment. Therefore, the current results present a system where the introduction of intrinsic n-type doping shows no effect on the band alignment between the active layer (Sn:Ca)$_{7:1}$O and MoO$_3$, allowing it to remain as a potential electron transport layer. By comparing core states, the difference in Fermi energies across the Ca/(Sn:Ca)$_{7:1}$O/MoO$_3$ system is 0.777 eV.

Whilst a set of oxides has been explored here for potential transport layers when using (Sn:Ca)$_{7:1}$O as the active layer, there are still other oxides that could be considered. Even though NiO became disordered during atomic relaxations, it could still be a viable candidate for an electron transport layer due to its favourable hole affinity of 6.7 eV [303]. Another potential candidate is CuO, which has a hole affinity of 5.9 ± 0.1 eV and a band gap of 1.2 eV [303]. A final potential candidate could be $CaCu_3Ti_4O_{12}$, which we find to have a hole affinity of 5.65 eV (terminated on (001) TiO_2 planes, as discussed in Chapter 3) and is known experimentally to have a band gap of 1.5 eV.

Having considered how oxygen vacancies affect the band alignment, we present two potential setups for an all-oxide solar cell with (Sn:Ca)$_{7:1}$O as the active layer. The first is CaO/(Sn:Ca)$_{7:1}$O/TiO_2 and the second is Ca/(Sn:Ca)$_{7:1}$O/MoO_3. Both designs present favourable alignment of the bands such that a driving field should be present over the system. Of these, we find the most viable to be the former. Thus, we suggest that the CaO/(Sn:Ca)$_{7:1}$O/TiO_2 be explored further as a potentially viable all-oxide solar cell design, with an effective energy shift of 0.525 eV.

5.7 Summary

Here we have explored the potential of doping SnO to improve its electronic properties for photovoltaic applications. It is found that a solid solution formed of SnO and CaO at a ratio of $7{:}1$ results in the band gap of SnO changing from indirect to direct and increasing the fundamental gap to 1.56 eV. Furthermore, the SnO structure shows strong thermal stability and anisotropic conduction properties. With all of these capabilities, the solid solution (Sn:Ca)$_{7:1}$O has the promise to be an efficient photovoltaic material.

However, whilst the electronic properties of the solid solution (Sn:Ca)$_{7:1}$O make it an intriguing candidate as an active layer in oxide solar cells, the poor band alignment between many other oxides makes it challenging to identify a suitable electron transport layer. Overall, CaO should be a viable hole transport layer due to its capability to sustain p-type doping and appropriate band alignment with the

active layer. For the electron transport layer, we see that TiO_2 is a promising candidate and, from preliminary studies, find that its intrinsic n-type doping should make it even more suitable. Thus, we recommend that a CaO/(Sn:Ca)$_{7:1}$O/TiO_2 device shows the most potential for an all-oxide solar cell, which would represent both a step forward in cost, as these materials are readily available, and an improvement in performance, due to the direct band gap of 1.56 eV. Finally, we also put forward a set of potential hole and electron transport layers that are worth further exploration.

In the following chapter, we shall expand upon the concept of using oxides to harness sunlight. We explore the use of oxide perovskites for harnessing sunlight in chemical bonds for energy storage applications.

Chapter 6

Water-splitting

“I believe that water will one day be employed as fuel, that hydrogen and oxygen which constitute it, used singly or together, will furnish an inexhaustible source of heat and light, of an intensity of which coal is not capable."

— Jules Verne

6.1 Introduction

Photoelectrochemical water-splitting as a form of hydrogen production is often described as the ’holy grail’ of electrochemistry and renewable energies [333]. The goal is to cleanly and efficiently produce hydrogen from water in order to fuel a hydrogen economy (where hydrogen is used as a green fuel to power a society). The only by-product of producing this fuel is oxygen gas, and the only by-product of using the fuel is water; thus, it is seen as a clean and cyclical fuel. Many of the processes that drive photocatalysis occur at the surface of the catalyst. To determine the capability and efficiency of a material for such a process, a thorough exploration of the surface reactions is of vital importance.

In this study, we investigate the surface properties of a set of tin-based perovskites, $CaSnO_3$, $SrSnO_3$, $BaSnO_3$ and $SnTiO_3$, as candidates for bifunctional photocatalysts of hydrogen and oxygen evolution reactions (HER and OER). We first present the current efficiencies and limitations of photoelectrochemical cells, detailing the different technologies and the use of each. Then, results of the bulk

properties of the four candidate materials are discussed, highlighting their electronic properties. Next, the surface properties for each of these are explored to determine their potential for photocatalysis. By highlighting the band alignment between a material and the hydrogen and oxygen evolution potentials, it is possible to determine whether it can perform water-splitting. To better understand the potential efficiencies of one of the candidate materials, a study of the adsorption energies for the individual reactants is presented. Next, the possibility of improving the water-splitting capabilities through introducing a thin surface coating (an overlayer) is explored. Finally, a summary of the results is presented.

Previously in this thesis, the notation of A|B was used to define general interfaces rather than specific orientations. However, for this chapter, slab|overlayer will denote an overlayer structure; this is due to the drastic phase change exhibited by the ZrO_2 overlayer on the $SrSnO_3$ surface and, as such, the initial Miller plane of the ZrO_2 material has little meaning here.

6.2 Background

As society moves towards greener energy sources, water-splitting has gained increasing attention as a method for producing *clean hydrogen* [334–337] (hydrogen produced through methods that do not release greenhouse gases). 95% of current hydrogen production involves significant use of fossil fuels – such as steam reforming – which negates the positive effects of utilising a green fuel [338–341]. Water-splitting offers the possibility of easy and clean hydrogen gas production, but is currently limited by the inefficiency and instability of the process, preventing it from being economically viable at present.

Figure 6.1 depicts the energetic process of photocatalysis, which requires a potential difference of 1.23 eV (corresponding to light with a wavelength of about 1000 nm) to be performed. For photocatalysis, the process is performed on a semiconductor surface (in contact with water). Here, incident photons create an electron-hole pair in the semiconductor bulk that is then drawn to the surface to react with the water to separate into O_2 gas and H^+ ions. The excess protons

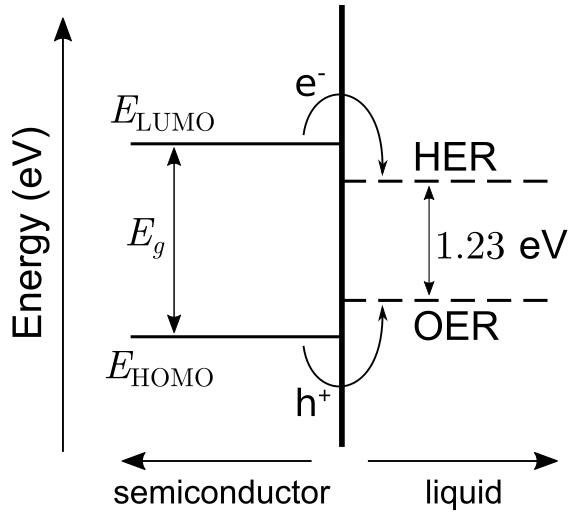

Figure 6.1: Energy diagram depicting the process of photocatalysis. Water-splitting occurs at the interface between a semiconducting surface and a liquid (in this case, water).

then react with excess electrons to form H_2 gas [342]. The hydrogen gas can then be used as an *energy carrier*. To release the stored energy, the hydrogen can be either burned or recombined with oxygen through redox reactions. For both methods the only resultant by-product is water.

For a material to be an effective water-splitting catalyst, it must have a sufficiently large band gap that straddles both the evolution reaction levels and their *overpotentials* [343] (further potential energy barriers, caused by under- or over-binding of the reactants to the semiconductor surface, that must be accounted for in order to facilitate photocatalysis). However, a material's capabilities can be improved through the introduction of an overlayer to its surface [39, 40]. This improvement has been attributed to an improved electron extraction, and a reduction of both the overpotential and the work function of the catalyst due to its inclusion. Whilst a range of overlayer materials have been considered, most are applied to the semiconductor haematite [344, 345], with very few studies considering other catalysts, such as perovskites [346].

With oxide perovskites having shown great promise in many areas [6, 219, 347, 348], including water-splitting [272, 349, 350], their bulk properties have been extensively explored [351]. Their ease of fabrication [352] and relative stability in water [353] make them suitable for water-splitting applications. The effectiveness

of a material as a *photocatalyst* (PC) is determined by its surface properties, which often differ from the bulk material [40, 354–356]. Thus, a thorough investigation of the surface is necessary to understand photocatalysts [357].

6.2.1 Realisation and current limitations

There are currently two main approaches towards photoelectrochemical cells (PECs): 1) The method of direct conversion from solar light to hydrogen production by using a semiconductor submerged in water as a photocatalyst; this process is also called the PC or *monolithic* design. 2) The use of a photovoltaic cell to supply current to another material that performs the electrolysis, *photovoltaic-electrolysis*; this method is also termed the PV-E or *non-monolithic* approach.

Whilst the body of this work will focus on the photocatalytic approach to photoelectrochemical cells, a discussion of the literature of both methods will be presented here as a comparison between their individual merits.

First, as the PV-E technology spatially separates the light harvesting and electrolytic water-splitting devices, it can directly use advances made in the both photovoltaic and electrolysis fields, which are currently much more developed and tested than PEC systems [358, 359]. As this technique builds on two already established fields, PV-E systems currently exhibit solar-to-hydrogen (STH) conversion efficiencies above $30\ \%$ [360].

Second, the PC technology is a monolithically integrated device, meaning that the entire process occurs within one device. For this reason, the method has the promise of being simpler and having cheaper production costs. This is due to the device needing to be only a photocatalytic semiconductor submerged in water (however, separating the H_2 and O_2 gases produced is easier with PV-E systems). As such, depending on the setup, the system requires no wires and only a single material needs to be grown. With fewer interfaces, and fewer components, there is less chance of failure. The current STH conversion efficiencies of these systems are around $10\ \%$ [361]. It should be noted, however, that the highest efficiencies for both PEC technologies are currently use multi-junction

(tandem) solar cells in order to improve the efficiencies, which increases the cost and difficultly of manufacturing than a single semiconductor.

Whilst PV-E and PC both show potential for water-splitting, each technologies also has its downsides. The PV-E design relies on two technology lines, with the accompanying difficulties of integrating them together and the research and development costs and timescales multiplied accordingly. The PC monolithic design currently suffers from issues with regards to the semiconductor|electrolyte interface, such as photocorrosion and many of the catalyst materials investigated so far exhibiting poor absorption rates across the solar spectrum. The photocatalyst materials also encounter issues of achieving simultaneously high efficiencies and stability. Whilst an issue for both forms of the technology, the problem of lifetime is more prominent in the of the PC systems, with it currently being a major concern.

The maximum theoretical STH conversion efficiency for a single-semiconductor PC is $30.7\ \%$ [362], whereas single-semiconductor PV-E systems are limited to the efficiency of a single-semiconductor solar cell, $33.7\ \%$ [288, 289]. However, both technologies have seen the use of multi-junction (tandem) architectures in attempts to surpass this single-semiconductor limit. Whilst the PV-E method offers greater potential maximum efficiencies, the PC approach has greater potential for low-cost hydrogen production over that of non-monolithic designs [358, 363], largely in part due to the requirement to install photovoltaic cells.

It should be noted that, due to the photocorrosion stability of the catalyst surfaces, the PC maximum efficiency is reduced in reality to $8\ \%$ [364–366] as the photocorrosion stability sets a minimum limit of $2.48\ \mathrm{V}$ for the height of the semiconductor band gap. However, this can be circumvented by use of thin oxide, wide band gap, overlayers [367, 368].

One of the leading issues with PC systems is the difficulty in identifying a material that simultaneously exhibits the right band gap and is stable in water. As such, most of the focus in this field has been on identifying, categorising and classifying materials for the photocatalytic capabilities.

Currently, no industrially practical device exists for water-splitting with pure water [369]. Whilst the technologies for two component reactions (separate H_2

production and O_2 production) are more developed, a bifunctional water-splitting device is still in the early stages of development [370]. The ability to perform simultaneous hydrogen and oxygen gas production would greatly improve the efficiency and ease of use of the device, as it should help to balance the process and not create excess by-products (depending on the relative efficiency of the two processes). This would be called a bifunctional water-splitter.

Hydrogen Fuel Cells

Current efficiencies of fuel cells are around 40–$60\ \%$ energy efficient. In comparison, typical internal combustion car engines are about 12–$30\ \%$ energy efficient [371]. The efficiency of a fuel-cell can be raised even further to $\sim 80\ \%$ through a method called *co-generation*, which involves heating the fuel cell. There exist methods for increasing the efficiency of fuel cells further. These involves heating the water, thereby introducing more initial energy into the system and reducing the required energy to split the water; this is called high-temperature electrolysis (HTE).

In comparison to electric motors, where the efficiency is about $90\ \%$, the hydrogen fuel cell will likely be less efficient. However, if the right method of hydrogen production is used, there are no green house gases released during any stage of this process (with the only by-product being water), which is vital in the post-CO_2 economy.

Electric motors, quite apart from requiring entirely separate means of production for the energy they use in the first place, typically fall victim to multitudinous efficiency losses - storage time, resistance in wires, and poor contacts at charging stations, to name a few. The use of *green hydrogen* (hydrogen produced through non-polluting means, i.e. photocatalysis) drastically reduces the inefficiencies of generation and storage of energy, as well as reducing the possible by-products of the process.

6.2.2 Methods

In this subsection, we shall outline the method used to derive the free energy steps and the overpotentials for the oxygen reactions calculated here, which follows the method derived by Nørskov *et al.* [372, 373].

Evolution reaction equations

The oxygen evolution reaction (in acidic solution) is given by the following four stages:

$$\mathrm{H_2O} + * \rightleftharpoons \mathrm{HO}* + \mathrm{H^+} + \mathrm{e^-}, \tag{6.1}$$

$$\mathrm{HO}* \rightleftharpoons \mathrm{O}* + \mathrm{H^+} + \mathrm{e^-}, \tag{6.2}$$

$$\mathrm{O}* + \mathrm{H_2O} \rightleftharpoons \mathrm{HOO}* + \mathrm{H^+} + \mathrm{e^-}, \tag{6.3}$$

$$\mathrm{HOO}* \rightleftharpoons * + \mathrm{O_2} + \mathrm{H^+} + \mathrm{e^-}, \tag{6.4}$$

where * denotes a surface site (e.g. O* denotes an oxygen atom adsorbed to the surface).

The hydrogen evolution reaction is given by:

$$\mathrm{H_2O} + \mathrm{e^-} + * \rightleftharpoons \mathrm{H}* + \mathrm{OH^-}, \quad (\mathrm{Volmer}) \tag{6.5}$$

$$\begin{aligned} \mathrm{H_2O} + \mathrm{H}* + \mathrm{e^-} &\rightleftharpoons \mathrm{H_2} + \mathrm{OH^-} + *, \quad (\mathrm{Heyrovsky}) \\ 2\mathrm{H}* &\rightleftharpoons \mathrm{H_2} + 2*. \quad (\mathrm{Tafel}) \end{aligned} \tag{6.6}$$

For this work, the reference potential is set to that of the standard hydrogen electrode (SHE). At this reference, the chemical potential (μ) of hydrogen gas ($\mu_{\mathrm{H_2(g)}}$) is equivalent to that of a proton and an electron,

$$\mu_{\mathrm{H^+}} + \mu_{\mathrm{e^-}} = \frac{1}{2}\mu_{\mathrm{H_2(g)}}, \tag{6.7}$$

where

$$\mu_{\mathrm{H^+}} = \mu^0_{\mathrm{H^+}} + k_B T \ln \mathrm{a}_{\mathrm{H^+}}, \tag{6.8}$$

$$\mu_{\mathrm{e^-}} = \mu^0_{\mathrm{e^-}} - eU, \tag{6.9}$$

$$\mu_{\mathrm{H_2(g)}} = \mu^0_{\mathrm{H_2}} + k_B T \ln \frac{p_{\mathrm{H_2}}}{p^0}. \tag{6.10}$$

Here, k_B is the Boltzmann constant, T is temperature, $\mathrm{a}_{\mathrm{H^+}}$ is the activity of protons, eU is the applied bias, $p_{\mathrm{H_2}}$ is the partial pressure of hydrogen gas and p^0 is the standard pressure ($p^0 = 1\mathrm{bar}$). μ^0 represents a chemical potential at standard conditions ($p_{\mathrm{H_2}} = 1$ bar, $\mathrm{a}_{\mathrm{H^+}} = 1$, $T = 298.15$ K). At these conditions, Equation (6.7) can be rewritten using μ^0:

$$\mu^0_{\mathrm{H^+}} + \mu^0_{\mathrm{e^-}} = \frac{1}{2}\mu^0_{\mathrm{H_2(g)}}, \tag{6.11}$$

In order to link these equations to DFT calculations, a relation between chemical potential (Gibbs' free energy, G) and DFT-calculated energy (E_{DFT}) is needed. For a more rigorous evaluation of the Gibbs' free energy at 0 K, we add the zero-point energy to E_{DFT}. These zero-point energies can be calculated using DFT by obtaining the vibrational frequencies [374]. To introduce a temperature- and pressure-dependence to this Gibbs' free energy term, we use

$$G(T,p) = E_{\mathrm{DFT}} + \mathrm{ZPE} - TS(T,p) = E_{\mathrm{DFT}} + G_{\mathrm{corr}} \tag{6.12}$$

where S is the entropy of the system. The required zero-point energies and entropies for the following reactions are listed in Table 6.1. The values of entropy are taken from standard tables, whereas the values of ZPE are taken from identical tables in literature [357, 375, 376]. The zero-point motions of the molecules is equivalent here as they are described in isolation. As for the adsorbate zero-point energies, the literature [357, 375, 376] has shown that, for binary oxides and oxide perovskites, the ZPE of adsorbates is found to be independent of the surface being adsorbed onto. We have calculated the zero-point energies for both oxygen adsorbed to the $SrSnO_3$ clean surface and hydrogen adsorbed to the $SrSnO_3|ZrO_2$ overlayer and find our value to agree with the tabulated values

to within the accuracy given in the tables from the previously mentioned articles. Two different adsorption species were tested to ensure general agreement. An adsorption on each surface was tested to ensure that both the perovskite clean surface and a binary oxide overlayer still agreed with this observation. Zero-point energies are obtained using the finite differences method (implemented using IBRION = 5 in VASP) to displace the surface adsorbate (whilst keeping all other atoms fixed) in order to obtain the Hessian associated with the displacements of this adsorbate along with its respective eigenvalues. Each eigenvalue can then be used to obtain the zero-point energy associated with it; with each zero-point energy being summed to get the total value for the adsorbate [374].

Using the aforementioned relation between Gibbs' free energy and DFT energy, the chemical potential for hydrogen is

$$\mu^0_{\mathrm{H_2(g)}} = E^{\mathrm{H_2(g)}}_{\mathrm{DFT}} + \mathrm{ZPE}_{\mathrm{H_2(g)}} - TS^0_{\mathrm{H_2(g)}}. \tag{6.13}$$

The liquid phase of water is approximated as the gas phase for use as a reference. This approximation taken at a pressure of 0.035 bar (and at $T = 298.15$ K) as, at this pressure, the chemical potentials of the gas and liquid phase of water are equal,

$$\mu_{\mathrm{H_2O(l)}} = \mu_{\mathrm{H_2O(g)}}. \tag{6.14}$$

In terms of DFT energies, this can be described as

$$\mu_{\mathrm{H_2O(g)}} = E^{\mathrm{H_2O(g)}}_{\mathrm{DFT}} + \mathrm{ZPE} - TS^0(0.035\ \text{bar}). \tag{6.15}$$

The final gas needed to be described is oxygen (O_2 gas). Since the O_2 molecule is known to be difficult to accurately model with DFT [375,377], we instead replace it with the reaction: $H_2O(l) \rightleftharpoons 1/2O_2(g) + H_2(g)$. However, this reaction costs 2.46 eV to perform (experimentally). Therefore, the energy for oxygen gas is

$$G^0_{\mathrm{O_2(g)}} = 4.92\ \text{eV} + 2\big(G^0_{\mathrm{H_2O(l)}} - G^0_{\mathrm{H_2(g)}}\big). \tag{6.16}$$

As such, neither the zero-point energy nor the entropy of O_2 is needed in the following equations.

Finally, for the clean slab (denoted with an asterisk ,*), the Gibbs free is taken as the DFT energy, without any corrections,

$$G^* = E^*_{\mathrm{DFT}}, \tag{6.17}$$

which means that it is taken at the athermal limit. This can be done as its temperature dependence is negligible when compared to the molecules and adsorbates, so is simply ignored. All adsorptions are denoted as the chemical symbol of the adsorbate followed by an asterisk (e.g. O^* denotes an oxygen adsorbed to the surface).

Table 6.1: Entropies (taken at $T = 298.15$ K), zero-point energies and the correction term for the molecules considered in this chapter.

Species	TS	ZPE	G_{corr}
H_2O(g)	0.671	0.550	-0.121
H_2(g)	0.403	0.265	-0.138
HO*	0.082	0.342	0.260
O*	0.051	0.075	0.024
HOO*	0.138	0.461	0.323
H*-Osite	0.007	0.307	0.300
H*-Bsite	0.032	0.118	0.086

Oxygen evolution reaction

Using the relation between Gibbs' free energy and DFT energies outlined in the previous subsection, Equations (6.1) – (6.4) can be redefined.

The first step of oxygen evolution (Equation Equation (6.1)) can be rewritten as

$$\begin{aligned}\Delta G_1 =& \Delta G_{\mathrm{HO}^*} - \Delta G_{\mathrm{H_2O}(l)} - eU + k_B T \ln a_{\mathrm{H}^+} \\ \Delta G_1 =& E^{\mathrm{HO}^*}_{\mathrm{DFT}} - E^{*}_{\mathrm{DFT}} - (E^{\mathrm{H_2O(g)}}_{\mathrm{DFT}} - \frac{1}{2}E^{\mathrm{H_2(g)}}_{\mathrm{DFT}}) \\ &+ \Delta G_{1,\mathrm{corr}} - eU + k_B T \ln a_{\mathrm{H}^+}.\end{aligned} \tag{6.18}$$

The second step of oxygen evolution (Equation (6.2)) becomes

$$\begin{aligned}\Delta G_2 =& \Delta G_{\mathrm{O}^*} - \Delta G_{\mathrm{HO}^*} - eU + k_B T \ln a_{\mathrm{H}^+} \\ \Delta G_2 =& E^{\mathrm{O}^*}_{\mathrm{DFT}} - E^{\mathrm{HO}^*}_{\mathrm{DFT}} + \frac{1}{2}E^{\mathrm{H_2(g)}}_{\mathrm{DFT}}) \\ &+ \Delta G_{2,\mathrm{corr}} - eU + k_B T \ln a_{\mathrm{H}^+}.\end{aligned} \tag{6.19}$$

For the third step (Equation (6.2)),

$$\begin{aligned}\Delta G_3 =& \Delta G_{\mathrm{HOO}^*} - \Delta G_{\mathrm{O}^*} - eU + k_B T \ln a_{\mathrm{H}^+} \\ \Delta G_3 =& E^{\mathrm{HOO}^*}_{\mathrm{DFT}} - E^{\mathrm{O}^*}_{\mathrm{DFT}} - (E^{\mathrm{H_2O(g)}}_{\mathrm{DFT}} - \frac{1}{2}E^{\mathrm{H_2(g)}}_{\mathrm{DFT}}) \\ &+ \Delta G_{3,\mathrm{corr}} - eU + k_B T \ln a_{\mathrm{H}^+}.\end{aligned} \tag{6.20}$$

Finally, the fourth step of the reaction (Equation (6.4)) is

$$\begin{aligned}\Delta G_4 =& \Delta G_{\mathrm{O_2}} - \Delta G_{\mathrm{HOO}^*} - eU + k_B T \ln a_{\mathrm{H}^+} \\ \Delta G_4 =& E^{*}_{\mathrm{DFT}} - E^{\mathrm{HOO}^*}_{\mathrm{DFT}} + (2E^{\mathrm{H_2O(g)}}_{\mathrm{DFT}} - \frac{3}{2}E^{\mathrm{H_2(g)}}_{\mathrm{DFT}}) \\ &+ 4.92 + \Delta G_{4,\mathrm{corr}} - eU + k_B T \ln a_{\mathrm{H}^+}.\end{aligned} \tag{6.21}$$

Below are the definitions for the Gibbs' free energy correction terms ($G_{x,\mathrm{corr}} = \Delta\mathrm{ZPE} - T\Delta S^0$, where $x = 1, 2, 3, 4$) for the four steps of the oxygen evolution reaction:

$$\Delta G_{1,\mathrm{corr}} = G_{\mathrm{corr,HO^*}} + \frac{1}{2}G_{\mathrm{corr,H_2}} - G_{\mathrm{corr,H_2O(g)}}, \tag{6.22}$$

$$\Delta G_{2,\mathrm{corr}} = G_{\mathrm{corr,O^*}} + \frac{1}{2}G_{\mathrm{corr,H_2}} - G_{\mathrm{corr,HO^*}}, \tag{6.23}$$

$$\Delta G_{3,\mathrm{corr}} = G_{\mathrm{corr,HOO^*}} + \frac{1}{2}G_{\mathrm{corr,H_2}} - G_{\mathrm{corr,H_2O(g)}} - G_{\mathrm{corr,O^*}}, \tag{6.24}$$

$$\Delta G_{4,\mathrm{corr}} = 2G_{\mathrm{corr,H_2O(g)}} - \frac{3}{2}G_{\mathrm{corr,H_2}} - G_{\mathrm{corr,HOO^*}}. \tag{6.25}$$

Hydrogen evolution reaction

We define the hydrogen evolution in the following environment. As the free energy diagrams are taken with respect to the standard hydrogen electrode (SHE, $\mathrm{pH} = 0$ and $U = 0$), then there are two main points to consider: 1) There is an abundance of hydrogen around and 2) there is no energy difference between the state of $\mathrm{H^+ + e^- = H_2}$. Point 1) means that there is no limit to the number of hydrogen ions available for adsorption. Hence, when an electron is introduced to the surface, the hydrogen ion with the surface binding energy closest to that of it in a H_2 molecule will desorb (regardless of whether it is positive or negative). The second point means that, instead of considering the full Volmer-Heyrovsky or Volmer-Tafel equations, they reduce down to simply three steps:

$$\begin{gathered}\mathrm{2H^+ + 2e^- \rightleftharpoons H^* + H^+ + e^- \rightleftharpoons 2H^+ + 2e^-} \\ (\mathrm{or}) \\ \mathrm{2H^+ + 2e^- \rightleftharpoons 2H^* \rightleftharpoons 2H^+ + 2e^-}\end{gathered} \tag{6.26}$$

The first and last step are equivalent (at the aforementioned equilibrium reduction potential, $U = 0$). Hence, the intermediate step of $|\Delta G_{\mathrm{H^*}}|$ is taken as the descriptor of the HER activity *for a wide variety of catalysts*. For spontaneous reaction without an activation barrier, we need $|\Delta G_{\mathrm{H^*}}|$ to be zero. To calculate the free

energy of the intermediate step, one can compare the energy of the H adsorbed to each potential surface site with the energy of it in a H_2 molecule,

$$\begin{aligned}\Delta G_{\mathrm{H}^*} =& G_{\mathrm{H}^*} - \frac{1}{2}\mu_{\mathrm{H}_2} \\ \Delta G_{\mathrm{H}^*} =& E_{\mathrm{DFT}}^{\mathrm{H}^*} - \frac{1}{2}E_{\mathrm{DFT}}^{\mathrm{H^2(g)}} \\ &+ \Delta G_{\mathrm{H}^*,\mathrm{corr}} - eU + k_B T \ln a_{\mathrm{H}^+}.\end{aligned} \tag{6.27}$$

Hydrogen is found to be more energetically favourable to adsorb on O sites for both $SrSnO_3$ and $SrSnO_3|ZrO_2$ systems, so we only need to consider the O-site adsorption correction energy. Therefore, the corrected Gibbs' free energy equation for hydrogen adsorption is

$$\Delta G_{\mathrm{H}^*,\mathrm{corr}} = E_{\mathrm{DFT}}^{\mathrm{H}^*} + G_{\mathrm{corr,H^*\text{-}Osite}}. \tag{6.28}$$

Overpotentials

Overpotentials define the deviation in each free energy step of a reaction pathway from that of the ideal case when at $U = 0$ V. For the OER, the ideal energy of each step (ΔG_x, $x = 1, 2, 3, 4$) is 1.23 eV. For the HER, the ideal energy of the intermediary step is 0 eV. The overpotential can be seen as the extra energy required to make the reaction pathway favourable (the maximum extra energy required for any one step of the free energy diagram). The theoretical overpotentials are independent of pH and are given for the standard conditions.

The overpotential for the OER, η^{OER}, is defined as

$$\begin{aligned}G^{\mathrm{OER}} &= \Big|\max\big[\Delta G_1, \Delta G_2, \Delta G_3, \Delta G_4\big]\Big|, \\ \eta^{\mathrm{OER}} &= (G^{\mathrm{OER}}/e) - 1.23\mathrm{V}.\end{aligned} \tag{6.29}$$

The HER overpotential, η^{HER}, is then defined as

$$G^{\mathrm{HER}} = \min\left[|\Delta G_{\mathrm{H\text{-}A}}|, |\Delta G_{\mathrm{H\text{-}B}}|, |\Delta G_{\mathrm{H\text{-}O}}|\right],$$
$$\eta^{\mathrm{HER}} = (G^{\mathrm{HER}}/e). \tag{6.30}$$

As the overpotentials are independent of pH, they are, instead, relative to the OER and HER. The OER and HER, however, do depend on pH, which can be taken into account by using a Nernstian correction [372],

$$\begin{aligned} V_{\mathrm{HER}} &= 0.00\ \mathrm{V} - \frac{RT}{F}\ln a_{\mathrm{H^+}} \\ V_{\mathrm{OER}} &= 1.23\ \mathrm{V} - \frac{RT}{F}\ln a_{\mathrm{H^+}} \end{aligned} \tag{6.31}$$

where F is the Faraday constant and R is the gas constant.

These corrections can be written in terms of pH by using the relation between pH and activity,

$$\mathrm{pH} = \log_{10}\left(\frac{1}{a_{\mathrm{H^+}}}\right). \tag{6.32}$$

However, as we compare to the vacuum energy (E_{vacuum}), it is more useful to consider the reaction levels with respect to E_{vacuum}. Hence, we restate our reaction levels as

$$\begin{aligned} E_{\mathrm{HER}} &= -4.44\ \mathrm{eV} + 2.303\ k_B T\ \mathrm{pH}, \\ E_{\mathrm{OER}} &= -5.67\ \mathrm{eV} + 2.303\ k_B T\ \mathrm{pH}. \end{aligned} \tag{6.33}$$

6.3 *Ab initio* simulation details

All calculations were completed using the PBE [63] functional. This includes structural relaxation, density of states and local potential calculations (see Appendix H for a description of the local potential). However, to accurately assess

materials for their potential as water-splitters, HSE06 [268] was used to accurately calculate the band gaps. As the primitive cells of $CaSnO_3$ and $SrSnO_3$ are orthorhombic, they contain four perovskite units (ABO_3), whereas the $BaSnO_3$ and $SnTiO_3$ primitive cells, being cubic, contain a single perovskite unit. All considerations of *k*-point grids are performed using a single cubic perovskite unit as the reference, with $9 \times 9 \times 9$ Monkhorst-Pack grid [88] equivalents being used.

It has been noted that perovskite structures prefer to terminate on (001) surfaces [378–380]. Thus, to generate our surface systems, supercells equivalent to a 2×2 ($\mathbf{a} \times \mathbf{b}$) extension of an orthorhombic unit cell were formed, with a 14 Å vacuum gap introduced along the [001] Miller direction. Our surfaces were structurally relaxed, and electronic properties studied, using appropriate *k*-point grids. Electronic structure calculations were carried out using slabs 4 formula units thick and clean-surface/adsorbate calculations were carried out with slabs 3 formula units thick. All slabs had an additional BO_2 layer to ensure both surfaces terminated with BO_2. This unit cell geometry leads to surface adsorptions with an effective concentration of 7.7×10^{13} cm^{-2}.

6.4 Bulk properties

The band structures for $CaSnO_3$, $SrSnO_3$, $BaSnO_3$ and $SnTiO_3$ are presented in Figure 6.2 (see Figure 6.3a for an example perovskite orthorhombic bulk unit cell). For the perovskites with the chemical formula $ASnO_3$, where A=(Ca, Sn, Ba), the low-lying conduction bands are found to be very dispersive, covering a range of 3–5 eV. In contrast, their valence bands are much more flat, leading to a far less dispersive set of bands. This leads to a large disparity in the in the density of states for these materials (hence why all density of states covering the conduction band regions presented in this chapter are magnified by 10 times). For $SnTiO_3$, the conduction bands and valence bands appear much more similar, with comparable dispersive qualities for both.

The hole and electron effective masses for the bulk materials are presented in Table 6.2. $CaSnO_3$ and $SrSnO_3$ exhibit similar trends of effective masses, with

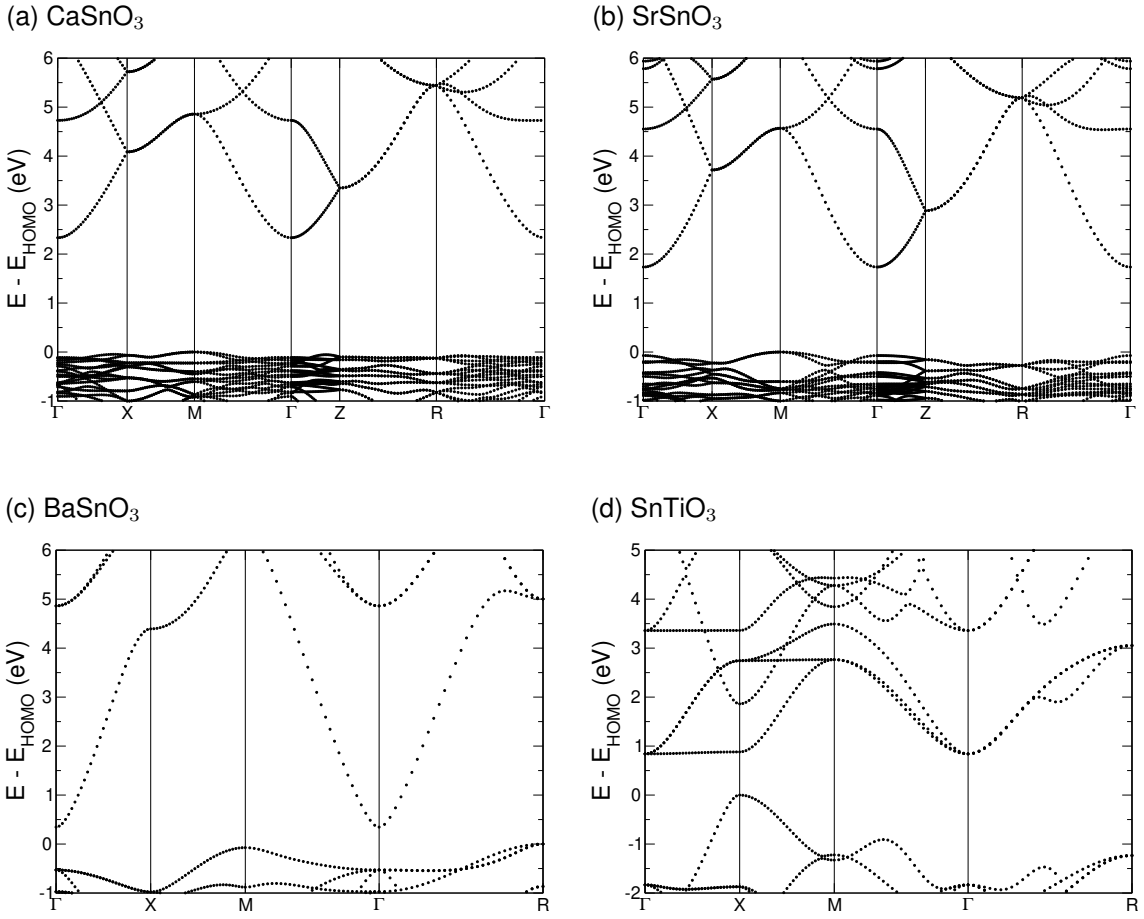

Figure 6.2: Band structures of bulk (a) $CaSnO_3$, (b) $SrSnO_3$, (c) $BaSnO_3$ and (d) $SnTiO_3$, obtained from first principles PBE calculations. Energies are given relative to the highest occupied molecular orbital (HOMO).

the electrons having $1/10^{th}$ the effective mass of the electrons. $BaSnO_3$ displays a similar disparity in its effective masses, although to a lesser extent ($1/6^{th}$). This lower electron effective mass is due to the strong dispersive nature of the conduction bands, leading to strongly delocalised conduction states. Again, $SnTiO_3$ is the most dissimilar. Here, we find that the electrons instead show a much greater effective mass than the holes, with a value of $28.4\ m_e$, which arises due to the extremely flat first conduction band along Γ–K. For $SnTiO_3$, the holes will be far more delocalised than the electrons.

The orbital-projected density of states (PDOS) for the four bulk materials considered in this chapter are seen in Figure 6.5 (for $CaSnO_3$, $BaSnO_3$ and $SnTiO_3$) and Figure 6.6a (for $SrSnO_3$). For the bulk structures of $CaSnO_3$, $SrSnO_3$ and $BaSnO_3$, the valence bands are found to be dominated by p-orbitals of the oxy-

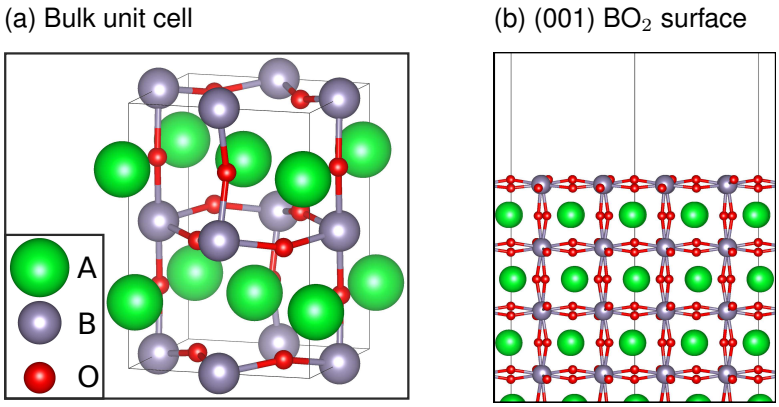

Figure 6.3: Ball and stick models depicting the atomic structure of an orthorhombic perovskite (a) bulk unit cell and (b) BO_2-termination.

gen atoms, whereas the conduction region is jointly contributed by both s- and p-orbitals (with s-orbitals contributions being $1.7\times$ larger than the p-orbitals). The d-orbital contribution is insignificant for the region between -2 eV and 3 eV (i.e. the energy range covered by the band structures in Figure 6.2). For $SnTiO_3$, the valence bands are equally composed of s- and p-orbitals. The conduction band is dominated by d-orbitals, with minor contributions from the p-orbitals. The large disparity between the $ASnO_3$ materials and $SnTiO_3$ clearly originates from the location of the Sn species in the perovskite structure. Due to Sn species occupying the covalent bonding site in the $ASnO_3$ structure, the states near the band gap are dominated by the Sn–O bonds. Whereas, in the $SnTiO_3$ case, the Sn atom takes up the ionic bonding site, thus leaving the states near the band gap to be dominated by the Ti–O bonds.

6.5 Surface properties

6.5.1 Choice of surface termination

In general, the (001) surface termination offers two potential surfaces, AO and BO_2. However, various oxide perovskites have been shown experimentally to favour the BO_2 surface [197–199]. Also, the electronic states associated with the A cation generally lie far away from the Fermi level [381]. As such, their states

Table 6.2: Hole affinities (χ_h), band gaps (E_g) and electron (m_{e}^*) and hole (m_{h}^*) effective masses for $CaSnO_3$, $SrSnO_3$, $BaSnO_3$ and $SnTiO_3$. The hole affinities and band gaps are in units of eV and the effective masses are in units of m_{e}. The bulk values of hole affinities are calculated aligning core states of the bulk with those of the slab. The electron and hole effective masses are obtained for the bulk materials. These effective masses values are obtained by fitting a parabolic to the conduction band minimum and valence band maximum, respectively. The form of the parabolic is then used to obtain the effective mass. The hole affinities and effective masses are obtained from PBE calculations, whilst the band gaps are calculated using HSE06.

Material	Bulk		Slab		m_{e}^*	m_{h}^*
	χ_h	$E_{g,\mathrm{bulk}}$	χ_h	$E_{g,\mathrm{slab}}$		
$CaSnO_3$	-6.520	3.812	-6.450	2.983	0.460	-4.643
$SrSnO_3$	-6.103	3.113	-6.126	2.432	0.460	-3.139
$BaSnO_3$	-6.672	2.149	-6.532	1.120	0.124	-0.760
$SnTiO_3$	-5.159	2.853	-4.939	2.022	28.420	-0.256

will be of less importance to the surface electronics. This gives reason to focus on just the BO_2 surfaces and, to support this further, we outline our investigation of the energetic and electronic properties of both potential surfaces.

First we consider the energetic stability of either surface termination. The following equations are used to calculate the A- and B-site vacancy formation energies, $E_{f,\mathrm{A}}$ and $E_{f,\mathrm{B}}$, respectively:

$$E_{f,\mathrm{A}} = E_{\mathrm{vac}} - E_{\mathrm{slab}} + \left(E_{\mathrm{ABO_3}} - E_{\mathrm{BO_2}} - \frac{1}{2} E_{\mathrm{O_2}} \right), \tag{6.34}$$

$$E_{f,\mathrm{B}} = E_{\mathrm{vac}} - E_{\mathrm{slab}} + \left(E_{\mathrm{ABO_3}} - E_{\mathrm{AO}} - E_{\mathrm{O_2}} \right). \tag{6.35}$$

Table 6.3 displays the energies of forming surface cation vacancies (with concentrations of 0.008 Å^{-2}, 0.008 Å^{-2} and 0.014 Å^{-2} for $CaSnO_3$, $SrSnO_3$ and $BaSnO_3$, respectively). From this table, it can be seen that, for $SrSnO_3$ and $CaSnO_3$, the energy cost of forming a surface cation vacancy is much lower on the AO surfaces than the BO_2 surfaces (where the cation on the AO surface is the A atom, and

Table 6.3: Formation energies of surface cation vacancies for the AO- and BO_2-termination surfaces (where the cation vacancy on the AO surface forms on the A-site, and the cation vacancy on the BO_2 surface forms on the B-site). These energies are obtained from first principles PBE calculations.

Material	Surface cation vacancy formation energy (eV)	
	AO-termination	BO_2-termination
$CaSnO_3$	0.83	2.18
$SrSnO_3$	0.78	1.57
$BaSnO_3$	1.74	1.24

the cation on the BO_2 surface is the B atom). As such, the AO-termination is less stable than the BO_2-termination.

We next explore the band gap values for the AO and BO_2-terminated slabs for $CaSnO_3$, $SrSnO_3$, $BaSnO_3$ and $SnTiO_3$. In Table 6.4, it is clear that the BO_2-termination results in a smaller band gap than the AO-termination. This can be explained as the electronic states being more strongly reconstructed at the BO_2 surface than the AO-termination. As such, the BO_2-termination represents the more significant deviation from the bulk, which can show us the extreme of forming a surface in this material. Note that the formation energies of vacancies for $SnTiO_3$ are not presented here due to the instability of its bulk (with a formation energy of 1.04 eV per perovskite unit). However, $SnTiO_3$ is still valid to consider for the purposes of water-splitting as thin layers of it are stable and have been produced experimentally [382].

Due to the exploration of the electronic and vacancy energetics outlined above, the remainder of this study focuses solely on the BO_2-termination for the perovskites considered in this study. The BO_2 surface of an example orthorhombic perovskite structure is presented in Figure 6.3b.

Table 6.4: Band gaps (E_g) relating to the AO- and BO_2-terminations of the perovskites $CaSnO_3$, $SrSnO_3$, $BaSnO_3$ and $SnTiO_3$. The values are calculated using PBE.

Material	$E_{g,\mathrm{slab}}$ (eV)	
	AO-termination	BO_2-termination
$CaSnO_3$	2.12	1.59
$SrSnO_3$	2.05	1.32
$BaSnO_3$	1.00	0.00
$SnTiO_3$	1.49	1.29

6.6 Core state alignment

Figure 6.4 highlights the alignment of core density of states peaks for the surface and bulk systems of the four perovskites considered. As the core states are more than 25 eV below the HOMO levels of the respective structures, we argue that these states are minimally affected by the formation of a surface. As such, alignment of these core states allows investigation of changes in higher energy states from the formation of a surface. This methodology allows us to align the bulk electronic states (and subsequently the band gap) with the surface electronic states and, hence, align the bulk band gap with respect to the vacuum energy.

The method used to obtain the vacuum energy involves calculating the electrostatic potential of a slab system (such a system includes a vacuum gap) in order to determine the potential of the vacuum region [310, 383], termed as the vacuum energy, E_{vacuum}. The hole affinities, found in Table 6.2, are calculated by using E_{vacuum} as a global reference energy to compare to the highest occupied molecular orbital, HOMO (or valence band maximum), of the slab. The distance between the HOMO and E_{vacuum} is the value of the hole affinity χ_{h}. E_{vacuum}, being a global energy reference, is then also used as the reference point for the hydrogen evolution reaction (HER). The HER is 4.44 eV below the vacuum energy [384] (as the absolute electrode potential is 4.44 ± 0.02 V for the standard hydrogen electrode [385]).

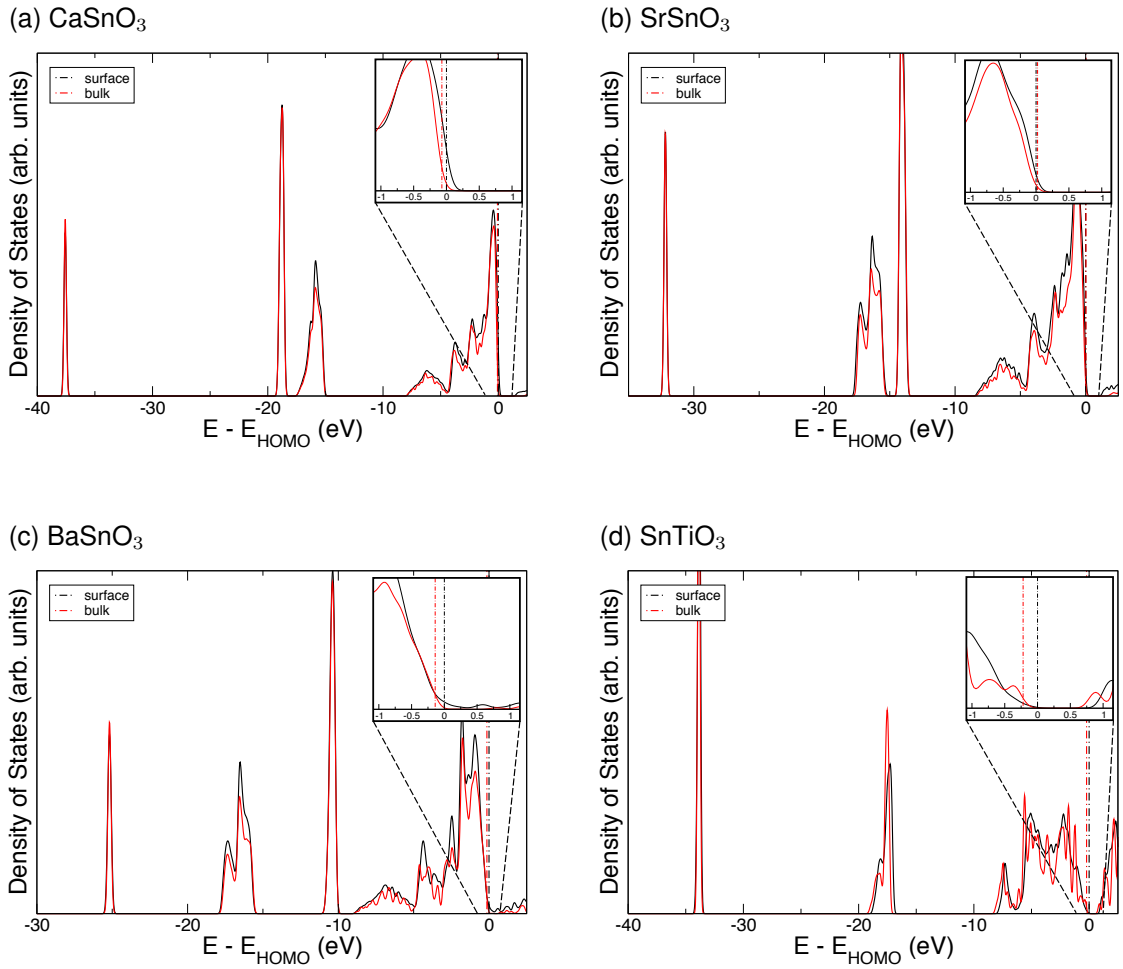

Figure 6.4: Alignment of the core states of the bulk and BO_2-terminated slab for a set of tin-based oxide perovskites. Density of states displaying the core states of bulk (a) $CaSnO_3$, (b) $SrSnO_3$, (c) $BaSnO_3$ and (d) $SnTiO_3$, obtained from first principles PBE calculations. The offset of the valence bands between the bulk and slab forms are seen, where the insets highlight the highest occupied molecular orbitals (HOMO). Energies are given relative to the surface HOMO.

6.7 Orbital analysis of surface states

The atom-summed orbital-projected density of states (PDOS) of the bulk systems, slab centres (all atoms in the slab excluding both surface layers) and slab surface layers for $CaSnO_3$, $BaSnO_3$ and $SnTiO_3$ are presented in Figure 6.5 for their bulks. In Figure 6.6, the PDOS for $SrSnO_3$ bulk structure, and PDOS for the slab centre and slab surface layers for both the $SrSnO_3$ clean slab and the $SrSnO_3|ZrO_2$ overlayer structures are presented.

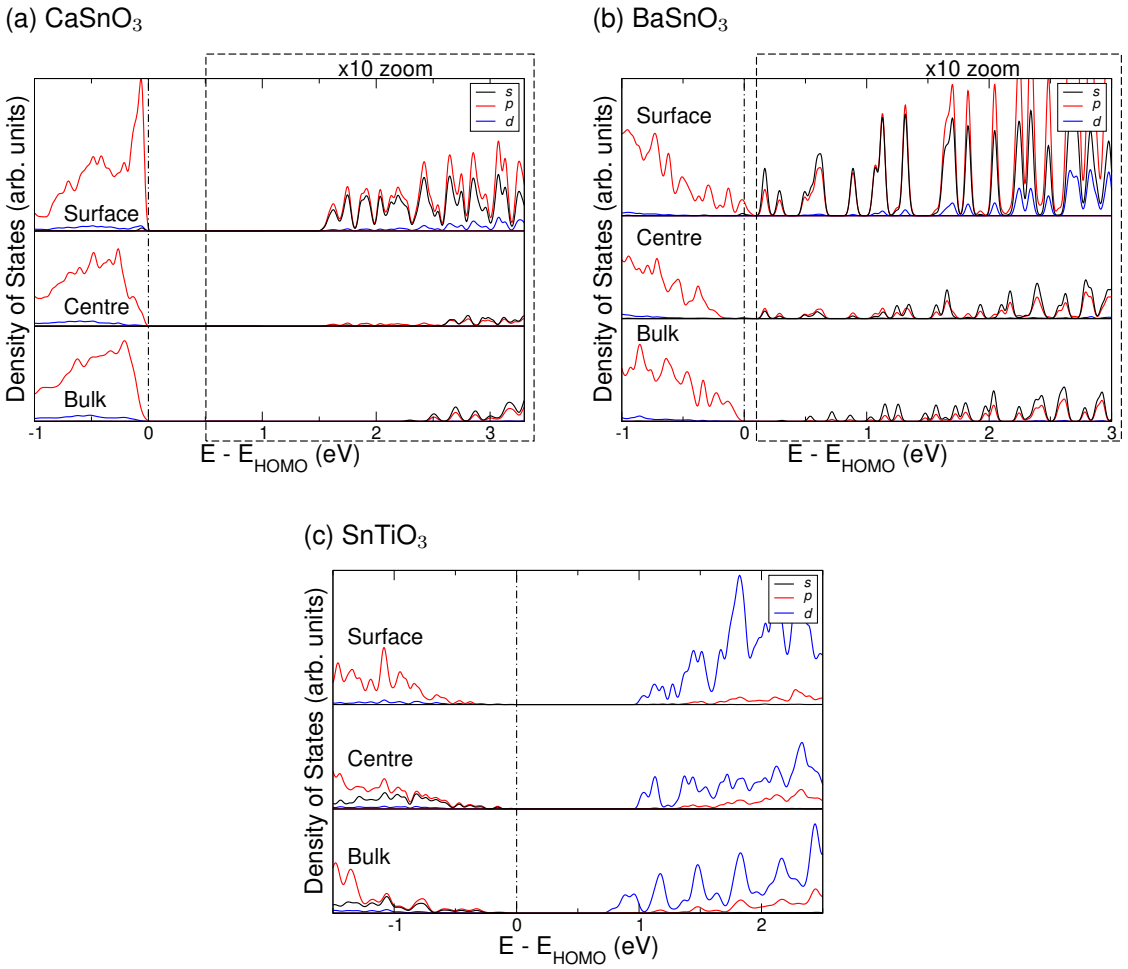

Figure 6.5: Orbital-projected density of states (PDOS) for (a) $CaSnO_3$, (b) $SnTiO_3$ and (c) $BaSnO_3$, obtained from first principles PBE calculations. Each figure shows PDOS for the bulk material, the centre of its surface-system and the BO_2 surface layer of its slab. Energies are given relative to each system's highest occupied molecular orbital (HOMO).

As seen in Table 6.2, the slab structures exhibit smaller band gaps (E_g) than their bulk counterparts. In the PDOS for $CaSnO_3$, $SrSnO_3$ and $BaSnO_3$, this reduction in E_g is found to be strongly associated with the surface states, with only minor bleeding of the states into the centre of the slab.

The orbital contributions of the slab centres are found to reproduce those of the bulk. The valence bands of $CaSnO_3$, $SrSnO_3$ and $BaSnO_3$ all see slight reconstruction in the slab, with most of the change localised to within 0.2 eV of the HOMO and no change in proportions of orbital contributions for either the slab-surface or the slab-centre. Slab-surfaces for these materials show greater re-

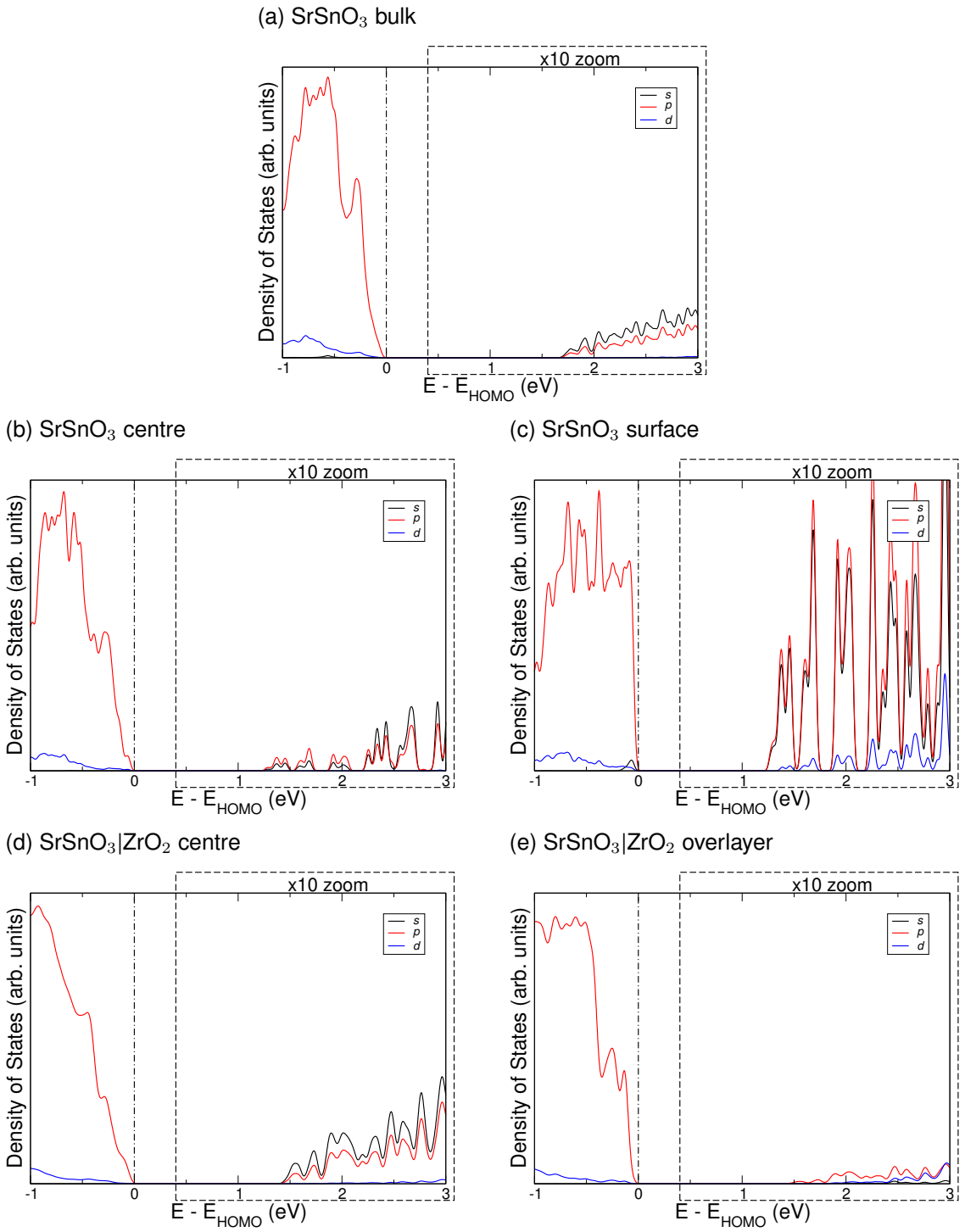

Figure 6.6: The orbital-projected density of states (PDOS) of (a) bulk $SrSnO_3$, (b) $SrSnO_3$ slab centre, (c) $SrSnO_3$ slab surface, (d) $SrSnO_3|ZrO_2$ centre and (e) $SrSnO_3|ZrO_2$ surface, obtained from first principles PBE calculations. The surface layer in (c) is referred to as the to BO_2 layer of the clean $SrSnO_3$ BO_2-terminated slab. Subfigure (e) refers to the entire overlayer of the $SrSnO_3|ZrO_2$ structure. Energies are given relative to the highest occupied molecular orbital (HOMO).

construction of the conduction band regions, represented as a swap from from s-majority in the bulk to p-majority at the surface. $SrSnO_3$, on the other hand, shows stronger change in the valence band region than the conduction band region, especially when it comes to orbital contributions.

The orbital-projected density of states for the $SrSnO_3|ZrO_2$ overlayer structure are presented in Figures 6.6d and 6.6e. Only minimal conduction band states are present at the surface below 3 eV, which is due to the larger band gap of ZrO_2. The slab-centre valence region more closely represents bulk $SrSnO_3$ than the $SrSnO_3$ slab-centre did. The slab-centre for this overlayer structure also shows much greater conduction band region agreement than the clean slab, when compared to the $SrSnO_3$ bulk.

6.7.1 Band alignment of the band gaps and the evolution reactions

The formation of a surface introduces surface states that drastically alter the electronic structure, leading to a large effective decrease in the band gap of these materials. This is shown in Figure 6.7, where the black bars indicate the band gap for each of the four bulk structures, whilst the red-shaded regions show the reduction of the gap due to the creation of a surface. In particular, we note that the formation of these surfaces significantly reduces the band gap via a lowering of the unoccupied states, which are mainly attributed to the Sn$5s$ states [386, 387]. This reduction can be significant enough to reduce the band gap below the 1.23 eV required to split water, as is the case with $BaSnO_3$, which has a band gap reduced from of 1.99 eV in bulk to 1.12 eV (see Table 6.2 for further numerical details of the band gap reductions).

In order for water-splitting to be viable at the surface, the band gap of the material should closely straddle the evolution potentials. As such, the alignment of the highest occupied molecular orbital (HOMO) and the lowest unoccupied molecular orbital (LUMO) with respect to the OER and HER, respectively, need to be considered. The alignments of the surface-systems are shown in Figure 6.7, with further numerical details found in Table 6.2. We show that the $BaSnO_3$ and $SnTiO_3$

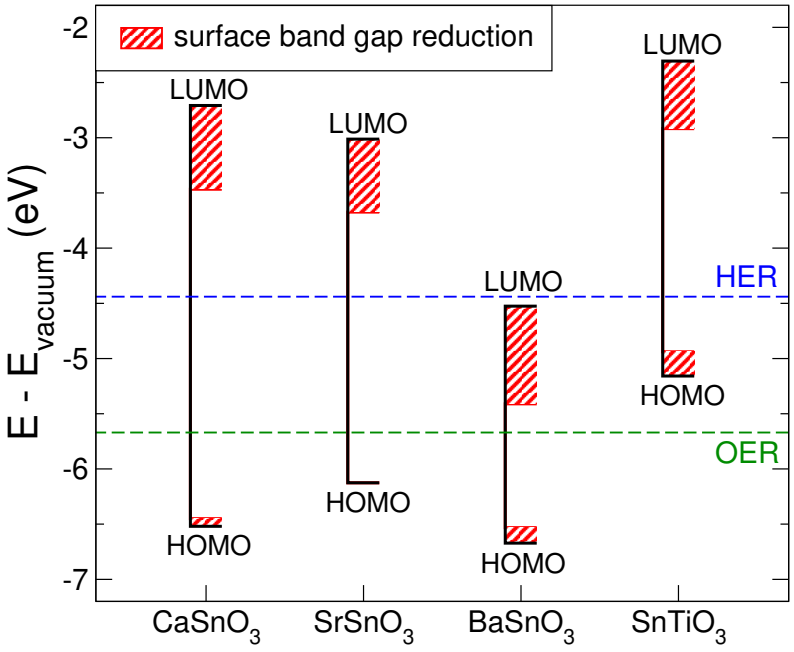

Figure 6.7: Comparison of the hydrogen/oxygen evolution reactions (HER/OER) with the bulk and surface band gaps for $CaSnO_3$, $SrSnO_3$, $BaSnO_3$ and $SnTiO_3$. The blue (green) dashed line indicates the HER (OER). The black bars denote the bulk band gap, with the red-hashed region highlighting their surface reduction. Energies are given relative to the vacuum energy. HOMO (LUMO) defines the highest occupied (lowest unoccupied) molecular orbital for each material. Hole affinities are obtained using PBE and band gaps are obtained using HSE06.

surface-systems do not straddle the reaction levels, with the LUMO of $BaSnO_3$ lying below the HER and the HOMO of $SnTiO_3$ above the OER. Hence, they are not ideal water-splitters and, instead, we will focus on $CaSnO_3$ and $SrSnO_3$.

6.7.2 Adsorptions

To better consider how the perovskite surfaces might behave in practical situations, we consider hydrogen atoms, oxygen atoms, HO groups, and HOO groups (separately) adsorbed to the surface, as these are the intermediates formed at the surfaces during the water-splitting process. Three potential adsorption sites were identified (see Figure 6.8). The HO and HOO groups energetically favour adsorption on the B-site (as also seen by Man *et al.* [376]), whereas the O adsorption is more favourable on the O-site. The most energetically favourable sites at each

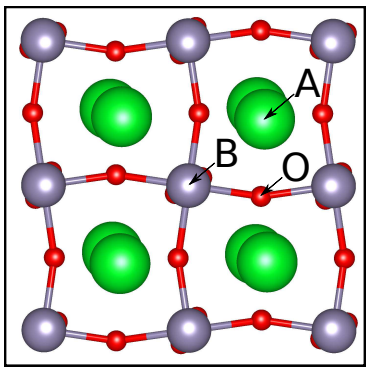

Figure 6.8: Ball and stick model depicting top-down view of an orthorhombic perovskite surface, where the three potential adsorption sites are denoted as A, B and O.

Table 6.5: Adsorption energies (ΔE_{ads}) of H, O, HO and HOO on the $SrSnO_3$ surface (in units of eV), obtained from first principles PBE calculations. The adsorption energies are obtained by comparing against the clean slab and the respective isolated molecule (1/2H_2 and 1/2O_2 in the case of H and O), $\Delta E_{ads} = E^{\mathrm{X}*}_{\mathrm{DFT}} - (E^{*}_{\mathrm{DFT}} + E^{\mathrm{X(isol)}}_{\mathrm{DFT}})$, where X is the adsorbate and $*$ denotes the surface.

Adsorption	ΔE_{ads}			
	$SrSnO_3$		$SrSnO_3$|ZrO_2	
	B-site	O-site	B-site	O-site
H	1.532	-1.120	–	-0.719
O	1.697	-0.013	-1.134	–
HO	-1.925	–	-3.082	–
HOO	-0.382	–	-0.741	–

step are used for the reaction pathways. As hydrogen adsorption is preferred on the O-site, we consider this site for the HER. See Table 6.5 for numerical values of adsorption energies (the definition of adsorption energy is detailed in Appendix G.5).

Figures 6.9a and 6.9b show the density of states for the $CaSnO_3$ and $SrSnO_3$ clean-surface systems (with a Figure 6.10a depicting an example clean-surface structure), and with hydrogen and oxygen adsorptions, with adsorptions introducing states into the band gap (Table 6.6). Whilst the addition of these states should not prevent $CaSnO_3$ and $SrSnO_3$ from being a viable water-splitter, the possibility

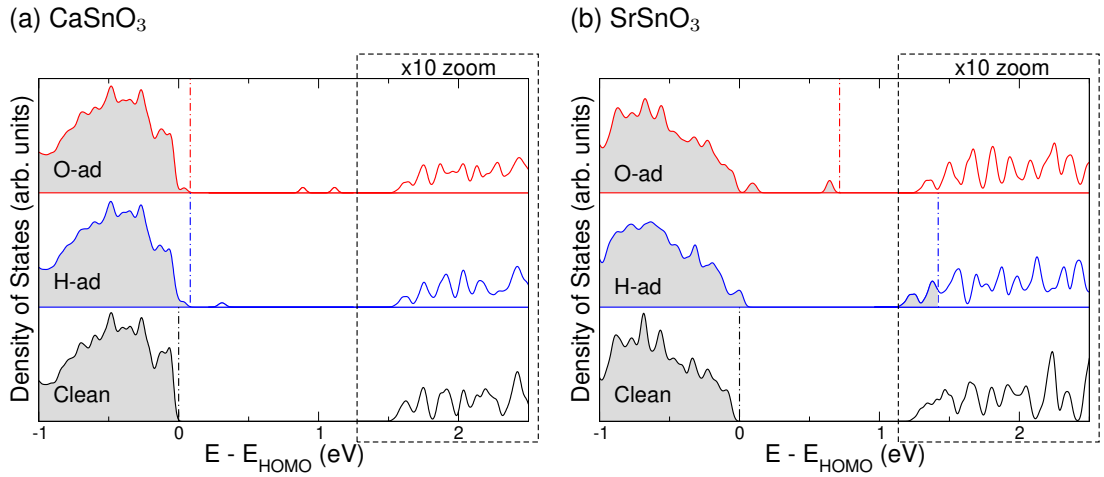

Figure 6.9: The density of states (DOS) for (a) $CaSnO_3$ and (b) $SrSnO_3$ systems, obtained form first principles PBE calculations. Black, blue and red lines indicate the DOS for the clean, hydrogen-adsorbed, and oxygen-adsorbed surface systems. Shaded regions indicates filled states, with the dash-dotted lines denoting the highest occupied molecular orbital (HOMO) of the individual system. The states within the dashed region are scaled by a factor of 10. The energies in each DOS are aligned using core states and given relative to the clean-surface HOMO.

for different excitation and recombination routes could reduce efficiency.

Simulations of O and H adsorptions starting on the A-site were found to be significantly less favourable than the B- and O-sites, and, as such, were not considered for later adsorptions. Due to the relative computational cost of HO* and HOO* adsorption calculations, only one adsorption site was fully relaxed for each. However, an initial set of geometric relaxation calculations were performed for the additions on each of the B- and O-sites, and the lowest energy of these structures were then followed up with more accurate geometric relaxations. For the HO* simulation, the adsorbate relaxed from the O-site back to the B-site. Whereas, in the case of the HOO* simulation, the adsorbate separated into an O adsorption on the O-site, leaving an unbound HO molecule in the vacuum gap, which was less energetically favourable than the HOO* adsorption on the B-site.

For the $SrSnO_3|ZrO_2$ system, only one adsorption site was fully relaxed for each adsorbate. However, initial sets of geometric relaxations are preformed for the adsorptions on both the B- and O-sites. After these initial relaxations, the most

Table 6.6: Details of changes to the electronic structure arising from surface adsorptions, obtained from first principles PBE calculations. All energies given with respect to the highest occupied molecular orbital at 0 eV. All $CaSnO_3$ defect states have the same spin, while all $SrSnO_3$ states are spin-independent. Here, (occ) and (unocc) are abbreviations of occupied and unoccupied, respectively.

Material	Adsorption State Details
$CaSnO_3$-H_{ads}	One state at 0.01 eV (occ), one state at 0.29 eV (unocc).
$CaSnO_3$-O_{ads}	One state at 0.02 eV (occ), two states at 0.89 eV and 1.11 eV (unocc).
$SrSnO_3$-H_{ads}	One state at 0.01 eV (occ), partially occupies first two conduction bands.
$SrSnO_3$-O_{ads}	Two states at 0.1 eV and 0.65 eV (occ).
$SrSnO_3$|ZrO_2-H_{ads}	No state in gap. Partially occupies the 1st conduction band state.
$SrSnO_3$|ZrO_2-O_{ads}	One state at 0.317 eV (occ).

energetically favourable site is focused on. All adsorbates for the oxygen evolution reactions (O, HO and HOO) were found to favour the B-site, whereas the H adsorption prefers the O site. Here, the B- and O-sites refer to the sites above the Zr and O surface atoms of the ZrO_2 overlayer, respectively.

The addition of defect states due to the surface adsorbates is seen in Table 6.6.

The free energy reaction pathways allow for the water-splitting capabilities of a material to be thoroughly explored. Figure 6.10c depicts the free energy changes associated with each step of the OER (Reactions 6.1-6.4) for both the $SrSnO_3$ surface and for the ideal water-splitter. For $SrSnO_3$, the Gibbs free energy changes of the steps are 1.74, 1.43, 1.95 and -0.20 eV, respectively. The HOO adsorption is found to be the rate limiting step, which is the case for oxides where oxygen binds strongly to the surface [376]. Hydrogen (0.75 eV) and oxygen (0.72 eV) overpotentials for $SrSnO_3$ are presented for a range of pH values (Figure 6.10d). The hydrogen overpotential extends beyond the surface LUMO for all pH, whilst the oxygen overpotential lies above the HOMO between $\mathrm{pH}\ 5$ and $\mathrm{pH}\ 14$.

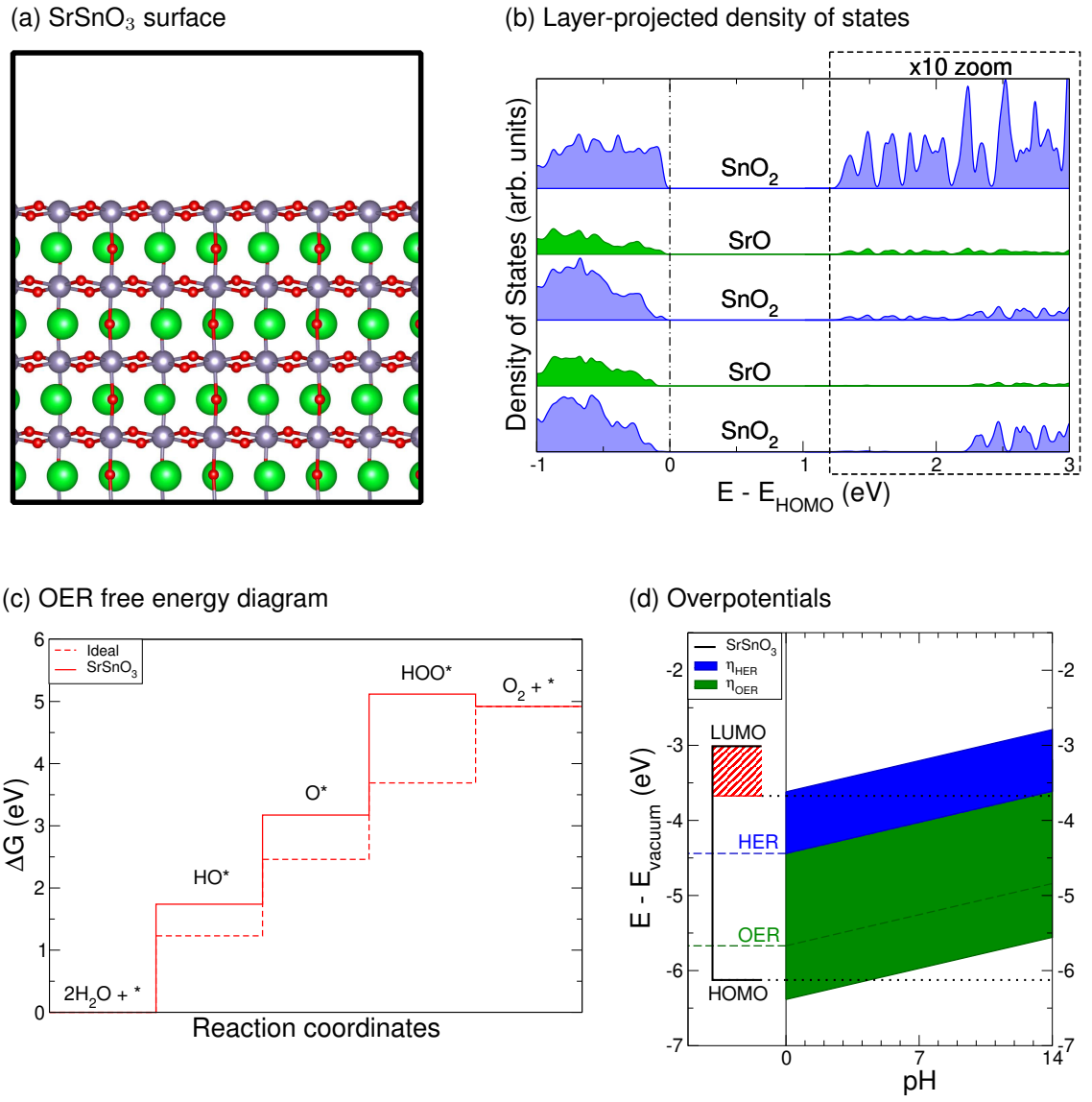

Figure 6.10: Electronic and energetic properties of the $SrSnO_3$ surface, obtained from first principles calculations. (a) Ball and stick model of the atomic structure and (b) layer-decomposed density of states for the $SrSnO_3$ slab (PBE result). Energies are given relative to the highest occupied molecular orbital (HOMO), the black dash-dotted line. The density of unoccupied states are scaled by a factor of 10. (c) Free energy diagram of oxygen evolution reaction (OER) performed on a $SrSnO_3$ surface (PBE result). (d) Hydrogen evolution reaction (HER) and OER overpotentials for a $SrSnO_3$ surface, given at 0 V versus the standard hydrogen electrode, and $\mathrm{pH}\ 0$ (PBE result). The band gap in (d) is calculated using HSE06.

Previously, Man *et al.* described a 3.2 eV difference between the HO* and HOO* steps for oxides [376]; we find a clear agreement for $SrSnO_3$, which has a value

of 3.38 eV. As such, we use this relation to identify the overpotentials for $CaSnO_3$ (see Appendix J). Both the hydrogen (1.77 eV) and the oxygen (1.20 eV) overpotentials are larger than those for $SrSnO_3$. Furthermore, the hydrogen overpotential of $CaSnO_3$ occurs at the same level as its LUMO, whilst, in $SrSnO_3$, it sits at the surface band edge – well below the bulk LUMO of $SrSnO_3$. As $SrSnO_3$ is shown to have a better alignment between its band gap and overpotentials, we now focus on this material.

6.8 Overlayers

Overlayers have seen interest for multiple reasons The use of overlayers to improve the photocatalytic properties of haematite, Fe_2O_3, has been studied in literature. However, there has been little focus on using overlayers on other materials to improve their water-splitting capabilities. Here, we explore the potential of overlayers to improve the capability of $SrSnO_3$ for photocatalysis. We choose to investigate overlayers for three reasons: 1) stabilisation of the surface adsorptions in order to reduce their overpotentials; 2) retain the bulk band gap of the oxide perovskite by suppressing the band gap reduction that occurs at the surface; 3) use a thin overlayer such that the photon absorption is still occurring in the perovskite slab. If these three objectives can be satisfied by an overlayer, then it should improve a material as a photocatalyst.

A set of lattice-matched oxide overlayers were added to the surface of $SrSnO_3$ using our in-house interface generator code, ARTEMIS (see Chapter 7). These overlayers (ZrO_2, TiO_2, Ta_2O_5, RuO_2 and SnO_2) were considered as each displays either strong stability in water, low overpotentials or desirable band alignments with respect to $SrSnO_3$ [314,345,376,388–394]. Of these, ZrO_2 was found to be the most favourable addition, with a surface formation energy of 0.03 eV/Å^2. The other considered oxides reduced the band gap below that of the clean surface, with the exception of Ta_2O_5, which was found to be unstable. The relaxed structure of the perovskite surface with a thin overlayer of ZrO_2 is shown in Figure 6.11a.

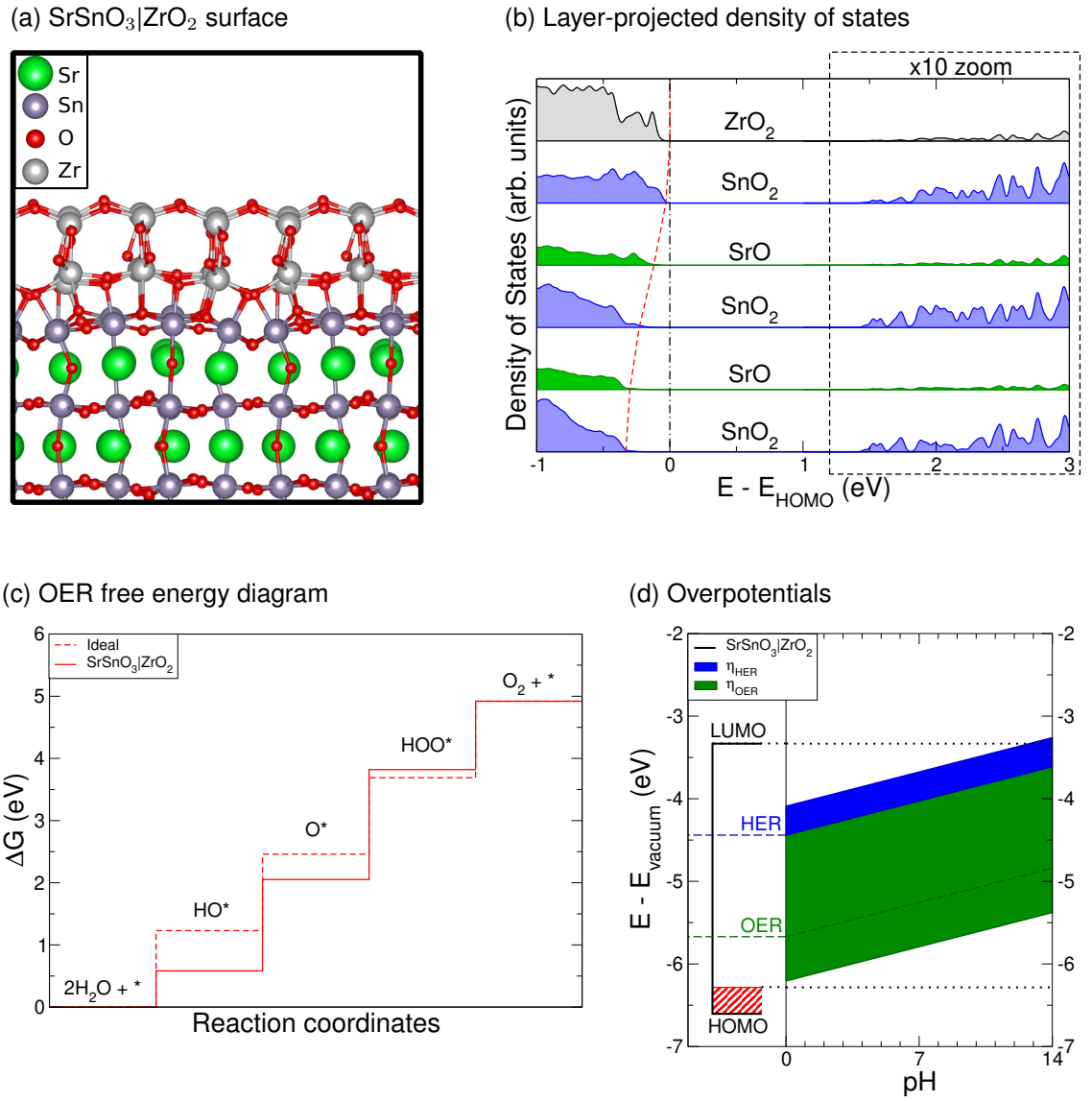

Figure 6.11: Electronic and energetic properties of the $SrSnO_3|ZrO_2$ surface, obtained from first principles calculations. (a) Ball and stick model of the atomic structure and (b) layer-decomposed density of states for a $SrSnO_3$ slab with a ZrO_2 overlayer (PBE result). The red dashed line denotes the band edge curvature of the highest occupied molecular orbital (HOMO) from the centre of the slab to the surface. Energies are given relative to the surface HOMO, black dash-dotted line. The density of unoccupied states are scaled by a factor of 10. (c) Free energy diagram of oxygen evolution reaction (OER) performed on a $SrSnO_3|ZrO_2$ surface (PBE result). (d) Hydrogen evolution reaction (HER) and OER overpotentials for a $SrSnO_3|ZrO_2$ surface, given at 0 V versus the standard hydrogen electrode, and $\mathrm{pH}\ 0$ (PBE result). The band gap in (d) is calculated using HSE06.

Figure 6.11b displays the layer-projected density of states (LPDOS) of the $SrSnO_3$ surface with a ZrO_2 overlayer. Comparing with Figure 6.10b, the inclusion of the overlayer is seen to suppress the band gap reduction seen for the perovskite surface, removing *s*-states and significantly reducing contributions from *p*- and *d*-states at the surface (Supporting Information). The unoccupied states of the coated surface also show far less reconstruction with respect to the clean $SrSnO_3$ surface. In addition, we see only minor variation in the LPDOS for the unoccupied states across the entire $SrSnO_3$ slab. The suppression of these surface states removes alternative decay paths that would otherwise hinder the efficiency of water-splitting. Further, a curvature arises in the valence band edge of 0.32 eV over 8.07 Å, which would manifest itself as an effective electric field across the catalyst, resulting in improved charge extraction.

The Gibbs free energy changes for the $SrSnO_3|ZrO_2$ are found to be 0.58, 1.47, 1.77 and 1.10 eV, respectively (Figure 6.11c). Here, the formation of the HOO* reactant is still the rate limiting step, indicating that the oxygen is still strongly bonded with the surface. Comparison between Figures 6.10d and 6.11d shows a reduction in the overpotentials, from 0.75 and 0.72 eV to 0.35 and 0.54 eV for hydrogen and oxygen, respectively. These are now straddled by the HOMO and LUMO of the $SrSnO_3|ZrO_2$ system for pH values between 0 and 12. With the improvement of the electronic properties, alongside the improvements to the reactivity with the various water-splitting adsorbates, $SrSnO_3$ with an overlayer of ZrO_2 offers great promise as a catalyst for the water-splitting process.

In this study, the overlayers are considered to cover the entire surface and to be very thin (4 Å). This overlayer is used to stabilise the surface's interactions and to suppress the surface band gap reduction (with the potential added benefit of increasing band edge curvature). For the real system to replicate these behaviours, it should be limited to a few nanometres to prevent the properties of the surface coating from dominating those of the perovskite. By being thin, it should appear as transparent to the incident light, thus still absorbing in the perovskite. Notably, such thin layers of ZrO_2 have already been experimentally realised [388, 395].

6.9 Summary

We present a first principles study of four oxide perovskites for photocatalysis. Though bulk band gap values of all candidates appear suitable for water-splitting, investigation of the surface properties reveals that both the LUMO of $BaSnO_3$ and the HOMO of $SnTiO_3$ are poorly aligned to the reaction potentials. Meanwhile, $CaSnO_3$ and $SrSnO_3$ maintain their ability to straddle the reaction levels. By extending the study to reaction pathways, we find that neither $CaSnO_3$ nor $SrSnO_3$ simultaneously straddle both their hydrogen and oxygen overpotentials. However, through inclusion of a ZrO_2 overlayer on $SrSnO_3$, we are able to reduce the hydrogen and oxygen overpotentials from 0.75 and 0.72 eV down to 0.35 and 0.54 eV, respectively. Also, the band gap of this system straddles both overpotentials for pH values between 0 and 12. This study demonstrates the importance of overlayers in water-splitting and presents $SrSnO_3|ZrO_2$ as a potential ideal candidate offering high efficiencies through means of lowering overpotentials and maintaining a suitable band gap, enabling simultaneous hydrogen and oxygen evolution. We believe this system, if fabricated, would be a leading candidate for bifunctional water-splitting.

Thus far, we have explored a set of core applications and interesting fields in which interfaces are found. The core physics relating to them has been studied. We shall, next, move onto discussing the fundamental theories underlying interface formation and will investigate where this can be taken to further interface structural prediction.

Chapter 7

ARTEMIS – *Ab initio* Restructuring Tools Enabling the Modelling of Interface Structures

“The interface is the device."

— Herbert Kroemer

7.1 Introduction

Here, we present ARTEMIS, a software package designed to produce a set of interface structures between two bulk materials. In this chapter, a current overview of the field of interface prediction methods is presented first. Next, we present our software package and detail its intended goals. A set of workflows are presented to describe the method used by the code to generate potential interfaces. The interface prediction method involves lattice matching and termination identification. The methods used by the program to identify interfaces within pregenerated interface structures is then detailed, showing how the code can be used for post-processing on the structure of an interface. The interface manipulation subroutines are then outlined, showing how the program can be used to probe interface alignment and intermixing. Finally, after a set of tests cases are presented to highlight the uses of the software package, a summary of the chapter is given.

7.2 Background

Two quotes are considered when discussing interfaces: 1) “Interface is the device” – H. Kroemer [396], who was emphasising how devices at their core are governed by the physics of the interface, and 2) “God made the bulk, the surface was invented by the devil” – W. Pauli [397], who was outlining the complexity and disorder that surfaces and hence interfaces possess. Hence, to understand a device one needs to understand the interface.

Heterostructures and metal-semiconductor interfaces display several unique features, such as Andersons- and Schottky-like band alignment [10, 14, 310, 398–400], thermal barrier effects [401–403], atomic reconstructions [404–407], and nanometre scale metamaterials [408, 409]. The modelling of these features is generally based upon atomic scale approaches, which require an accurate interface structure, or a close approximation, such that atomic simulations can find the ground state. However, the complexity of the interface is vast, due to the issues of lattice matching, surface termination, intermixing, the large size of the unit cells, poor initial guesses and reaction kinetics, which can be further hindered by unintended human biases. The electronic properties are sometimes considered using Anderson’s rule, but atomic scale physics and measurements have shown repeatedly that this rule is misapplied [16–18] and, therefore, to accurately predict the band alignment requires the interface structure. Similarly, thermal boundary resistance is governed by the structure and make up of the interface [401, 402]. Thus the need for an accurate atomic structure is great. In addition, interfaces can yield unique physical phenomena such as quantum wells, new material phases [32, 410, 411] and conductivity between insulators [6, 347], all of which require accurate modelling. All these issues are compounded by the fact that experimental characterisation of an interface is exceptionally difficult. The best characterisations, such as transmission electron microscopy [412, 413], X-ray-diffraction [414, 415], and others [416–418], can only provide hints as to the structure, the range of intermixing, and which surface reconstruction formed the interface.

7.2.1 Current approaches

The last 40 years have seen significant interest in methods to define, identify and consider the properties of interfaces and, in particular, for examining and calculating the most favourable interface between two materials. Starting in 1984, Zur *et al.* [84] presented a method of lattice matching that lay the foundation for subsequent methods [419–424]. Watson *et al.* [419, 420] developed METADISE to explore and identify energy minima for defects (dislocations, surfaces and interfaces), with a focus on surface energies. Raclariu *et al.* [421] implemented Zur's method for lattice matching and applied a nearest neighbour method to estimate the optimum position of the two materials with respect to each other. Mathew *et al.* [422] developed a series of scripts with capabilities to predict surface structures according to Wulff construction, and also match interfaces using Zur's lattice matching algorithm. Daniele and Jelver *et al.* [423, 424] implemented the method by Zur and extended it by introducing the elastic tensors of the two individual crystals in order to determine the energy cost of performing a lattice match. Whilst these methodologies involve lattice matching, little focus is placed on the surface stoichiometry of the materials at this interface and the potential diffusion of atoms across it.

Another approach to interface prediction involves random structure searches [425–427]. Von Alfthan *et al.* [425] developed an approach which randomly swapped atoms at a grain boundary of Si. This approach was expanded by Chua *et al.* [426], who developed a method for exploring grain boundaries, which involves hopping atoms from one site to another based on a genetic algorithm, creating permutations of the interface. The methodology put forward by Schusteritsch *et al.* [427] involves generating an interface and randomly moving the atoms within a region around the interface; the generated structures are then modelled using first principles methods in order to determine the most energetically favourable configuration. All of these approaches are promising, but currently limited to grain boundaries between two materials with matching stoichiometry, simply circumventing the need for lattice matching. The use of these methods allows for the modelling of the diffusion of materials across the interface, which cannot be captured by first principles relaxation methods alone (due to the large energy barriers

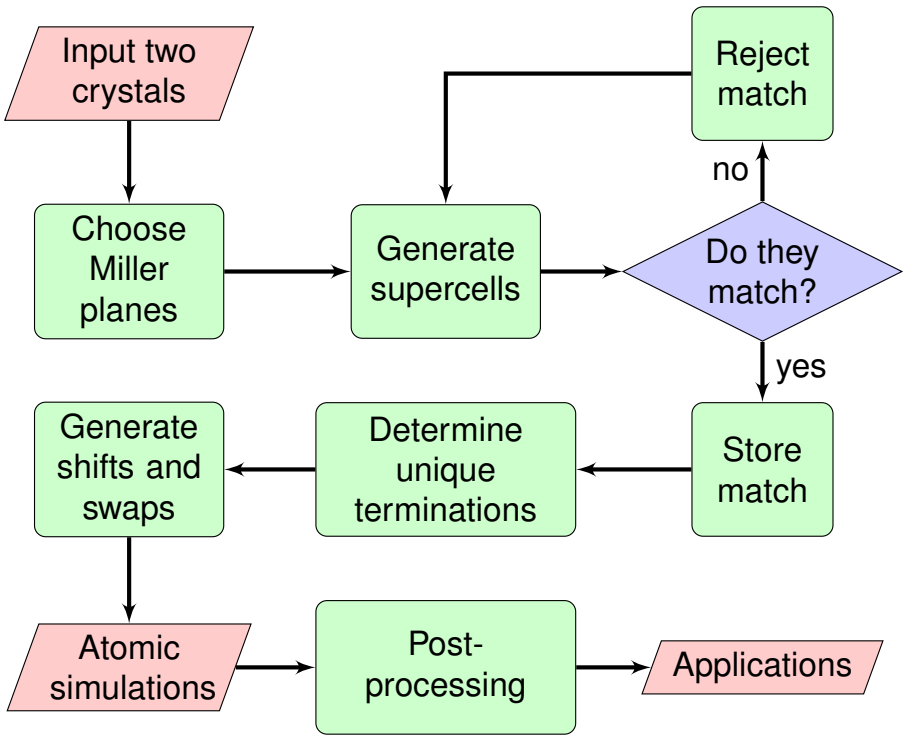

Figure 7.1: Workflow outlining the key stages of ARTEMIS.

involved in relaxing such a system).

There has been little focus on joining these two approaches of lattice matching and random-structure generation, mainly due to the significant number of systems that one would need to explore before finding the true interface for a pair of materials. The software package presented here attempts to go beyond these previous methods by fully exploring the surface stoichiometry of slabs, developing a method to more accurately predict the optimum position of two materials with respect to each other, and developing a methodology for investigating diffusion alongside the lattice matching method.

To the best of the author's knowledge, most of the interface generation software packages referenced here have stopped being updated and developed soon after their publication. As such, many of these methods stop at the lattice matching stage and go no further towards identifying the true interface.

7.3 ARTEMIS outline

The ARTEMIS software package generates interfaces as outlined in Figure 7.1. It takes two parents crystals and then considers a set of Miller planes over which to search for matches. On each plane, it generates supercells for both materials and determines whether they match each other, as detailed in Section 7.4. When successful matches are found, unique terminations of those Miller planes are used to generate interfaces. The two slabs of materials are then shifted (displaced) with respect to each other, both parallel and perpendicular to the interface, and in the process, a set of shifted interface structures are generated. Output structure files are then written for each configuration for use in atomic simulation software packages. The software also has the option to take in pregenerated interface structures and perform further shifts or intermixings on them. The goal of ARTEMIS is to aid users in the study of interfaces between any two materials. From the generated interfaces, one can use either empirical or *ab initio* software to refine the structure, rank the stability of the various potential interfaces by energy, and then calculate the desired properties. Implemented into ARTEMIS is also a system for estimating the optimum interface separation, a first step towards predictive interface generation.

The ARTEMIS software package is written in Fortran, using a set of default Fortran functions and in-house developed functions and subroutines and is developed to read and output crystal structure files in Quantum Espresso, CASTEP (.cell) and VASP (POSCAR, .vasp) structure file formats. Additional formats can be achieved by using tools such as VESTA [92].

The workflow for producing the interface structures follows a logical progression, allowing the user to modify settings as they wish. To aid in this, there is a built-in help function accessible via the use of flags. This help function details the possible tags for use in the software's input file. Furthermore, ARTEMIS can be run using flags, though the recommended method of running is using the input file.

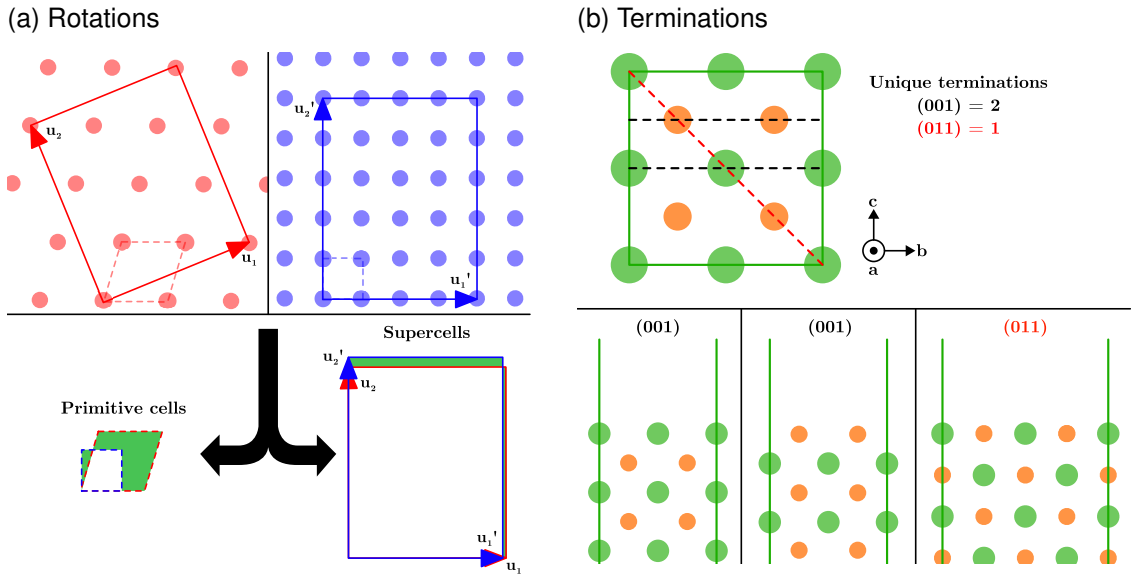

Figure 7.2: Schematics outlining two main stages of lattice matching. (a) Rotations (supercells) of two surfaces can lead to better matching and, hence, less strain. The top two panels depict the lattice of two crystal surfaces, along with the primitive and a supercell for each lattice. The bottom panel displays the poor matching (highlighted in green) of the two primitive cells and the better matching of the chosen supercells. (b) Potential surface terminations of the crystal for the (001) and (011) planes. The top panel shows the different potential cleavage planes. The bottom left and bottom middle panels depict the two unique surface terminations for the (001) Miller plane. The bottom right panel depicts the unique surface terminations for the (011) plane.

7.4 Lattice matching

In order to construct an interface between two crystals, one needs to consider how one would match the lattices of the two structures. The first objective is to create a set of interfaces between the two parent crystals that minimises the potential strain caused by mismatch between them. The second is to identify the interfaces with minimal supercell area so as to reduce the total number of atoms in each structure. This second objective allows for more feasible computational simulation of the structures using various atomic scale approaches.

Here, we outline the algorithms for lattice matching and how, within this routine,

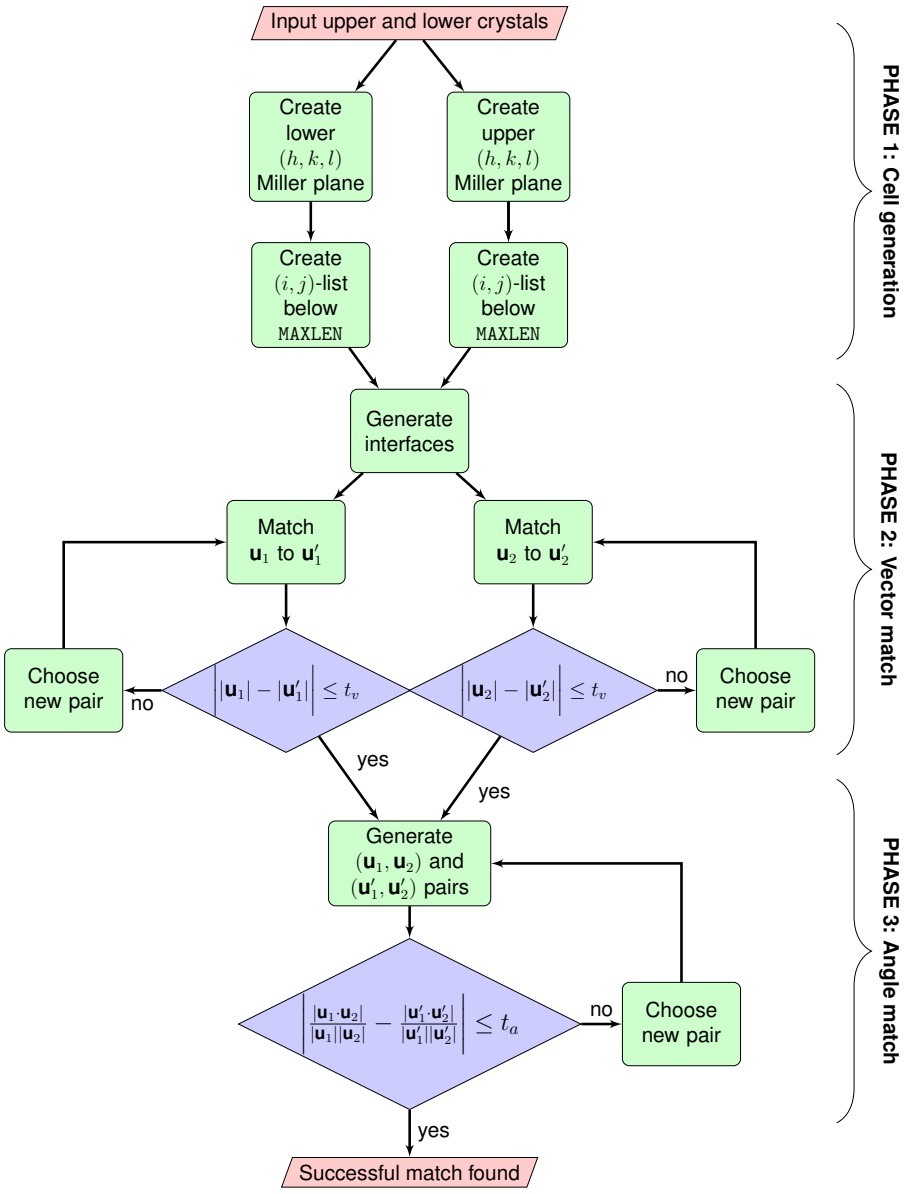

Figure 7.3: Workflow of the lattice matching method implemented in ARTEMIS. The method is split into three phases labelled cell generation, vector match and angle match. t_v and t_a correspond to the `TOL_VEC` and `TOL_ANG` input file tags, respectively.

Miller planes are generated, unique surface terminations are identified and vector matching is performed. A schematic of this can be seen in Figure 7.2a. The approach developed here for lattice matching is similar to that developed by Zur *et al.* [84] and Jelver *et al.* [424].

Figure 7.3 represents the workflow of the lattice matching method. We first define our two crystals, whose lattices are defined by lattice vectors $(\mathbf{a}_1, \mathbf{a}_2, \mathbf{a}_3)$ and $(\mathbf{a}'_1, \mathbf{a}'_2, \mathbf{a}'_3)$. Vectors relating to the upper crystal will be defined by a prime ($'$) in

this section, with all other vectors being related to the lower crystal. For both crystals, a set of Miller planes are generated to be tested for lattice matching (the user can specify the desired Miller planes if preferred). Planes are constructed such that (h, k, l) obeys the condition of $-10 \leq h, k, l \geq 10$. Symmetry operations of the crystals are then applied to their respective Miller planes in order to reduce these sets to the unique Miller planes. The two Miller plane sets are then cycled over, determining the primitive lattice vectors for each plane in turn.

To determine the primitive translation vectors of a specific Miller plane (h, k, l), we must first identify an arbitrary pair of vectors in the plane. To obtain these, we first reorder the Miller indices (h, k, l) such that they are in descending order of magnitude (m_1, m_2, m_3). A transformation matrix $\mathbf{M}$ is then generated,

$$\mathbf{M} = \begin{pmatrix} -m_2 & m_1 & 0 \\ -m_3 & 0 & m_1 \\ m_1 & m_2 & m_3 \end{pmatrix}. \tag{7.1}$$

The first two rows of the matrix will, when applied to the lattice $\mathbf{A}$, transform the first two lattice vectors, $\mathbf{a}_1$ and $\mathbf{a}_2$, onto the Miller plane. These rows (and, hence, the subsequent in-Miller plane vectors) must be the primitive translation vectors of the plane in order to find all available lattice points in-plane. To ensure this, the Lenstra-Lenstra-Lovász basis reduction method [428] (see Appendix K) is used to reduce the first two rows, resulting in the reduced transformation matrix $\mathbf{M}_{\text{red}}$. The order change that was applied to the Miller indices is now reversed on the transformation matrix by swapping the necessary columns in the transformation matrix such that the third row $\{m_1, m_2, m_3\}$ is now equivalent to (h, k, l).

Finally, the transformation matrix, $\mathbf{M}_{\text{red}}$, is then applied to the lattice $\mathbf{A}$ to obtain the primitive supercell lattice matrix $\mathbf{S}$, where the $\mathbf{c}$-face lies in the (h, k, l) Miller plane,

$$\mathbf{S} = \mathbf{M}_{\text{red}}\mathbf{A}. \tag{7.2}$$

The same method is then applied to the second crystal to obtain the lattice matrix $\mathbf{S}'$. The first two rows of the matrix $\mathbf{S}$ ($\mathbf{S}'$) are the shortest surface lattice vectors of

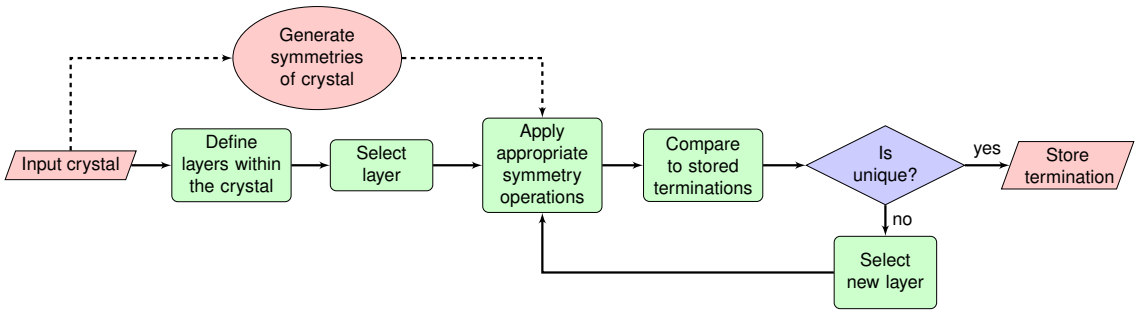

Figure 7.4: Surface identification workflow diagram. The process by which ARTEMIS identifies unique surface terminations.

the (h, k, l) Miller plane, $\mathbf{b}_1$ and $\mathbf{b}_2$ ($\mathbf{b}'_1$ and $\mathbf{b}'_2$). Using the two new lattice matrices S and S', we can perform lattice matching using the desired Miller planes.

For each Miller plane, integer quantities of the two surface vectors are then combined to generate a list of lattice vectors that span this plane (i.e. $\mathbf{u} = i\mathbf{b}_1 + j\mathbf{b}_2$). These lattice vectors are then generated with the condition $|\mathbf{u}| \leq$ `MAXLEN` (`MAXLEN`, default = 20 Å). The lists of lattice vectors obtained for the two parent crystals are then compared to find matching pairs of $(\mathbf{u}_1, \mathbf{u}'_1)$ and $(\mathbf{u}_2, \mathbf{u}'_2)$. These pairs are obtained when the magnitude of $\mathbf{u}_1$ ($\mathbf{u}_2$) matches the magnitude of $\mathbf{u}'_1$ ($\mathbf{u}'_2$) to within the user-defined tolerance (`TOL_VEC`, default = 5 %). The lists of lattice vector pairs defined above are then cycled through to find potential lattice matches. By joining two lattice vector pairs, it can be determined whether the angle between $\mathbf{u}_1$ and $\mathbf{u}_2$ matches that of $\mathbf{u}'_1$ and $\mathbf{u}'_2$ to within a tolerance defined by `TOL_ANG` (`TOL_ANG`, default = 1°). Pairs matching this criteria are then stored as a suitable lattice match. The set is then ordered by their vector and angular mismatch. A weighting is applied to favour matches of a smaller area, as such matches are more likely to be modellable. The user can define the number of most favourable lattice matches to be generated (`NMATCH`, default = 5).

7.5 Termination identification

A method is implemented in ARTEMIS to distinguish the atomic layers within each material (with respect to the surface plane) and thus allow for unique terminations to be defined. However, in doing so, non-physical surfaces can be generated and

care must be taken, especially for 2D materials.

In order to define unique surface terminations, we first need to specify what constitutes a *layer*. We define distinct atomic layers within a crystal as regions parallel to the chosen Miller direction that are separated by vacuum gaps of greater than LAYER_SEP (LAYER_SEP, default = 1 Å). This definition creates atomic layers appropriate to the chosen Miller direction, with the caveat that high atomic density regions remain grouped. Cleaving through such high-density regions is forbidden as this would be expected to result in a high cleavage energy (akin to cutting through a large number of bonds). Using this technique alone to create layers can result in two different layers being defined which are symmetrically equivalent. To determine if a layer is unique, we consider whether there exists a symmetry operation that matches the layer to another layer within the set (excluding mirror symmetries in the Miller direction); if a symmetry operation matches two layers in such a way, then one of these is discarded. From this set, the top atom for each of these layers is then defined as a unique surface termination. This process is performed for both crystals for each Miller plane being considered. The result is a set of unique surface terminations for each crystal. Figure 7.2b depicts potential terminations of a crystal structure based on the choice of Miller plane and the workflow can be seen in Figure 7.4.

The ideal end goal of the surface termination finding process is to generate two symmetrically equivalent interfaces. This is intended to prevent the creation of spurious electric fields and model a single unique interface per simulation. However, ARTEMIS does allow the user to create asymmetric interfaces if they wish. The initial thickness of each slab is defined by the number of symmetrically equivalent layers, perpendicular to the Miller plane, within the parent crystal. The user can define the number of equivalent layers to be contained within the lower (upper) slab using the parameter LW_SLAB_THICKNESS (UP_SLAB_THICKNESS).

Two notable exceptions to the surface termination process are allowed within ARTEMIS. Firstly, to account for layered materials, such as MoS_2, we include an input parameter LW_LAYERED. If LW_LAYERED (UP_LAYERED) is set to true, then only stoichiometric surface terminations are considered for the lower (upper) material. This prevents one from cleaving the constituent atoms within each layer of a van

der Waals structure, such as in transition metal dichalcogenides [429]. And secondly, when a material displays neither S_n nor C_{nh} symmetries [430] ($n = 1, ..., 6$) in the Miller plane, such as in the case of fresnoite (see Chapter 4), ARTEMIS will create two unique interfaces in the system and, therefore, users have the option to change the surface termination of each slab. This is done using the `LW_SURFACE` (`UP_SURFACE`) tags. These same parameters can be also be used for symmetric structures if the user wishes.

7.6 Interface identification

Both to examine existing structures that have been made by other users, and to allow reruns on existing interface structures, ARTEMIS includes a subroutine capable of reading a structure and identifying the interfaces within it. The code has the capability to perform interface manipulations (as outlined in Section 7.7) on pregenerated interface structures. To begin with, we define the direction perpendicular to the interface as the 'interface direction'. To locate the interfaces in the pregenerated structures, ARTEMIS identifies the interface direction using a process we name DON and the location of the interfaces along this axis are identified using CAD. These two processes are discussed below.

7.6.1 DON - Density of Neighbours

In order to determine the interface direction, correlation functions are employed to determine the axis of greatest dissimilarity. To do so, we start by generating a species-dependent density of neighbours (sDON). The DON is an angle-independent description of the distance of atoms akin to the nearest neighbour profile used to characterise amorphous materials [239] and Figure 7.5a gives a visual description of how it works. For each atom in the structure, a DON is generated in order to describe their local environments. The sDON and DON are given

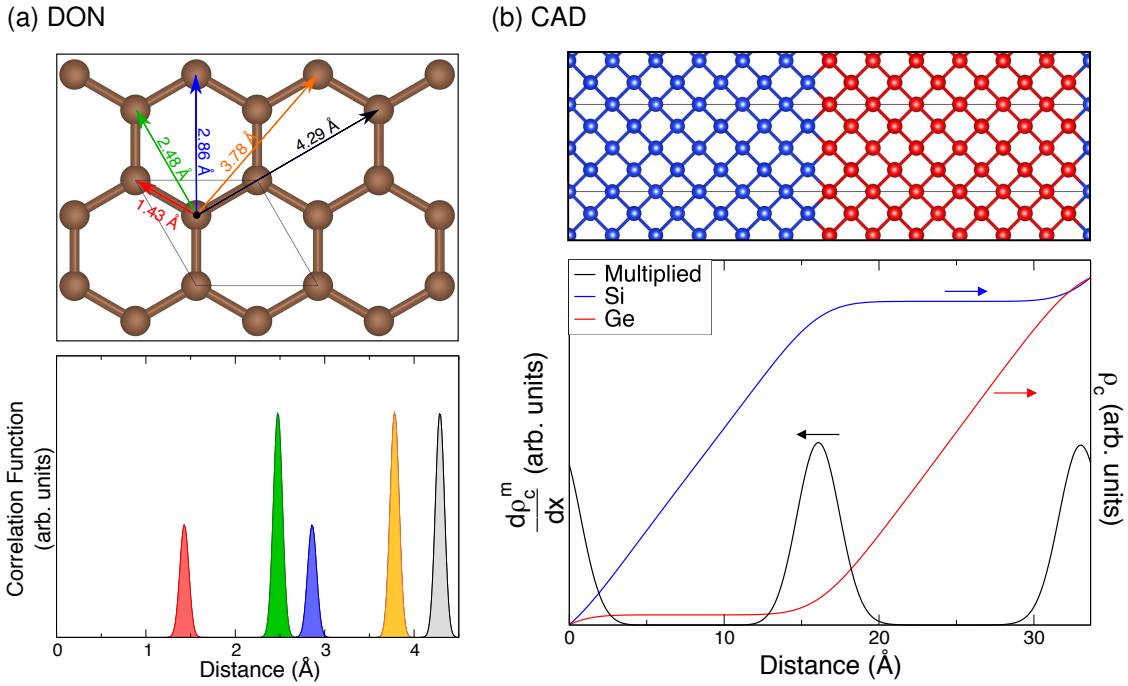

Figure 7.5: The two methods implemented in ARTEMIS for interface identification. (a) Density Of Neighbours (DON), with a graphene monolayer used as an example. The top panel shows a ball and stick model of the structure, with the five shortest unique bond lengths labelled. Bottom panel displays the radial distribution of bond lengths as Gaussian peaks, where the height of the peak relates to the number of that bond length present. (b) Cumulative Atomic Density (CAD), with an Si|Ge interface used as an example. The top panel shows a ball and stick model depicting Si|Ge interface atomic structure. The bottom panel graph plots the species-dependent cumulative atomic density (ρ_c) and its derivative ($d\rho_c^m/dx$). The arrows on the graph indicate which data relates to which axis.

$$\text{sDON}_{s,i}(p,\Delta r) = \sum_{j}^{n_{\text{atom},p}} \exp\left(-\frac{(\Delta r - |\mathbf{r}_{s,i} - \mathbf{r}_{p,j}|)^2}{2\sigma^2}\right), \tag{7.3}$$

$$\text{DON}_{s,i}(\Delta r) = \sum_{p}^{n_{\text{spec}}} \text{sDON}_{s,i}(p,\Delta r), \tag{7.4}$$

where $\mathbf{r}_{s,i}$ and Δr are the location of and distance from atom i in species s, respectively. n_{spec} is the total number of species in the system, $n_{\text{atom},p}$ defines the number of atoms associated with species p, and $\sigma = 0.05$ Å. The sDON of each

atom is then compared with all the other atoms in order to determine the *similarity* of that one atom to the rest of the structure (with a heavier weighting placed on the atoms nearby, offering a description for the similarity of the local environment). We define this similarity, sim, as

$$\text{sim}_{s,i} = \sum_{x}^{x_{\text{cutoff}}} \sum_{j}^{n_{\text{atom},s}} \text{mDON}_{s,i,j}(x) \exp\left(-\frac{|\mathbf{r}_{s,i} - \mathbf{r}_{s,j}|}{r_0}\right), \tag{7.5}$$

where $x_{\text{cutoff}} = 4$ Å, $r_0 = 1$ Å and

$$\text{mDON}_{s,i,j}(\Delta r) = \sum_{p}^{n_{\text{spec}}} \min\Big(\text{sDON}_{s,i}(p, \Delta r), \text{sDON}_{s,j}(p, \Delta r)\Big). \tag{7.6}$$

Then we compare the range of these similarity values associated with each axis and define this range as the *dissimilarity coefficient*,

$$\text{dissim}_{\alpha} = \max\Bigg(|\text{sim}_{s,i} - \text{sim}_{s,j}|\, f\left(\mathbf{r}_{s,i}(\alpha) - \mathbf{r}_{s,j}(\alpha)\right) \Bigg)_{s,i,j}, \tag{7.7}$$

with

$$f(x) = \begin{cases} 1, & |x| \leq 1 \text{ Å} \\ 0, & \text{otherwise}, \end{cases} \tag{7.8}$$

where $\alpha = 1, 2, 3$ refers to the $\mathbf{a}_1'', \mathbf{a}_2'', \mathbf{a}_3''$ axes, respectively. The dissimilarity is associated with planes normal to a given axis. For each axis α, the function $f(x)$ is used to constrain similarity value comparisons to atoms within 1 Å along the α axis of each other whilst disregarding the atoms' other axes coordinates. As such, the *dissimilarity coefficient* for an axis is defined by the plane with the largest dissimilarity. Hence, for all axes other than the interfacial axis, this check will result in a large dissimilarity and, therefore, the axis with the smallest *dissimilarity coefficient* determines the interface direction, defined as β. Having determined the interfacial axis, the locations along this axis relating to the two interfaces need to be identified.

7.6.2 CAD - Cumulative Atomic Density

After having defined the interface direction (β), we now need to determine the interface location along that axis. The use of this method can be seen in Figure 7.5b. Firstly, the species-dependent cumulative atomic density profile (CAD) for the interfacial axis is calculated from

$$\mathrm{CAD}_\beta(s, \Delta r_\beta) = \sum_{x=0}^{\Delta r_\beta} \sum_{i}^{n_{\mathrm{atom},s}} \exp\left(-\frac{(x - r_{\beta,s,i})^2}{2\sigma^2}\right), \tag{7.9}$$

where $\sigma = 2$ Å, $r_{\beta,s,a}$ is the β^{th} element of the position vector of atom$_{s,a}$ and Δr_β defines the position along the β^{th} axis. The derivative at each point is then determined for each species. Finally, all of the species-dependent cumulative atomic density derivative profiles are multiplied together and the two greatest maxima of this function are defined as the two interfaces of the system (as the structures are periodic, two interfaces are present in a cell).

$$\mathrm{multiCADD}_\beta(\Delta r_\beta) = \left| \prod_{s}^{n_{\mathrm{spec}}} \frac{d}{dx} \mathrm{CAD}_\beta(s, \Delta r_\beta) \right|. \tag{7.10}$$

The CAD process identifies the two interfaces within the cell as the two locations with greatest $\mathrm{multiCADD}_\beta(\Delta r_\beta)$. The location of these interfaces along the interface direction are stored as $x_{\mathrm{intf},1}$ and $x_{\mathrm{intf},2}$. This method works for nearly all interfaces with the exception of planar defects where the material effectively has a stacking fault.

7.7 Interface manipulation

Matching two crystals' lattice vectors is the first stage of making an interface. However, as discussed previously, many other factors need to be considered. Chief among these are sources of stress in the structure. These can originate from the misalignment of the two materials, or from broken bonds or a lack of intermixing across the interface. In this section, we outline the various methods

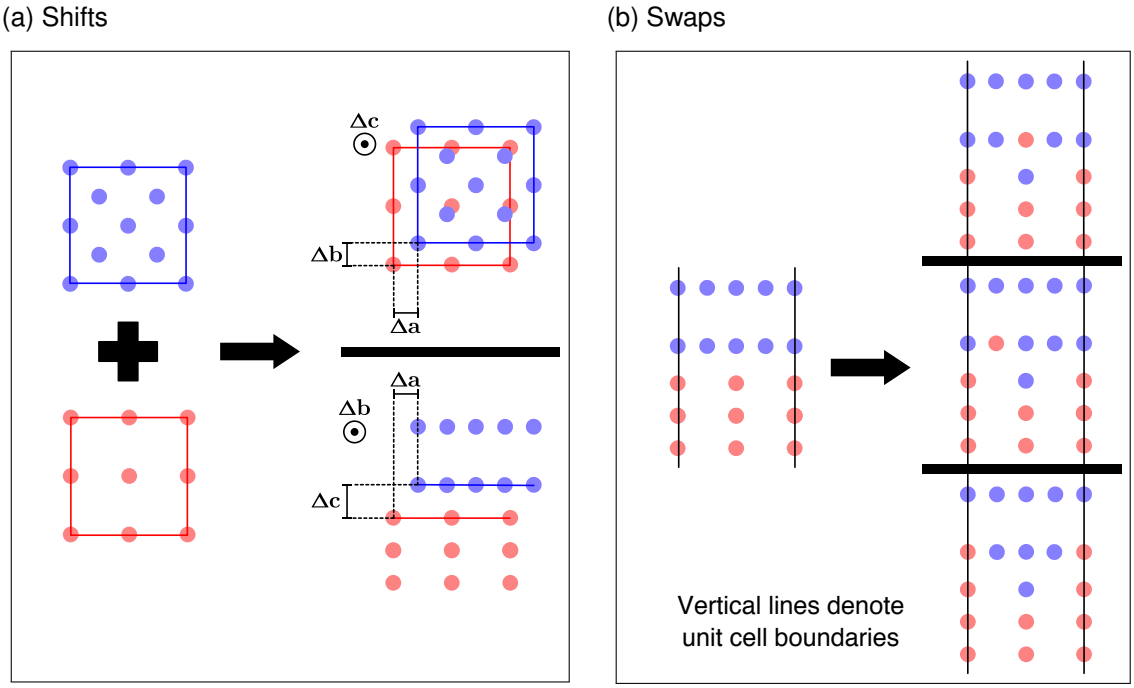

Figure 7.6: Schematics outlining shifting (alignment) and swapping (intermixing) used to relieve interface strain. (a) Shifts: the left panel shows two crystal surfaces. The top right panel depicts the shifts in the interface plane, whilst the bottom right panel highlights shifts parallel to the interface direction. (b) Swaps: the left panel depicts a non-intermixed interface. The three unique swap structures are shown in the right panel as top, middle and bottom, with the structures being separated by the bold black bars. The vertical black lines denote the boundaries of the unit cell; as such, any atoms lying on a black line are repeated on the opposite black line.

available within ARTEMIS to generate structures with different interface alignments (shifts) and to include atomic diffusion (in the form of atomic swaps). These structures are generated so that the user can examine the energy space dependence on these factors and assess the various interfaces and their favourability.

7.7.1 Shifting

We define the shifting of material A with respect to material B as the *interfacial alignment*. Interface alignment is the first step in reducing stress. When determining shifts, it is important to consider the bonds that have been cleaved through in order form a surface from a crystal. Here, these *cut* (broken) bonds are termed

as missing bonds. Having matched lattice vectors, one needs next to consider the correct alignment of the basis of the two separate structures in order to best accommodate for these missing bonds at the interface. A depiction of interfacial alignment can be seen in Figure 7.6a.

A set of methods are available in ARTEMIS to manipulate interface alignment via generating and performing sets of shifts, δ. A shift is defined as a displacement of one surface with respect to the other. These methods are selected using the ISHIFT tag. ISHIFT = 0 allows for user-defined shift values, 1 uses random shifts, 2 matches the average interfacial bond to the two materials' bulk bonds and 3 and 4 attempt to predict a set of descriptive bonds. In particular, ISHIFT = 3 and 4 represent ARTEMIS at its most comprehensive, generating a set of interfaces with different shift values. The number of shifted structures generated per lattice match is determined by NSHIFT (NSHIFT, default = 5).

ISHIFT = 0 allows the user to specify the tag SHIFT = a b c, where a, b and c are the manual shifts defined by the user and each can be any real number.

ISHIFT = 1 creates NSHIFT number of random shifts of the interface structure.

ISHIFT = 2 ensures that the average minimum separation between atoms either side of the interface best matches to the mean of the two parent crystals' averaged bond lengths.

ISHIFT = 3 begins using the ISHIFT = 2 methodology and then produces a set of NSHIFT shifts parallel to the interface plane, whilst maintaining its interfacial separation (the spacing parallel to the interface direction). By fixing the interface separation to that determined by ISHIFT = 2, a new set of shifts (parallel to the interface) are generated that allow for the average interface bond to most and least match to the average bulk bonds (best, worst, second best, second worst, etc.). These sets of shifts are intended to be descriptive of the energetic space of potential interface shifts, which allows the user to determine how drastically the energy can change depending on the alignment for chosen systems.

ISHIFT = 4 is a method of shifting which attempts to match the bond lengths across the interface to the missing bulk bond lengths of the surface atoms. By de-

termining the shortest missing bond of the surface atoms of each crystal (and the number of those bonds missing for each of them), the opposite crystal's structure can be used to supplement these absent bonds. This is similar to the broken-bond rule for metal surfaces, which assumes that the cleaving energy is directly related to the number of broken bonds for the metal's surface. Thus our method here assumes that the most energetically favourable alignment of two surfaces is to compensate for the highest number of missing bonds [431, 432].

To determine the missing bonds for `ISHIFT` = 4, we generate, for each individual atom within each component slab, a DON. We then subtract the individual DONs from their Wyckoff bulk counterparts (i.e. symmetrically equivalent bulk counterparts). This produces a nearest neighbour profile which highlights the missing bonds of each atom. These missing bonds are characterised by both their bond length and the number of such missing bonds. We then store the value of the shortest missing bond for each atom for later reference, where the shortest bond of an atom must be smaller than `MBOND_MAXLEN` (`MBOND_MAXLEN`, default = 4 Å).

Next, the two slabs are placed on top of each other such that the top of the lower slab's surface and the bottom of the upper slab's surface occur at the same point (i.e. zero separation). No initial shift is applied either parallel or perpendicular to the interface plane. In order to determine a set of suitable shifts, the code evaluates a bond ideality factor, $D_{\mathbf{s}}$, for each possible shift (δ) and generates `NSHIFT` number of structures using the shifts with the smallest bond ideality factors. In the case of a perfectly matching interface, the bond ideality factor has a value of 0. The value of $D_{\mathbf{s}}$ is given as

$$D_{\boldsymbol{\delta}} = d_{\boldsymbol{\delta},lu} + d_{\boldsymbol{\delta},ul} \tag{7.11}$$

where

$$d_{\boldsymbol{\delta},lu} = \sum_{m}^{l} \left[\left| N_m - \sum_{n}^{u} f(|\mathbf{r}_m + \boldsymbol{\delta} - \mathbf{r}'_n| - b_m) \right| + \sum_{n}^{u} g\left(\frac{|\mathbf{r}_m + \boldsymbol{\delta} - \mathbf{r}'_n| - b_m}{b_m} \right) \right]. \tag{7.12}$$

$d_{\boldsymbol{\delta},lu}$ quantifies how well slab u compensates for the missing bonds in the surface of slab l, which is generally distinct from $d_{\boldsymbol{\delta},ul}$. Here, l and u are the sets of missing bonds for atoms from the lower and upper slabs, respectively. N_m is the total number of missing bonds for atom m, $\mathbf{r}_m$ is the location of atom m and $\mathbf{r}'_n$ is the location of atom n. b_m is the length of the missing bond for atom m. We also include a pair of weighting functions,

$$f(x) = \frac{1 - \tanh(9(|x| - 1/4))}{2} \tag{7.13}$$

and

$$g(x) = \begin{cases} \frac{8}{3}|\tan(\pi x/2)|, & x < 0 \\ 0, & \text{otherwise}, \end{cases} \tag{7.14}$$

where the $f(x)$ function weights the set of shifts towards ones that compensate for the surface atoms' missing bonds, whilst $g(x)$ helps to prevent shifts that place atoms too close to one another. The specific forms of these two functions are used in order to satisfy the three following conditions. Firstly, $f(x)$ and $g(x)$ should be at their maximum and minimum, respectively, when a bond across the interface perfectly matches the missing bond length. Secondly, $f(x)$ should decrease with increasing disagreement between the interface bond and missing bond lengths. Finally, $g(x)$ should tend towards infinity when an interface bond approaches 0.

To further validate this approach, `ISHIFT = 4` can be used between two identical bulk crystals. This methodology identifies appropriate shifts to reproduce a crystal's bulk bonds (to within 0.1 Å) across the interface and has been tested on numerous bulks containing either single or multiple species.

7.7.2 Intermixing

In order to enable exploration of diffusion across the interface, sets of structures are generated in which atoms from either material are intermixed (swapped), as demonstrated in Figure 7.6b. Intermixing is introduced to serve three main pur-

poses. Firstly, we previously observed [405] that the intermixing both reduces strain and produces interface structures more favourable than the initial abrupt boundary model. Secondly, by introducing disorder, it allows for interfaces involving more elaborate reconstructions to be explored, such as the GaAs β(2×4) surface [433,434]. Finally, such intermixing allows one to model grain boundaries, such as those considered by von Alfthan [425] and Schusteritsch [427].

The concentration of intermixing is governed by the SWAP_DENSITY tag (units of Å^2) and the number of uniquely intermixed structures generated per shift is determined by NSWAP. Each set of swaps in a structure is generated randomly, excluding symmetrically equivalent swaps. New swaps are performed until the SWAP_DENSITY has been reached. By default, intermixing is turned off (ISWAP = 0). To turn on random intermixing, set ISWAP = 1. To use the physics-based swapping procedure, set ISWAP = 2.

ISWAP = 1 is a purely random swapping routine, based upon the user specifying a depth (SWAP_DEPTH, default = 3 Å), and the swapping density (SWAP_DENSITY, default = 0.05 Å^2). ARTEMIS then randomly swaps atoms either side of the interface to create a more graded interface.

ISWAP = 2 is based upon the observation [405] that the amount of intermixing exponentially decays with distance. As such, we use the following function to weight the chance of swapping:

$$s(x) = \exp\left(-\frac{x - x_{\mathrm{intf}}}{2\sigma_{\mathrm{swap}}^2}\right), \tag{7.15}$$

where x_{intf} is the location of the interface and σ_{swap} defines the decay of the probability of atoms further from the interface being swapped (SWAP_SIGMA, default = 0.05 Å). This function mimics the behaviour seen in reference [405] by selecting atoms to swap with an exponential weighting towards those closer to the interface.

For a system where the two interfaces are symmetrically equivalent, any swaps performed across one interface are then mirrored to the opposite interface. In doing so, each generated structure still has two interfaces in the unit cell, with those two interfaces still being symmetrically equivalent. In doing so, this will

(a) $BaTiO_3$ (001) (b) $CaCu_3Ti_4O_{12}$ (121)

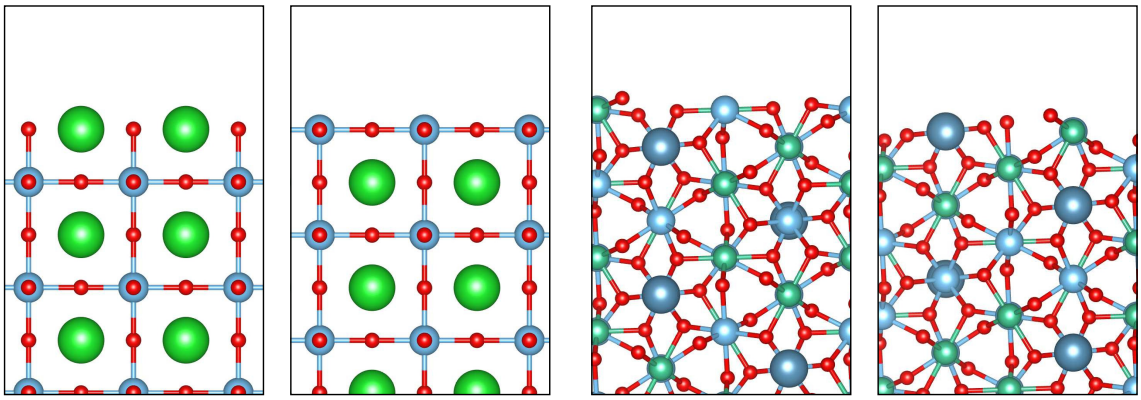

Figure 7.7: Ball and stick models depicting the two unique surface planes as identified by ARTEMIS for the (a) $BaTiO_3$ (001) Miller plane and (b) $CaCu_3Ti_4O_{12}$ (121) Miller plane.

prevent the introduction of spurious electric fields into the system.

7.8 Test cases

7.8.1 Surface terminations

Using the `LSURF_INFO` tag, users can get the surface terminations of the lower (upper) parent crystal along the Miller plane specified by the `LW_MILLER` (`UP_MILLER`) tag. The surface is generated using the 1×1 unit cell reconstruction with the shortest lattice vectors on that plane. The number of symmetrically equivalent layers in the lower (upper) slab is specified using the following tag: `LW_SLAB_THICKNESS` (`UP_SLAB_THICKNESS`).

The surface termination identification method used in ARTEMIS has been tested on a large set of structures. In Figure 7.7, the unique surfaces identified by ARTEMIS are shown for $BaTiO_3$ and $CaCu_3Ti_4O_{12}$ for the (001) and the (121) Miller planes, respectively. For all of the test cases, ARTEMIS generates the surfaces using the smallest lattice vectors parallel to the surface.

For the (001) Miller plane, the $BaTiO_3$ crystal is shown to have two unique sur-

faces – the AO-rich and the BO_2-rich surfaces (where a perovskite's chemical formula is given as ABO_3). These are the two most common surfaces of perovskites, with the BO_2 being the most commonly studied [379, 380, 435–438].

In the case of examples similar to the $CaCu_3Ti_4O_{12}$ (121) Miller plane, more care needs to be taken. As can be seen in Figure 7.7b, surface terminations are less clearly identifiable and, as such, defining surfaces is more difficult. Still, two unique surface terminations are identified, with these being chosen due to possessing the largest interplanar spacing.

Surface terminations have been generated for the two-atom primitive cell of silicon using the (101) Miller plane. It is found to properly identify the well-known surface (001) termination with the [110] and $[1\bar{1}0]$ in-plane lattice vectors [439–441].

7.8.2 Interface identification

Interface identification is tested on a set of sample structures as shown in Figure 7.8. As can be seen, ARTEMIS identifies the interface in all cases. These four interface structures are used to exhibit different structural features an interface may have (only the $CaCu_3Ti_4O_{12}$|CuO structure has been relaxed, all others are generated examples for testing). The Si|Ge system is used as an example of structurally identical regions that differ only by species. The graphite|TiO_2 system shows an interface between 2D layered and a 3D bulk crystals. The $CaCu_3Ti_4O_{12}$|CuO system demonstrates a chemically diverse and disordered interface. Finally, the graphite|diamond interface demonstrates a transition between two phases of the same material. In each structural scenario, the interface is successfully identified.

7.8.3 Shifting

Here, the `ISHIFT` = 4 interface alignment setting is tested and presented on three 2D layered|3D bulk (Figure 7.9a) and two 3D bulk|3D bulk (Figure 7.9b) interface structures. To test this method, we generate a set of 20 interface separations

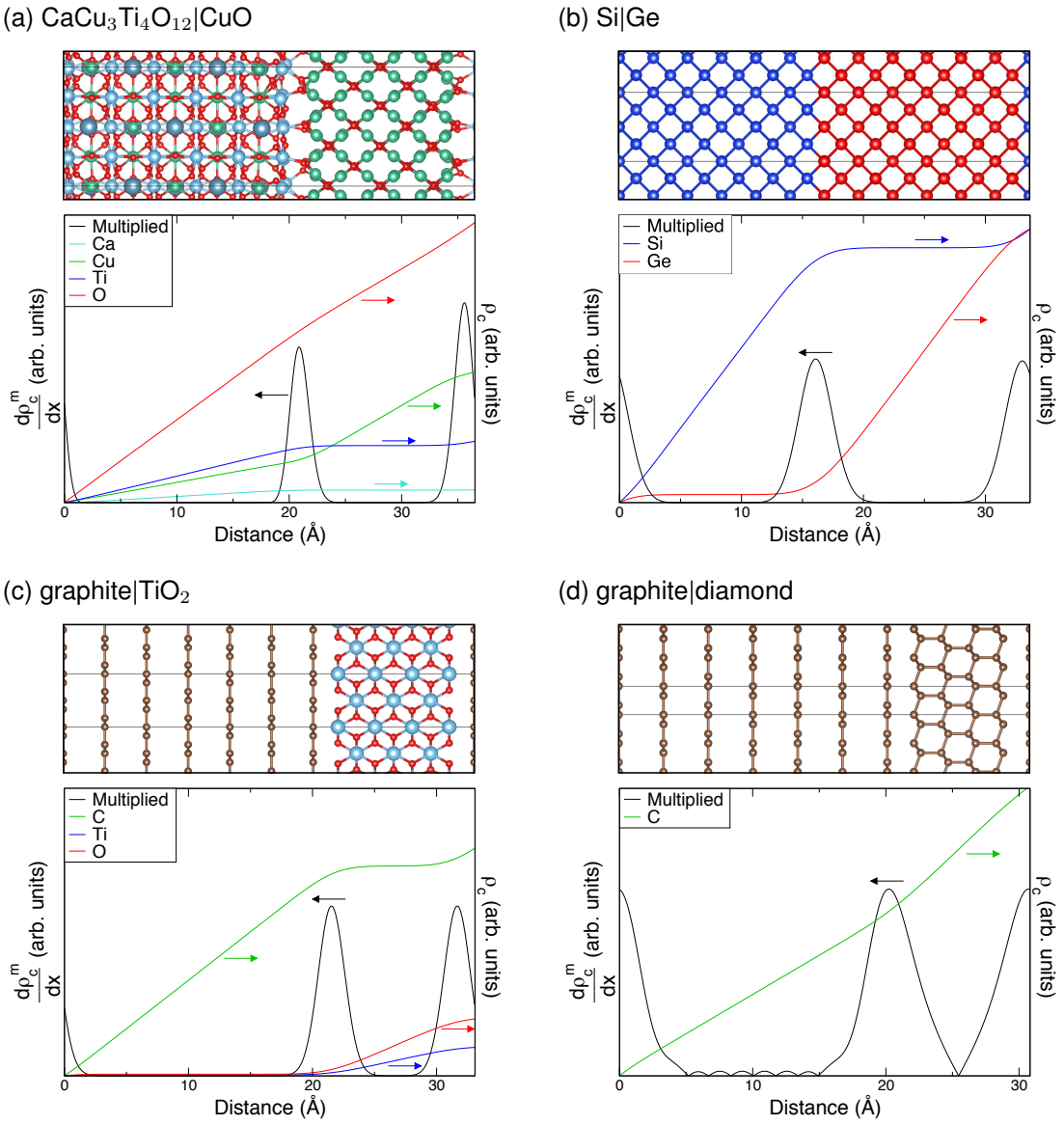

Figure 7.8: Interface identification performed on four structures. Cumulative atomic density derivative plots shown for (a) $CaCu_3Ti_4O_{12}$|CuO, (b) Si|Ge, (c) graphite|TiO_2 and (d) graphite|diamond interfaces. The arrows on the graphs indicate which data relates to which axis. These interfaces are used to display four different qualities interfaces can exhibit. For all plots, the right-hand axis denotes the cumulative density for each species in the system, whilst the left-hand axis denotes the 1^{st}-order derivative of the species-multiplied cumulative atomic density (multiCADD). The top panel in each subfigure shows a ball and stick model depicting the interface structure.

within the range shown on the separation axes for each structure and calculate the energy for each. The interface separation predicted by ARTEMIS is then indi-

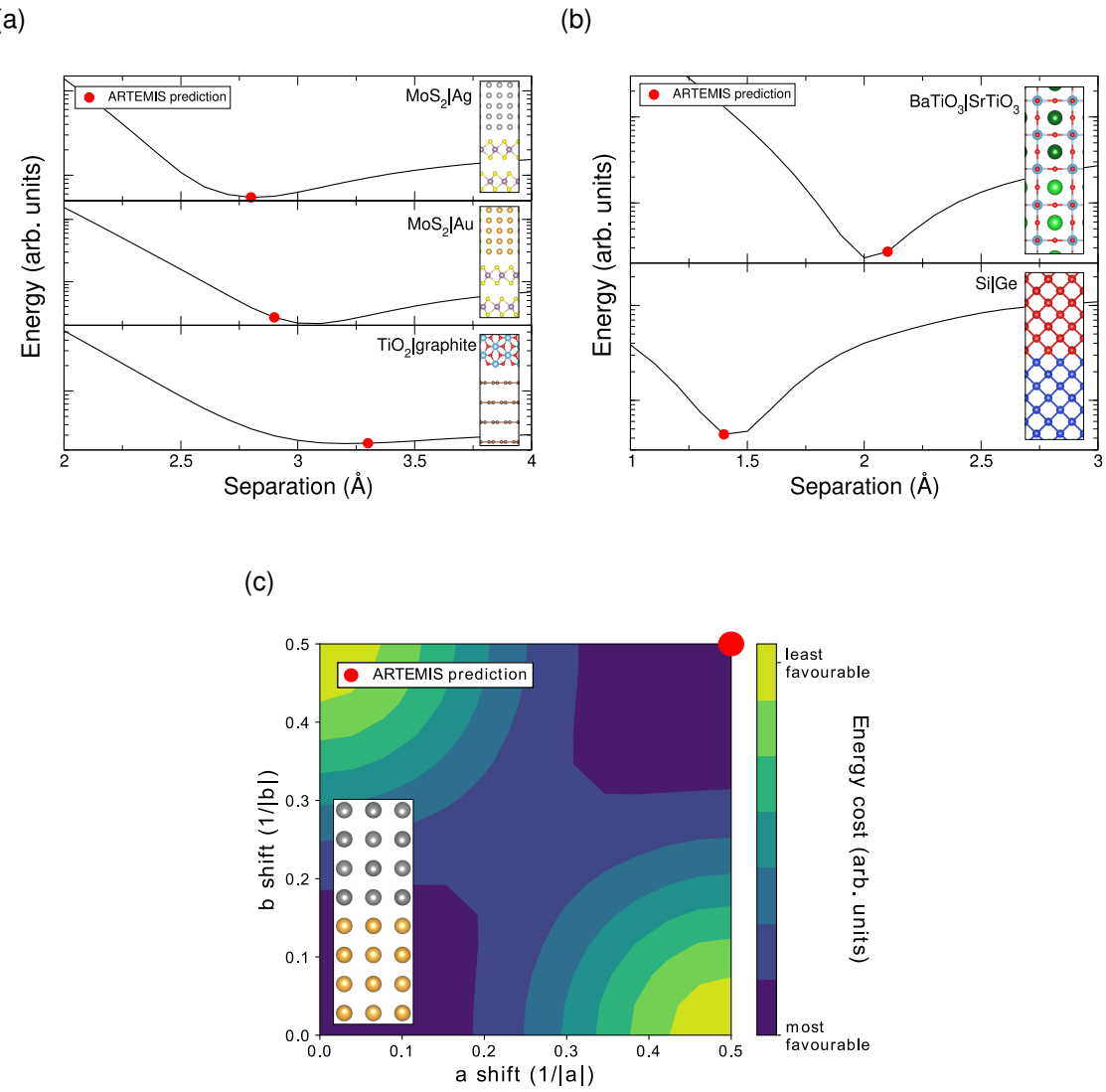

Figure 7.9: The relationship between energy and the alignment of the two parent crystals. (a) and (b) show the relation between energy and the interface separation for 2D|3D and 3D|3D interfaces, respectively. The optimum separation as estimated by ARTEMIS for each interface structure is is denoted by the red dots. The energies are obtained using the VASP density functional theory software package. (c) displays the energy cost of different shifts parallel to the interface plane for an Au|Ag interfacial structure. The optimum shift as estimated by ARTEMIS for each interface structure is is denoted by the red dot. For each subfigure, the inset displays a ball and stick model depicting the interface structure.

cated on these lines by a red dot. We find that, in all cases, the default interface separation prediction is close to the most energetically favourable separation (to

within 0.2 Å in these cases shown). This initial estimate of the separation of the two slabs means that the structure can be relaxed to its optimum distance using external first principles software packages. This suggests the method of `ISHIFT = 4` discussed in Section 7.7.1 is an appropriate method for interface separation estimation.

For shifts parallel to the interface, a test case of an Au|Ag interface has been chosen. The chosen Miller planes are (001) for both parent crystals. The energetic space of the in-plane shifts is shown in Figure 7.9c, with the shift predicted by ARTEMIS being labelled with a red dot. The shift determined by ARTEMIS is found to be the most favourable alignment for this metal-metal interface. Currently, this method has only been found to automatically identify the most favourable parallel shift for interfaces between simple, single-species crystals. For more complicated structures, the number of required structures (as generated by `ISHIFT= 4`) increases and the user needs to consider each case. However, it should be emphasised that interface separation predicted by ARTEMIS is generally found within the first iteration.

All energies reported in this subsection are obtained using density functional theory as implemented in the Vienna Ab initio Simulation Package (VASP). The energy for each shifted structure has been obtained by performing self-consistent field calculations on the generated, unrelaxed structures. The calculations have been performed using the PBE GGA functional with PAW pseudopotentials and an energy convergence of 10^{-7} eV. *k*-point grids of $3 \times 3 \times 2$ have been used for each structure.

7.8.4 Multiple interfaces

As mentioned previously, ARTEMIS can be used to reduce the difficulty of exploring the potential interfaces between crystals. There can exist a wide range in the number of potential lattice matches between any two crystals, which depends on their individual lattice shapes and sizes. The ideal goal of ARTEMIS is to make the process of determining potential lattice matches easier, along with identifying the potential surface terminations for each crystal and the relative alignments of

the two (outlined in Section 7.8.1 and Section 7.8.3, respectively).

For an insight into the capability of ARTEMIS to aid in determining the most energetically favourable interface structure from two given parent crystals, see Chapters 3 and 5. The software has been used throughout this thesis to help generate and explore interface structures.

7.9 Current limitations

Whilst ARTEMIS shows great promise for its use in interface exploration and prediction, it is important to highlight its current limitations that need to be addressed in future versions.

One of the major limitations of the software package is that it can only generate structures. It does not currently have a way to inform the interface search using elastic tensor and energetic arguments. As such, users need to feed the generated structures into simulations manually. ARTEMIS does not yet use the elastic tensor of each constituent bulk materials when forming the interface; if this were done, then it would more reasonably determine the upper limit of strain for each constituent and share the mismatch between the two materials based on their elastic properties. ARTEMIS cannot yet make predictions on the order of energetic favourability of the interfaces it generates; even a simplified method, such as the Harris functional [442, 443], may allow for initial energy estimates that can guide the search. Furthermore, a software interface between ARTEMIS and various atomic simulation package would be useful to help automate the submission and running of energetic and relaxation calculations.

Additionally, ARTEMIS cannot currently identify non-uniform (non-idealised) surfaces, such as the previously mentioned GaAs $\beta(2\times4)$ surface [433, 434], when identifying surface terminations; addressing this limitation will be a challenge as it requires detailed understanding of a surface's energetics. In future versions, the bond matching method outlined in Section 7.7.1 will need to take account of the atomic species involved to better match missing bonds at the surface; a similar consideration is needed for the intermixing method outlined in Section 7.7.2,

where understanding of the atomic masses involved would allow for more informed cross-interface swaps.

Whilst these limitations are present at the time of writing this work, the software is being continually developed and there are clear paths to addressing them. Being clear on its limitations allows users to better understand where ARTEMIS should be used and where improvements should be made.

7.10 Summary

In this chapter, we have presented a our software package, ARTEMIS, for the generation of potential interfaces between any two materials; here the parent materials can be single-species or multi-species, layered or bulk. Through the use of the software, users can more easily automate the task of interface generation and identification; for example, sets of interfacial alignments and intermixings can be easily generated, allowing for more thorough studies of potential interfaces between two parent crystals and their energy landscapes. With the lattice matching method able to scan over large sets of Miller planes, users can quickly identify low-strain matches which would otherwise be laborious. The test cases outlined in Section 7.8 show how the `ISHIFT` = 4 method can help in identifying the most favourable interface separation. This software should aid in exploring and understanding interface systems, which are critical to understanding the capabilities and efficiencies of many devices and many fundamental physical phenomena.

Chapter 8

Conclusions and outlook

“Spare me your space-age techno-babble."

— Zapp Brannigan

8.1 Summary

In this work, the effects and potential uses of interfaces for various devices have been explored, with a particular focus on those formed in oxide heterostructures. Chapter 1 introduces the concept of interfaces and details their use in technology and society thus far. Particular focus is put toward their use for energy-related applications such as solar energy harvesting. In Chapter 2, the *ab initio* methods used for modelling these interface systems are introduced and discussed. Core definitions of crystals and structural prediction are also presented.

In Chapter 3, the material $CaCu_3Ti_4O_{12}$ is investigated in an attempt to determine the fundamental mechanism causing experimentally-grown samples of it to exhibit colossal permittivity. By exploring and modelling the naturally occurring interfaces in samples of this material (grain boundaries), it is determined that a metallic interface forms between the stoichiometric $CaCu_3Ti_4O_{12}$ grains and the inter-grain material, CuO, which is responsible for the appearance of irregularly high permittivity values. Through use of *ab initio* and circuit-model simulations, it is shown that this large dielectric response can be enhanced by either adding (or

in reality increasing the concentration of) the concentration of oxygen vacancies or by increasing the grain sizes. This chapter provides a new understanding of oxide interfaces and colossal permittivity, and suggests that native $CaCu_3Ti_4O_{12}$ is unsuitable for energy storage; hence, other colossal permittivity systems should be considered for such applications.

Chapter 4 details a study of the electronic and mechanical properties of fresnoite ($Ba_2TiSi_2O_8$) a material known to form at the interface between $BaTiO_3$ and Si. The purpose of this study is to characterise the interface material to allow for a better understanding of the properties displayed by $Ba_2TiSi_2O_8$/Si heterostructures. This material is shown to be strongly anisotropic, with a strong difference between the a and c elastic and dielectric responses. Due to the strong Ti–O bonding, we see a very large band gap of 5.72 eV. This wide band gap oxide is also shown to exhibit a second, smaller band gap of 0.33 eV just above the conduction band minima. The two bands at the conduction band minima (below this second gap) are related to the Ti atoms, which act as defect-like bands within the more prominent Si–O bonding structure. Here, Ti appears almost as a $1/3$ dopant within the Si sub-structure. With the electronic, Raman, optical, mechanical and dielectric properties of $Ba_2TiSi_2O_8$ having been presented here using the screened hybrid functional HSE06, identification of this material at $BaTiO_3$/Si interfaces should be easier.

The goal set out in Chapter 5 is to propose an all-oxide solar cell, where each layer of the device is an oxide material. Oxides are relatively cheap and easy to fabricate and relatively stable in both air and water. Incorporating these properties into solar cells would help to revolutionise the photovoltaic industry. To this end, we partnered with a company, Solaris Photonics, to study SnO for its potential as an active layer in a photovoltaic device. SnO shows strong thermal stability and anisotropic conduction properties, which could allow it to be a very useful photovoltaic material; however, it has a small indirect band gap of 0.88 eV, which significantly reduces its potential as an effective active layer. By forming a solid solution between it and CaO (with a stoichiometry of $(Sn{:}Ca)_{7:1}O$), we detail how its optical properties can be improved for solar cell applications. The aim of forming a solid solution is to maintain the desirable properties of SnO, whilst

introducing some of the beneficial properties of CaO. The improvements in the material's properties include changing the fundamental gap from indirect to direct and increasing the band gap to 1.56 eV. With all of these capabilities, the solid solution (Sn:Ca)$_{7:1}$O has the promise to be an efficient photovoltaic material.

To fully understand the capability of the solid solution (Sn:Ca)$_{7:1}$O as an active layer in a solar cell device, the band alignment between it and potential transport layers must be explored. A set of materials are studied as potential hole and electron transport layers. It is found that its hole affinity value of 4.93 eV results in many oxides acting as hole transport layers to this active layer. As such, identifying a viable electron transport layer is the main challenge to realising this setup. We identify CaO as a potential hole transport layer and TiO_2 as an electron transport layer. MoO_3 is provided as another potential electron transport layer.

In Chapter 6, we present study of four oxide perovskites for photocatalysis – $CaSnO_3$, $SrSnO_3$, $BaSnO_3$ and $SnTiO_3$. By analysing the electrostatic potential for each perovskite, we determine that the band gaps of $BaSnO_3$ and $SnTiO_3$ are poorly aligned to the hydrogen and oxygen reaction potentials; meanwhile, $CaSnO_3$ and $SrSnO_3$ maintain their ability to straddle the reaction levels. We further the study by exploring the energetics of the reactants adsorbed to the surfaces of $CaSnO_3$ and $SrSnO_3$ and determine the overpotentials for both are too large to allow for simultaneous hydrogen and oxygen water-splitting. However, by introducing a thin ZrO_2 overlayer onto the surface of $SrSnO_3$, we show how it is possible to reduce the overpotentials – in this case, the hydrogen and oxygen overpotentials are reduced from 0.75 and 0.72 eV down to 0.35 and 0.54 eV, respectively. This structure of $SrSnO_3$|ZrO_2 results in a system where both overpotentials are straddled by the system's band gap for pH values between 0 and 12. Here, we highlight the importance of overlayers in water-splitting devices and present $SrSnO_3$|ZrO_2 as a potential candidate for bifunctional water-splitting.

Chapter 7 details the software package, ARTEMIS, that we have developed for the generation of potential interfaces between any two crystals. In the current version, the software is intended to work with materials that are single-species or multi-species, layered or bulk. To improve use of the software further, it has been developed to output structure files in a set of different formats for use with

plane-wave density functional theory programs. The code has been developed with the capability of identifying the location of the interface in a pregenerated interface structure to allow users to further study an already tested interface. Post processing tools on interface structures include interface identification, interface alignment and intermixing. Combined, the tools of ARTEMIS allow the user to thoroughly test the energetic hyperspace of an interface between any two crystals.

8.2 Future work

Several areas of study presented in this thesis warrant further investigation. Other systems that exhibit colossal permittivity, such as laminates and co-doped materials, deserve a similar study to that presented in Chapter 3, in particular, for energy storage applications. Having thoroughly characterised $Ba_2TiSi_2O_8$ in Chapter 4, it would be worth studying interfaces between $BaTiO_3$ and $Ba_2TiSi_2O_8$, as well as those between Si (or SiO_2) and $Ba_2TiSi_2O_8$. This would link back to the aforementioned extension of study on Chapter 3 by exploring another colossal permittivity system. Both of these studies would also aid in finding a common link between all of these unusual systems that display these irregularly high permittivity values. It should be noted that, due to its strongly asymmetric unit cell, $Ba_2TiSi_2O_8$ would form highly polar interfaces, which would present an unusual challenge for theoretical modelling.

In Chapter 5, an initial study of the study of the $(Sn:Ca)_{7:1}O$ solid solution has been provided for its use as the active layer in an all-oxide solar cell. In future work, this should be extended to explore a much larger phase space of this compound to determine its most energetically favourable form. This would allow for a better understanding of the energetic and optical properties of this solid solution. We have presented a study of potential oxide transport layers for an $(Sn:Ca)_{7:1}O$-based solar cell. A useful extension to this work would be to investigate further sets of oxides for transport layers in an attempt to identify a candidate electron transport layer. It would also be worth exploring possible contacts for such a system by looking into new potential transparent conducting oxides; with the large band gap

displayed by $Ba_2TiSi_2O_8$ in Chapter 4, there is a chance that doping this structure could allow for it to exhibit the necessary transparent conductive properties. Overall, further exploration of oxides for each component of a photovoltaic cell would be desirable, perhaps with a focus on finding an oxide with a larger hole affinity to function as the active layer. Finally, it would be beneficial to thoroughly explore the effects of intrinsic dopants within each of the device layers, with a particular focus on how vacancies affect the solid solution $(Sn:Ca)_{7:1}O$. Whilst preliminary data has been obtained on oxygen vacancies in the heterostructures, further study to determine their localisation, concentration and effects on the optical properties would allow for a much greater understanding of the potential device.

Chapter 6 has potential for both experimental and theoretical extensions to the work presented here. On the experimental side, manufacturing such a setup would allow for an understanding of where the physical and operational limits of it lie. This study would help to determine the maximal thickness of the oxide overlayers. As for theory, further exploration of potential oxide overlayers and their stability on oxide perovskite surfaces would be valuable for understanding how thin these overlayers need to be, as well as when overlayers function on the perovskites. Identifying whether the use of overlayers can improve the photocatalytic capabilities of other oxide perovskites would be of great importance.

Finally, the software presented in Chapter 7 has shown great promise in aiding the study of interface structures. Throughout this work, the software has been used to determine the best lattice-matched systems to explore. Going forward, a detailed study and further development of the lattice alignment methods presented in the aforementioned chapter would help to determine how generally these can be applied, as well as identify how these can be improved. Currently, it is believed that introducing an understanding of charge states into the method will help to improve the balancing of bond lengths. The intermixing subroutine should also be extended further by considering the masses and atomic radii of the swapped atoms; atoms of greater mass may displace pairs of lighter atoms in the opposite material. By continuing to develop this software, it has the potential to change the way we study interfaces.

8.3 Closing remarks

This thesis has explored the potential of interfaces for use in several energy storage and energy generation applications. Naturally-occurring and artificial interfaces between oxide materials are studied in order to understand both the unique physical properties they can exhibit and their effects on the component materials. Finally, a tool for generating interfaces between any two materials is presented and the methods implemented within for identifying and predicting the most energetically favourable interface are discussed.

Appendix A

An alternative description of Miller planes

An alternative understanding for Miller planes is as follows: for each point (hkl) in reciprocal space, there exists a corresponding set of lattice planes (hkl) in real space. The direction of this reciprocal vector is normal to the real-space planes. Because of this, the interplanar spacing d can be determined by taking the reciprocal of the length of the reciprocal vector:

$$d = \frac{2\pi}{|\mathbf{g}_{hkl}|}. \tag{A.1}$$

These crystallographic planes can be used to identify crystal structure through use of X-ray or neutron diffraction (see Figure A.1) [3]. Let us first consider the Miller planes of a material as diffraction gratings. Incident waves will reflect off of these sets of planes, which will interfere with each other to form a diffraction pattern. Constructive interference occurs at specific angles of incidence θ reflecting off of parallel Miller planes (where $\theta = 0$ corresponds to the light being parallel to the plane). The angle at which this occurs for a specific Miller plane is defined by Bragg's law:

$$2d \sin\theta = n\lambda. \tag{A.2}$$

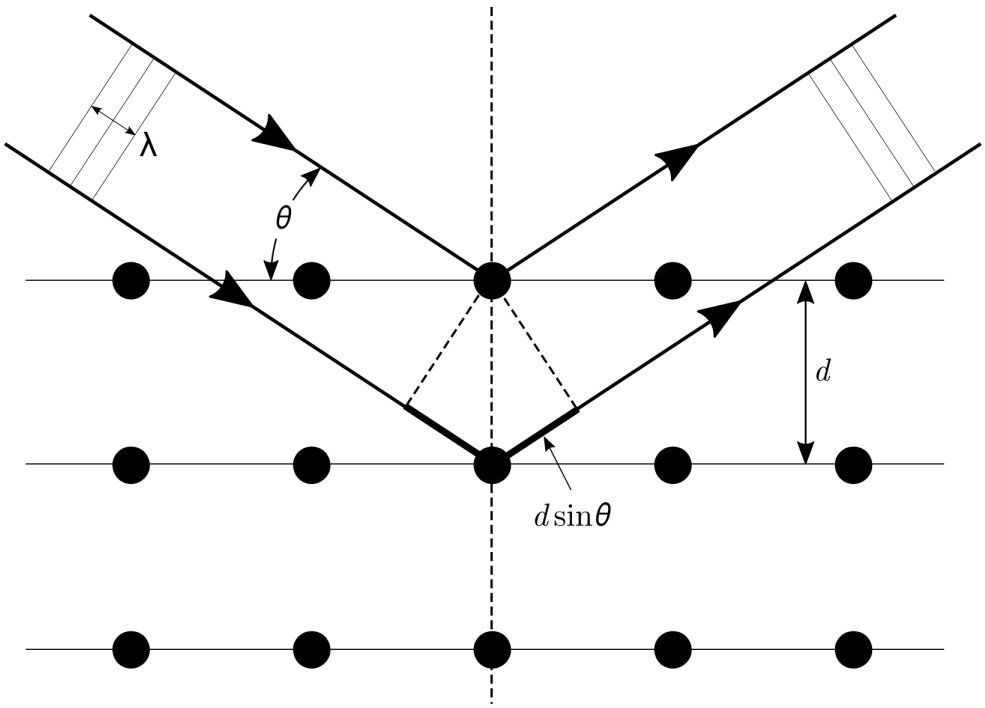

Figure A.1: Schematic of X-ray diffraction used to determine the interplanar spacing d using the angle of incidence θ and the wavelength λ of the probing electromagnetic wave. The filled circles represent atoms and the parallel lines intersecting these indicate Miller planes within the crystal.

Here, d is the interplanar spacing, n is an integer and λ is the wavelength of the incident light. From this, it is clear that the phase shift of the two reflected waves must be a multiple of 2π. By using the wavelength of the incident light and recording the angles of incidence/reflection, one can determine the interplanar spacing of different Miller planes, allowing one to describe the periodicity and symmetries of the crystal.

To refer to the set of planes symmetrically equivalent to (hkl), "curly" brackets are used: $\{hkl\}$. To refer to the set of Miller directions symmetrically equivalent to $[hkl]$, then one uses "triangular" brackets: $\langle hkl \rangle$.

Appendix B

Hartree Fock: Exchange-correlation hole

Electrons form an interacting many-body system, with a wave function, in general, given by $\Psi(\mathbf{r}_1, \cdots, \mathbf{r}_{N_e})$. The interactions in such a system always involve pairs of electrons, it is, therefore, sufficient to use two-body correlation functions to determine many of the electronic properties, such as the energy. To do so, we give the joint probability $n^{\sigma,\sigma'}(\mathbf{r}, \mathbf{r}')$ of finding electrons of spin σ and point $\mathbf{r}$ and of spin σ' at point $\mathbf{r}'$ as

$$\begin{aligned} & n^{\sigma,\sigma'}(\mathbf{r}, \mathbf{r}') \\ & = \left\langle \sum_{i \neq j} \delta(\mathbf{r} - \mathbf{r}_i)\delta(\sigma - \sigma_i)\delta(\mathbf{r}' - \mathbf{r}_j)\delta(\sigma' - \sigma_j) \right\rangle \\ & = N_e(N_e - 1) \sum_{\sigma_3, \cdots, \sigma_{N_e}} \int |\Psi(\mathbf{r}, \sigma; \mathbf{r}', \sigma'; \mathbf{r}_3, \sigma_3; \cdots, \mathbf{r}_{N_e}, \sigma_{N_e})|^2 \, d\mathbf{r}_3 \cdots d\mathbf{r}_{N_e}, \end{aligned} \quad \text{(B.1)}$$

with Ψ being normalised to unity. For uncorrelated particles, the joint probability is just the product of probabilities. Therefore, the measure of correlation $\Delta n^{\sigma,\sigma'}(\mathbf{r}, \mathbf{r}')$ is the difference between the joint probability for the correlated and uncorrelated systems

$$n^{\sigma,\sigma'}(\mathbf{r}, \mathbf{r}') = n^{\sigma}(\mathbf{r}) n^{\sigma'}(\mathbf{r}') + \Delta n^{\sigma,\sigma'}(\mathbf{r}, \mathbf{r}'). \quad \text{(B.2)}$$

As mentioned earlier, Hartree-Fock neglects all correlations except those required by Pauli exclusion (exchange). This exchange term represents two interactions: 1) the self-term that must be subtracted to cancel the spurious self-term in the Coulomb Hartree energies, and 2) the Pauli exclusion term. The effect of these is always to lower the energy, which can be interpreted as the interaction of each electron with a positive 'exchange hole' surrounding it.

The orthonormal single-electron wave functions $\psi_i(\mathbf{x}_i)$ can be written as a product of the wave functions associated with the spatial (ϕ) and spin (α) coordinates $\psi_i(\mathbf{x}_j) = \phi_i^{\sigma}(\mathbf{r}_j) \times \alpha_i(\sigma_j)$, where σ denotes the spin. Using this, Equation (2.95) can be rewritten as the pair distribution function

$$n_{\mathrm{HF}}^{\sigma,\sigma'}(\mathbf{r},\mathbf{r}') = \frac{1}{2!}\sum_{ij}\begin{vmatrix}\psi_i(\mathbf{r},\sigma) & \psi_i(\mathbf{r}',\sigma')\\ \psi_j(\mathbf{r},\sigma) & \psi_j(\mathbf{r}',\sigma')\end{vmatrix}^2, \tag{B.3}$$

which leads to the exchange hole being defined as

$$\Delta n_{\mathrm{x}}^{\sigma,\sigma'}(\mathbf{r},\mathbf{r}') = \Delta n_{\mathrm{HF}}^{\sigma,\sigma'}(\mathbf{r},\mathbf{r}') = -\delta_{\sigma,\sigma'}\left|\sum_i \phi_i^{\sigma}(\mathbf{r})\phi_i^{\sigma}(\mathbf{r}')\right|^2. \tag{B.4}$$

From Equation (B.4), it becomes immediately clear that the exchange hole of an electron is only present for electrons of the same spin; hence, the probability vanishes, as it must, for two electrons of the same spin at the same point. The energy relating to the exchange potential in Equation (2.102) can be interpreted as the lowering of the total energy of the system due to each electron interacting with its positive exchange hole,

$$E_{\mathrm{x}} = \frac{1}{2}\sum_{\sigma}\int\frac{\delta n_{\mathrm{x}}^{\sigma,\sigma'}(\mathbf{r},\mathbf{r}')}{|\mathbf{r}-\mathbf{r}'|}d\mathbf{r}d\mathbf{r}'. \tag{B.5}$$

For other approximations where the full correlation is accounted for, a similar hole can be defined for Coulomb correlation n_{c}. As such, the full exchange-correlation hole can be defined as

$$\Delta n^{\sigma,\sigma'}(\mathbf{r},\mathbf{r}') \equiv n_{\mathrm{xc}}^{\sigma,\sigma'}(\mathbf{r},\mathbf{r}') = n_{\mathrm{x}}^{\sigma,\sigma'}(\mathbf{r},\mathbf{r}') + n_{\mathrm{c}}^{\sigma,\sigma'}(\mathbf{r},\mathbf{r}'). \tag{B.6}$$

Appendix C

Pseudopotentials: the expansion of the expectation value

The definition of the coefficients α_{cv} in Equation (2.137) are determined by enforcing the orthogonality $\langle\psi_c|\phi_v\rangle = 0$,

$$\begin{aligned}
\langle\psi_c|\phi_v\rangle &= \langle\psi_c|\left[|\psi_v\rangle - \sum_{c'=1}^{N_{\text{core}}} \alpha_{c'v}\,|\psi'_c\rangle\right] \\
&= \langle\psi_c|\psi_v\rangle - \sum_{c'=1}^{N_{\text{core}}} \alpha_{c'v}\,\langle\psi_c|\psi'_c\rangle \\
&= \langle\psi_c|\psi_v\rangle - \sum_{c'=1}^{N_{\text{core}}} \alpha_{c'v}\delta_{c',c} \\
0 &= \langle\psi_c|\psi_v\rangle - \alpha_{cv}.
\end{aligned}$$

This leads to the aforementioned result of

$$\alpha_{cv} = \langle\psi_c|\psi_v\rangle\,. \tag{C.1}$$

Let us now consider the expectation of the Hamiltonian with respect to these new smooth valence functions ϕ_v,

$$
\begin{aligned}
\langle\phi_{v'}|\hat{H}|\phi_v\rangle &= \langle\phi_{v'}|\,\hat{H}\left[|\psi_v\rangle - \sum_c \alpha_{ci}\,|\psi_c\rangle\right] \\
&= \langle\phi_{v'}|\left[\hat{H}\,|\psi_v\rangle - \sum_c \alpha_{ci}\hat{H}\,|\psi_c\rangle\right] \\
&= \langle\phi_{v'}|\hat{H}|\psi_v\rangle - \sum_c \alpha_{ci}E_c\,\langle\phi_{v'}|\psi_c\rangle \\
&= \langle\phi_{v'}|\hat{H}|\psi_v\rangle \\
&= \left[\langle\psi_{v'}| - \sum_{c'}\alpha^*_{c'v'}\,\langle\psi_{c'}|\right]\hat{H}\,|\psi_v\rangle \\
&= \left[\langle\psi_{v'}| - \sum_{c'}\left(\langle\psi_{c'}|\psi_{v'}\rangle\right)^*\langle\psi_{c'}|\right]\hat{H}\,|\psi_v\rangle \\
&= \left[\langle\psi_{v'}| - \sum_{c'}\langle\psi_{v'}|\psi_{c'}\rangle\,\langle\psi_{c'}|\right]\hat{H}\,|\psi_v\rangle \\
&= \langle\psi_{v'}|\left[\hat{H} - \sum_{c'}|\psi_{c'}\rangle\,\langle\psi_{c'}|\,\hat{H}\right]|\psi_v\rangle \\
&= \langle\psi_{v'}|\left[\hat{H} - \sum_c E_c\,|\psi_c\rangle\,\langle\psi_c|\right]|\psi_v\rangle\,.
\end{aligned}
$$

We now do the same derivation for the expectation value of the energy:

$$
\begin{aligned}
\langle\phi_{v'}|E|\phi_v\rangle &= \langle\phi_{v'}|\,E\left[|\psi_v\rangle - \sum_c \alpha_{ci}\,|\psi_c\rangle\right] \\
&= E\left[\langle\phi_{v'}|\psi_v\rangle - \sum_c \alpha_{ci}\,\langle\phi_{v'}|\psi_c\rangle\right] \\
&= E\,\langle\phi_{v'}|\psi_v\rangle \\
&= E\left[\langle\psi_{v'}| - \sum_{c'}\alpha^*_{c'v'}\,\langle\psi_{c'}|\right]|\psi_v\rangle \\
&= E\left[\langle\psi_{v'}| - \sum_{c'}\left(\langle\psi_{c'}|\psi_{v'}\rangle\right)^*\langle\psi_{c'}|\right]|\psi_v\rangle \\
&= \langle\psi_{v'}|\left[E - E_c\sum_c|\psi_c\rangle\,\langle\psi_c|\right]|\psi_v\rangle\,.
\end{aligned}
$$

Combining these two results, we get

$$
\begin{aligned}
\langle \phi_{v'} | \hat{H} - E | \phi_v \rangle &= \langle \phi_{v'} | \hat{H} | \phi_v \rangle - \langle \phi_{v'} | E | \phi_v \rangle \\
&= \langle \psi_{v'} | \left[\hat{H} - \sum_c E_c \left| \psi_c \right\rangle \left\langle \psi_c \right| \right] | \psi_v \rangle \\
&\qquad - \langle \psi_{v'} | \left[E - E_c \sum_c \left| \psi_c \right\rangle \left\langle \psi_c \right| \right] | \psi_v \rangle \\
&= \langle \psi_{v'} | \left[\hat{H} - \sum_c E_c \left| \psi_c \right\rangle \left\langle \psi_c \right| - E + E \sum_c \left| \psi_c \right\rangle \left\langle \psi_c \right| \right] | \psi_v \rangle \\
&= \langle \psi_{v'} | \left[\hat{H} - E + \sum_c (E - E_c) \left| \psi_c \right\rangle \left\langle \psi_c \right| \right] | \psi_v \rangle \\
&= \langle \psi_{v'} | \left[\hat{H}^{\text{eff}} - E \right] | \psi_v \rangle \, .
\end{aligned}
$$

Here, we have expanded and solved the expectation value of the Hamiltonian and energy using these smooth valence function.

Appendix D

Conjugate gradient method

The conjugate gradient method is a form of identifying local minima in an N-dimensional space, assuming the form of the functional is quadratic [44]. This method offers a much improved ability to find the local minimum over that of simpler methods such as steepest descent, with conjugate gradient being able to exactly solve the problem of a quadratic in N-dimensional space within N steps.

Consider the quadratic functional

$$F(\{x_i\}) \equiv F(\mathbf{x}) = \frac{1}{2}\mathbf{x} \cdot \mathbf{H}\mathbf{x}, \tag{D.1}$$

with gradients

$$\mathbf{g} = -\frac{\partial F}{\partial \mathbf{x}} = -\mathbf{H} \cdot \mathbf{x}. \tag{D.2}$$

The first step of the conjugate gradient method is the same as steepest descent, which involves minimisation of F along a line $\mathbf{x}^{(1)} = \mathbf{x}^{(0)} + \alpha^{(1)}\mathbf{d}^{(0)}$, where $\mathbf{d}^{(0)} = \mathbf{g}^{(0)}$. For this and all subsequent steps, minimum occurs at

$$\mathbf{d}^{(n)} \cdot \mathbf{g}(\mathbf{x}^{(n+1)}) = 0. \tag{D.3}$$

The best choice of direction in which to minimise the $n+1$ step is one that keeps

the gradient along the previous line $\mathbf{d}^{(n)}$ equal to zero. As $\Delta\mathbf{g} = \alpha^{(n+1)}\mathbf{H}\cdot\mathbf{d}^{(n+1)}$, the condition on the line becomes

$$\mathbf{d}^{(n)}\cdot\mathbf{H}\cdot\mathbf{d}^{(n+1)} = 0. \tag{D.4}$$

This defines the *conjugate direction*, which is orthogonal to the previous direction (the orthogonality is in the space defined by the metric $\mathbf{H} = H_{ij}$). If this condition is satisfied at each step, then the conjugate condition is maintained for all steps

$$\mathbf{d}^{(n')}\cdot\mathbf{H}\cdot\mathbf{d}^{(n+1)} = 0. \quad \text{for all} \quad n' \leq n \tag{D.5}$$

This restriction on the directions preserves the minimisation performed in all of the previous steps, only adding independent (i.e. conjugate) variations. As such, this method reaches the minimum *exactly* in N steps, where N is the dimension of the space x_i, $i = 1, N$.

For actual calculations, it is useful to specify the new conjugate gradient directions $\mathbf{d}^{(n+1)}$ in terms of the quantities already available (i.e. the current gradient and the previous direction),

$$\mathbf{d}^{(n+1)} = \mathbf{g}^{(n+1)} + \gamma^{(n+1)}\mathbf{d}^{(n)}. \tag{D.6}$$

By using the quantity $\mathbf{y}^{(n)} = \mathbf{d}^{(n)}\cdot\mathbf{H}$, we can write Equation (D.6) as

$$\begin{aligned}
\gamma^{(n+1)}\left\langle\mathbf{y}^{n}\middle|\mathbf{d}^{(n)}\right\rangle &= \left\langle\mathbf{y}^{(n)}\middle|\mathbf{d}^{(n+1)}\right\rangle - \left\langle\mathbf{y}^{(n)}\middle|\mathbf{g}^{(n+1)}\right\rangle \\
\gamma^{(n+1)} &= \frac{\left\langle\mathbf{y}^{(n)}\middle|\mathbf{d}^{(n+1)}\right\rangle - \left\langle\mathbf{y}^{(n)}\middle|\mathbf{g}^{(n+1)}\right\rangle}{\left\langle\mathbf{y}^{(n)}|\mathbf{d}^{(n)}\right\rangle} \\
\gamma^{(n+1)} &= \frac{\left\langle\mathbf{y}^{(n)}\middle|\mathbf{d}^{(n+1)}\right\rangle}{\left\langle\mathbf{y}^{(n)}|\mathbf{d}^{(n)}\right\rangle}.
\end{aligned} \tag{D.7}$$

This is defined as the Hestens-Steifel form. For the case of a quadratic functional, this is equivalent to the Fletcher-Reeves form:

$$\gamma^{(n+1)} = \frac{\mathbf{g}^{(n+1)} \cdot \mathbf{g}^{(n+1)}}{\mathbf{g}^{(n)} \cdot \mathbf{g}^{(n)}}, \tag{D.8}$$

with $\gamma^{(1)} = 0$. Using these, one then must perform line minimisation along the conjugate direction, then repeat the procedure on each subsequent conjugate gradient until suitable minimisation has been reached. Keep note that this algorithm is designed for quadratic functionals.

Appendix E

Sampling of the Brillouin zone

E.1 Sampling of the Brillouin zone

Evaluation of many physical properties, such as energy and density, involves an integral over the Brillouin zone. To accurately capture the integration using a discrete set of points in the Brillouin zone, one must take care in selecting sufficient points in regions where the integrand varies rapidly. This is exemplified when considering the differences between insulators and metals; in the case of the former, the filled bands can be integrated using only a few well-chosen points – *special* points. For the latter, careful integration is required near where bands cross the Fermi-level. As mentioned in Section 2.2.2, the scale of such a calculation can first be reduced by considering only symmetrically inequivalent points.

For a given integrand $f_i(\mathbf{k})$ that is some function of the eigenfunctions $\psi_{i,\mathbf{k}}$ and eigenvalues $\varepsilon_{i,\mathbf{k}}$, it is a smoothly varying and periodic function of $\mathbf{k}$. As such, it can be expanded in Fourier space,

$$f_i(\mathbf{k}) = \sum_{\mathbf{T}} f_i(\mathbf{T}) \exp(\mathrm{i}\mathbf{k} \cdot \mathbf{T}), \tag{E.1}$$

where $\mathbf{T}$ are the translation vectors of the crystal. The contribution of the rapidly varying terms at large $\mathbf{T}$ decreases exponentially, so that the above sum can be truncated to a finite sum. Special points are then chosen for efficient integration

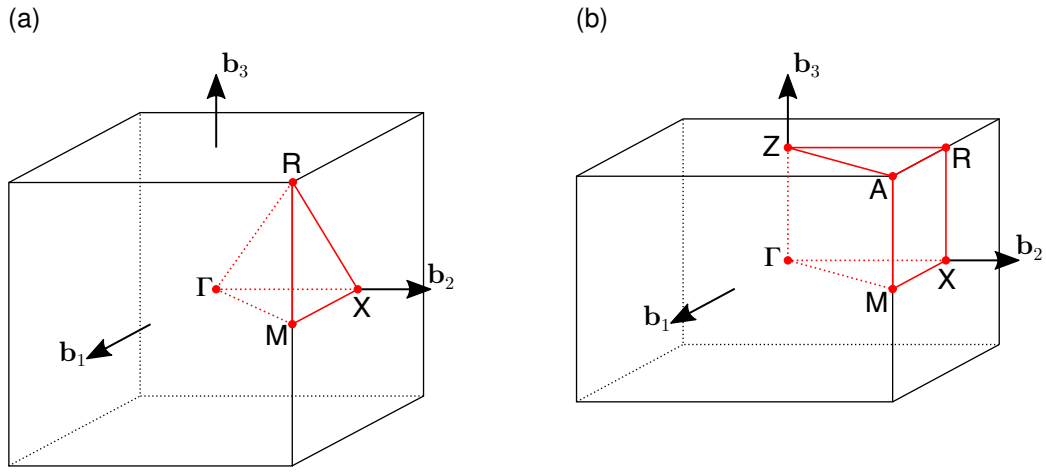

Figure E.1: Points (red circles) and lines (red lines) of high symmetry in and long the Brillouin zone for a (a) cubic and (b) tetragonal cell. Dashes define that a line is partially obscured by a boundary face.

of the smooth, periodic function.

The most widely used method for determining a set of special points to evaluate in the Brillouin zone is that proposed by Monkhorst and Pack [88]. This scheme uses a simple formula, valid for any crystal, to determine a uniform set points based on the given number of subdivisions, N_1, N_2, N_3, along each reciprocal lattice vector. The resultant set of points (for a system with three dimensions) are given by

$$\mathbf{k}_{n_1,n_2,n_3} \equiv \sum_{i}^{3} \frac{2n_i - N_i - 1}{2N_i}\mathbf{b}_i, \tag{E.2}$$

where $\mathbf{b}_i$ are the primitive reciprocal lattice vectors, and $n_i = 1, 2, \cdots, N_i$. By using a shift vector, this grid can be chosen to always be centred on the Γ-point.

E.2 Brillouin zone example

Figure E.1 displays a schematic of the Brillouin zone for cubic and tetragonal cells. These have been presented as they are the two types of Brillouin zones discussed throughout this work.

Appendix F

Convergence test results

For each chapter, convergence of the energetic and electronic properties has been tested for the bulk materials, in addition to certain slab structures to ensure consistency for more complex systems. An example of that convergence testing is detailed here for $CaCu_3Ti_4O_{12}$ bulk, explored in Chapter 3.

Convergence is tested for both the *k*-point grid and the energy cutoff for the plane-wave basis set. Total energy and fundamental band gap are used to determine whether convergence for the two input parameters has been achieved. It should be noted that, whilst band gap is considered for convergence of the *k*-point grid size, it is not the determining factor as the size of the band gap is dependent on the specific *k*-points being used in the calculation (i.e. a material with a direct fundamental gap at Γ will appear to have a larger band gap for a calculation performed without using the Γ-point).

Previous studies by Lejaeghere *et al.* [444, 445] have calculated the energy accuracy of VASP when compared to all-electron calculations to be within 0.6 meV/atom. As such, for this work, we shall define a parameter to be converged when an increase in its size results in energy values changing by less than 1 meV/atom – here, these two parameters are *k*-point grid size and energy cutoff.

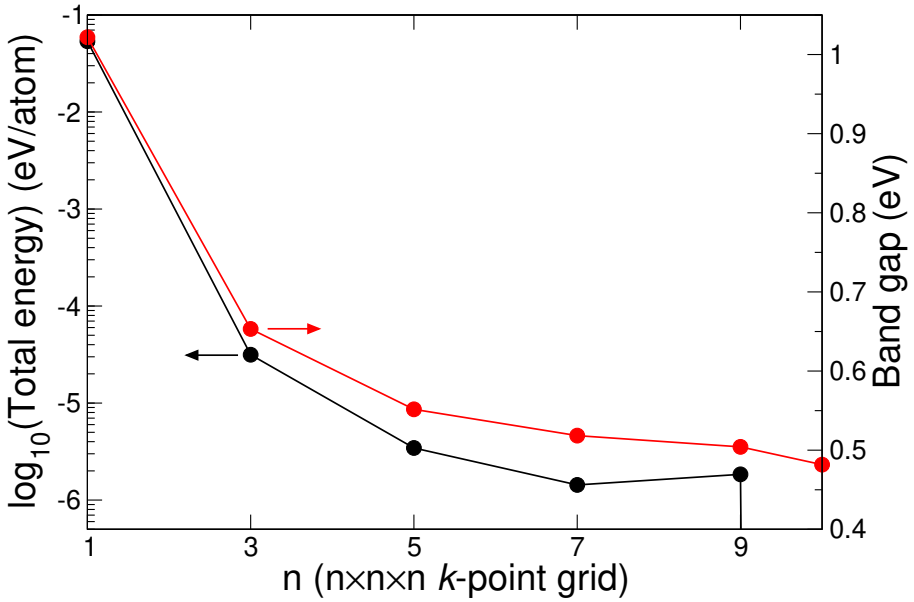

Figure F.1: Convergence of the total energy (per atom) and band gap of bulk $CaCu_3Ti_4O_{12}$ with respect to the *k*-point grid size. The total energy is given with respect to the energy at a $10 \times 10 \times 10$ *k*-point grid.

F.1 *k*-point convergence

As mentioned previously, sampling of the *k*-point grid is performed using the Monkhorst Pack method, and its grid size is used as a parameter to converge via total energy (i.e. less than 1 meV/atom change in total energy between subsequently larger grid sizes) for a 40-atom $CaCu_3Ti_4O_{12}$ unit cell. This method defines a grid of equally space *k*-points and retains a subset such that all remaining are symmetrically inequivalent and appropriately weighted. The grid size (the number of points along each axis) is defined by the user using the `KPOINTS` input file. All grids here are Γ-centred. In Figure F.1, *k*-point grids larger than $3 \times 3 \times 3$ are shown to be suitably convergence for total energy, whilst grids of $7 \times 7 \times 7$ are considered suitable for band gap accuracy.

F.2 Energy cutoff convergence

Energy cutoff is specified in VASP in units of eV using the `ENCUT` tag in the `INCAR` input file. Here, the energy cutoff is converged with respect to total energy (i.e.

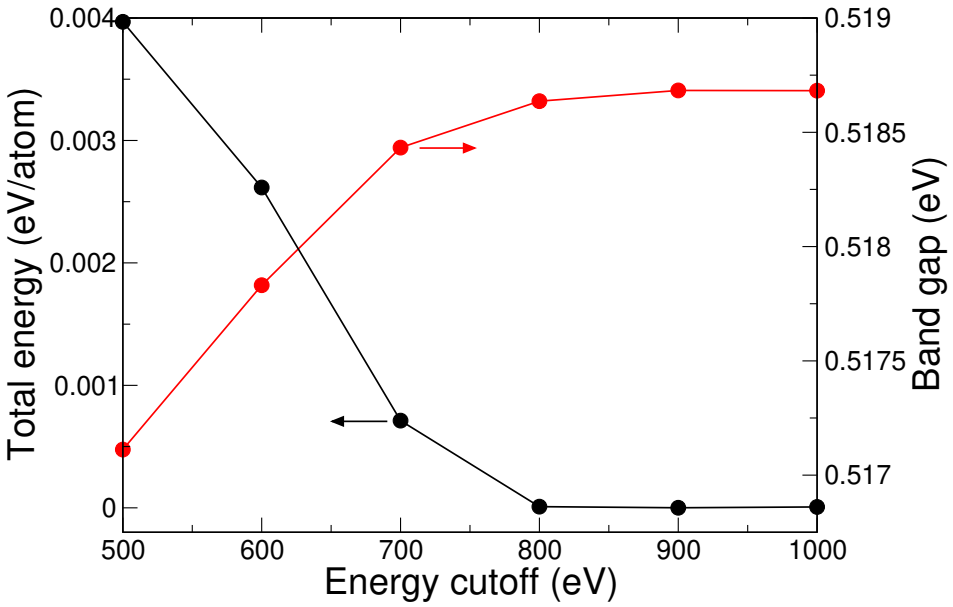

Figure F.2: Convergence of the total energy and band gap of bulk $CaCu_3Ti_4O_{12}$ with respect to the energy cutoff, `ENCUT`. The total energy is given with respect to the lowest total energy value (obtained at 900 eV).

less than 1 meV/atom change in total energy between subsequently larger cutoff energies) for a 40-atom $CaCu_3Ti_4O_{12}$ unit cell. From Figure F.2, we consider the total energy and band gap to be sufficiently converged for 700 eV and above.

Appendix G

Formation energy

For all of the formation energies described below, a negative formation energy is representative of a system where the considered structure is more energetically favourable than the constituent compounds it is being compared to. When determining the formation energy, all systems being compared use the same energy cutoff and equivalent *k*-point grids (this ensures comparability between energetic values, in addition to other properties).

G.1 Bulk formation energy

To determine the formation energy for a bulk material $E_{f,\mathrm{bulk}}$, the bulk energy is compared to stable constituent compounds. In the case of oxides, as is the majority of work in this thesis, these compounds are typically monoxides or binary oxides. As an example, the equation to determine formation energy for a ternary oxide ABO_3 is

$$E_{f,\mathrm{bulk}} = E_{\mathrm{ABO_3}} - E_{\mathrm{AO}} - E_{\mathrm{BO_2}}, \tag{G.1}$$

where the energy for each of these compounds is taken at their most energetically favourable phase. If the formation energy is negative, then the considered bulk material is more energetically favourable than the compounds it has been

compared to. This means that the material is stable. The formation energy is given with respect to a single unit of the material, so as to not be affected by use of supercells.

G.2 Surface formation energy

To determine the formation energy of forming a particular surface termination $E_{f,\mathrm{surface}}$ (i.e. cleaving energy), the energy of a slab with identical surface terminations on both sides E_{slab} is compared to the energy of the bulk material E_{bulk} and any additional compounds E_i required to satisfy equivalent stoichiometry between the slab structure and the bulk plus the considered compounds (i ranges over the required set of additional compounds). By doing this comparison, it can also be determined whether, upon cleaving, the surface layers would prefer to form the surface or the individual compounds. The equation for surface termination formation energy is

$$E_{f,\mathrm{surface}} = \frac{E_{\mathrm{slab}} - mE_{\mathrm{bulk}} + \sum_i n_i E_i}{2A}. \tag{G.2}$$

m and n_i are integer values such that the number of atoms accounted for due to the bulk and compounds is equivalent to the number of atoms in the in the slab structure (both with the same stoichiometry). Here, A is the area of the surface in the unit cell being used. The formation energy is divided by two lots of the area due to there being two surfaces in a slab calculation (one either side of the slab). For surface formation energies, a negative value describes a system where the material would prefer to separate and form a surface rather than remain as the bulk composite materials. If a negative surface formation energy is obtained for non-stoichiometric surfaces, then it is a likely an error in the materials chosen for comparison. If a negative value is obtained for stoichiometric surfaces, then it describes a material that is unstable in the bulk form.

G.3 Interface formation energy

The interface formation energy $E_{f,\text{interface}}$ is calculated by comparing the energy of the interface structure to that of the two constituent slabs $E_{\text{slab},1}$ and $E_{\text{slab},2}$. The equation is

$$E_{f,\text{interface}} = \frac{E_{\text{interface}} - E_{\text{slab},1} - E_{\text{slab},2}}{2A}. \tag{G.3}$$

Here, A is the area of the interface considered by the unit cell. The area is taken into account twice as the interface structures considered in this work model two symmetrically equivalent interfaces in each unit cell. For an interface structure, a negative formation energy describes a system where the heterostructure is more stable than the constituent slabs. The more negative value, the stronger the bonding at the interface.

G.4 Vacancy formation energies

Vacancy formation energies are determined by comparing the energy of the system with ($E_{\text{vacancy system}}$, the defected system) and without (E_{system}, the defect free system) the considered atom being vacant. The formation energy $E_{f,vacancy}$ of a vacancy is

$$E_{f,\text{adsorption}} = E_{\text{vacancy system}} - E_{\text{system}} + E_{\text{vacancy bulk}}. \tag{G.4}$$

Here, $E_{\text{vacancy bulk}}$ is the energy relating to the bulk that would be formed of the vacant atom. A negative formation energy describes an atom that is more energetically favourable to exist in its bulk phase than in the system.

G.5 Adsorption formation energies

Adsorption energies are determined by comparing the energy of the surface with the adsorbate attached to those of the clean surface and the adsorbate isolated. The formation energy $E_{f,\mathrm{adsorption}}$ of an adsorption structure is as follows:

$$E_{f,\mathrm{adsorption}} = E_{\mathrm{adsorbate+surface}} - E_{\mathrm{surface}} - E_{\mathrm{adsorbate}}. \tag{G.5}$$

A negative adsorption formation energy describes an adsorbate that would prefer to be adsorbed to the surface than be an isolated molecule. The more negative the value, the stronger the adsorption bond.

Appendix H

Common terminology

H.1 Projected density of states

The concept of projected density of states is used throughout this work, appearing in the form of orbital-projected, atom-projected, species-projected, and even layer-projected. A projected density of states is defined as a density of states where contributions of each state are associated with particular *contributors* – here, a contributor is defined as either an orbital, an atom, a species or an atomic layer. As this work uses projector augmented wave (PAW) pseudopotentials, the task of associating contributions of a state to particular orbitals is simplified when compared to methods using other forms of pseudopotentials.

To determine the projected density of states, the overlap between the wave function and a projector must be calculated. As the method employed for PAW pseudopotentials already determines the coefficients relating to the overlap of the atomic orbital projectors with the electron wave functions during the self consistent field cycle, a projected density of states comes at no additional computational cost. To obtain species-projected (layer-projected) density of states, the contributions associated with atoms of a specific species (atomic layer) are summed.

H.2 Local potential

The local potential is formed of the external (ionic) and Hartree potentials, the V_{ext} and V_{H} terms in Equation (2.123) – this is also often termed as the electrostatic potential. It is spatially dependent and, at each point in space, describes the background potential felt by a test charge. The choice of including only the external and Hartree potentials is made due to their much more rapid convergence to the vacuum energy than the exchange-correlation term of the functional, which allows for a more accurate calculation of the work functions and hole affinities.

For local potential plots found in this work, the potential has been averaged across a plane to reduce it down to a one-dimensional function, with the variable being the direction perpendicular to the plane (always the $\mathbf{c}$-axis in this work). The local potential is used to determine the value of the background potential felt in a vacuum region, the vacuum energy; by comparing this value to the Fermi energy, one can determine the hole affinity (work function) of an insulator (metal).

Appendix I

Oxide solar cell transport layers

The bulk density of states for Ca, CaO TiO_2, MoO_3 and $(Sn:Ca)_{7:1}O$ are calculated using the PBE functional. These allow for a comparison between their bulk forms and the heterostructures formed between them.

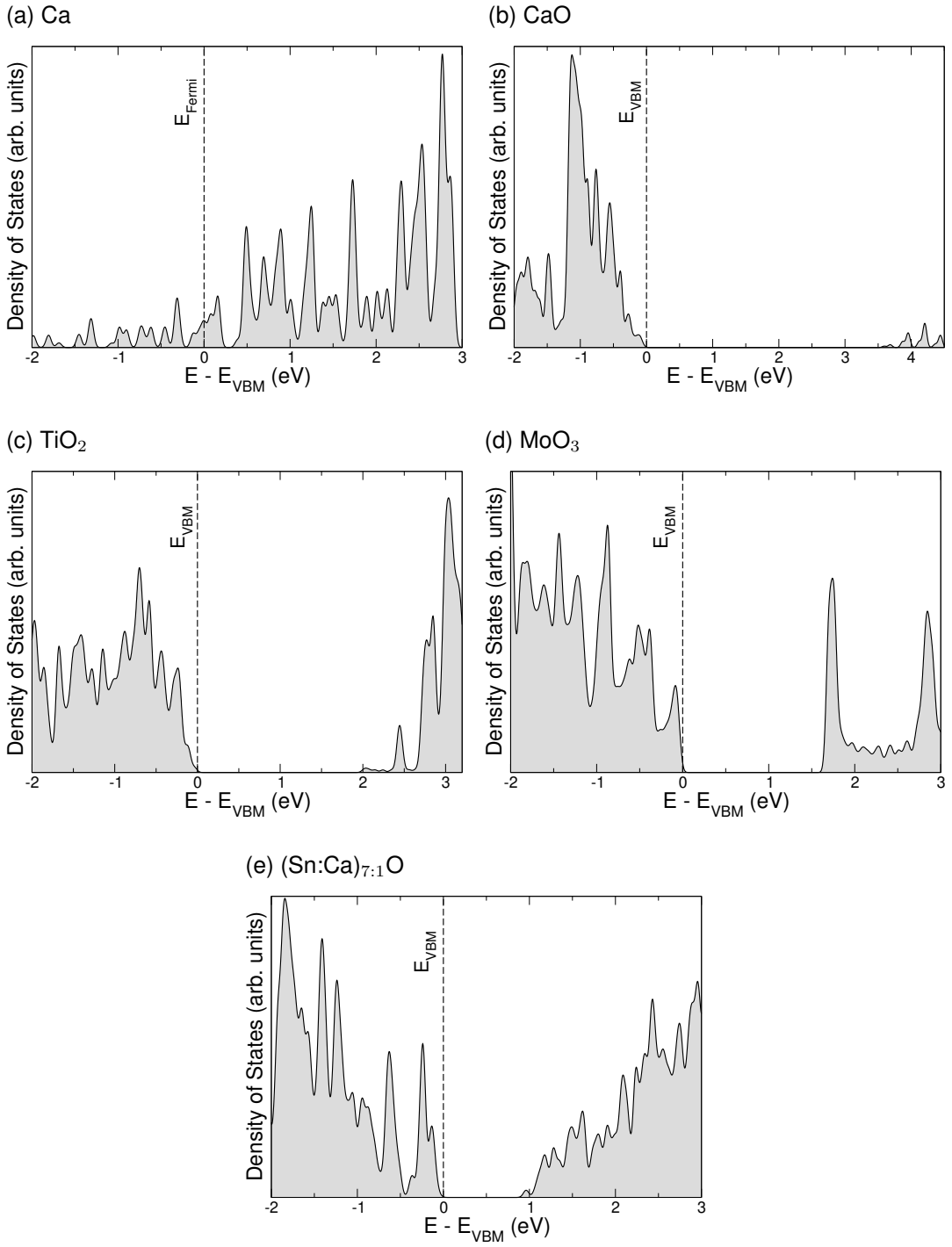

Figure I.1: Electronic density of states for bulk (a) Ca, (b) CaO, (c) TiO_2, (d) MoO_3, and (e) $(Sn:Ca)_{7:1}O$, calculated using PBE.

Appendix J

Calcium stannate overpotential

The overpotentials are evaluated for $CaSnO_3$ and presented in Figure J.1. This was done using the relation between ΔG_2 and ΔG_3 put forward by Man *et al.* for binary oxides and oxide perovskites [376], as well as their noting of these steps always being the rate-limiting step for such materials. Hence, only the adsorption of O, H and OH were modelled in order to obtain these overpotentials. When comparing to the overpotentials of $SrSnO_3$ shown in the main text, we find that $CaSnO_3$ displays much hydrogen and oxygen overpotentials of 1.77 eV and 1.20 eV, respectively (at $\mathrm{pH} = 0$). Neither the hydrogen nor the oxygen overpotentials lie within the surface or bulk band gap of the material. As such, $CaSnO_3$ is disregarded for further study of its water-splitting potential.

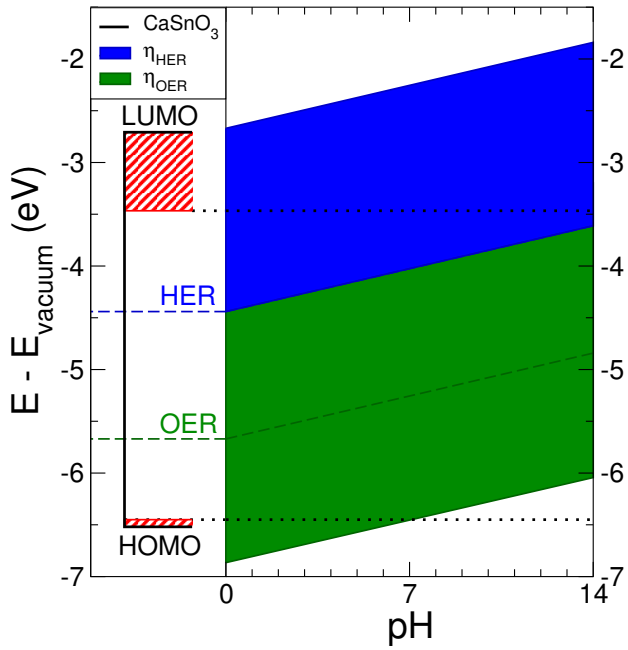

Figure J.1: Overpotential of $CaSnO_3$ in comparison to its bulk and surface band gap. The red hashed regions show to reduction in band gap from the material's bulk band gap (black line). The overpotential has been calculated using Man's rule that highlights that the rate limiting step of oxides and oxide perovskites is step 1 (ΔG_2). The overpotential shown here has been calculated for the standard hydrogen electrode.

Appendix K

Lenstra-Lenstra-Lovász basis reduction

The Lenstra-Lenstra-Lovász (LLL) basis reduction algorithm [428] is used to reduce a basis set $\mathbf{B} = \{\mathbf{b}_1, \mathbf{b}_2, \cdots, \mathbf{b}_d\}$ composed of d basis vectors with n-dimensional integer coordinates (that span a lattice $\mathbf{L}$ with $d \leq n$) down to a short and nearly orthogonal basis set. Effectively, the LLL algorithm attempts to find the shortest vectors, which are as orthogonal as possible, that can represent the lattice $\mathbf{L}$.

Whilst the LLL reduction method cannot definitively identify the shortest possible vectors for systems of greater than 4 dimensions, it is sufficient to identify the shortest possible vectors for the systems we consider (these being three dimensions and lower). Note, this difficulty in pertaining to higher dimensions is faced by all reduction methods.

We start with a basis set

$$\mathbf{B} = \{\mathbf{b}_1, \mathbf{b}_2, \cdots, \mathbf{b}_d\}, \tag{K.1}$$

and use this to set up the Gram-Schmidt process [446] orthogonal vectors $\mathbf{b}^*$,

$$\mathbf{b}_i^* = \mathbf{b}_i - \sum_{j=1}^{i-1} \mathrm{proj}_{\mathbf{b}_j^*}(\mathbf{b}_i), \tag{K.2}$$

where $\mathrm{proj}_{\mathbf{u}}(\mathbf{v})$ (the *projection operator*) defines the projection of vector $\mathbf{v}$ onto vector $\mathbf{u}$,

$$\mathrm{proj}_{\mathbf{u}}(\mathbf{v}) = \frac{\langle \mathbf{v}, \mathbf{u} \rangle}{\langle \mathbf{u}, \mathbf{u} \rangle} \mathbf{u}. \tag{K.3}$$

Note that $\langle \mathbf{u}, \mathbf{v} \rangle$ – the inner product – is equivalent to $\mathbf{u}^{\mathrm{T}}\mathbf{v}$ for real numbers, which is the case in this work. Using the individual vectors, we can define the Gram-Schmidt process orthogonal basis as

$$\mathbf{B}^* = \{\mathbf{b}_1^*, \mathbf{b}_2^*, \cdots, \mathbf{b}_n^*\}, \tag{K.4}$$

which has Gram-Schmidt coefficients of

$$\mu_{i,j} = \frac{\langle \mathbf{b}_i, \mathbf{b}_j^* \rangle}{\langle \mathbf{b}_j^*, \mathbf{b}_j^* \rangle} \quad \text{for any} \quad 1 \leq j \leq i \leq n. \tag{K.5}$$

The basis can be said to be LLL-reduced if there exists a parameter δ in the range $(0.25, 1)$ where the following conditions are satisfied:

1) For $1 \leq j \leq n : |\mu_{i,j}| \leq 0.5$, which guarantees the length reduction of the ordered basis (size-reduced).

2) For $k = 1, 2, \cdots, n : \delta |\mathbf{b}_{k-1}^*|^2 \leq |\mathbf{b}_k^*|^2 + \mu_{k,k-1}^2 |\mathbf{b}_{k-1}^*|^2$ (Lovász condition).

By using the initial basis set (K.1), one can determine the Gram-Schmidt orthogonal basis and its coefficients in order to determine whether the basis is LLL-reduced. If it is not, then the individual basis vectors are updated as follows:

$$\mathbf{b}_i = \mathbf{b}_i - |\mu_{i,j}| \mathbf{b}_j. \tag{K.6}$$

After any basis vector is modified, the appropriate Gram-Schmidt basis and coefficients must also be updated to use the newest basis set. This process is repeated until both conditions 1) and 2) are met, at which point, the basis set is considered LLL-reduced, where each vector in the basis set should be the shortest, and most orthogonal, possible basis vectors for the lattice. Note that this method works only for bases composed of integer coordinates.

Bibliography

[1] P. the Elder. *The Natural History*. Taylor and Francis, London, 1855.

[2] H. Jinno, K. Fukuda, X. Xu, S. Park, Y. Suzuki, *et al.* Stretchable and waterproof elastomer-coated organic photovoltaics for washable electronic textile applications. *Nature Energy*, **2**(10), (2017), pp. 780–785.

[3] C. Kittel. *Introduction to Solid State Physics*. Wiley, 8th edition, 2004.

[4] K. J. Jin, H. B. Lu, K. Zhao, C. Ge, M. He, *et al.* Novel multifunctional properties induced by interface effects in perovskite oxide heterostructures. *Advanced Materials*, **21**(45), (2009), pp. 4636–4640.

[5] P. Yu, Y. H. Chu, and R. Ramesh. Oxide interfaces: Pathways to novel phenomena. *Materials Today*, **15**(7-8), (2012), pp. 320–327.

[6] H. Hwang, Y. Iwasa, M. Kawasaki, B. Keimer, N. Nagaosa, *et al.* Emergent phenomena at oxide interfaces. *Nature Materials*, **11**(2), (2012), pp. 103–113.

[7] K. Aust. Principles of crystal growth from the solid state in relation to the preparation of large crystals. *Journal of Crystal Growth*, **13-14**(C), (1972), pp. 57–61.

[8] I. Kaur, Y. Mishin, and W. Gust. *Fundamentals of grain and interphase boundary diffusion*. Wiley, Chichester, UK, 3rd edition, 1995.

[9] W. Schottky. Vereinfachte und erweiterte Theorie der Randschicht-gleichrichter. *Zeitschrift für Physik*, **118**(9-10), (1942), pp. 539–592.

[10] J. Bardeen. Surface states and rectification at a metal semi-conductor contact. *Physical Review*, **71**(10), (1947), pp. 717–727.

[11] J. L. MacManus-Driscoll, M. P. Wells, C. Yun, J. W. Lee, C. B. Eom, *et al.* New approaches for achieving more perfect transition metal oxide thin films. *APL Materials*, **8**(4), (2020), p. 040904.

[12] H. Ibach and H. Lüth. *Solid-State Physics*. Springer Berlin Heidelberg, Berlin, Heidelberg, 2009.

[13] A. R. Gerson, R. K. Druitt, Y. Ikuma, S. J. Kang, J. Nowotny, *et al.* Development of novel materials through interface engineering. *Ionics*, **7**(4-6), (2001), pp. 241–246.

[14] N. F. Mott. Note on the contact between a metal and an insulator or semi-conductor. *Mathematical Proceedings of the Cambridge Philosophical Society*, **34**(4), (1938), pp. 568–572.

[15] W. Schottky. Abweichung vom Ohmschen Gesetz in Halbleitern. *Zeitschrift für Physik*, **41**, (1940), pp. 570–573.

[16] J. F. Wager. Transparent electronics: Schottky barrier and heterojunction considerations. *Thin Solid Films*, **516**(8), (2008), pp. 1755–1764.

[17] S. Gariglio, N. Reyren, A. D. Caviglia, and J. M. Triscone. Superconductivity at the $LaAlO_3/SrTiO_3$ interface. *Journal of Physics Condensed Matter*, **21**(16), (2009), pp. 2–5.

[18] M. Ribeiro, L. R. Fonseca, and L. G. Ferreira. First-principles calculation of the AlAs/GaAs interface band structure using a self-energy-corrected local density approximation. *Europhysics Letters*, **94**(2), (2011), p. 27001.

[19] M. Coll, J. Fontcuberta, M. Althammer, M. Bibes, H. Boschker, *et al.* Towards oxide electronics: a roadmap. *Applied Surface Science*, **482**, (2019), pp. 1–93.

[20] S. A. Campbell, D. C. Gilmer, X. C. Wang, M. T. Hsieh, H. S. Kim, *et al.* MOSFET transistors fabricated with high permitivity TiO_2 dielectrics. *IEEE Transactions on Electron Devices*, **44**(1), (1997), pp. 104–109.

[21] M. Lorenz, M. S. Ramachandra Rao, T. Venkatesan, E. Fortunato, P. Barquinha, *et al.* The 2016 oxide electronic materials and oxide interfaces roadmap. *Journal of Physics D: Applied Physics*, **49**(43), (2016), p. 433001.

[22] Y. Zhou, Z. Zhang, Z. Fang, M. Qiu, L. Ling, *et al.* Defect engineering of metal-oxide interface for proximity of photooxidation and photoreduction. *Proceedings of the National Academy of Sciences of the United States of America*, **116**(21), (2019), pp. 10232–10237.

[23] P. Zubko, S. Gariglio, M. Gabay, P. Ghosez, and J.-M. Triscone. Interface physics in complex oxide heterostructures. *Annual Review of Condensed Matter Physics*, **2**(1), (2011), pp. 141–165.

[24] R. Schmidt and D. C. Sinclair. *$CaCu_3Ti_4O_{12}$ (CCTO) Ceramics for Capacitor Applications*. Nova Science Publishers, 2013.

[25] Y. Zhang, W. Li, Z. Wang, Y. Qiao, Y. Yu, *et al.* Ultrahigh energy storage and electrocaloric performance achieved in $SrTiO_3$ amorphous thin films: Via polar cluster engineering. *Journal of Materials Chemistry A*, **7**(30), (2019), pp. 17797–17805.

[26] Y. Fan, Z. Zhou, Y. Chen, W. Huang, and X. Dong. A novel lead-free and high-performance barium strontium titanate-based thin film capacitor with ultrahigh energy storage density and giant power density. *Journal of Materials Chemistry C*, **8**(1), (2019), pp. 50–57.

[27] S. De Almeida-Didry, C. Autret, C. Honstettre, A. Lucas, F. Pacreau, *et al.* Capacitance scaling of grain boundaries with colossal permittivity of $CaCu_3Ti_4O_{12}$ -based materials. *Solid State Sciences*, **42**, (2015), pp. 25–29.

[28] J. Li, F. Li, C. Li, G. Yang, Z. Xu, *et al.* Evidences of grain boundary capacitance effect on the colossal dielectric permittivity in (Nb + In) co-doped TiO_2 ceramics. *Scientific Reports*, **5**, (2015), pp. 2–7.

[29] A. V. Kimmel, I. Jorge, M. G. Cain, and P. V. Sushko. Neutral and charged oxygen vacancies induce two-dimensional electron gas near $SiO_2/BaTiO_3$ interfaces. *The Journal of Physical Chemistry Letters*, **4**, (2013), p. 333.

[30] C. Xu, Z. Zhang, J. Zhang, L. Lei, D. Zhang, *et al.* A new route to fabricate barium titanate with high permittivity. *Ceramics International*, **40**(7), (2014), pp. 10927–10931.

[31] S. Cho, C. Yun, Y. S. Kim, H. H. Wang, J. Jian, *et al.* Strongly enhanced dielectric and energy storage properties in lead-free perovskite titanate thin films by alloying. *Nano Energy*, **45**(September 2017), (2018), pp. 398–406.

[32] U.-C. Chung, C. Elissalde, F. Mompiou, J. Majimel, S. Gomez, *et al.* Interface investigation in nanostructured $BaTiO_3$/Silica composite ceramics. *Journal of the American Ceramic Society*, **93**(3), (2010), pp. 865–874.

[33] P. Chen, S. Wu, P. Li, J. Zhai, and B. Shen. Great enhancement of energy storage density and power density in BNBT/*x*BFO multilayer thin film hetero-structures. *Inorganic Chemistry Frontiers*, **5**(9), (2018), pp. 2300–2305.

[34] C. Diao, H. Liu, G. Lou, H. Zheng, Z. Yao, *et al.* Structure and electric properties of sandwich-structured $SrTiO_3$/$BiFeO_3$ thin films for energy storage applications. *Journal of Alloys and Compounds*, **781**, (2019), pp. 378–384.

[35] A. Chandra, G. Anderson, S. Melkote, W. Gao, H. Haitjema, *et al.* Role of surfaces and interfaces in solar cell manufacturing. *CIRP Annals - Manufacturing Technology*, **63**(2), (2014), pp. 797–819.

[36] A. Agresti, A. Pazniak, S. Pescetelli, A. Di Vito, D. Rossi, *et al.* Titanium-carbide MXenes for work function and interface engineering in perovskite solar cells. *Nature Materials*, **18**(11), (2019), pp. 1228–1234.

[37] O. Björneholm, M. H. Hansen, A. Hodgson, L. M. Liu, D. T. Limmer, *et al.* Water at interfaces. *Chemical Reviews*, **116**(13), (2016), pp. 7698–7726.

[38] Y. Hu, C. Gao, and Y. Xiong. Surface and interface design for photocatalytic water splitting. *Dalton Transactions*, **47**(35), (2018), pp. 12035–12040.

[39] O. Neufeld, N. Yatom, and M. Caspary Toroker. A first-principles study on the role of an Al_2O_3 overlayer on Fe_2O_3 for water splitting. *ACS Catalysis*, **5**(12), (2015), pp. 7237–7243.

[40] F. Le Formal, N. Tétreault, M. Cornuz, T. Moehl, M. Grätzel, *et al.* Passivating surface states on water splitting hematite photoanodes with alumina overlayers. *Chemical Science*, **2**(4), (2011), pp. 737–743.

[41] S. H. Simon. *The Oxford Solid State Basics*. Oxford University Press, Oxford, UK, 2013.

[42] S. M. Girvin and K. Yang. *Modern Condensed Matter Physics*. Cambridge University Press, Cambridge, UK, 2019.

[43] W. H. Miller. *A Treatise on Crystallography*. J. & J. J. Deighton, Cambridge, 1839.

[44] R. M. Martin. *Electronic Structure: Basic Theory and Practical Methods*. Cambridge University Press, Cambridge, 2004.

[45] M. Born and R. Oppenheimer. Zur Quantentheorie der Molekeln. *Annalen der Physik*, **389**(20), (1927), pp. 457–484.

[46] W. Ritz. Über eine neue Methode zur Lösung gewisser Variationsprobleme der mathematischen Physik. *Journal fur die Reine und Angewandte Mathematik*, **135**(1), (1909), pp. 1–61.

[47] D. R. Hartree. The wave mechanics of an atom with a non-coulomb central field. Part I. Theory and Methods. *Mathematical Proceedings of the Cambridge Philosophical Society*, **24**(1), (1928), pp. 89–110.

[48] J. C. Slater. Note on Hartree's Method. *Physical Review*, **35**(2), (1930), pp. 210–211.

[49] V. Fock. Näherungsmethode zur Lösung des quantenmechanischen Mehrkörperproblems. *Zeitschrift für Physik*, **61**(1-2), (1930), pp. 126–148.

[50] V. Fock. "Selfconsistent field" mit Austausch für Natrium. *Zeitschrift für Physik*, **62**(11-12), (1930), pp. 795–805.

[51] J. C. Slater. The self consistent field and the structure of atoms. *Physical Review*, **32**(3), (1928), pp. 339–348.

[52] P. Hohenberg and W. Kohn. Inhomogeneous electron gas. *Physical Review*, **136**(3B), (1964), pp. B864–B871.

[53] W. Kohn and L. J. Sham. Self-consistent equations including exchange and correlation effects. *Physical Review*, **140**(4A), (1965), pp. A1133–A1138.

[54] M. Levy. Universal variational functionals of electron densities, first-order density matrices, and natural spin-orbitals and solution of the v-representability problem. *Proceedings of the National Academy of Sciences of the United States of America*, **76**(12), (1979), pp. 6062–6065.

[55] M. Levy. Electron densities in search of Hamiltonians. *Physical Review A*, **26**(3), (1982), pp. 1200–1208.

[56] E. H. Lieb. Density functionals for coulomb systems. *International Journal of Quantum Chemistry*, **24**(3), (1983), pp. 243–277.

[57] L. Hedin, B. I. Lundqvist, and S. Lundqvist. Local exchange-correlation potentials. *Solid State Communications*, **9**(9), (1971), pp. 537–541.

[58] J. P. Perdew and A. Zunger. Self-interaction correction to density-functional approximations for many-electron systems. *Physical Review B*, **23**(10), (1981), pp. 5048–5079.

[59] S. H. Vosko, L. Wilk, and M. Nusair. Accurate spin-dependent electron liquid correlation energies for local spin density calculations: a critical analysis. *Canadian Journal of Physics*, **58**(8), (1980), pp. 1200–1211.

[60] D. C. Langreth and M. J. Mehl. Beyond the local-density approximation in calculations of ground-state electronic properties. *Physical Review B*, **28**(4), (1983), pp. 1809–1834.

[61] A. D. Becke. Density-functional exchange-energy approximation with correct asymptotic behavior. *Physical Review A*, **38**(6), (1988), pp. 3098–3100.

[62] J. P. Perdew, J. A. Chevary, S. H. Vosko, K. A. Jackson, M. R. Pederson, *et al.* Atoms, molecules, solids, and surfaces: Applications of the generalized gradient approximation for exchange and correlation. *Physical Review B*, **46**(11), (1992), pp. 6671–6687.

[63] J. P. Perdew, K. Burke, and M. Ernzerhof. Generalized gradient approximation made simple. *Physical Review Letters*, **77**(18), (1996), pp. 3865–3868.

[64] R. Van Noorden, B. Maher, and R. Nuzzo. The top 100 papers. *Nature*, **514**(7524), (2014), pp. 550–553.

[65] L. He, F. Liu, G. Hautier, M. J. Oliveira, M. A. Marques, *et al.* Accuracy of generalized gradient approximation functionals for density-functional perturbation theory calculations. *Physical Review B*, **89**(6), (2014), p. 064305.

[66] G. X. Zhang, A. M. Reilly, A. Tkatchenko, and M. Scheffler. Performance of various density-functional approximations for cohesive properties of 64 bulk solids. *New Journal of Physics*, **20**(6), (2018), p. 063020.

[67] A. D. Becke. A new mixing of Hartree-Fock and local density-functional theories. *Journal of Chemical Physics*, **98**(2), (1993), pp. 1372–1377.

[68] A. J. Garza and G. E. Scuseria. Predicting band gaps with hybrid density functionals. *The Journal of Physical Chemistry Letters*, **7**(20), (2016), pp. 4165–4170.

[69] J. P. Perdew, M. Ernzerhof, and K. Burke. Rationale for mixing exact exchange with density functional approximations. *Journal of Chemical Physics*, **105**(22), (1996), pp. 9982–9985.

[70] K. Kim and K. D. Jordan. Comparison of density functional and MP2 calculations on the water monomer and dimer. *The Journal of Physical Chemistry*, **98**(40), (1994), pp. 10089–10094.

[71] P. J. Stephens, F. J. Devlin, C. F. Chabalowski, and M. J. Frisch. *Ab Initio* calculation of vibrational absorption and circular dichroism spectra using density functional force fields. *The Journal of Physical Chemistry*, **98**(45), (1994), pp. 11623–11627.

[72] J. Heyd, G. E. Scuseria, and M. Ernzerhof. Hybrid functionals based on a screened Coulomb potential. *Journal of Chemical Physics*, **118**(18), (2003), pp. 8207–8215.

[73] O. A. Vydrov, J. Heyd, A. V. Krukau, and G. E. Scuseria. Importance of short-range versus long-range Hartree-Fock exchange for the performance of hybrid density functionals. *The Journal of Chemical Physics*, **125**(7), (2006), p. 074106.

[74] C. Herring. A new method for calculating wave functions in crystals. *Physical Review*, **57**(12), (1940), pp. 1169–1177.

[75] E. Antončík. Approximate formulation of the orthogonalized plane-wave method. *Journal of Physics and Chemistry of Solids*, **10**(4), (1959), pp. 314–320.

[76] J. C. Phillips and L. Kleinman. New method for calculating wave functions in crystals and molecules. *Physical Review*, **116**(2), (1959), pp. 287–294.

[77] P. E. Blöchl. Projector augmented-wave method. *Physical Review B*, **50**(24), (1994), pp. 17953–17979.

[78] G. Kresse. From ultrasoft pseudopotentials to the projector augmented-wave method. *Physical Review B*, **59**(3), (1999), pp. 1758–1775.

[79] H. Hellmann. *Einführung in die Quantenchemie*. Franz Deticke, Leipzig, 1937.

[80] R. P. Feynman. Forces in molecules. *Physical Review*, **56**(4), (1939), pp. 340–343.

[81] G. P. Srivastava. *Theoretical Modelling of Semiconductor Surfaces*. World Scientific, 1999.

[82] C. J. Pickard and R. J. Needs. High-pressure phases of silane. *Physical Review Letters*, **97**(4), (2006), p. 045504.

[83] C. J. Pickard and R. J. Needs. Ab initio random structure searching. *Journal of Physics: Condensed Matter*, **23**(5), (2011), p. 053201.

[84] A. Zur and T. C. McGill. Lattice match: An application to heteroepitaxy. *Journal of Applied Physics*, **55**(2), (1984), pp. 378–386.

[85] G. Kresse and J. Hafner. Ab initio molecular dynamics for liquid metals. *Physical Review B*, **47**(1), (1993), pp. 558–561.

[86] G. Kresse and J. Furthmüller. Efficient iterative schemes for ab initio total-energy calculations using a plane-wave basis set. *Physical Review B*, **54**(16), (1996), pp. 11169–11186.

[87] G. Kresse and J. Furthmüller. Efficiency of ab-initio total energy calculations for metals and semiconductors using a plane-wave basis set. *Computational Materials Science*, **6**(1), (1996), pp. 15–50.

[88] H. J. Monkhorst and J. D. Pack. Special points for Brillouin-zone integrations. *Physical Review B*, **13**(12), (1976), pp. 5188–5192.

[89] S. Baroni and R. Resta. Ab initio calculation of the macroscopic dielectric constant in silicon. *Physical Review B*, **33**(10), (1986), pp. 7017–7021.

[90] N. Sai, K. M. Rabe, and D. Vanderbilt. Theory of structural response to macroscopic electric fields in ferroelectric systems. *Physical Review B*, **66**(10), (2002), pp. 1041081–10410817.

[91] Y. Le Page and P. Saxe. Symmetry-general least-squares extraction of elastic data for strained materials from *ab initio* calculations of stress. *Physical Review B*, **65**(10), (2002), p. 104104.

[92] K. Momma and F. Izumi. VESTA 3 for three-dimensional visualization of crystal, volumetric and morphology data. *Journal of Applied Crystallography*, **44**(6), (2011), pp. 1272–1276.

[93] C. G. Broyden. A class of methods for solving nonlinear simultaneous equations. *Mathematics of Computation*, **19**(92), (1965), p. 577.

[94] P. Pulay. Convergence acceleration of iterative sequences. The case of SCF iteration. *Chemical Physics Letters*, **73**(2), (1980), pp. 393–398.

[95] D. D. Johnson. Modified Broyden's method for accelerating convergence in self-consistent calculations. *Physical Review B*, **38**(18), (1988), pp. 12807–12813.

[96] R. K. Pandey, W. A. Stapleton, J. Tate, A. K. Bandyopadhyay, I. Sutanto, *et al.* Applications of CCTO supercapacitor in energy storage and electronics. *AIP Advances*, **3**(6), (2013), p. 062126.

[97] R. Löhnert, H. Bartsch, R. Schmidt, B. Capraro, and J. Töpfer. Microstructure and electric properties of $CaCu_3Ti_4O_{12}$ multilayer capacitors. *Journal of the American Ceramic Society*, **98**(1), (2015), pp. 141–147.

[98] M. A. Ponce, M. A. Ramirez, F. Schipani, E. Joanni, J. P. Tomba, *et al.* Electrical behavior analysis of n-type $CaCu_3Ti_4O_{12}$ thick films exposed to different atmospheres. *Journal of the European Ceramic Society*, **35**(1), (2015), pp. 153–161.

[99] M. A. Subramanian, D. Li, N. Duan, B. A. Reisner, and a. W. Sleight. High dielectric constant in $ACu_3Ti_4O_{12}$ and $ACu_3Ti_3FeO_{12}$ phases. *Journal of Solid State Chemistry*, **151**(2), (2000), pp. 323–325.

[100] J. C. Maxwell. *A Treatise on Electricity and Magnetism*. A Treatise on Electricity and Magnetism. Clarendon Press, 1873.

[101] K. W. Wagner. Erklärung der dielektrischen Nachwirkungsvorgänge auf Grund Maxwellscher Vorstellungen. *Archiv für Elektrotechnik*, **2**(9), (1914), pp. 371–387.

[102] R. Sillars. The properties of a dielectric containing semiconducting particles of various shapes. *Institution of Electrical Engineers - Proceedings of the Wireless Section of the Institution*, **12**(35), (1937), pp. 139–155.

[103] W. Rothwell. Complex permittivity of conductor-dielectric mixtures (correspondence). *IEEE Transactions on Microwave Theory and Techniques*, **19**(4), (1971), pp. 413–415.

[104] A. I. Kingon, S. K. Streiffer, C. Basceri, and S. R. Summerfelt. High-permittivity perovskite thin films for dynamic random-access memories. *MRS Bulletin*, **21**(7), (1996), pp. 46–52.

[105] D. E. Kotecki. A review of high dielectric materials for dram capacitors. *Integrated Ferroelectrics*, **16**(1-4), (1997), pp. 1–19.

[106] Y.-S. Shen, C.-C. Ho, and B.-S. Chiou. Impedance spectroscopy of $CaCu_3Ti_4O_{12}$ films showing resistive switching. *Journal of The Electrochemical Society*, **156**(6), (2009), pp. H466–H470.

[107] J. Gao, Y. Wang, Y. Liu, X. Hu, X. Ke, *et al.* Enhancing dielectric permittivity for energy-storage devices through tricritical phenomenon. *Scientific Reports*, **7**(January), (2017), p. 40916.

[108] P. Mao, J. Wang, S. Liu, L. Zhang, Y. Zhao, *et al.* Improved dielectric and nonlinear properties of $CaCu_3Ti_4O_{12}$ ceramics with Cu-rich phase at grain boundary layers. *Ceramics International*, **45**(12), (2019), pp. 15082–15090.

[109] M. Li, X. Chen, D. Zhang, W. Wang, and W. Wang. Humidity sensitive properties of pure and Mg-doped $CaCu_3Ti_4O_{12}$. *Sensors and Actuators B: Chemical*, **147**(2), (2010), pp. 447–452.

[110] M. Ahmadipour, M. F. Ain, and Z. A. Ahmad. A short review on copper calcium titanate (CCTO) electroceramic: synthesis, dielectric properties, film Deposition, and sensing application. *Nano-Micro Letters*, **8**(4), (2016), pp. 291–311.

[111] J. S. Toll. Causality and the Dispersion Relation: Logical Foundations. *Physical Review*, **104**(6), (1956), pp. 1760–1770.

[112] A. Deschanvres, B. Raveau, and F. Tollemer. Substitution of copper for a bivalent metal in titanates of perovskite type. *Bulletin de la Societe Chimique de France*, (11), (1967), p. 4077.

[113] M. K. Bera and C. K. Maiti. Electrical properties of SiO_2/TiO_2 high-k gate dielectric stack. *Materials Science in Semiconductor Processing*, **9**(6), (2006), pp. 909–917.

[114] K. Yim, Y. Yong, J. Lee, K. Lee, H. H. Nahm, *et al.* Novel high-κ dielectrics for next-generation electronic devices screened by automated ab initio calculations. *NPG Asia Materials*, **7**(6), (2015), pp. 1–6.

[115] B. Wang, W. Huang, L. Chi, M. Al-Hashimi, T. J. Marks, *et al.* High-k Gate Dielectrics for Emerging Flexible and Stretchable Electronics. *Chemical Reviews*, **118**(11), (2018), pp. 5690–5754.

[116] S. Krohns, P. Lunkenheimer, S. G. Ebbinghaus, and A. Loidl. Colossal dielectric constants in single-crystalline and ceramic $CaCu_3Ti_4O_{12}$ investigated by broadband dielectric spectroscopy. *Journal of Applied Physics*, **103**(8), (2008), p. 084107.

[117] K. Prompa, E. Swatsitang, C. Saiyasombat, and T. Putjuso. Very high performance dielectric and non-Ohmics properties of $CaCu_3Ti_{4.2}O_{12}$ ceramics for X8R capacitors. *Ceramics International*, **44**(11), (2018), pp. 13267–13277.

[118] P. B. A. Fechine, A. F. L. Almeida, F. N. A. Freire, M. R. P. Santos, F. M. M. Pereira, *et al.* Dielectric relaxation of $BaTiO_3$ (BTO)-$CaCu_3Ti_4O_{12}$ (CCTO) composite screen-printed thick films at low temperatures. *Materials Chemistry and Physics*, **96**(2-3), (2006), pp. 402–408.

[119] O. a. a. Abdelal, A. a. Hassan, and M. E.-s. Ali. Dielectric properties of Calcium Copper Titanates ($CaCu_3Ti_4O_{12}$) synthesized by solid state reaction. *International Journal of Advanced Research in Chemical Science*, **45**(2), (2014), pp. 354–361.

[120] L. C. Kretly, A. F. L. Almeida, P. B. A. Fechine, R. S. De Oliveira, and A. S. B. Sombra. Dielectric permittivity and loss of $CaCu_3Ti_4O_{12}$ (CCTO) substrates for

microwave devices and antennas. *Journal of Materials Science: Materials in Electronics*, **15**(10), (2004), pp. 657–663.

[121] Y. Wang, W. Jie, C. Yang, X. Wei, and J. Hao. Colossal Permittivity Materials as Superior Dielectrics for Diverse Applications. *Advanced Functional Materials*, **29**(27), (2019), p. 1808118.

[122] A. von Hippel, R. G. Breckenridge, F. G. Chesley, and L. Tisza. High dielectric constant ceramics. *Industrial & Engineering Chemistry*, **38**(11), (1946), pp. 1097–1109.

[123] A. R. West, T. B. Adams, F. D. Morrison, and D. C. Sinclair. Novel high capacitance materials:- $BaTiO_3$:La and $CaCu_3Ti_4O_{12}$. *Journal of the European Ceramic Society*, **24**(6), (2004), pp. 1439–1448.

[124] T. Adams, D. Sinclair, and A. West. Giant barrier layer capacitance effects in $CaCu_3Ti_4O_{12}$ ceramics. *Advanced Materials*, **14**(18), (2002), pp. 1321–1323.

[125] D. C. Sinclair, T. B. Adams, F. D. Morrison, and A. R. West. $CaCu_3Ti_4O_{12}$: One-step internal barrier layer capacitor. *Applied Physics Letters*, **80**(12), (2002), pp. 2153–2155.

[126] P. Salame, R. Drai, O. Prakash, and A. R. Kulkarni. IBLC effect leading to colossal dielectric constant in layered structured Eu_2CuO_4 ceramic. *Ceramics International*, **40**(3), (2014), pp. 4491–4498.

[127] A. Koitzsch, G. Blumberg, A. Gozar, B. Dennis, A. P. Ramirez, *et al.* Antiferromagnetism in $CaCu_3Ti_40_{12}$ studies by magnetic Raman spectroscopy. *Physical Review B*, **65**(5), (2002), p. 052406.

[128] G.-L. Li, Z. Yin, and M.-S. Zhang. First-principles study of the electronic and magnetic structures of $CaCu_3Ti_4O_{12}$. *Physics Letters A*, **344**(2-4), (2005), pp. 238–246.

[129] C. C. Homes, T. Vogt, S. M. Shapiro, S. Wakimoto, and A. P. Ramirez. Optical Response of High-Dielectric-Constant Perovskite-Related Oxide. *Science*, **293**(5530), (2001), pp. 673–676.

[130] A. P. Litvinchuk, C. L. Chen, N. Kolev, V. N. Popov, V. G. Hadjiev, *et al.* Optical properties of high-dielectric-constant $CaCu_3Ti_4O_{12}$ films. *Physica Status Solidi (A) Applied Research*, **195**(2), (2003), pp. 453–458.

[131] L. He, J. B. Neaton, D. Vanderbilt, and M. H. Cohen. Lattice Dielectric Response of $CdCu_3Ti_4O_{12}$ and $CaCu_3Ti_4O_{12}$ from First Principles. *Physical Review B*, **67**(1), (2003), pp. 121031–121034.

[132] C. Kant, T. Rudolf, F. Mayr, S. Krohns, P. Lunkenheimer, *et al.* Broadband dielectric response of $CaCu_3Ti_4O_{12}$: From dc to the electronic transition regime. *Physical Review B*, **77**(4), (2008), p. 045131.

[133] G. Li, Z. Yin, and M. Zhang. Study on optical and dielectric properties of $CaCu_3Ti_4O_{12}$ by first-principles calculation. *Materials Science and Engineering: B*, **150**(3), (2008), pp. 163–167.

[134] P. Lunkenheimer, S. Krohns, S. Riegg, S. G. Ebbinghaus, A. Reller, *et al.* Colossal dielectric constants in transition-metal oxides. *European Physical Journal: Special Topics*, **180**(1), (2009), pp. 61–89.

[135] M. C. Ferrarelli, D. C. Sinclair, A. R. West, H. a. Dabkowska, A. Dabkowski, *et al.* Comment on the origin(s) of the giant permittivity effect in $CaCu_3Ti_4O_{12}$ single crystals and ceramics. *Journal of Materials Chemistry*, **19**(33), (2009), p. 5916.

[136] S. De Almeida-Didry, C. Autret, A. Lucas, C. Honstettre, F. Pacreau, *et al.* Leading role of grain boundaries in colossal permittivity of doped and undoped CCTO. *Journal of the European Ceramic Society*, **34**(15), (2014), pp. 3649–3654.

[137] S. F. Shao, J. L. Zhang, P. Zheng, W. L. Zhong, and C. L. Wang. Microstructure and electrical properties of $CaCu_3Ti_4O_{12}$ ceramics. *Journal of Applied Physics*, **99**(8), (2006), p. 084106.

[138] P. Thongbai, S. Pinitsoontorn, V. Amornkitbamrung, T. Yamwong, S. Maensiri, *et al.* Reducing Loss Tangent by Controlling Microstructure and Electrical Responses in $CaCu_3Ti_4O_{12}$ Ceramics Prepared by a Simple Combustion Method. *International Journal of Applied Ceramic Technology*, **10**(January 2015), (2013), pp. E77–E87.

[139] T. Adams, D. Sinclair, and A. West. Influence of Processing Conditions on the Electrical Properties of $CaCu_3Ti_4O_{12}$ Ceramics. *Journal of the American Ceramic Society*, **89**(10), (2006), pp. 3129–3135.

[140] W. Li, O. Auciello, R. N. Premnath, and B. Kabius. Giant dielectric constant dominated by Maxwell-Wagner relaxation in Al_2O_3/TiO_2 nanolaminates synthesized by atomic layer deposition. *Applied Physics Letters*, **96**(16), (2010), p. 162907.

[141] P. Walke, R. Bouregba, A. Lefevre, G. Parat, F. Lallemand, *et al.* Giant dielectric constant in TiO_2/Al_2O_3 nanolaminates grown on doped silicon substrate by pulsed laser deposition. *Journal of Applied Physics*, **115**(9), (2014), p. 094103.

[142] C.-F. Yang. Improvement of the sintering and dielectric characteristics of surface barrier layer capacitors by CuO addition. *Japanese Journal of Applied Physics*, **35**(3), (1996), pp. 1806– 1813.

[143] C.-F. Yang. An equivalent cicuit for CuO modified surface barrier layer capacitors. *Japanese Journal of Applied Physics*, **36**(Part 1, No. 1A), (1997), pp. 188–193.

[144] S. Sarkar, P. K. Jana, B. K. Chaudhuri, and H. Sakata. Copper (II) oxide as a giant dielectric material. *Applied Physics Letters*, **89**(21), (2006), p. 212905.

[145] P. Cheng, H. Liu, L. Song, and C. Xia. Dielectric response of $CaCu_3Ti_4O_{12}$ materials. In *2011 Second International Conference on Mechanic Automation and Control Engineering*, volume 94, pp. 7303–7306. IEEE, 2011.

[146] P. Lunkenheimer, R. Fichtl, S. G. Ebbinghaus, and A. Loidl. Nonintrinsic origin of the colossal dielectric constants in $CaCu_3Ti_4O_{12}$. *Physical Review B*, **70**(17), (2004), p. 172102.

[147] K. Chen, G. L. Li, F. Gao, J. Liu, J. M. Liu, *et al.* Conducting grain boundaries in the high-dielectric-constant ceramic $CaCu_3Ti_4O_{12}$. *Journal of Applied Physics*, **101**(7), (2007), p. 074101.

[148] M. Li, Z. Shen, M. Nygren, A. Feteira, D. C. Sinclair, *et al.* Origin(s) of the apparent high permittivity in $CaCu_3Ti_4O_{12}$ ceramics: Clarification on the contributions from internal barrier layer capacitor and sample-electrode contact effects. *Journal of Applied Physics*, **106**(10), (2009), p. 104106.

[149] M. Li, D. C. Sinclair, and A. R. West. Extrinsic origins of the apparent relaxorlike behavior in $CaCu_3Ti_4O_{12}$ ceramics at high temperatures: A cautionary tale. *Journal of Applied Physics*, **109**(8), (2011), p. 084106.

[150] T. B. Adams, D. C. Sinclair, and A. R. West. Characterization of grain boundary impedances in fine- and coarse-grained $CaCu_3Ti_4O_{12}$ ceramics. *Physical Review B*, **73**(9), (2006), p. 094124.

[151] I.-D. Kim, A. Rothschild, and H. L. Tuller. Direct current bias effects on grain boundary Schottky barriers in $CaCu_3Ti_4O_{12}$. *Applied Physics Letters*, **88**(7), (2006), p. 072902.

[152] A. A. Felix, M. O. Orlandi, and J. A. Varela. Schottky-type grain boundaries in CCTO ceramics. *Solid State Communications*, **151**(19), (2011), pp. 1377–1381.

[153] G. Blatter and F. Greuter. Carrier transport through grain boundaries in semiconductors. *Physical Review B*, **33**(6), (1986), pp. 3952–3966.

[154] M. H. Cohen, J. B. Neaton, L. He, and D. Vanderbilt. Extrinsic models for the dielectric response of $CaCu_3Ti_4O_{12}$. *Journal of Applied Physics*, **94**(5), (2003), pp. 3299–3306.

[155] T. T. Fang, L. T. Mei, and H. F. Ho. Effects of Cu stoichiometry on the microstructures, barrier-layer structures, electrical conduction, dielectric responses, and stability of $CaCu_3Ti_4O_{12}$. *Acta Materialia*, **54**(10), (2006), pp. 2867–2875.

[156] C. Wang, H. J. Zhang, P. M. He, and G. H. Cao. Ti-rich and Cu-poor grain-boundary layers of $CaCu_3Ti_4O_{12}$ detected by x-ray photoelectron spectroscopy. *Applied Physics Letters*, **91**(5), (2007), pp. 10–13.

[157] K. Chen, Y. F. Liu, F. Gao, Z. L. Du, J. M. Liu, *et al.* Ti deficiency effect on the dielectric response of $CaCu_3Ti_4O_{12}$ ceramics. *Solid State Communications*, **141**(8), (2007), pp. 440–444.

[158] S. Kwon and D. P. Cann. Relationship among the phase equilibria, microstructures, and dielectric properties of $CaCu_3Ti_4O_{12}$ ceramics via different sintering time. *Journal of Materials Science*, **44**(15), (2009), pp. 4117–4123.

[159] P. Thomas, K. Dwarakanath, and K. Varma. Effect of calcium stoichiometry on the dielectric response of $CaCu_3Ti_4O_{12}$ ceramics. *Journal of the European Ceramic Society*, **32**(8), (2012), pp. 1681–1690.

[160] B. K. Kim, H. S. Lee, J. W. Lee, S. E. Lee, and Y. S. Cho. Dielectric and grain-boundary characteristics of hot pressed $CaCu_3Ti_4O_{12}$. *Journal of the American Ceramic Society*, **93**(9), (2010), pp. 2419–2422.

[161] S. De Almeida-Didry, C. Autret, C. Honstettre, A. Lucas, M. Zaghrioui, *et al.* Central role of TiO_2 anatase grain boundaries on resistivity of $CaCu_3Ti_4O_{12}$-based materials probed by Raman spectroscopy. *Solid State Sciences*, **61**, (2016), pp. 102–105.

[162] J. J. Mohamed, S. D. Hutagalung, M. Fadzil, and Z. A. Ahmad. Effect of excess TiO_2 in $CaCu_3Ti_4O_{12}$ on the microstructure and dielectric properties. *Journal of Ceramic Processing Research*, **12**(5), (2011), pp. 496–499.

[163] W. X. Yuan, Z. Luo, and C. Wang. Investigation on effects of CuO secondary phase on dielectric properties of $CaCu_3Ti_4O_{12}$ ceramics. *Journal of Alloys and Compounds*, **562**(75), (2013), pp. 1–4.

[164] L. Wei, X. Zhao-Xian, and X. Hao. Preparation and electrical properties of $CaCu_3Ti_4O_{12}$; Thin ceramic sheets via water-based tape casting. *Journal of Inorganic Materials*, **29**(11), (2014), p. 1228.

[165] O. a. a. Abdelal, A. a. Hassan, and M. E.-s. Ali. Dielectric Properties of Calcium Copper Titanates ($CaCu_3Ti_4O_{12}$) Synthesized by Solid State Reaction. *International Journal of Science and Research*, **3**(11), (2014), pp. 354–361.

[166] J. W. Lee, G. H. Lee, D. J. Shin, J. Kim, S. J. Jeong, *et al.* Ag-migration effects on the metastable phase in $CaCu_3Ti_4O_{12}$ capacitors. *Scientific Reports*, **8**(1), (2018), p. 1392.

[167] X. Wang, P. Jia, L. Sun, B. Zhang, X. Wang, *et al.* Improved dielectric properties in $CaCu_3Ti_4O_{12}$ ceramics modified by TiO_2. *Journal of Materials Science: Materials in Electronics*, **29**(3), (2017), pp. 2244–2250.

[168] T. Lebey, S. Guillemet, V. Bley, M. Boulos, and B. Durand. Origin of the colossal permittivity and possible application of CCT ceramics. *IEEE Electronic*, **55**, (2005), pp. 1248–1253.

[169] R. Schmidt, S. Pandey, P. Fiorenza, and D. C. Sinclair. Non-stoichiometry in "$CaCu_3Ti_4O_{12}$" (CCTO) ceramics. *Rsc Advances*, pp. 14580–14589.

[170] R. Schmidt, M. C. Stennett, N. C. Hyatt, J. Pokorny, J. Prado-Gonjal, *et al.* Effects of sintering temperature on the internal barrier layer capacitor (IBLC) structure in $CaCu_3Ti_4O_{12}$ (CCTO) ceramics. *Journal of the European Ceramic Society*, **32**(12), (2012), pp. 3313–3323.

[171] J. J. Mohamed, S. D. Hutagalung, and Z. A. Ahmad. Influence of sintering parameters on melting CuO phase in $CaCu_3Ti_4O_{12}$. *Journal of King Saud University - Engineering Sciences*, **25**(1), (2013), pp. 35–39.

[172] J. Jumpatam, B. Putasaeng, N. Chanlek, P. Kidkhunthod, P. Thongbai, *et al.* Improved giant dielectric properties of $CaCu_3Ti_4O_{12}$ via simultaneously tuning the electrical properties of grains and grain boundaries by F-substitution. *RSC Advances*, **7**(7), (2017), pp. 4092–4101.

[173] Y. H. Lin, J. Cai, M. Li, C. W. Nan, and J. He. High dielectric and nonlinear electrical behaviors in TiO_2-rich $CaCu_3Ti_4O_{12}$ ceramics. *Applied Physics Letters*, **88**(17), (2006), p. 172902.

[174] C. Zhao and J. Wu. Effects of secondary phases on the high-performance colossal permittivity in titanium dioxide ceramics. *ACS Applied Materials and Interfaces*, **10**(4), (2018), pp. 3680–3688.

[175] M. S. Ivanov, F. Amaral, V. A. Khomchenko, J. A. Paixão, and L. C. Costa. Investigation of micro- and nanoscale barrier layer capacitance mechanisms of conductivity in $CaCu_3Ti_4O_{12}$ via scanning probe microscopy technique. *RSC Adv.*, **7**(65), (2017), pp. 40695–40704.

[176] J. Sun, R. Ahmed, G. J. Wang, S. T. Wang, J. Wang, *et al.* Colossal dielectric behavior and dielectric anomalies in Sr_2TiCrO_6 ceramics. *Journal of Materials Science*, pp. 6323–6331.

[177] S. De Almeida-Didry, M. M. Nomel, C. Autret, C. Honstettre, A. Lucas, *et al.* Control of grain boundary in alumina doped CCTO showing colossal permittivity by core-shell approach. *Journal of the European Ceramic Society*, **38**(9), (2018), pp. 3182–3187.

[178] P. Mao, J. Wang, L. Zhang, Z. Wang, F. Kang, *et al.* Significantly enhanced breakdown field with high grain boundary resistance and dielectric response in $0.1Na_{0.5}Bi_{0.5}TiO_3$-$0.9BaTiO_3$ doped $CaCu_3Ti_4O_{12}$ ceramics. *Journal of the European Ceramic Society*, **40**(8), (2020), pp. 3011–3018.

[179] R. Jia, X. Zhao, J. Li, and X. Tang. Colossal breakdown electric field and dielectric response of Al-doped $CaCu_3Ti_4O_{12}$ ceramics. *Materials Science and Engineering B*, **185**(1), (2014), pp. 79–85.

[180] D. Xu, K. He, R. Yu, X. Sun, Y. Yang, *et al.* High dielectric permittivity and low dielectric loss in sol-gel derived Zn doped $CaCu_3Ti_4O_{12}$ thin films. *Materials Chemistry and Physics*, **153**, (2015), pp. 229–235.

[181] M. A. Sulaiman, S. D. Hutagalung, J. J. Mohamed, Z. A. Ahmad, M. F. Ain, *et al.* High frequency response to the impedance complex properties of Nb-doped $CaCu_3Ti_4O_{12}$ electroceramics. *Journal of Alloys and Compounds*, **509**(18), (2011), pp. 5701–5707.

[182] J. Hubbard. Electron correlations in narrow energy bands. *Proceedings of the Royal Society of London. Series A. Mathematical and Physical Sciences*, **276**(1365), (1963), pp. 238–257.

[183] S. L. Dudarev, G. A. Botton, S. Y. Savrasov, C. J. Humphreys, and A. P. Sutton. Electron-energy-loss spectra and the structural stability of nickel oxide: An LSDA+U study. *Physical Review B*, **57**(3), (1998), pp. 1505–1509.

[184] H. Im, M. Iwataki, S. Yamazaki, T. Usui, S. Adachi, *et al.* Electronic structure of Mott-insulator $CaCu_3Ti_4O_{12}$: Photoemission and inverse photoemission study. *Solid State Communications journal*, **217**, (2015), pp. 17–20.

[185] K. M. Shrestha, C. M. Sorensen, and K. J. Klabunde. Synthesis of CuO Nanorods , Reduction of CuO into Cu Nanorods , and Diffuse Reflectance Measurements of CuO and Cu Nanomaterials in the Near Infrared Region. *Scanning Electron Microscopy*, **114**(ii), (2010), pp. 14368–14376.

[186] B. K. Meyer, A. Polity, D. Reppin, M. Becker, P. Hering, *et al.* Binary copper oxide semiconductors: From materials towards devices. *Physica Status Solidi (B) Basic Research*, **249**(8), (2012), pp. 1487–1509.

[187] D. O. Scanlon, B. J. Morgan, and G. W. Watson. Modeling the polaronic nature of p -type defects in Cu_2O: The failure of GGA and GGA+U. *Journal of Chemical Physics*, **131**(12), (2009), p. 124703.

[188] R. F. W. Bader. A quantum theory of molecular structure and its applications. *Chemical Reviews*, **91**(5), (1991), pp. 893–928.

[189] L. He, J. B. Neaton, M. H. Cohen, D. Vanderbilt, and C. C. Homes. First-principles study of the structure and lattice dielectric response of $CaCu_3Ti_4O_{12}$. *Physical Review B*, **65**(21), (2002), p. 214112.

[190] N. Kolev, R. P. Bontchev, A. J. Jacobson, V. N. Popov, V. G. Hadjiev, *et al.* Raman spectroscopy of $CaCu_3Ti_4O_{12}$. *Physical Review B*, **66**(13), (2002), p. 132102.

[191] S. B. Fagan, A. G. S. Filho, A. P. Ayala, and J. M. Filho. Ab initio calculations of $CaCu_3Ti_4O_{12}$ under high pressure: Structural and electronic properties. *Physical Review B*, **72**(1), (2005), p. 014106.

[192] F. Ricci, P. Alippi, A. Filippetti, and V. Fiorentini. Multigap absorption in $CaCu_3Ti_4O_{12}$ and the prediction capabaility of ab initio methods. *Physical Review B*, **90**(4), (2014), p. 045132.

[193] B. Himmetoglu, R. M. Wentzcovitch, and M. Cococcioni. First-principles study of electronic and structural properties of CuO. *Physical Review B*, **84**(11), (2011), p. 115108.

[194] A. K. Mishra, A. Roldan, and N. H. De Leeuw. CuO Surfaces and CO_2 Activation: A Dispersion-Corrected DFT+U Study. *The Journal of Physical Chemistry C*, **120**(4), (2016), pp. 2198–2214.

[195] J. M. McCoy and J. P. LaFemina. Structure and stability of steps on the GaAs(110) surface. *Physical Review B*, **54**(20), (1996), pp. 14511–14517.

[196] E. Heifets, J. Ho, and B. Merinov. Density functional simulation of the $BaZrO_3$ (011) surface structure. *Physical Review B*, **75**(15), (2007), p. 155431.

[197] F. Sánchez, C. Ocal, and J. Fontcuberta. Tailored surfaces of perovskite oxide substrates for conducted growth of thin films. *Chemical Society Reviews*, **43**(7), (2014), pp. 2272–2285.

[198] A. Slassi, M. Hammi, and O. El Rhazouani. Surface Relaxations, Surface Energies and Electronic Structures of $BaSnO_3$ (001) Surfaces: Ab Initio Calculations. *Journal of Electronic Materials*, **46**(7), (2017), pp. 4133–4139.

[199] X. Zhang, J. Hu, Y. Cao, J. Xie, W. Jia, *et al.* Insights into Crystal Facets of Perovskite $SrSnO_3$ as High-Performance Photocatalysts toward Environmental Remediation. *Chemistry - A European Journal*, **24**(53), (2018), pp. 14111–14118.

[200] Y. Wang, S. Lany, J. Ghanbaja, Y. Fagot-Revurat, Y. P. Chen, *et al.* Electronic structures of Cu_2O, Cu_4O_3, and CuO: A joint experimental and theoretical study. *Physical Review B*, **94**(24), (2016), p. 245418.

[201] M. F. A. Rahman, M. J. Abu, M. F. Ain, J. J. Mohamed, and Z. A. Ahmad. Effect of Calcination Temperature on Dielectric Properties of $CaCu_3Ti_4O_{12}$ Ceramics. *Procedia Chemistry*, **19**, (2016), pp. 910–915.

[202] D. Fu, H. Taniguchi, T. Taniyama, M. Itoh, and S.-y. Koshihara. Origin of Giant Dielectric Response in Nonferroelectric $CaCu_3Ti_4O_{12}$: Inhomogeneous Conduction Nature Probed by Atomic Force Microscopy. *Chemistry of Materials*, **20**(5), (2008), pp. 1694–1698.

[203] W. Hao, P. Xu, M. Wang, S. Yang, W. Yupeng, *et al.* Microstructure and dielectrical properties of $CaCu_3Ti_4O_{12}/TiO_2$ composite ceramics with core-shell structure. *Journal of Alloys and Compounds*, **740**, (2018), pp. 1159–1164.

[204] M. Li, X. Chen, D. Zhang, Q. Liu, and C. Li. The effect of grain boundary resistance on the dielectric response of $CaCu_3Ti_4O_{12}$. *Ceramics International*, **41**(10), (2015), pp. 14854–14859.

[205] D. Fu, Y. Arima, H. Taniguchi, T. Taniyama, M. Itoh, *et al.* Conductive boundary layer in $CaCu_3Ti_4O_{12}$ with giant-dielectric-response. *Ferroelectrics*, **347**, (2007), pp. 140–144.

[206] A. Cho, C. S. Han, M. Kang, W. Choi, J. Lee, *et al.* Direct Correlations of Grain Boundary Potentials to Chemical States and Dielectric Properties of Doped $CaCu_3Ti_4O_{12}$ Thin Films. *ACS Applied Materials and Interfaces*, **10**(18), (2018), pp. 16203–16209.

[207] B. W. Veal, S. K. Kim, P. Zapol, H. Iddir, P. M. Baldo, *et al.* Interfacial control of oxygen vacancy doping and electrical conduction in thin film oxide heterostructures. *Nature Communications*, **7**(1), (2016), p. 11892.

[208] S. J. Jenkins and G. P. Srivastava. Bonding and structure of the Si(001) (2×1)-Sb surface. *Surface Science*, **352-354**, (1996), pp. 411–415.

[209] L. Fang, M. Shen, and W. Cao. Effects of postanneal conditions on the dielectric properties of $CaCu_3Ti_4O_{12}$ thin films prepared on Pt/Ti/SiO_2/Si substrates. *Journal of Applied Physics*, **95**(11), (2004), p. 6483.

[210] C. Masingboon, T. Eknapakul, S. Suwanwong, P. Buaphet, H. Nakajima, *et al.* Anomalous change in dielectric constant of $CaCu_3Ti_4O_{12}$ under violet-to-ultraviolet irradiation. *Applied Physics Letters*, **102**(20), (2013), p. 202903.

[211] F. Y. Liao, C. L. Chen, D. Y. Feng, M. Gao, L. B. Jin, *et al.* Reducing dielectric loss in $CaCu_3Ti_4O_{12}$ thin films by high-pressure oxygen annealing. *Journal of Materials Chemistry C*, **3**(14), (2015), pp. 3438–3444.

[212] P. Mao, J. Wang, S. Liu, L. Zhang, Y. Zhao, *et al.* Grain size effect on the dielectric and non-ohmic properties of $CaCu_3Ti_4O_{12}$ ceramics prepared by the sol-gel process. *Journal of Alloys and Compounds*, **778**, (2019), pp. 625–632.

[213] T. T. Fang and C. P. Liu. Evidence of the internal domains for inducing the anomalously high dielectric constant of $CaCu_3Ti_4O_{12}$. *Chemistry of Materials*, **17**(20), (2005), pp. 5167–5171.

[214] N. J. Kidner, N. H. Perry, T. O. Mason, and E. J. Garboczi. The Brick Layer Model Revisited: Introducing the Nano-Grain Composite Model. *Journal of the American Ceramic Society*, **91**(6), (2008), pp. 1733–1746.

[215] I. M. Hodge, M. D. Ingram, and A. R. West. Impedance and modulus spectroscopy of polycrystalline solid electrolytes. *Journal of Electroanalytical Chemistry*, **74**(2), (1976), pp. 125–143.

[216] J. T. S. Irvine, D. C. Sinclair, and A. R. West. Electroceramics: Characterization by Impedance Spectroscopy. *Advanced Materials*, **2**(3), (1990), pp. 132–138.

[217] M. J. Pan and B. A. Bender. A bimodal grain size model for predicting the dielectric constant of calcium copper titanate ceramics. *Journal of the American Ceramic Society*, **88**(9), (2005), pp. 2611–2614.

[218] J.-B. Jorcin, M. E. Orazem, N. Pébère, and B. Tribollet. CPE analysis by local electrochemical impedance spectroscopy. *Electrochimica Acta*, **51**(8-9), (2006), pp. 1473–1479.

[219] S. Y. Chung, I. D. Kim, and S. J. L. Kang. Strong nonlinear current-voltage behaviour in perovskite-derivative calcium copper titanate. *Nature materials*, **3**(11), (2004), pp. 774–778.

[220] Y. Mogulkoc, Y. O. Ciftci, K. Colakoglu, and E. Deligoz. The structural, electronic, elastic, vibration and thermodynamic properties of GdMg. *Solid State Sciences*, **16**, (2013), pp. 168–174.

[221] N. Song, H. Momida, T. Oguchi, and B. G. Kim. Polar phase transitions and physical properties in fresnoite $A_2TiSi_2O_8$ (A= Ba, Sr) by first principles calculations. *Journal of Solid State Chemistry*, **242**, (2016), pp. 136–142.

[222] D. Rappoport, N. R. M. Crawford, F. Furche, and K. Burke. Approximate Density Functionals: Which Should I Choose? In *Encyclopedia of Inorganic Chemistry*, pp. 159–172. John Wiley & Sons, Ltd, Chichester, UK, 2009.

[223] L. Hedin. New method for calculating the one-particle Green's function with application to the electron-gas problem. *Physical Review*, **139**(3A).

[224] C. Freysoldt, B. Grabowski, T. Hickel, J. Neugebauer, G. Kresse, *et al.* First-principles calculations for point defects in solids. *Reviews of Modern Physics*, **86**(1), (2014), pp. 253–305.

[225] M. Gerosa, C. E. Bottani, L. Caramella, G. Onida, C. Di Valentin, *et al.* Electronic structure and phase stability of oxide semiconductors: Performance of dielectric-dependent hybrid functional DFT, benchmarked against GW band structure calculations and experiments. *Physical Review B*, **91**(15), (2015), p. 155201.

[226] B. Wang, C. Århammar, X. Jiang, C. M. Araujo, and R. Ahuja. A Comparison Between Hybrid Functional, GW Approach and the Bethe Salpether Equation: Optical Properties of High Pressure Phases of TiO_2. *Science of Advanced Materials*, **6**(6), (2014), pp. 1170–1178.

[227] B. Wul. Dielectric Constants of Some Titanates. *Nature*, **156**(3964), (1945), p. 480.

[228] P. Duran, D. Gutierrez, J. Tartaj, and C. Moure. Densification behaviour, microstructure development and dielectric properties of pure $BaTiO_3$ prepared by thermal decomposition of (Ba, Ti)-citrate polyester resins. *Ceramics International*, **28**, (2002), pp. 283–292.

[229] Z. Q. Shi, Q. X. Jia, and W. A. Anderson. High-Performance barium titanate capacitors with double layer structure. *Journal of Electronic Materials*, **20**(11), (1991), pp. 939–944.

[230] D. Collier. Ferroelectric phase shifters for phased array radar applications. In *ISAF '92: Proceedings of the Eighth IEEE International Symposium on Applications of Ferroelectrics*, pp. 199–201. IEEE, 1992.

[231] J. F. Scott. Applications of modern ferroelectrics. *Science (New York, N.Y.)*, **315**(February), (2007), pp. 954–959.

[232] E. A. Stefanescu, X. Tan, Z. Lin, N. Bowler, and M. R. Kessler. Multifunctional fiberglass-reinforced PMMA-$BaTiO_3$ structural/dielectric composites. *Polymer*, **52**(9), (2011), pp. 2016–2024.

[233] Z. Wang, J. K. Nelson, N. Koratkar, L. S. Schadler, H. Hillborg, *et al.* Dielectric properties of electrospun barium titanate fibers/graphene/silicone rubber composites. In *2011 Annual Report Conference on Electrical Insulation and Dielectric Phenomena*, pp. 640–643. IEEE, 2011.

[234] E. Tuncer, I. Sauers, D. R. James, A. R. Ellis, M. P. Paranthaman, *et al.* Electrical properties of epoxy resin based nano-composites. *Nanotechnology*, **18**(2), (2006), p. 025703.

[235] D. Nuzhnyy, J. Petzelt, V. Bovtun, M. Kempa, M. Savinov, *et al.* High-Frequency Dielectric Spectroscopy of $BaTiO_3$ Core - Silica Shell Nanocomposites: Problem of Interdiffusion. *Journal of Advanced Dielectrics*, **01**(3), (2011), pp. 309–317.

[236] W. Reainthippayasakul. *Silica-coated BaTiO3/P(VDF-CTFE) nanocomposites for electrical energy Storage*. Ph.D. thesis, Pennsylvania State University, 2014.

[237] J. P. George, J. Beeckman, W. Woestenborghs, P. F. Smet, W. Bogaerts, *et al.* Preferentially oriented $BaTiO_3$ thin films deposited on silicon with thin intermediate buffer layers. *Nanoscale research letters*, **8**(1), (2013), p. 62.

[238] U.-C. Chung, D. Michau, C. Elissalde, S. Li, A. Klein, *et al.* Evidence of diffusion at $BaTiO_3$/silicon interfaces. *Thin Solid Films*, **520**(6), (2012), pp. 1997–2000.

[239] A. V. Kimmel and P. V. Sushko. Mechanisms of formation of chemical bonding and defect formation at the a-SiO_2/$BaTiO_3$ interfaces. *Journal of Physics: Condensed Matter*, **27**(47), (2015), p. 475006.

[240] G. Pilania, K. Slenes, and R. Ramprasad. First principles study of the interface between silicone and undoped/doped $BaTiO_3$. *Journal of Applied Physics*, **113**(6), (2013), p. 064316.

[241] A. Halliyal, A. S. Bhalla, S. A. Markgraf, L. E. Cross, and R. E. Newnham. Unusual pyroelectric and piezoelectric properties of fresnoite ($Ba_2TiSi_2O_8$) single crystal and polar glass-ceramics. *Ferroelectrics*, **62**(1), (1985), pp. 27–38.

[242] A. Halliyal, A. S. Bhalla, L. E. Cross, and R. E. Newnham. Dielectric, piezoelectric and pyroelectric properties of $Sr_2TiSi_2O_8$ polar glass-ceramic: A new polar material. *Journal of Materials Science*, **20**(10), (1985), pp. 3745–3749.

[243] B. Rangarajan, T. Shrout, and M. Lanagan. Crystallization kinetics and dielectric properties of fresnoite BaO-TiO_2-SiO_2 glass-ceramics. *Journal of the American Ceramic Society*, **92**(11), (2009), pp. 2642–2647.

[244] C. Shen, H. Zhang, H. Cong, H. Yu, J. Wang, *et al.* Investigations on the thermal and piezoelectric properties of fresnoite $Ba_2TiSi_2O_8$ single crystals. *Journal of Applied Physics*, **116**(4), (2014), p. 044106.

[245] J. T. Alfors, M. C. Stinson, R. A. Matthews, and A. Pabst. Seven new barium minerals from eastern fresno county, California. *American Mineralogist*, **50**(3-4), (1965), pp. 314–340.

[246] C. R. Robbins. Synthesis and Growth of Fresnoite ($Ba_2TiSi_2O_8$) from a TiO_2 Flux and Its Relation to the System $BaTiO_3$-SiO_2. *J. Res. Natl. Bur. Std.*, **74A**(2), (1970), pp. 229–232.

[247] S. A. Markgraf, A. Halliyal, A. S. Bhalla, R. E. Newnham, and C. T. Prewitt. X-ray structure refinement and pyroelectric investigation of fresnoite, $Ba_2TiSi_2O_8$. *Ferroelectrics*, **62**(1), (1985), pp. 17–26.

[248] S. Haussühl, J. Eckstein, K. Recker, and F. Wallrafen. Growth and physical properties of fresnoite $Ba_2TiSi_2O_8$. *Journal of Crystal Growth*, **40**(2), (1977), pp. 200–204.

[249] P. B. Moore and J. Louisnathan. Fresnoite: Unusal Titanium Coordination. *Science*, **156**(3780), (1967), pp. 1361–1362.

[250] M. Kimura, Y. Fujino, and T. Kawamura. New piezoelectric crystal: Synthetic fresnoite ($Ba_2Si_2TiO_8$). *Applied Physics Letters*, **29**(4), (1976), pp. 227–228.

[251] M. Kimura. Elastic and piezoelectric properties of $Ba_2Si_2TiO_8$. *Journal of Applied Physics*, **48**(7), (1977), pp. 2850–2856.

[252] M. C. Foster, D. J. Arbogast, R. M. Nielson, P. Photinos, and S. C. Abrahams. Fresnoite: A new ferroelectric mineral. *Journal of Applied Physics*, **85**(4), (1999), pp. 2299–2303.

[253] V. K. Lamer and R. H. Dinegar. Theory, Production and Mechanism of Formation of Monodispersed Hydrosols. *Journal of the American Chemical Society*, **72**(11), (1950), pp. 4847–4854.

[254] J. Turkevich, P. C. Stevenson, and J. Hillier. A study of the nucleation and growth processes in the synthesis of colloidal gold. *Discussions of the Faraday Society*, **11**(c), (1951), pp. 55–75.

[255] A. I. Ekimov, A. A. Onuschenko, and V. A. Tsekhomskii. Exciton light absorption by CuCl microcrystals in glass matrix. *Sov. Glass Phys. Chem*, **6**, (1980), pp. 511–512.

[256] A. L. Efros and A. L. Efros. Interband Light Absorption in Semiconductor Spheres. *Soviet Physics Semiconductors*, **16**(7), (1982), pp. 772–775.

[257] L. E. Brus. Electron-electron and electron-hole interactions in small semiconductor crystallites: The size dependence of the lowest excited electronic state. *The Journal of Chemical Physics*, **80**(9), (1984), pp. 4403–4409.

[258] A. Henglein. Small-Particle Research: Physicochemical Properties of Extremely Small Colloidal Metal and Semiconductor Particles. *Chemical Reviews*, **89**(8), (1989), pp. 1861–1873.

[259] L. Spanhel, H. Weller, and A. Henglein. Photochemistry of Semiconductor Colloids. 22. Electron Injection from Illuminated CdS into Attached TiO_2 and ZnO Particles. *Journal of the American Chemical Society*, **109**(22), (1987), pp. 6632–6635.

[260] M. Haase, H. Weller, and A. Henglein. Photochemistry and radiation chemistry of colloidal semiconductors. 23. Electron storage on zinc oxide particles and size quantization. *The Journal of Physical Chemistry*, **92**(2), (1988), pp. 482–487.

[261] C. F. Hoener, K. A. Allan, A. J. Bard, A. Campion, M. A. Fox, *et al.* Demonstration of a shell-core structure in layered cadmium selenide-zinc selenide small particles by x-ray photoelectron and Auger spectroscopies. *The Journal of Physical Chemistry*, **96**(9), (1992), pp. 3812–3817.

[262] S. Oldenburg, R. Averitt, S. Westcott, and N. Halas. Nanoengineering of optical resonances. *Chemical Physics Letters*, **288**(2-4), (1998), pp. 243–247.

[263] K. Bi, M. Bi, Y. Hao, W. Luo, Z. Cai, *et al.* Ultrafine core-shell $BaTiO_3$@SiO_2 structures for nanocomposite capacitors with high energy density. *Nano Energy*, **51**(July), (2018), pp. 513–523.

[264] L. Wu, X. Wang, and L. Li. Core-shell $BaTiO_3$@$BiScO_3$ particles for local graded dielectric ceramics with enhanced temperature stability and energy storage capability. *Journal of Alloys and Compounds*, **688**, (2016), pp. 113–121.

[265] Q. Yuan, J. Cui, Y. Wang, R. Ma, and H. Wang. Significant enhancement in breakdown strength and energy density of the $BaTiO_3$/$BaTiO_3$@SiO_2 layered ceramics with strong interface blocking effect. *Journal of the European Ceramic Society*, **37**(15), (2017), pp. 4645–4652.

[266] L. Li, D. Zhang, J. Liu, and Y. Li. Dielectric properties and microstructure of $BaTiO_3$-SiO_2 nanocomposites using vacuum treated barium titanate nanoparticles. *Materials Research Express*, **6**(12), (2020), p. 125210.

[267] X. Su, B. C. Riggs, M. Tomozawa, J. K. Nelson, and D. B. Chrisey. Preparation of $BaTiO_3$/low melting glass core-shell nanoparticles for energy storage capacitor applications. *Journal of Materials Chemistry A*, **2**(42), (2014), pp. 18087–18096.

[268] A. V. Krukau, O. A. Vydrov, A. F. Izmaylov, and G. E. Scuseria. Influence of the exchange screening parameter on the performance of screened hybrid functionals. *Journal of Chemical Physics*, **125**(22), (2006), p. 224106.

[269] S. H. Wemple. Polarization fluctuations and the optical-absorption edge in $BaTiO_3$. *Physical Review B*, **2**(7), (1970), pp. 2679–2689.

[270] R. M. Wentzcovitch, A. Navrotsky, and K. R. Poeppelmeier. *Perovskite materials: symposium*. Materials Research Society, San Fancisco, 2002.

[271] C. L. Wong, S. Madhavi, N. Phonthammachai, and T. J. White. Synthesis and crystal chemical evolution of fresnoite powders. *Journal of Solid State Chemistry*, **187**, (2012), pp. 165–171.

[272] S. Piskunov, E. Heifets, R. Eglitis, and G. Borstel. Bulk properties and electronic structure of $SrTiO_3$, $BaTiO_3$, $PbTiO_3$ perovskites: an ab initio HF/DFT study. *Computational Materials Science*, **29**(2), (2004), pp. 165–178.

[273] N. Soga. Temperature and Pressure Derivatives of Isotropic Sound Velocities of Alpha Quartz. *Journal of Geophysical Research*, **73**(2), (1968), pp. 827–829.

[274] P. Heyliger, H. Ledbetter, and S. Kim. Elastic constants of natural quartz. *The Journal of the Acoustical Society of America*, **114**(2), (2003), pp. 644–650.

[275] R. Hill. The Elastic Behaviour of a Crystalline Aggregate. *Proceedings of the Physical Society. Section A*, **65**(5), (1952), pp. 349–354.

[276] H. Colder, B. Domengès, C. Jorel, P. Marie, M. Boisserie, *et al.* Structural characterisation of $BaTiO_3$ thin films deposited on $SrRuO_3$/YSZ buffered silicon substrates and silicon microcantilevers. *Journal of Applied Physics*, **115**(5), (2014), p. 053506.

[277] F. Mouhat and F. X. Coudert. Necessary and sufficient elastic stability conditions in various crystal systems. *Physical Review B*, **90**(22), (2014), p. 224104.

[278] H. Kimizuka, S. Ogata, J. Li, and Y. Shibutani. Complete set of elastic constants of α-quartz at high pressure: A first-principles study. *Physical Review B*, **75**(5), (2007), p. 054109.

[279] M. Gabelica-Robert and P. Tarte. Vibrational spectrum of fresnoite ($Ba_2TiOSi_2O_7$) and isostructural compounds. *Physics and Chemistry of Minerals*, **7**(1), (1981), pp. 26–30.

[280] S. A. Markgraf, S. K. Sharma, and A. S. Bhalla. Raman study of fresnoite-type materials: Polarized single crystal, crystalline powders, and glasses. *J. Mater. Res.*, **8**, (1993), pp. 635–648.

[281] G. Sophia, P. Baranek, C. Sarrazin, M. Rérat, and R. Dovesi. First-principles study of the mechanisms of the pressure-induced dielectric anomalies in ferroelectric perovskites. *Phase Transitions*, **86**(11), (2013), pp. 1069–1084.

[282] C. Shen, H. Zhang, D. Wang, J. Wang, and R. Boughton. Optical Properties of the Fresnoite $Ba_2TiSi_2O_8$ Single Crystal. *Crystals*, **7**(2), (2017), p. 53.

[283] T. H. DiStefano and D. E. Eastman. The band edge of amorphous SiO_2 by photoinjection and photoconductivity measurements. *Solid State Communications*, **9**(24), (1971), pp. 2259–2261.

[284] P. Ghosez, X. Gonze, and J. P. Michenaud. First-principles characterization of the four phases of barium titanate. *Ferroelectrics*, **220**(1), (1999), pp. 1–15.

[285] D. Bagayoko, G. L. Zhao, J. D. Fan, and J. T. Wang. Ab initio calculations of the electronic structure and optical properties of ferroelectric tetragonal $BaTiO_3$. *Journal of physics. Condensed matter : an Institute of Physics journal*, **10**, (1998), pp. 5645–5655.

[286] V. Sarritzu, N. Sestu, D. Marongiu, X. Chang, S. Masi, *et al.* Optical determination of Shockley-Read-Hall and interface recombination currents in hybrid perovskites. *Scientific Reports*, **7**(1), (2017), p. 44629.

[287] D. Luo, R. Su, W. Zhang, Q. Gong, and R. Zhu. Minimizing non-radiative recombination losses in perovskite solar cells. *Nature Reviews Materials*, **5**(1), (2020), pp. 44–60.

[288] W. Shockley and H. J. Queisser. Detailed Balance Limit of Efficiency of p-n Junction Solar Cells. *Journal of Applied Physics*, **32**(3), (1961), pp. 510–519.

[289] S. Rühle. Tabulated values of the Shockley-Queisser limit for single junction solar cells. *Solar Energy*, **130**, (2016), pp. 139–147.

[290] E. Pelayo, A. Zazueta, R. Lopez, E. Saucedo, R. Ruelas, *et al.* Silicon solar cell efficiency improvement employing the photoluminescent, down-shifting effects of carbon and CdTe quantum dots. *Materials for Renewable and Sustainable Energy*, **5**(2), (2016), pp. 1–7.

[291] J. F. Geisz, R. M. France, K. L. Schulte, M. A. Steiner, A. G. Norman, *et al.* Six-junction III–V solar cells with 47.1% conversion efficiency under 143 Suns concentration. *Nature Energy*, **5**(4), (2020), pp. 326–335.

[292] P. K. Nayak, S. Mahesh, H. J. Snaith, and D. Cahen. Photovoltaic solar cell technologies: analysing the state of the art. *Nature Reviews Materials*, **4**(4), (2019), pp. 269–285.

[293] A. Richter, M. Hermle, and S. W. Glunz. Reassessment of the limiting efficiency for crystalline silicon solar cells. *IEEE Journal of Photovoltaics*, **3**(4), (2013), pp. 1184–1191.

[294] S. Dubey, N. Y. Jadhav, and B. Zakirova. Socio-economic and environmental impacts of silicon based photovoltaic (PV) technologies. *Energy Procedia*, **33**, (2013), pp. 322–334.

[295] H. Joël Tchognia Nkuissi, F. Kouadio Konan, B. Hartiti, and J.-M. Ndjaka. Toxic Materials Used in Thin Film Photovoltaics and Their Impacts on Environment. In *Reliability and Ecological Aspects of Photovoltaic Modules*, pp. 1–18. IntechOpen, 2020.

[296] R. A. Afre, N. Sharma, M. Sharon, and M. Sharon. Transparent conducting oxide films for various applications: A review. *Reviews on Advanced Materials Science*, **53**(1), (2018), pp. 79–89.

[297] D. Konios, G. Kakavelakis, C. Petridis, K. Savva, E. Stratakis, *et al.* Highly efficient organic photovoltaic devices utilizing work-function tuned graphene oxide derivatives as the anode and cathode charge extraction layers. *Journal of Materials Chemistry A*, **4**(5), (2016), pp. 1612–1623.

[298] H. A. Kavuri, S. Kihara, D. J. McGillivray, and G. Willmott. Poly(vinyl pyrrolidone)-modified metal oxide anode interlayers for stable organic solar cells. *Journal of Photonics for Energy*, **10**(04), (2020), p. 1.

[299] N. Winkler, S. Edinger, J. Kaur, R. A. Wibowo, W. Kautek, *et al.* Solution-processed all-oxide solar cell based on electrodeposited Cu_2O and ZnMgO by spray pyrolysis. *Journal of Materials Science*, **53**(17), (2018), pp. 12231–12243.

[300] T. Gershon. Metal oxide applications in organic-based photovoltaics. *Materials Science and Technology*, **27**(9), (2011), pp. 1357–1371.

[301] T. Dimopoulos. *All-Oxide Solar Cells*. Elsevier Inc., 2018.

[302] S. Giménez and J. Bisquert. *Photoelectrochemical Solar Fuel Production: From Basic Principles to Advanced Devices*. Springer International Publishing, 2016.

[303] M. T. Greiner, M. G. Helander, W. M. Tang, Z. B. Wang, J. Qiu, *et al.* Universal energy-level alignment of molecules on metal oxides. *Nature Materials*, **11**(1), (2012), pp. 76–81.

[304] H. Peng, A. Bikowski, A. Zakutayev, and S. Lany. Pathway to oxide photovoltaics via band-structure engineering of SnO. *APL Materials*, **4**(10), (2016), p. 106103.

[305] R. Wang, M. Mujahid, Y. Duan, Z. K. Wang, J. Xue, *et al.* A Review of Perovskites Solar Cell Stability. *Advanced Functional Materials*, **29**(47), (2019), p. 1808843.

[306] Q. Wali, F. J. Iftikhar, M. E. Khan, A. Ullah, Y. Iqbal, *et al.* Advances in stability of perovskite solar cells. *Organic Electronics*, **78**(February 2019), (2020), p. 105590.

[307] K. Niwa, I. Yamai, and T. Wada. A Study of Tin Oxides by X-Ray Diffraction Method. *Bulletin of the Chemical Society of Japan*, **31**(6), (1958), pp. 725–727.

[308] A. Balderschi, S. Baroni, and R. Resta. Band offsets in lattice-matched heterojunctions: A model and first-principles calculations for GaAs/AlAs. *Physical Review Letters*, **61**(6), (1988), pp. 734–737.

[309] L. Colombo, R. Resta, and S. Baroni. Valence-band offsets at strained Si/Ge interfaces. *Physical Review B*, **44**(11), (1991), pp. 5572–5579.

[310] K. T. Delaney, N. A. Spaldin, and C. G. Van De Walle. Theoretical study of Schottky-barrier formation at epitaxial rare-earth-metal/semiconductor interfaces. *Physical Review B*, **81**(16), (2010), p. 165312.

[311] Y. Ogo, H. Hiramatsu, K. Nomura, H. Yanagi, T. Kamiya, *et al.* *p*-channel thin-film transistor using *p*-type oxide semiconductor, SnO. *Applied Physics Letters*, **93**(3), (2008), p. 032113.

[312] R. C. Whited, C. J. Flaten, and W. C. Walker. Exciton thermoreflectance of MgO and CaO. *Solid State Communications*, **13**(11), (1973), pp. 1903–1905.

[313] M. Batzill. Fundamental aspects of surface engineering of transition metal oxide photocatalysts. *Energy and Environmental Science*, **4**(9), (2011), pp. 3275–3286.

[314] M. T. Greiner and Z. H. Lu. Thin-film metal oxides in organic semiconductor devices: Their electronic structures, work functions and interfaces. *NPG Asia Materials*, **5**(7), (2013), p. e55.

[315] J. Kim, K. Yamamoto, S. Iimura, S. Ueda, and H. Hosono. Electron Affinity Control of Amorphous Oxide Semiconductors and Its Applicability to Organic Electronics. *Advanced Materials Interfaces*, **5**(23), (2018), p. 1801307.

[316] L. R. Fonseca, A. A. Knizhnik, A. V. Gavrikov, I. M. Iskandarova, A. A. Bagatur'yants, *et al.* Fermi Pinning in Metal-Oxide-Semiconductor Structures Results from Low Oxygen Content at the Metal-Oxide Interface. In *ECS Transactions*, volume 4, pp. 227–235. ECS, 2007.

[317] M. Kröger, S. Hamwi, J. Meyer, T. Riedl, W. Kowalsky, *et al.* Role of the deep-lying electronic states of MoO_3 in the enhancement of hole-injection in organic thin films. *Applied Physics Letters*, **95**(12), (2009), p. 123301.

[318] H. Tang, F. Lévy, H. Berger, and P. E. Schmid. Urbach tail of anatase TiO_2. *Physical Review B*, **52**(11), (1995), pp. 7771–7774.

[319] G. A. Sawatzky and J. W. Allen. Magnitude and origin of the band gap in NiO. *Physical Review Letters*, **53**(24), (1984), pp. 2339–2342.

[320] G. W. Rubloff. Far-Ultraviolet Reflectance Spectra and the Electronic Structure of Ionic Crystals. *Physical Review B*, **5**(2), (1972), pp. 662–684.

[321] D. M. Roessler and W. C. Walker. Electronic spectrum of crystalline lithium fluoride. *Journal of Physics and Chemistry of Solids*, **28**(8), (1967), pp. 1507–1515.

[322] H. L. Skriver and N. M. Rosengaard. Surface energy and work function of elemental metal. *Physical Review B*, **44**(11), (1992), pp. 7157–7168.

[323] X. Pan, M. Q. Yang, X. Fu, N. Zhang, and Y. J. Xu. Defective TiO_2 with oxygen vacancies: Synthesis, properties and photocatalytic applications. *Nanoscale*, **5**(9), (2013), pp. 3601–3614.

[324] H. A. Wriedt. The O-W (oxygen-tungsten) system. *Bulletin of Alloy Phase Diagrams*, **10**(4), (1989), pp. 368–384.

[325] J. ichi Fujisawa, T. Eda, and M. Hanaya. Comparative study of conduction-band and valence-band edges of TiO_2, $SrTiO_3$, and $BaTiO_3$ by ionization potential measurements. *Chemical Physics Letters*, **685**, (2017), pp. 23–26.

[326] S. Singh Surah, M. Vishwakarma, R. Kumar, R. Nain, S. Sirohi, *et al.* Tuning the electronic band alignment properties of TiO_2 nanotubes by boron doping. *Results in Physics*, **12**(November 2018), (2019), pp. 1725–1731.

[327] R. L. Nelson and A. J. Tench. Chemisorption on some alkaline earth oxides. Part 2.—Intrinsic bulk defects and adsorption of oxygen on MgO, CaO and SrO. *Transactions of the Faraday Society*, **63**, (1967), pp. 3039–3059.

[328] B. Henderson and A. Tomlinson. Some studies of defects in calcium oxide-II. Intrinsic lattice defects. *Journal of Physics and Chemistry of Solids*, **30**(7), (1969), pp. 1801–1809.

[329] X. Shao, P. Myrach, N. Nilius, and H. J. Freund. Growth and morphology of calcium-oxide films grown on Mo(001). *The Journal of Physical Chemistry C*, **115**(17), (2011), pp. 8784–8789.

[330] J. P. Allen, D. O. Scanlon, L. F. Piper, and G. W. Watson. Understanding the defect chemistry of tin monoxide. *Journal of Materials Chemistry C*, **1**(48), (2013), pp. 8194–8208.

[331] B. J. Morgan and G. W. Watson. Intrinsic n-type defect formation in TiO_2: A comparison of rutile and anatase from GGA+U calculations. *The Journal of Physical Chemistry C*, **114**(5), (2010), pp. 2321–2328.

[332] H. Peelaers, M. L. Chabinyc, and C. G. Van De Walle. Controlling n-Type Doping in MoO3. *Chemistry of Materials*, **29**(6), (2017), pp. 2563–2567.

[333] A. J. Bard and M. A. Fox. Artificial Photosynthesis: Solar Splitting of Water to Hydrogen and Oxygen. *Accounts of Chemical Research*, **28**(3), (1995), pp. 141–145.

[334] K. Maeda and K. Domen. Photocatalytic water splitting: Recent progress and future challenges. *The Journal of Physical Chemistry Letters*, **1**(18), (2010), pp. 2655–2661.

[335] C. Acar, I. Dincer, and G. F. Naterer. Review of photocatalytic water-splitting methods for sustainable hydrogen production. *International Journal of Energy Research*, **40**(11), (2016), pp. 1449–1473.

[336] N. Fajrina and M. Tahir. A critical review in strategies to improve photocatalytic water splitting towards hydrogen production. *International Journal of Hydrogen Energy*, **44**(2), (2019), pp. 540–577.

[337] L. Ge, H. Yuan, Y. Min, L. Li, S. Chen, *et al.* Predicted Optimal Bifunctional Electrocatalysts for the Hydrogen Evolution Reaction and the Oxygen Evolution Reaction Using Chalcogenide Heterostructures Based on Machine Learning Analysis of in

Silico Quantum Mechanics Based High Throughput Screening. *The Journal of Physical Chemistry Letters*, **11**(3), (2020), pp. 869–876.

[338] J. M. Ogden. Prospects for building a hydrogen energy infrastructure. *Annual Review of Energy and the Environment*, **24**(1), (1999), pp. 227–279.

[339] K. Liu, C. Song, and V. Subramani. Hydrogen and Syngas Production and Purification Technologies. *Focus on Catalysts*, **2010**(7), (2010), p. 8.

[340] M. A. Rosen and S. Koohi-Fayegh. The prospects for hydrogen as an energy carrier: an overview of hydrogen energy and hydrogen energy systems. *Energy, Ecology and Environment*, **1**(1), (2016), pp. 10–29.

[341] I. Staffell, D. Scamman, A. Velazquez Abad, P. Balcombe, P. E. Dodds, *et al.* The role of hydrogen and fuel cells in the global energy system. *Energy and Environmental Science*, **12**(2), (2019), pp. 463–491.

[342] A. Fujishima and K. Honda. Electrochemical Photolysis of Water at a Semiconductor Electrode. *Nature*, **238**(5358), (1972), pp. 37–38.

[343] H. Ahmad, S. K. Kamarudin, L. J. Minggu, and M. Kassim. Hydrogen from photocatalytic water splitting process: A review. *Renewable and Sustainable Energy Reviews*, **43**, (2015), pp. 599–610.

[344] A. G. Tamirat, J. Rick, A. A. Dubale, W.-N. Su, and B.-J. Hwang. Using hematite for photoelectrochemical water splitting: a review of current progress and challenges. *Nanoscale Horizons*, **1**(4), (2016), pp. 243–267.

[345] S. Ho-Kimura, B. A. Williamson, S. Sathasivam, S. J. Moniz, G. He, *et al.* Origin of High-Efficiency Photoelectrochemical Water Splitting on Hematite/Functional Nanohybrid Metal Oxide Overlayer Photoanode after a Low Temperature Inert Gas Annealing Treatment. *ACS Omega*, **4**(1), (2019), pp. 1449–1459.

[346] K. Domen, S. Naito, M. Soma, T. Onishi, and K. Tamaru. Photocatalytic decomposition of water vapour on an NiO-$SrTiO_3$ catalyst. *Journal of the Chemical Society, Chemical Communications*, (12), (1980), pp. 543–544.

[347] A. Ohtomo and H. Y. Hwang. A high-mobility electron gas at the LAO/STO heterointerface. *Nature*, **427**(6973), (2004), pp. 423–426.

[348] I. H. Lone, J. Aslam, N. R. Radwan, A. H. Bashal, A. F. Ajlouni, *et al.* Multiferroic ABO_3 Transition Metal Oxides: a Rare Interaction of Ferroelectricity and Magnetism. *Nanoscale Research Letters*, **14**(1), (2019), p. 142.

[349] I. E. Castelli, D. D. Landis, K. S. Thygesen, S. S. Dahl, I. Chorkendorff, *et al.* New cubic perovskites for one- and two-photon water splitting using the computational materials repository. *Energy and Environmental Science*, **5**(10), (2012), pp. 9034–9043.

[350] W. J. Yin, B. Weng, J. Ge, Q. Sun, Z. Li, *et al.* Oxide perovskites, double perovskites and derivatives for electrocatalysis, photocatalysis, and photovoltaics. *Energy and Environmental Science*, **12**(2), (2019), pp. 442–462.

[351] M. A. Peña and J. L. Fierro. Chemical structures and performance of perovskite oxides. *Chemical Reviews*, **101**(7), (2001), pp. 1981–2017.

[352] E. A. R. Assirey. Perovskite synthesis, properties and their related biochemical and industrial application. *Saudi Pharmaceutical Journal*, **27**(6), (2019), pp. 817–829.

[353] W. Zhang, J. Tang, and J. Ye. Structural, photocatalytic, and photophysical properties of perovskite $MSnO_3$ (M = Ca, Sr, and Ba) photocatalysts. *Journal of Materials Research*, **22**(7), (2007), pp. 1859–1871.

[354] A. J. Bard, F.-R. F. Fan, A. S. Gioda, G. Nagasubramanian, and H. S. White. On the role of surface states in semiconductor electrode photoelectrochemical cells. *Faraday Discussions of the Chemical Society*, **70**, (1980), pp. 19–31.

[355] O. Zandi and T. W. Hamann. Enhanced water splitting efficiency through selective surface state removal. *The Journal of Physical Chemistry Letters*, **5**(9), (2014), pp. 1522–1526.

[356] M. G. Ahmed, I. E. Kretschmer, T. A. Kandiel, A. Y. Ahmed, F. A. Rashwan, *et al.* A Facile Surface Passivation of Hematite Photoanodes with TiO_2 Overlayers for Efficient Solar Water Splitting. *ACS Applied Materials and Interfaces*, **7**(43), (2015), pp. 24053–24062.

[357] J. H. Montoya, M. Garcia-Mota, J. K. Nørskov, and A. Vojvodic. Theoretical evaluation of the surface electrochemistry of perovskites with promising photon absorption properties for solar water splitting. *Physical Chemistry Chemical Physics*, **17**(4), (2015), pp. 2634–2640.

[358] B. A. Pinaud, J. D. Benck, L. C. Seitz, A. J. Forman, Z. Chen, *et al.* Technical and economic feasibility of centralized facilities for solar hydrogen production via photocatalysis and photoelectrochemistry. *Energy and Environmental Science*, **6**(7), (2013), pp. 1983–2002.

[359] M. Reuß, J. Reul, T. Grube, M. Langemann, S. Calnan, *et al.* Solar hydrogen production: a bottom-up analysis of different photovoltaic-electrolysis pathways. *Sustainable Energy and Fuels*, **3**(3), (2019), pp. 801–813.

[360] J. Jia, L. C. Seitz, J. D. Benck, Y. Huo, Y. Chen, *et al.* Solar water splitting by photovoltaic-electrolysis with a solar-to-hydrogen efficiency over 30%. *Nature Communications*, **7**(1), (2016), p. 13237.

[361] M. M. May, H. J. Lewerenz, D. Lackner, F. Dimroth, and T. Hannappel. Efficient direct solar-to-hydrogen conversion by in situ interface transformation of a tandem structure. *Nature Communications*, **6**, (2015), pp. 1–7.

[362] I. Holmes-Gentle and K. Hellgardt. A versatile open-source analysis of the limiting efficiency of photo electrochemical water-splitting. *Scientific Reports*, **8**(1), (2018), p. 12807.

[363] P. Zhai, S. Haussener, J. Ager, R. Sathre, K. Walczak, *et al.* Net primary energy balance of a solar-driven photoelectrochemical water-splitting device. *Energy and Environmental Science*, **6**(8), (2013), pp. 2380–2389.

[364] J. R. Bolton, S. J. Strickler, and J. S. Connolly. Limiting and realizable efficiencies of solar photolysis of water. *Nature*, **316**(6028), (1985), pp. 495–500.

[365] M. Grätzel. Photoelectrochemical cells. *Nature*, **414**(6861), (2001), pp. 338–344.

[366] K. T. Fountaine, H. J. Lewerenz, and H. A. Atwater. Efficiency limits for photoelectrochemical water-splitting. *Nature Communications*, **7**(1), (2016), p. 13706.

[367] B. Neppolian, S. Sakthivel, B. Arabindoo, M. Palanichamy, and V. Murugesan. Degradation of textile dye by solar light using TiO_2 and ZnO photocatalysts. *Journal of Environmental Science and Health - Part A Toxic/Hazardous Substances and Environmental Engineering*, **34**(9), (1999), pp. 1829–1838.

[368] L. J. Guo, J. W. Luo, T. He, S. H. Wei, and S. S. Li. Photocorrosion-Limited Maximum Efficiency of Solar Photoelectrochemical Water Splitting. *Physical Review Applied*, **10**(6), (2018), p. 064059.

[369] R. Chaubey, S. Sahu, O. O. James, and S. Maity. A review on development of industrial processes and emerging techniques for production of hydrogen from renewable and sustainable sources. *Renewable and Sustainable Energy Reviews*, **23**, (2013), pp. 443–462.

[370] J. M. Buriak, C. Toro, and K. S. Choi. Chemistry of Materials for Water Splitting Reactions. *Chemistry of Materials*, **30**(21), (2018), pp. 7325–7327.

[371] J. Thomas. Drive Cycle Powertrain Efficiencies and Trends Derived from EPA Vehicle Dynamometer Results. *SAE International Journal of Passenger Cars - Mechanical Systems*, **7**(4), (2014), pp. 1374–1384.

[372] J. K. Nørskov, J. Rossmeisl, A. Logadottir, L. Lindqvist, J. R. Kitchin, *et al.* Origin of the overpotential for oxygen reduction at a fuel-cell cathode. *The Journal of Physical Chemistry B*, **108**(46), (2004), pp. 17886–17892.

[373] J. K. Nørskov, T. Bligaard, A. Logadottir, J. R. Kitchin, J. G. Chen, *et al.* Trends in the Exchange Current for Hydrogen Evolution. *Journal of The Electrochemical Society*, **152**(3), (2005), p. J23.

[374] A. P. Scott and L. Radom. Harmonic vibrational frequencies: An evaluation of Hartree-Fock, Møller-Plesset, quadratic configuration interaction, density functional theory, and semiempirical scale factors. *The Journal of Physical Chemistry*, **100**(41), (1996), pp. 16502–16513.

[375] J. Rossmeisl, A. Logadottir, and J. K. Nørskov. Electrolysis of water on (oxidized) metal surfaces. *Chemical Physics*, **319**(1-3), (2005), pp. 178–184.

[376] I. C. Man, H. Y. Su, F. Calle-Vallejo, H. A. Hansen, J. I. Martínez, *et al.* Universality in Oxygen Evolution Electrocatalysis on Oxide Surfaces. *ChemCatChem*, **3**(7), (2011), pp. 1159–1165.

[377] P. E. Blöchl. First-principles calculations of defects in oxygen-deficient silica exposed to hydrogen. *Physical Review B*, **62**(10), (2000), pp. 6158–6179.

[378] D. Chen and J. Ye. $SrSnO_3$ nanostructures: Synthesis, characterization, and photocatalytic properties. *Chemistry of Materials*, **19**(18), (2007), pp. 4585–4591.

[379] R. I. Eglitis. Ab initio calculations of $SrTiO_3$, $BaTiO_3$, $PbTiO_3$, $CaTiO_3$, $SrZrO_3$, $PbZrO_3$ and $BaZrO_3$ (001), (011) and (111) surfaces as well as F centers, polarons, KTN solid solutions and Nb impurities therein. *International Journal of Modern Physics B*, **28**(17), (2014), p. 1430009.

[380] R. I. Eglitis and A. I. Popov. Systematic trends in (0 0 1) surface ab initio calculations of ABO_3 perovskites. *Journal of Saudi Chemical Society*, **22**(4), (2018), pp. 459–468.

[381] V. E. Henrich and P. A. Cox. *The Surface Science of Metal Oxides*. Cambridge University Press, Cambridge, UK, 1996.

[382] P. Sirajudheen and K. M. Muhammed Ismayil. Synthesis Characterization and Photocatalytic Activity of $SnTiO_3$ Prepared by Co-Precipitation Peroxide Method. *Chemical Sciences Journal*, **6**(4), (2015), p. 1000111.

[383] J. Halldin Stenlid, A. J. Johansson, and T. Brinck. The local electron attachment energy and the electrostatic potential as descriptors of surface–adsorbate interactions. *Physical Chemistry Chemical Physics*, **21**(31), (2019), pp. 17001–17009.

[384] S. Trasatti. The absolute electrode potential: an explanatory note (Recommendations 1986). *Pure and Applied Chemistry*, **58**(7), (1986), pp. 955–966.

[385] J. Rumble, editor. *CRC Handbook of CHemstry and Physics*. CRC Press, 100th edition, 2019.

[386] W. F. Zhang, J. Tang, and J. Ye. Photoluminescence and photocatalytic properties of $SrSnO_3$ perovskite. *Chemical Physics Letters*, **418**(1-3), (2006), pp. 174–178.

[387] H. R. Liu, J. H. Yang, H. J. Xiang, X. G. Gong, and S. H. Wei. Origin of the superior conductivity of perovskite Ba(Sr)SnO_3. *Applied Physics Letters*, **102**(11), (2013), p. 112109.

[388] C. C. Fulton, G. Lucovsky, and R. J. Nemanich. Electronic properties of the Zr-ZrO_2-SiO_2-Si (100) gate stack structure. *Journal of Applied Physics*, **99**(6), (2006), p. 063708.

[389] J. Y. Lim, G. Rahman, S. Y. Chae, K.-Y. Lee, C.-S. Kim, *et al.* Highly stable RuO_2/SnO_2 nanocomposites as anode electrocatalysts in a PEM water electrolysis cell. *International Journal of Energy Research*, **38**(7), (2014), pp. 875–883.

[390] V. Pfeifer, P. Erhart, S. Li, K. Rachut, J. Morasch, *et al.* Energy band alignment between anatase and rutile TiO_2. *The Journal of Physical Chemistry Letters*, **4**(23), (2013), pp. 4182–4187.

[391] H. Dong, Z. Zan, and X. Zhou. Theoretical investigation on structures, stabilities, and hydrolysis reactions of small RuO_2 nanoclusters. *Chinese Journal of Chemistry*, **32**(6), (2014), pp. 527–537.

[392] T. Hisatomi, K. Takanabe, and K. Domen. Photocatalytic Water-Splitting Reaction from Catalytic and Kinetic Perspectives. *Catalysis Letters*, **145**(1), (2015), pp. 95–108.

[393] N. S. McCool, J. R. Swierk, C. T. Nemes, C. A. Schmuttenmaer, and T. E. Mallouk. Dynamics of Electron Injection in SnO2/TiO2 Core/Shell Electrodes for Water-Splitting Dye-Sensitized Photoelectrochemical Cells. *The Journal of Physical Chemistry Letters*, **7**(15), (2016), pp. 2930–2934.

[394] T. Jafari, E. Moharreri, A. S. Amin, R. Miao, W. Song, *et al.* Photocatalytic water splitting - The untamed dream: A review of recent advances. *Molecules*, **21**(7), (2016), p. 900.

[395] I. Bespalov, M. Datler, S. Buhr, W. Drachsel, G. Rupprechter, *et al.* Initial stages of oxide formation on the Zr surface at low oxygen pressure: An in situ FIM and XPS study. *Ultramicroscopy*, **159**, (2015), pp. 147–151.

[396] H. Kroemer. Nobel Lecture: Quasielectric fields and band offsets: teaching electrons new tricks. *Reviews of Modern Physics*, **73**(3), (2001), pp. 783–793.

[397] B. Jamtveit and P. Meakin, editors. *Growth, Dissolution and Pattern Formation in Geosystems*. Springer Netherlands, Dordrecht, 1999.

[398] R. L. Anderson. Germanium-Gallium Arsenide Heterojunctions. *IBM Journal of Research and Development*, **4**(3), (1960), pp. 283–287.

[399] D. O. Scanlon, C. W. Dunnill, J. Buckeridge, S. A. Shevlin, A. J. Logsdail, *et al.* Band alignment of rutile and anatase TiO_2. *Nature Materials*, **12**(9), (2013), pp. 798–801.

[400] R. Saive, H. Emmer, C. T. Chen, C. Zhang, C. Honsberg, *et al.* Study of the interface in a GaP/Si heterojunction solar cell. *IEEE Journal of Photovoltaics*, **8**(6), (2018), pp. 1568–1576.

[401] S.-M. Lee, D. G. Cahill, and R. Venkatasubramanian. Thermal conductivity of Si–Ge superlattices. *Applied Physics Letters*, **70**(22), (1997), pp. 2957–2959.

[402] S. P. Hepplestone and G. P. Srivastava. Lattice dynamics and thermal properties of phononic semiconductors. *Physical Review B*, **84**(11), (2011), p. 115326.

[403] L. Wang, X. H. Zhong, Y. X. Zhao, J. S. Yang, S. Y. Tao, *et al.* Effect of interface on the thermal conductivity of thermal barrier coatings: A numerical simulation study. *International Journal of Heat and Mass Transfer*, **79**, (2014), pp. 954–967.

[404] R. M. Martin. Atomic reconstruction at polar interfaces of semiconductors. *Journal of Vacuum Science and Technology*, **17**(5), (1980), pp. 978–981.

[405] S. P. Hepplestone and P. V. Sushko. Effect of metal intermixing on the Schottky barriers of Mo(100)/GaAs(100) interfaces. *Journal of Applied Physics*, **116**(19), (2014), p. 193703.

[406] F. Liu, D. Y. Xie, M. Bugnet, T. Majdi, J. S. Preston, *et al.* Temperature-Induced Atomic Reconstruction At Au/$MgAl_2O_4$ Interfaces. *Advanced Materials Interfaces*, **5**(12), (2018), p. 1701664.

[407] H. Yoo, R. Engelke, S. Carr, S. Fang, K. Zhang, *et al.* Atomic and electronic reconstruction at the van der Waals interface in twisted bilayer graphene. *Nature Materials*, **18**(5), (2019), pp. 448–453.

[408] S. P. Hepplestone and G. P. Srivastava. Theory of interface scattering of phonons in superlattices. *Physical Review B*, **82**(14), (2010), p. 144303.

[409] T. Wu and P. Gao. Development of perovskite-type materials for thermoelectric application. *Materials*, **11**(6), (2018), p. 999.

[410] G. Schusteritsch, S. P. Hepplestone, and C. J. Pickard. First-principles structure determination of interface materials: The Ni_xInAs nickelides. *Physical Review B*, **92**(5), (2015), p. 054105.

[411] B. Hinterleitner, I. Knapp, M. Poneder, Y. Shi, H. Müller, *et al.* Thermoelectric performance of a metastable thin-film Heusler alloy. *Nature*, **576**(7785), (2019), pp. 85–90.

[412] W. H. Zou, X. D. Han, R. Wang, Z. Zhang, W. Z. Zhang, *et al.* TEM and HREM study of the interphase interface structure of Ti_3Ni_4 precipitates and parent phase in an aged TiNi shape memory alloy. *Materials Science and Engineering A*, **219**(1-2), (1996), pp. 142–147.

[413] L. Zou, J. Li, D. Zakharov, E. A. Stach, and G. Zhou. In situ atomic-scale imaging of the metal/oxide interfacial transformation. *Nature Communications*, **8**(1), (2017), p. 307.

[414] E. D. Specht, G. E. Ice, C. J. Peters, C. J. Sparks, N. Lucas, *et al.* X-ray-diffraction measurement of interface structure in GaAs/Si(001). *Physical Review B*, **43**(15), (1991), pp. 12425–12430.

[415] H. Chen. Surface/interface X-ray diffraction. *Materials Chemistry and Physics*, **43**(2), (1996), pp. 116–125.

[416] D. A. Bonnell, I. Solomon, G. S. Rohrer, and C. Warner. Direct measurement of local properties of interfaces with scanning tunneling microscopy. *Acta Metallurgica Et Materialia*, **40**(SUPPL.), (1992), pp. 161–171.

[417] N. I. Plusnin. Application of AES and EELS for surface/interface characterization. *Journal of Electron Spectroscopy and Related Phenomena*, **137-140**(SPEC. ISS.), (2004), pp. 161–164.

[418] M. J. Zachman, J. A. Hachtel, J. C. Idrobo, and M. Chi. Emerging Electron Microscopy Techniques for Probing Functional Interfaces in Energy Materials. *Angewandte Chemie - International Edition*, pp. 1384–1396.

[419] G. W. Watson, E. T. Kelsey, N. H. de Leeuw, D. J. Harris, and S. C. Parker. Atomistic simulation of dislocations, surfaces and interfaces in MgO. *Journal of the Chemical Society, Faraday Transactions*, **92**(3), (1996), p. 433.

[420] G. W. Watson, P. M. Oliver, and S. C. Parker. Computer simulation of the structure and stability of forsterite surfaces. *Physics and Chemistry of Minerals*, **25**(1), (1997), pp. 70–78.

[421] A. M. Raclariu, S. Deshpande, J. Bruggemann, W. Zhuge, T. H. Yu, *et al.* A fast method for predicting the formation of crystal interfaces and heterocrystals. *Computational Materials Science*, **108**(PA), (2015), pp. 88–93.

[422] K. Mathew, A. K. Singh, J. J. Gabriel, K. Choudhary, S. B. Sinnott, *et al.* MPInterfaces: A Materials Project based Python tool for high-throughput computational screening of interfacial systems. *Computational Materials Science*, **122**, (2016), pp. 183–190.

[423] D. Stradi, L. Jelver, S. Smidstrup, and K. Stokbro. Method for determining optimal supercell representation of interfaces. *Journal of Physics: Condensed Matter*, **29**(18), (2017), p. 185901.

[424] L. Jelver, P. M. Larsen, D. Stradi, K. Stokbro, and K. W. Jacobsen. Determination of low-strain interfaces via geometric matching. *Physical Review B*, **96**(8), (2017), p. 085306.

[425] S. von Alfthan, P. D. Haynes, K. Kaski, and A. P. Sutton. Are the Structures of Twist Grain Boundaries in Silicon Ordered at 0 K? *Physical Review Letters*, **96**(5), (2006), p. 055505.

[426] A. L. Chua, N. A. Benedek, L. Chen, M. W. Finnis, and A. P. Sutton. A genetic algorithm for predicting the structures of interfaces in multicomponent systems. *Nature Materials*, **9**(5), (2010), pp. 418–422.

[427] G. Schusteritsch and C. J. Pickard. Predicting interface structures: From $SrTiO_3$ to graphene. *Physical Review B*, **90**(3), (2014), p. 035424.

[428] A. K. Lenstra, H. W. Lenstra, and L. Lovász. Factoring polynomials with rational coefficients. *Mathematische Annalen*, **261**(4), (1982), pp. 515–534.

[429] A. K. Geim and I. V. Grigorieva. Van der Waals heterostructures. *Nature*, **499**(7459), (2013), pp. 419–425.

[430] I. Novak. Molecular isomorphism. *European Journal of Physics*, **16**(4), (1995), pp. 151–153.

[431] I. Galanakis, G. Bihlmayer, V. Bellini, N. Papanikolaou, R. Zeller, *et al.* Broken-bond rule for the surface energies of noble metals. *Europhysics Letters*, **58**(5), (2002), pp. 751–757.

[432] Y. Y. Sun, H. Xu, Y. P. Feng, A. C. Huan, and A. T. Wee. Rule for structures of open metal surfaces. *Physical Review Letters*, **93**(13), (2004), p. 136102.

[433] J. E. Northrup and S. Froyen. Structure of GaAs(001) surfaces: The role of electrostatic interactions. *Physical Review B*, **50**(3), (1994), pp. 2015–2018.

[434] G. Srivastava and S. Jenkins. Atomic geometry and bonding on the GaAs(001)-$\beta 2(2 \times 4)$ surface from *ab initio* pseudopotential calculations. *Physical Review B*, **53**(19), (1996), pp. 12589–12592.

[435] S. Piskunov, E. A. Kotomin, and E. Heifets. The electronic and atomic structure of $SrTiO_3$, $BaTiO_3$, and $PbTiO_3$(001) surfaces: Ab initio DFT/HF hybrid calculations. *Microelectronic Engineering*, **81**(2-4), (2005), pp. 472–477.

[436] S. Piskunov, E. A. Kotomin, E. Heifets, J. Maier, R. I. Eglitis, *et al.* Hybrid DFT calculations of the atomic and electronic structure for ABO_3 perovskite (001) surfaces. *Surface Science*, **575**(1-2), (2005), pp. 75–88.

[437] Y. L. Lee and D. Morgan. *Ab initio* defect energetics of perovskite (001) surfaces for solid oxide fuel cells: A comparative study of $LaMnO_3$ versus $SrTiO_3$ and $LaAlO_3$. *Physical Review B*, **91**(19), (2015), p. 195430.

[438] J. J. Brown, Z. Ke, W. Geng, and A. J. Page. Oxygen Vacancy Defect Migration in Titanate Perovskite Surfaces: Effect of the A-Site Cations. *The Journal of Physical Chemistry C*, **122**(26), (2018), pp. 14590–14597.

[439] S. Jenkins and G. Srivastava. Structure and energetics of segregated and nonsegregated Ge(001)/Si(2×1). *Physical Review B*, **57**(15), (1998), pp. 8794–8796.

[440] R. J. Dixon, C. F. McConville, S. J. Jenkins, and G. P. Srivastava. Structure and stability of the Si(001) $c(4 \times 4)$-Sb surface. *Physical Review B*, **57**(20), (1998), pp. R12701–R12704.

[441] R. H. Miwa and G. P. Srivastava. Energetic stability, equilibrium geometry, and electronic properties of Bi-induced Si (001) - $(2 \times n)$ surfaces. *Physical Review B*, **74**(3), (2006), p. 035301.

[442] J. Harris. Simplified method for calculating the energy of weakly interacting fragments. *Physical Review B*, **31**(4), (1985), pp. 1770–1779.

[443] G. D. Bellchambers and F. R. Manby. An approximate density-functional method using the Harris-Foulkes functional. *The Journal of Chemical Physics*, **135**(8), (2011), p. 084105.

[444] K. Lejaeghere, V. Van Speybroeck, G. Van Oost, and S. Cottenier. Error estimates for solid-state density-functional theory predictions: An overview by means of the ground-state elemental crystals. *Critical Reviews in Solid State and Materials Sciences*, **39**(1), (2014), pp. 1–24.

[445] K. Lejaeghere, G. Bihlmayer, T. Bjorkman, P. Blaha, S. Blugel, *et al.* Reproducibility in density functional theory calculations of solids. *Science*, **351**(6280), (2016), pp. aad3000–aad3000.

[446] S. J. Leon, Å. Björck, and W. Gander. Gram-Schmidt orthogonalization: 100 years and more. *Numerical Linear Algebra with Applications*, **20**(3), (2013), pp. 492–532.